Karlsruher Institut für Technologie

Ytterbium ions and color centers in silicon carbide as cavity-integrated quantum nodes with near-infrared optical transitions

Zur Erlangung des akademischen Grades eines
DOKTORS DER NATURWISSENSCHAFTEN (Dr. rer. nat.)

von der KIT-Fakultät für Physik des
Karlsruher Instituts für Technologie (KIT)
angenommene

DISSERTATION

von

M.Sc. Jannis Hessenauer

Tag der mündlichen Prüfung: 23.05.2025
Erster Gutachter: Prof. Dr. David Hunger
Zweiter Gutachter: Prof. Dr. Heinz Kalt

The presence of those seeking the truth
is infinitely to be preferred
to the presence of those
who think they've found it.

TERRY PRATCHETT

Zusammenfassung

Quantentechnologien aller Art, wie Quantencomputer und Quantensensoren, entwickeln sich rasant fort. Daraus resultiert ein großes technologisches Bedürfnis, Quanteninformationen zwischen solchen lokalen Systemen über große Distanzen hinweg auszutauschen. Hierfür benötigt man effiziente Quanten-Netzwerkschnittstellen, die es erlauben Quanteninformationen auf Photonen zu übertragen. Optisch aktive Defektzentren und dotierte Ionen in Festkörpern sind ideale Kandidaten für solche Quanten-Netzwerkschnittstellen, da sie sowohl über einen langlebigen und kohärenten Spin-Freiheitsgrad, als auch kohärente optische Übergange verfügen. Um die optischen Übergänge effizient zu machen und auf diese Weise hohe Kommunikationsraten zu erzielen, müssen diese photonisch verstärkt werden. Dies kann durch die Kopplung an faserbasierte Fabry-Pérot Mikroresonatoren hoher Güte erzielt werden. Diese Arbeit untersucht die Eignung von Ytterbiumionen sowie Defektzentren in Siliziumkarbid als Quantennetzwerkschnittstellen in solch einer resonatorbasierten Geometrie. Zu Beginn werden Ytterbiumdotanden in nanoskaligen Kristallen spektroskopisch untersucht. Diese zeigen schmale Ensemble-Linienbreiten bei kryogenen Temperaturen. Mit Hilfe von Sättigungspektroskopie wurde zum ersten Mal für dieses Material eine Obergrenze für die optische Linienbreite eines einzelnen Ions von 5 MHz bestimmt. Zudem wurde gezeigt, dass sich diese Nanokristalle in einen faserbasierten Resonatoraufbau integrieren lassen, der optische Spektroskopie erlaubt. Anschließend wurden die optischen Eigenschaften von Ytterbiumionen in verschiedenen organischen Molekülen charakterisiert. Diese unterscheiden sich teilweise deutlich voneinander. Durch einen systematischen Vergleich wurde versucht, diese Variationen durch die molekulare Struktur zu erklären. Insbesondere für die nichtradiative Zerfallsrate wurden dabei erste Korrelationen gefunden. Schließlich wurden Experimente an Farbzentren in Siliziumkarbid in einem kryogenen Resonatorsystem durchgeführt. Dafür wurde eine wenige Mikrometer dicke Membran aus Siliziumkarbid in einen faserbasierten Hohlraumresonator integriert. Das Resonatorsystem wurde sorgfältig charakterisiert und für gut geeignet befunden, da nur minimale Verluste durch die Membran entstanden. Durch die hohe spektrale Selektivität des Resonator konnten die kohärenten Übergänge einzelner Farbzentren bei kryogenen Temperaturen aufgelöst werden, was durch Analyse der Photonenstatistik verifiziert wurde. Schließlich wurde die Purcell-Verstärkung anhand einer verstimmungsabhängigen Lebenszeitmessung bestimmt. Durch die Kopplung an den Resonator wird der kohärente Übergang eines einzelnen Farbzentrums bis zu 13-fach verstärkt, was zu einer hohen Rate an kohärenten Einzelphotonen führt.

Abstract

Quantum computers and quantum sensors, among other quantum technologies, continue to rapidly develop. This results in a great technological need to exchange quantum information between these local systems over long distances. Such quantum networks require efficient quantum network nodes, which allow to efficiently map quantum information onto photons. Optically active defects and dopants in solid state systems are ideal candidates for quantum network nodes, because they can posses a long-lived and coherent spin degree of freedom, as well as coherent optical transitions. In order to make these optical transitions more efficient and thereby achieve high communication rates, they need to be photonically enhanced. This can be achieved by coupling them to fiber-based Fabry-Pérot micro resonators with high quality factors. This work investigates the suitability of ytterbium dopants and defect centers in silicon carbide as quantum network nodes in such a resonator-based geometry. At the beginning, ytterbium dopants in nanoscale crystals are investigated spectroscopically. They show narrow inhomogeneous ensemble linewidths at cryogenic temperatures. Using saturation spectroscopy techniques, an upper limit for the single ion linewidth of 5 MHz was determined for the first time in this material system. Additionally, it was demonstrated that these nanocrystals can be integrated into a fiber-based resonator in a manner that allows for optical spectroscopy. Subsequently, the optical properties of ytterbium ions in different organic molecules were characterized. The ions properties were found to differ significantly among each other, depending on the coordinating organic ligands. By a systematic comparison an attempt was made to link these variations to the chemical structure. First correlations were found especially for the non-radiative decay rate. Finally, experiments were conducted on color centers in silicon carbide inside a cryogenic resonator system. Therefore, a few microns thick silicon carbide membrane was integrated into a fiber-based cavity. The cavity system was characterized carefully and found to be well suited, because only minimal losses were caused by the membrane. Utilizing the high spectral selectivity of the resonator, the coherent transitions of single color centers, verified by the analysis of their photon statistics, could be spectrally resolved. Finally, the Purcell enhancement was determined by a detuning-dependent lifetime measurement. By coupling it to the resonator, the coherent transition of a single color center could be enhanced 13-fold, resulting in a high rate of single, coherent photons.

Contents

1. Introduction

Quantum technologies are at the forefront of technology development. The United Nations have declared the year 2025, in which this thesis is submitted, as the "International Year of Quantum Science and Technology" [1], highlighting the transformative potential of these technologies, and claiming that "quantum science and technology is vital for economic advancement and that its potential applications could address basic needs such as food, health, sustainable cities and communities, communications, clean water and energy, and support climate action" [1]. Certainly, it will be a long time until these technologies will have such a widespread and direct impact on society. However, it is undeniable that, as researchers become able to detect and manipulate single quantum systems, technological applications of these quantum systems arise [2]. Individual quantum systems can be used as extremely efficient sensors [3, 4, 5]. Quantum computers, while still some way away from offering an universal advantage over classical computers, have been realized in different implementations, and are being pushed forwards in all directions [6, 7]. It has been proposed that they could be used to simulate complex quantum systems, such as the quantum mechanical structure of molecules, which for example could guide medical drug design [8]. One of the main motivators for the development of quantum computers is the existence of Shor's algorithm, who showed that a quantum computer can factorize prime numbers much faster than the most efficient classical algorithms [9]. Because most of modern cryptography relies on factorizing large prime numbers, any actor who could first get their hand on such a device could potentially decrypt sensitive information. This makes it clear why the United States, the European Union and China all have identified quantum technologies as a critical area of research and development [10].
Luckily, quantum mechanics provides a way of secure communication. By encoding information in the quantum state of a photon, a single quantum of light, any potential eavesdropping attack can be detected. This is due to the no-cloning theorem, which states that a quantum state can never be duplicated, or "cloned" [11, 12]. In other words, any measurement by a potential eavesdropper on the quantum state collapses the wavefunction, which changes the result for the original receiver, revealing the attack. Besides the obvious security implications of quantum communication, similar schemes can be used to share quantum information between individual quantum systems, such as quantum sensors or quantum computers, improving the capability of the combined system beyond that of an individual system [13, 14, 15].

Quantum networks

Individual quantum systems that are linked together are referred to as quantum networks. Their fundamental building blocks are quantum nodes, which are local quantum systems that might posses different local processing or sensing capabilities. These nodes are linked to each other by quantum channels in order to form a quantum network [16, 17]. The only sensible choice for quantum channels that need to cover longer distances are photonic channels, which are either realized as optical fiber links or using satellite-based free-space communication [18, 19]. This is because photons interact so weakly with the environment, that they retain the quantum information under ambient conditions [20]. Consequentially, the nodes need to be able to map the quantum information of the local qubit implementation onto a a photon. Often, this is realized by encoding the local quantum information in the spin degree of freedom of an atom or atom-like system. The spin energy levels are connected to optically excited states, which then allows to coherently map the quantum information onto a photon, to be sent over the quantum channel. This important realization of a quantum node is therefore called a **spin-photon interface**. Such spin-photon interfaces have been implemented in different systems, such as various defect centers in diamond [21, 22, 23], silicon [24] and silicon carbide [25, 26], trapped atoms in vacuum [27], and rare earth dopants in solid state hosts [28]. These implementations differ in the coherence and capabilities of the local qubit, the efficiency of the photonic channel, and the experimental overhead and potential scalability. It is clear that no best candidate has yet been found, and it is doubtful if there will ever be one best candidate. Instead, a hybridized approach, with different quantum nodes and channels for different application profiles, seems to be realistic. Consequentially, a multitude of quantum systems are currently investigated for their suitability as quantum nodes.

Efficient solid state quantum nodes

In this thesis, I investigate two different possible implementation of solid state spin-photon interfaces: ytterbium ion dopants in multiple host materials, and silicon vacancy centers in silicon carbide. Both exhibit optical transitions in the near infrared region of the electromagnetic spectrum, and a long-lived spin degree of freedom. The solid state nature is reflected in the fact that they are individual quantum systems located inside a host crystal. Solid state quantum systems are especially of interest because they can be scaled up efficiently. In addition, the spin used to create spin-photon entanglement, can be coupled to nearby quantum systems, significantly increasing the local processing capabilities of the node [29, 30]. One drawback of solid state systems is that they are intrinsically noisy, which makes careful characterization and material engineering mandatory to optimize the quantum properties [31].
One fundamental limitation of the efficiency of a quantum network are the entanglement generation rates, that is how long it takes to generate entanglement between two

nodes. In order to increase this rate, there are two important tuning knobs. First of all, the harnessed photon rate from an individual node must be made as large as possible. Secondly, the losses of the transmission channel must be minimized.
The first task can be accomplished by integrating the quantum node with an optical resonator [32, 33, 34]. Such resonators can boost the light matter interaction, thereby significantly increasing the coherent photon rates and possibly even making the spin-photon coupling deterministic, ensuring interaction of a photon with the node. The channel losses are, for optical fiber links, governed by the fiber losses, which scale exponentially with the fiber length. To minimize the losses, it is desirable to operate the quantum channel in the telecommunication C-Band ($\lambda \approx 1550\,\mathrm{nm}$), where fiber losses are minimal. However, the emission wavelength is governed by the investigated quantum system, and nodes that emit at this wavelength can have other disadvantageous properties. It is worth to note that quantum frequency conversion can be used to coherently convert the photon wavelength of visible or near infrared emitters to the telecommunication C-Band using non-linear optical processes. This is however experimentally challenging and causes additional conversion losses [35, 36]. Therefore, quantum nodes emitting in the near-infrared range $\lambda = 900\,\mathrm{nm}$ to $1000\,\mathrm{nm}$ constitute an interesting alternative. The fiber losses are still below 1 dB/km, almost an order of magnitude smaller than for emitters emitting in the visible range (6 dB/km) [32]. Simultaneously, these wavelengths facilitate the integration with highly resonant structure, because the often limiting intrinsic absorption and surface scattering losses scale favorably with longer wavelengths. Therefore, near-infrared emitting quantum nodes warrant investigation of their optical properties and how they can be combined with optical cavities to form an efficient spin-photon interface, which one day may serve as a node in a quantum network.

Outline of this thesis

This thesis is structured as follows: In Chapter 2, I introduce **fiber-based Fabry-Pérot cavities**, the resonator platform of choice for this work. I present the important figures of merit that characterize the resonator, and discuss the fabrication and parameter design choices of the resonators used in this work. I present how these resonators can be used to enhance the light-matter interaction. Finally, I characterize a novel fabrication method of Fabry-Pérot resonators using 3D-direct laser writing. I show that this method, while limiting the resonator performance, offers a high degree of control over the resonator geometry and its related properties.

In the next chapter, I discuss one of the potential quantum nodes investigated in this work: **ytterbium dopants in yttria nanocrystals**. I briefly introduce their optical and spin properties and discuss their potential for quantum networking applications. Then, I present a characterization of their room temperature properties, and show that they

can be integrated in a fiber-based Fabry-Pérot microcavity. I confirm this by observing characteristic fluorescence signals using cavity-enhanced spectroscopy. Finally, I investigate their spectroscopic properties at cryogenic temperatures. I observe signatures from dopants in two different crystal lattice sites and determine the homogeneous linewidth of the dopants, using a saturation spectroscopic technique.

In the next section, I apply the toolbox developed for cryogenic spectroscopy of Ytterbium ions to the investigation of **Ytterbium based molecular materials**. I motivate the investigation of this novel material class and discuss the peculiarities of these systems when compared to the more conventional host in the previous section. I spectroscopically investigate molecular crystals formed by the molecule Yb-Trensal, which has already shown excellent spin properties, and observe strong optical transitions and narrow optical inhomogeneous linewidths, demonstrating potential for optical readout of the spin degree of freedom. In order to verify design principles employed during the synthesis of these molecules, I systematically compare five different molecular materials and their spectroscopic properties, and find correlations that corroborate these hypotheses.

Finally, In the last chapter, I turn towards the **investigation of defect centers in silicon carbide by cryogenic cavity spectroscopy**. After briefly introducing this emitter system, I show that it lends itself uniquely to the integration into a Fabry-Pérot cavity in the form of a thin membrane. I study the emerging cavity-membrane system and find excellent agreement with the observed behavior and the theoretical model. The resonator losses introduced by the membrane are minimal and its natural birefringence ensures an ideal coupling of the cavity to the emitter. Finally, I demonstrate cavity-enhanced photon emission of a single defect at cryogenic temperatures. The resonator enhancement is carefully characterized and leads to a high observed rate of coherent photons, demonstrating a clear enhancement of light-matter interaction using an optical cavity.

I conclude this thesis by summarizing the results obtained in this work and discuss their potential for further experiments.

2. Fiber-based Fabry-Pérot-resonators

Optical resonators confine and store light whose frequency matches the resonance frequency of the resonator. Their applications are manifold: They are used as filters, frequency references, for sensing applications and are an integral part of lasers. They also play an important role in quantum optics: By coupling an atomic transition to a resonance of an optical resonator, one can enhance the light-matter interaction up to the point where the interaction becomes deterministic, meaning a single photon will always interact with the atom. This is a desirable property for a node in a quantum network, where one would like to create spin-photon entanglement at the press of a button. Further increasing the coupling leads to interesting new regimes of physics, the strong coupling regime, where the atomic and photonic character of the excitation can not be separated anymore [37]. The coupling of a quantum system to a resonator is treated in the formalism of cavity quantum electrodynamics (cQED).[1] In the following, I will introduce the optical resonators utilized in this work: fiber-based Fabry-Pérot cavity (FFPC). I will discuss the quantities used to characterize the resonator performance. I will report on the fabrication and operation of the FFPCs used in this work. Then, I will summarize the Purcell regime of cQED, which is relevant for the experiments in this thesis. Finally, I will present results on an alternative way of fabricating FFPCs, based on direct laser writing.

2.1. Basics of Fabry-Pérot resonators

The Fabry-Pérot resonator is the conceptually most simple realization of an optical resonator. It is formed by two opposing mirrors. Incoupled light is reflected between the two mirrors, confining the light, and leading to interference of the reflected waves. The interference is constructive when the distance between the two mirrors d is an integer multiple of a wavelength λ:

$$d = q\frac{\lambda}{2}, \quad q \in \mathbb{N}^+ \tag{2.1}$$

where q is called the longitudinal mode order. The constructive interference leads to the formation of a standing wave, with q nodes and $q + 1$ antinodes. This simple

[1] A cavity is a specific implementation of an optical resonator, but the terms are often used interchangeably.

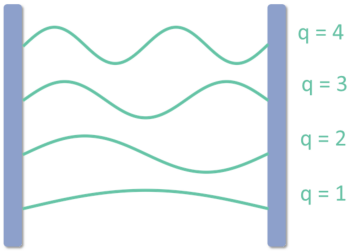

(a) Simple illustration of a Fabry-Pérot cavity

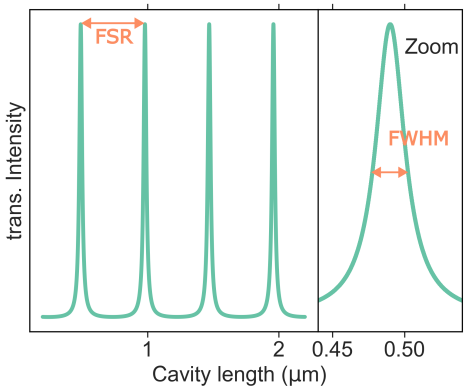

(b) Exemplary transmission spectrum of a Fabry-Pérot resonator.

Figure 2.1.: Simple illustration of a Fabry-Pérot cavity and its resonances. A standing wave forms when the cavity is length is an integer q multiple of half a wavelength.

picture considers perfect, planar mirrors with reflectivity, $R = 1$, and an incoming monochromatic plane wave and is sketched in Figure 2.1. In reality, the light experiences losses inside the cavity each roundtrip. The losses per round trip stem from:

- The finite mirror transmission T_1 and T_2 at the first and second mirror.
- Absorption A_1 and A_2 at the first and second mirror.
- Scattering S_1 and S_2 at the mirror surfaces due to residual surface roughness.
- Additional extinction E, for example due to a scattering and/or absorbing sample inside the resonator.

For small round trip losses, which is the case for the resonators used in this work, the individual cavity resonances can be approximated as Lorentizan lines [38, 39]:

$$I_{\text{trans}} \approx I_0 T_1 T_2 \left(\frac{\mathcal{F}}{\pi}\right)^2 \frac{\frac{1}{4}\left(\frac{\pi}{\mathcal{F}}\right)^2}{\frac{1}{4}\left(\frac{\pi}{\mathcal{F}}\right)^2 + (\varphi_0 - \hat{\varphi})^2}, \tag{2.2}$$

$$\tag{2.3}$$

where we have defined the finesse $\mathcal{F}$ as:

$$\mathcal{F} = \frac{2\pi}{\sum \text{All Roundtrip Losses}} = \frac{2\pi}{T_1 + T_2 + A_1 + A_2 + S_1 + S_2 + E}. \tag{2.4}$$

An exemplary transmission spectrum of a cavity is depicted in Figure 2.1.

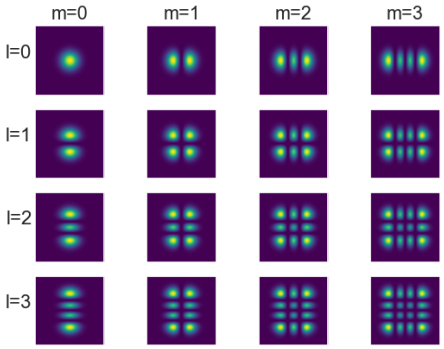

(a) Transversal intensity profile of the first 16 Hermite-Gauss modes.

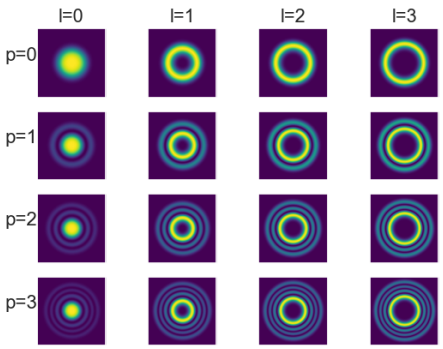

(b) Transversal intensity profile of the first 16 Laguerre-Gauss modes.

Figure 2.2.: Transversal intensity profile of the first 16 Hermite-Gauss and Laguerre-Gauss modes.

2.1.1. Transversal mode profile

In order to derive the spatial modes of the resonator modes, one needs to solve the Helmholtz equation in the paraxial approximation for fixed boundary conditions imposed by the geometry of the mirrors. For spherical mirrors, the fundamental solution is the well-known Gaussian beam, characterized by its slowly varying envelope [40]:

$$A(\rho, z) = A_0 \frac{w_0}{w(z)} \exp\left(-\frac{\rho^2}{w^2(z)}\right) \exp\left(-ikz - ik\frac{\rho^2}{2R(z)} + i\zeta(z)\right), \tag{2.5}$$

with $\rho = \sqrt{x^2 + y^2}$ and:

$$w_0 = \sqrt{\frac{\lambda z_0}{\pi}}, \tag{2.6}$$

$$w(z) = w_0 \sqrt{1 + \left(\frac{z}{z_0}\right)^2}, \tag{2.7}$$

$$R(z) = z\left(1 + \left(\frac{z_0}{z}\right)^2\right), \tag{2.8}$$

$$\zeta(z) = \arctan\left(\frac{z}{z_0}\right). \tag{2.9}$$

It is fully determined by the wavelength, λ, and the minimal beam waist, w_0. The *Rayleigh range* z_0 is related to the depth of focus of the beam and defines the distance over which the beam waist expands by a factor of $\sqrt{2}$ from the focus. The phase term $ik\frac{\rho^2}{2R(z)}$ is

related to the parabolic wavefront curvature $R(z)$. $\zeta(z)$ is the *Gouy phase*, which causes an additional phase shift of π as the beam passes the focus. An attempt at an intuitive explanation of the Gouy phase can be found in reference [41].
Higher-order Gaussian beams are solutions to the paraxial Helmholtz equation that share the same parabolic wavefront, and therefore propagate in the same manner, but have a different transverse mode profile. Depending on the mirror symmetry, either Hermite-Gaussian, characterized by Hermite polynomials $\{H_l(x), H_m(y)\}$, or Laguerre-Gaussian modes, characterized by generalized Laguerre polynomials $L_p^{|l|}(\rho)$ are observed. The first few modes of both families are displayed in Figure 2.2.
Importantly, higher order modes experience an additional Gouy phase $(l + m + 1)\zeta(z)$ [40]. Consequentially, they appear at slightly shifted spectral positions compared to the fundamental mode. The resonance condition for a a rotational symmetric mirror profile with radius of curvature R_c for a plano-concave resonator in terms of cavity separation reads:

$$d_{qlm} = \frac{\lambda}{2}\left(q + \frac{l+m+1}{\pi}\arccos\left(\sqrt{1-\frac{d}{R_c}}\right)\right). \tag{2.10}$$

A more detailed treatment can be found for example in reference [42]. Which mode shape is observed for a resonator depends largely on the degree of symmetry of the resonator mirrors. When the spherical symmetry is broken significantly, the eigenmodes are better described as Hermite-Gaussian modes, while for spherical symmetric mirror profiles, the shape will be Laguerre-Gaussian. More precisely, Laguerre-Gaussian modes are observed when the cavity resonances for light polarized along the long and short axes of the mirror are degenerate in frequency.

2.1.2. Figures of merit

After sketching the derivation of the resonances of a resonator, I will in this section summarize the figures of merit for optical resonators, following reference [38].

Free spectral range

The spectral separation of two fundamental resonances is called the free spectral range (FSR). It is often useful to express the FSR in terms of the resonant frequencies of a resonator for a fixed cavity length d:

$$\Delta_{\mathrm{FSR}} = \frac{c}{2d}. \tag{2.11}$$

Finesse

The finesse $\mathcal{F}$ of a resonator is determined by the ratio of the cavity FSR Δ_{FSR} to the cavity linewidth $\Delta\nu$:

$$\mathcal{F} = \frac{\Delta_{\mathrm{FSR}}}{\Delta\nu} = \frac{2\pi}{\sum \text{Roundtrip losses}}. \tag{2.12}$$

The finesse $\mathcal{F}$ of a FP cavity depends only on the roundtrip losses of the cavity and is notably independent on the cavity length, as long as the losses are independent of the cavity length. This is usually a good assumption as long as the resonator is within the stability range and does not experience resonant mode mixing which can cause sharp drops in the finesse at specific mode orders [43, 44]. An instructive way to think about the finesse is the number of round trips the light takes in the cavity. More accurately, the light intensity will be reduced by $\frac{1}{\mathrm{e}}$ after $\frac{\mathcal{F}}{\pi}$ roundtrips. Experimentally, the finesse is determined in this work by measuring the free spectral range and cavity linewidth in cavity length units by recording a cavity transmission spectrum. By fitting the fundamental mode orders with a series of Lorentzian peaks, the linewidth and FSR can be determined in one measurement.

Quality factor

The quality factor Q is a measure for how long light is stored inside a resonator. It can be expressed as the ratio of the absolute frequency of a resonance ν and its linewidth in frequency units $\Delta\nu$:

$$Q = \omega\tau = \frac{\nu}{\Delta\nu}. \tag{2.13}$$

τ is the decay time constant of the light intensity stored inside the resonator, and in a particle picture can be thought of as the mean cavity photon lifetime. The quality factor can be measured by determining the resonance frequency and linewidth, e.g. by probing the cavity resonance with a tunable laser, or by measuring the decay constant of light coupled into the cavity (*Cavity ring-down spectroscopy*). Importantly, the quality factor is also directly related to the finesse $\mathcal{F}$ of the cavity by the longitudinal mode order q:

$$Q = q\mathcal{F}. \tag{2.14}$$

The quality factor is a fundamental property of any resonator, including mechanical and electrical oscillators. It is often used to compare different types of optical resonators, such as whispering gallery mode (WGM) or photonic crystal cavity resonators.[1]

[1] For many resonator types, the quality factors are a better figure of merit than the finesse, because the quality factor is independent on the resonator dimensions, while for FP cavities the finesse is independent on the resonator length while the quality factor is not. This is due to the fact that for a FP cavity, losses are assumed to occur only at the mirrors, i.e. per round trip, while e.g. for WGM resonators, losses are the same at all points and occur per distance traveled.

Mode volume

The mode volume is a measure of the spatial confinement of light inside a resonator. It is defined as:

$$V = \frac{\int_V \varepsilon(\vec{r})|E(\vec{r})|^2 \mathrm{dV}}{\max(\varepsilon(\vec{r})|E(\vec{r})|^2)}. \tag{2.15}$$

For a FP cavity, this quantity is limited by diffraction to values on the order of $V_{\mathrm{min}} \approx \lambda^3$, which is only achieved at minimal mirror separation $d = \lambda/2$. Significantly lower values can be achieved using near fields which are not limited by diffraction, for example in photonic crystal cavities or plasmonic resonators [45, 46]. A low mode volume corresponds to high local intensities, making it useful to enhance e.g. optical transitions of atoms or non-liner optical processes.

Stability range

Given the requirement that the solutions to the paraxial Helmholtz equation are indeed a Gaussian beam, that is the Rayleigh range, z_0, is a real number, leads to the condition:

$$0 < \left(1 + \frac{d}{R_1}\right)\left(1 + \frac{d}{R_2}\right) < 1 \tag{2.16}$$

where the radii of curvature, R_i, are defined as positive (negative) when the mirror is convex (concave) as seen by the impinging ray[1]. Configurations that fulfill this criterion are said to be stable.
From this it becomes evident that a symmetric ($R_1 = R_2$) stable cavity can only be operated up to a cavity length $d = 2R_\mathrm{c}$. A planar-concave cavity, as typically used in this work, can be operated up to radii of $d = R_\mathrm{c}$, where R_c is the radius of curvature of the concave mirror. This configuration is equivalent to a symmetric cavity with distance $d = 2R_\mathrm{c}$, if the planar mirror is considered as a mirror plane of the system.
In realistic micro-cavity experiments, we often observe drops in the finesse associated with additional losses long before the theoretical stability limit is reached. This can be attributed to diffraction losses due to the finite extent of the concave mirror profile produced by CO_2 laser milling. For CO_2 laser machined fiber profiles typically used in this work, the cavity can usually be operated up to $d \approx R_\mathrm{c}/2$ before experiencing additional losses [43]. This can be alleviated by using other fabrication techniques that can produce large diameter spherical profiles, such as focused ion beam (FIB) or direct laser writing (DLW). An example of this will be discussed in Section 2.4.

[1] The same result can be obtained by ray optics.

Beam waist

For a homogeneously filled Fabry-Pérot (FP)-resonator, the fundamental mode is a Gaussian beam and the mode volume can be solved analytically. The mode volume is given by:

$$V = \frac{\pi w_0^2 d}{4}, \tag{2.17}$$

and depends on the mode waist w_0 and the cavity length d. For a plano-concave mirror, the waist is located directly on the planar mirror. It is determined by the radius of curvature R_c of the curved mirror and the cavity length d:

$$w_0 = \sqrt{\frac{\lambda d}{\pi}\sqrt{\frac{R_\mathrm{c}}{d} - 1}}. \tag{2.18}$$

The beam radius at any other point is then obtained by propagating the Gaussian beam according to beam optics. This yields:

$$w_d = \sqrt{\frac{\lambda d}{\pi}\sqrt{\frac{R_\mathrm{c}^2}{d(R_\mathrm{c} - d)}}}, \tag{2.19}$$

at the curved mirror. Both quantities are visualized in Figure 2.3 (a). One can see that the minimal waist is obtained for short mirror separation or when the resonator is operated close to the maximal stable mirror separation $d = R_\mathrm{c}$. For many applications it is desirable to minimize the beam waist, e.g. to achieve a smaller point spread function or to maximize the Purcell factor (see Section 2.3.1). This can be achieved by utilizing short radii of curvature, which however poses a challenge for many fabrication techniques.

Mode matching

Mode matching describes how effectively light is coupled into or out of the cavity. It is determined by how closely the incoupling- and outcoupling mode, usually either a Gaussian laser beam or a fiber mode for a fiber-based cavity, matches the cavity mode. Mathematically, this is determined by the overlap integral of the two different modes:

$$\epsilon = \int_{-\infty}^{\infty} E_\mathrm{f}^*(x, y, z_0) E_\mathrm{c}(x, y, z_0) \mathrm{d}x\mathrm{d}y \tag{2.20}$$

$$= \frac{4}{\left(\frac{w_\mathrm{f}}{w_\mathrm{c}} + \frac{w_\mathrm{c}}{w_\mathrm{f}}\right)^2 + \left(\frac{\pi n_\mathrm{f} w_\mathrm{f} w_\mathrm{c}}{\lambda R}\right)^2} \approx \left(\frac{2 w_\mathrm{c} w_\mathrm{f}}{w_\mathrm{c}^2 + w_\mathrm{f}^2}\right)^2, \tag{2.21}$$

where $E_{\{\mathrm{c,f}\}}$ are the normalized field amplitudes of the cavity and fiber mode at the mirror position. $w_{\{\mathrm{c,f}\}}$ are the respective mode waists, and R_c is the radius of curvature of the

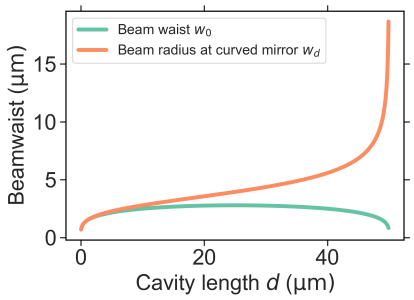

(a) Beam waist as a function of the cavity length at the planar (green) and concave (orange) mirror for a radius of curvature $R_c = 50\,\mu\text{m}$ and a wavelength $\lambda = 980\,\text{nm}$.

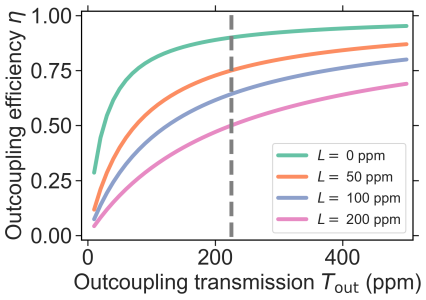

(b) Outcoupling efficiency η as a function of the outcoupling transmission T_{out} and additional losses L. Second mirror transmission is fixed at $T_1 = 25\,\text{ppm}$. Grey dashed line indicates the configuration most commonly used in this work.

Figure 2.3.: Beam waist and outcoupling efficiency of a Fabry-Pérot resonator.

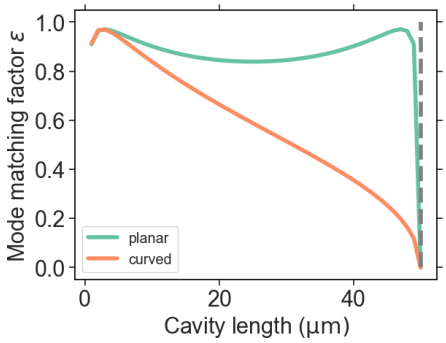

(a) Theoretical mode matching efficiency calculated according to Equation 2.21 when coupling out via the curved or planar mirror in a concave-planar cavity for a radius of curvature of $R_C = 50\,\mu\text{m}$.

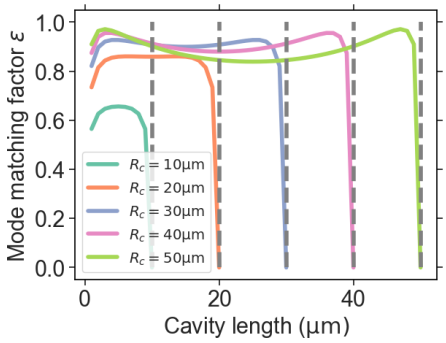

(b) Mode matching efficiency on planar cavity mirror in a plano-concave cavity geometry for different radii of curvature as a function of the cavity length.

Figure 2.4.: Calculated mode matching efficiencies for different settings in a plano-concave fiber-cavity, for a fiber mode waist of $w_f = 1.92\,\mu\text{m}$ and wavelength $\lambda = 980\,\text{nm}$.

mirror [47]. This derivation assumes both the cavity and the fiber mode to be fundamental Gaussian modes and does not take into account lateral or angular misalignment of the cavity and the in-coupling mode. Figure 2.4 illustrates the calculated mode matching efficiency for a cavity mode to a fiber mode for a plano-concave cavity, which is the type of cavity most commonly used in this work.

Intra-cavity power

The standing wave in the cavity goes hand in hand with an enhancement of the electric field and the corresponding optical power. At an antinode, the peak power is given by:

$$P_{\text{Peak}} \approx 4T_1 \frac{\mathcal{F}^2}{\pi^2} P_{\text{in}}. \tag{2.22}$$

For high finesse resonators the intra-cavity power can become large even for comparably low input power, such that effects like optical trapping, photo-thermal effects and even damage to the mirrors can occur [48, 49].

Outcoupling efficiency

The outcoupling efficiency is the probability of a photon scattered into the cavity mode to leave the cavity via either mirror. It is defined as:

$$\eta_i = \frac{T_i}{\sum \text{All Roundtrip Losses}}, \tag{2.23}$$

for the i-th mirror. For a large asymmetric reflectivity, e.g. $T_1 >> T_2$, almost all of the light is coupled out at the highly transmissive mirror. This is visualized in Figure 2.3 (b) for different additional losses L. This is an important quantity to optimize when investigating emitters inside the cavity in order to maximize the photon rate at the detector.
The outcoupling efficiency should not be confused with the transmission and reflection of a light beam impinging on the cavity. Assuming no additional losses, an impinging light beam is fully transmitted when on resonance with the cavity for a symmetric cavity. Meanwhile, a photon scattered into the cavity mode has an equal chance to leave the cavity at either mirror for the symmetric case.

2.2. Fiber-based micro Fabry-Pérot resonators

While FP-cavities are conceptually simple, they can take many forms dictated by their applications. In this work the focus lies on minimizing the cavity length and mirror size, in order to strongly boost the light-matter interaction. Therefore, I utilize fiber-based Fabry-Pérot cavitys (FFPCs), where one of the mirrors is fabricated on the concave end facet of an optical fiber [47]. A schematic representation of such a cavity is depicted in Figure 2.5. This configuration enables operation at very small cavity lengths, while simultaneously maintaining fast tunability of the lateral and longitudinal mirror positioning. It also provides an intrinsic coupling to the cavity via the fiber mode. In this section, I will give an overview over the fabrication of the fiber mirrors used in this work.

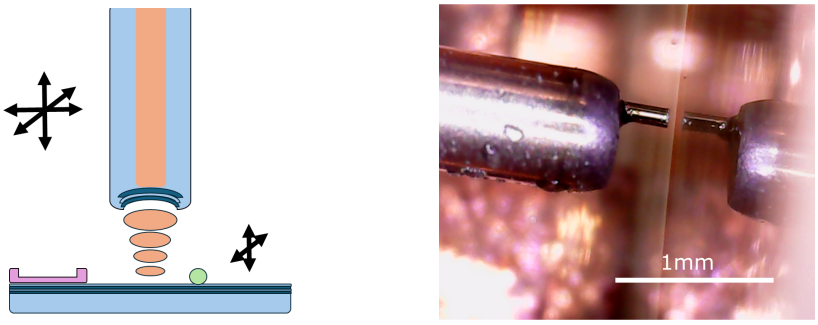

Figure 2.5.: (a) Schematic representation of a fiber-based Fabry-Pérot scanning cavity. The fiber can be scanned quickly over the mirror. Green and pink shapes indicate the types of samples studied in the cavity in this work: thin membranes and nanoparticles. (b) Picture of a fiber mirror and its reflection in a planar, macroscopic mirror, forming a cavity. The fiber is glued into a steel needle.

2.2.1. Fabrication of fiber mirrors via CO_2 laser milling

Many different techniques have been established in order to fabricate concave mirror profiles for FP resonators. Desirable properties for most applications are:

- **Low surface roughness** compatible with highly reflective coatings. In the Rayleigh limit where the surface imperfections are much smaller than the wavelength, the scattering losses induced by surface scattering can be modeled as [47]:

$$S = \left(\frac{4\pi\sigma_{\mathrm{rms}}}{\lambda}\right)^2, \tag{2.24}$$

  where σ_{rms} is the root mean square (rms) surface roughness over an area as seen by the cavity mode. The scattering losses and the resulting finesse are plotted in Figure 2.6 for realistic parameters used in this work. It becomes evident that operation of a cavity at finesses $\mathcal{F} > 40000$ requires the rms surface roughness to be significantly below one nanometer.

- A high degree of **control over the profile shape**. Being able to control the ellipticity, radius of curvature, depth and lateral extent of the profiles allows to tailor the mirror geometry to the desired application. A mismatch of the mirror geometry to the wavefront of the cavity mode leads to additional diffraction losses and undesirable mode mixing [43].

- **Compatibility** with different substrates, i.e. not all fabrication techniques are suitable to produce profiles on optical fibers.

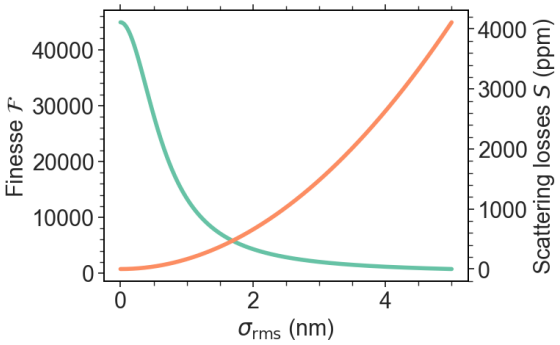

Figure 2.6.: Calculated scattering losses (orange) and resulting finesse (green) as a function of the root mean square surface roughness σ_{rms}. Parameters used in the calculation are: $\lambda = 980\,\mathrm{nm}$, $T_1 = T_2 = 25\,\mathrm{ppm}$, $A_1 = A_2 = 10\,\mathrm{ppm}$.

- **High reproducibility**, i.e. fabrication runs with the same parameters lead to the same profiles.
- **High throughput**: Fabrication techniques should either allow for parallel processing or minimize the time it takes to fabricate a profile. Since the applications discussed here are focused on research, it is not important to scale production up to mass fabrication. Nevertheless, fabrication speed should be high enough to allow for quick iterations and to produce a sufficient amount of mirror profiles, which consequently allows for less conservative use of the produced fibers.

There is no technique that fulfills all of these requirements at once. The lowest surface roughnesses required for high finesse cavities are achieved by mechanical-chemical polishing [50], different etching techniques [51, 52] and CO_2 laser machining [47, 53]. Among these techniques, only CO_2 laser machining is compatible with optical fibers. Focused ion beam (FIB) milling can produce arbitrary profiles in optical fibers with high precision, but suffers from long machining times and limited surface quality [54]. Recently, a combination of FIB milling and surface treatment using a CO_2 laser has shown promise in combining the two techniques, although the problem of long machining times persists [55].

Principles of CO_2 laser machining

Next, I will briefly describe the machining process used to fabricate the FFPCs used in this work.

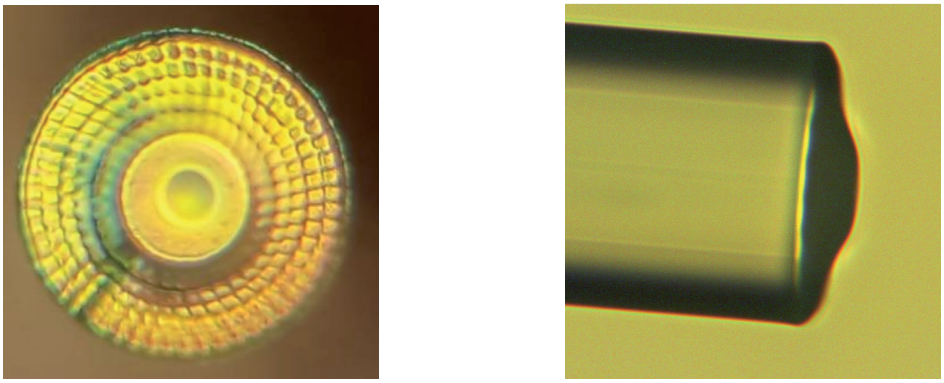

(a) Front view.

(b) Side view.

Figure 2.7.: Photographs from the front and side of machined optical fibers. Image (a) was taken by Hanno Kaupp, (b) was taken by Julia Benedikter. Reproduced from [42].

The front part of an optical fiber is stripped of its metallic coating and subsequently cleaved in order to produce a planar front facet. The fiber is then positioned in front of a lens, which focuses a high power pulse of mid infrared laser light ($\lambda = 10\,\mu m$) onto the fiber end facet. This simultaneously causes surface evaporation creating a concave depression, and melting of the surface causing a reflow process, which creates an atomically flat surface [53]. The central part of the produced profile is to first order proportional to the impinging laser beam, and therefore generally well fit by a Gaussian [1]. A much more detailed description and modeling of this process can be found in [53]. The center of this Gaussian profile can be approximated by a parabola of the form ax^2, which corresponds to a sphere with radius $R = 1/2a$. Since the cavity mode waist is typically small on the curved mirror, it samples mostly the parabolic part, such that the mathematical description developed in Section 2.1 can be applied. For larger beam radii, the deviation from a parabolic shape leads to additional diffraction and clipping losses, which manifests itself in a drop in the finesse before the stability limit is reached [43].

Depending on how tightly the beam is focused onto the fiber, radii of curvature between $R_c \approx 10\,\mu m$ and $R_c \approx 200\,\mu m$ are typically achieved in our setup, although radii of curvature higher than 1 mm have been produced using this method [56]. The laser power and pulse length is controlled via an acousto-optic modulator (AOM), which allows additional control over the created profiles. The created profiles can be characterized in the same setup by using a white-light interferometric microscope. By taking multiple interferometric images longitudinally offset by $\lambda/4$ to each other, and applying

[1] Depending on the used laser parameters, there is often a bulging observed at the rim due to the reflow process. For most applications, this is insignificant.

a phase-unwrapping algorithm, one can accurately reconstruct the surface profile. Two exemplary reconstructed profiles are shown in Figure 2.10. In addition to the fabrication of the mirror profiles, the fibers are typically tapered, that is material is removed from the sides of the fiber end-facet via a many shot CO_2 milling process. After the tapering, only a pedestal centered on the fiber core with a diameter of $d \approx 20\,\mu\text{m}$ and a height of $z \approx 20\,\mu\text{m}$ remains. This allows for greater fiber maneuverability when approaching the fiber closely to a planar mirror. Photographs of machined fibers that also show the tapering are depicted in Figure 2.7. For a more detailed description of the used setup, the reader is referred to previous works in our research group [39, 57].

2.2.2. Distributed Bragg reflectors

After producing a sufficient amount of fibers with the desired geometry, a mirror coating needs to be applied. For high-finesse coatings, the only sensible choice are high-quality distributed Bragg reflectors (DBRs) grown via ion beam sputtering, which are applied by a specialized company[1].
DBRs are mirrors formed by alternating layers of high and low refractive index materials that rely on the interference of the partial waves reflected at the interfaces according to the Fresnel equations [58]. Choosing layer thicknesses of $d_i = \frac{\lambda_c}{4n_i}$ leads to constructive (destructive) interference of the reflected (transmitted) partial waves. By increasing the number of layer pairs, the reflectivity can be made almost arbitrarily large, such that the maximal achievable mirror reflectivity is only limited by scattering losses due to surface roughness and absorption losses due to residual impurities in the DBR layers. Therefore, fabrication methods have been optimized to minimize surface roughness and achieve very high material purities, enabling ultra-high finesse coatings typically produced by ion beam sputtering, which can feature losses per mirror of $S + A \approx 1\,\text{ppm}$, allowing finesses of $\mathcal{F} > 10^6$ [59]. The details generally depend on the wavelength utilized. The coatings used here consist of 12 (14) layer pairs of SiO_2 and Nb_2O_5 for the high (low) transitivity coating, leading to a transmission of 222 ppm and 25 ppm at the design wavelength of $\lambda_c = 985\,\text{nm}$. The coating and resulting transmittance are plotted in Figure 2.8. The reflectivity decreases when the wavelength is detuned from the central wavelength. The spectral region where the reflectivity is high is referred to as the *stopband*. Its spectral width can be approximated as:

$$\Delta\omega_{\text{DBR}} \approx \omega_c \frac{2}{\pi} \frac{\Delta n}{\overline{n}}, \tag{2.25}$$

with the refractive index contrast $\Delta n = n_2 - n_1$ and the mean refractive index $\overline{n} = \frac{n_1+n_2}{2}$ [60]. In reality, some of the layers are not exactly quarter wave stacks $d = \frac{\lambda_c}{4n_i}$. By slightly deviating from the ideal thickness, the reflectivity and the exit phase can be fine

[1] *Laseroptik, Garbsen, Germany*

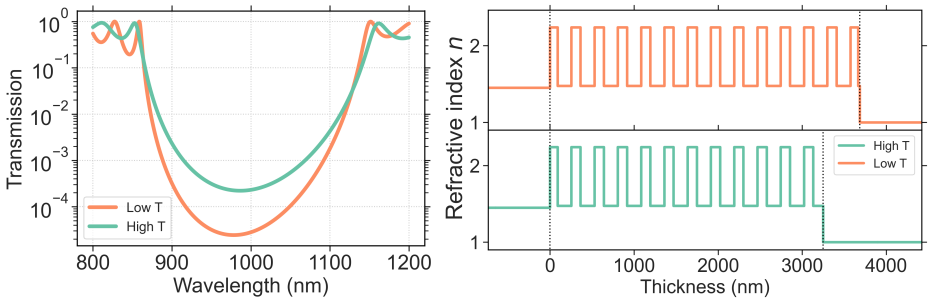

(a) Simulated Transmission.

(b) Refractive index profile of DBR layers.

Figure 2.8.: Transmission and layer stack of the two DBR coatings employed in this work.

tuned. The exit phase is important in cavity experiments, where the sample is placed on a mirror at a set distance from the interface, since the exit phase determines where the nodes and antinodes are positioned in relation to the mirror interfaces.

We chose to fabricate two different coatings to be able to employ an asymmetric cavity, consisting a of a high and low transmittance mirror. This achieves a high outcoupling efficiency of photons emitted due to emitter-cavity coupling. For the designed coatings, the outcoupling efficiency according to Equation 2.23 at the low transmittance mirror side is $\eta_{\mathrm{cav}} = 72\,\%$, when assuming additional losses due to scattering and absorption of $E = 60\,\mathrm{ppm}$, which is extracted from the best observed finesse values of $\mathcal{F} = 20\,000$ ($\eta = 90\,\%$ for $E = 0$).

Because many partial waves need to interfere to achieve high reflectivities, the light needs to penetrate significantly into the DBR stack. The penetration depth d_{pen} defined as an 1/e drop in optical intensity is approximately given by [60]:

$$d_{\mathrm{pen}} = \frac{\lambda_{\mathrm{c}}}{4\Delta n}. \tag{2.26}$$

This limits the minimal achievable cavity length when using DBR mirrors.
In reality, the penetration depth in Equation 2.26 is not the only relevant length scale: Different lengths have to be considered when calculating e.g. the reflection phase, the time delay and the imaging properties of the mirror. A detailed treatment can be found in [60].
In order to capture all of these effects, our group makes use of a simulation code based on a transfer matrix model. The code was developed by Julia Benedikter based on the book by Furman [58] and adapted to Python by Kerim Köster.

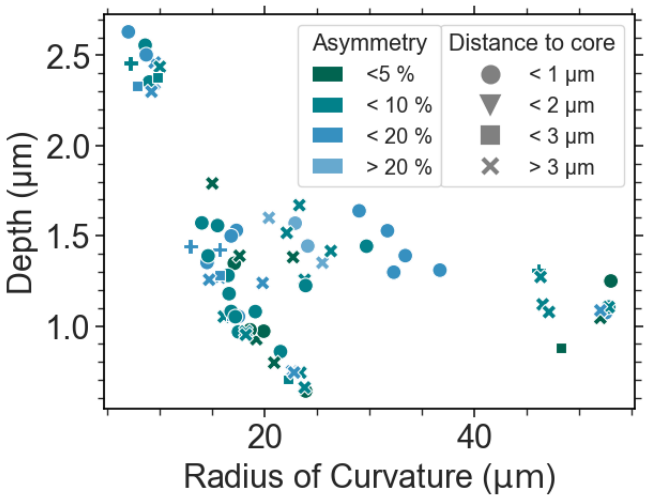

Figure 2.9.: Scatter plot showcasing the distribution of radii of curvature and corresponding profile depth of the fibers produced in this work. The color encodes the asymmetry of the profile and the centering of the core is encoded in the symbols.

2.2.3. Fibers produced in this work

During this work, a set of 110 fibers with coatings centered around 985 nm, compatible with the cryogenic transition wavelength of Yb^{3+}:Y_2O_3, were produced. At the time, we considered cavities formed by a fiber mirror and a macroscopic planar mirror, as well as a fiber-fiber cavity consisting of two fiber mirrors. Therefore, the fabrication run covered many different fiber mirror geometries, three types of fibers and two coatings, which were achieved by interrupting the sputtering process and removing half of the fibers before adding the last DBR layer pairs.

Curved fibers

Curved fibers with radii of curvature between $R_{\mathrm{min}} = 10\,\mu\mathrm{m}$ and $R_{\mathrm{max}} = 50\,\mu\mathrm{m}$ were produced on near infrared (NIR) single mode optical fibers.[1] The smaller radii of curvature were chosen to minimize the mode volume and maximize the Purcell factor. The higher radii of curvature offer a longer stability range, making them easier to set up, and are compatible with experiments in which the cavity length is constrained by the sample, for example by a few micron thick membrane. Additionally, a set of curved fibers were

[1] *Cu 800,ivg-fiber*, $\lambda = 800\,\mathrm{nm}$

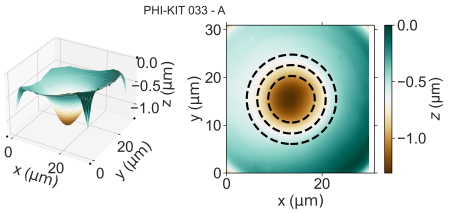

(a) Reconstructed surface profile of a curved fiber. Spherical fit indicated as contours.

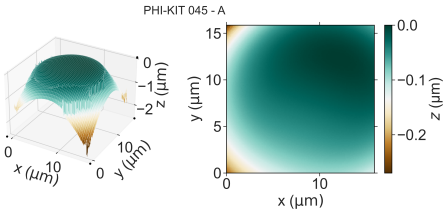

(b) Reconstructed surface profile of a planar fiber.

Figure 2.10.: Reconstruction of a curved and a planar fiber profile produced in this work.

produced on a multi mode fiber [1]. This can facilitate photon collection via the fiber due to the large core diameter and higher numerical aperture (NA). An overview of all the curved fiber profile parameters produced in this work can be found in Figure 2.9. Fiber asymmetry causes a frequency splitting of the polarization modes [61], and is for most fibers here kept under 20%. The alignment of the center of the profile is checked via backside illumination of the fiber core while observing the mirror profile in a high magnification objective. This is precise to about 1 µm. Most fibers have a core distance below 3 µm. Bad centering significantly reduces the mode matching between the fiber mode and the cavity mode. This is especially problematic when fluorescence is collected via the fiber. An exemplary reconstructed surface profile is depicted in Figure 2.10 (a).

Planar fibers

Instead of producing a concave depression, the CO_2 laser is used to produce reflow of the surface, leading to a planar but smooth surface. This is achieved by using longer exposure times with lower pulse powers. The idea is to use these in conjunction with a curved fiber mirror to assemble a fiber-fiber cavity. This allows for miniaturized and robust designs, as demonstrated in micro-fluidic experiments in our group [62]. Using a planar fiber to couple out light compared to a curved fiber maximizes the mode matching into the fiber and therefore maximizes collection efficiency. This is illustrated in Figure 2.4. The downside of such an experiment is that it is hard to integrate the sample into the cavity. In his master thesis, Tobias Krom demonstrated the reliable pick-up of fluorescing nanoparticles on such planar fibers, centered on the single mode fiber core with a precision of about 1 µm. More details about the procedure and more in-depth considerations about the planar fiber design can be found in his thesis [63]. A prototype for a cryogenic fiber-fiber cavity that should make use of these fibers was assembled

[1] *G50/125/250, DATWYLER*

and characterized by Christopher Hins in his bachelor's thesis, which I supervised [64]. 33 Planar fibers were produced in this work, of which 22 were produced on single mode fibers and 11 were produced on multi-mode fibers[1]. An exemplary reconstructed surface profile is depicted in Figure 2.10 (b).

2.3. Light-matter interactions inside optical resonators

The main application of optical resonators in this work is to enhance the light-matter interaction between light and an atom-like optical transition. This enhancement can take many forms, with an entire formalism of cQED devoted to describing such problems. In the following discussion, I will focus on the regime of weak coupling, which is the relevant regime for the systems discussed in this work.

2.3.1. The Purcell effect

The Purcell effect [65] describes the enhancement of the spontaneous emission rate of an optical transition when the transition frequency is resonant with a cavity mode. The enhancement factor C_0 is called the Purcell factor and is given by:

$$C_0 = \frac{3}{4\pi^2}\frac{\lambda^3}{n^3}\frac{Q}{V} = \frac{6}{\pi^2}\frac{\lambda^2}{n^2}\frac{\mathcal{F}}{\pi w_0^2}, \tag{2.27}$$

where the right-hand side rewrites the formula for a FP-resonator in terms of finesse $\mathcal{F}$ and waist w_0 using Equations 2.14 and 2.17. n is the refractive index inside the cavity, where we assume a homogeneously filled cavity. The Purcell effect can be perhaps most easily understood as the resonator modifying the local density of states, which via Fermi's golden rule changes the corresponding transition rate. I will briefly describe this argument in the following.

Free space emission rate

Following [66], consider an ideal two level system with ground state $|g\rangle$ and excited state $|e\rangle$. For a purely electric-dipole mediated transition with dipole moment $\vec{\mu} = -e\vec{r}$, the transition rate γ_{rad} is given by Fermi's golden rule:

$$\gamma_{\text{rad}} = \frac{2\pi}{\hbar^2}\left|\langle e|\vec{\mu}\cdot\vec{E}|g\rangle\right|^2 \rho(\omega)\Lambda(\omega) \tag{2.28}$$

[1] *GI50-125CB, Oxford Electronic Limited*

In free space, the photon density of states $\rho(w)$ is quadratically increasing with ω, corresponding to a spherical shell in k-space:

$$\rho(\omega) = \frac{\omega^2 V_0}{\pi^2 c^3}. \tag{2.29}$$

The density of states of the emitter $\Lambda(\omega)$ can be approximated as a delta-distribution $\Lambda(\omega) = \delta(\omega - \omega_0)$, where $\omega_0 = \frac{E_e - E_g}{\hbar}$ is the transition frequency of the emitter. Inserting the vacuum field $E_{\text{vac}} = \sqrt{\frac{\hbar\omega}{2\epsilon_0 V}}$ and defining the dipole transition element: $\mu_{\text{eg}} = |\langle e|\vec{\mu} \cdot \vec{E}|g\rangle|$, we obtain the spontaneous emission rate:

$$\gamma_0 = \frac{1}{\tau_0} = \frac{\mu_{\text{eg}}^2 \omega_0^3}{3\pi\epsilon_0 \hbar c^3}, \tag{2.30}$$

where we have averaged over all possible dipole moment orientations.

Emission into a resonant cavity

However, an optical cavity, or more generally any structured dielectric environment, can modify the density of states significantly. For an optical cavity, the density of states is given by the (normalized) Lorentzian lineshape:

$$\rho(\omega) = \frac{2}{\pi\Delta\omega_c} \frac{\Delta\omega_c^2}{4(\omega - \omega_c)^2 + \Delta\omega_c^2}. \tag{2.31}$$

Inserting this into Equation 2.28, and assuming both perfect spectral overlap of emitter and cavity ($\omega_e = \omega_c$) and maximal dipole overlap ($\vec{\mu}||\vec{E}$), we arrive at [66]:

$$\gamma_{\text{cav}} = \frac{3}{4\pi^2} \frac{\lambda^3}{n^3} \frac{Q}{V} \gamma_0 = C_0 \gamma_0. \tag{2.32}$$

It is important to understand the implications of this result. First of all, it is clear to see that the Purcell enhancement scales with $\frac{Q}{V}$, which is therefore an often cited figure of merits of a resonator-emitter system. Secondly, the decay due to the Purcell effect is an additional decay channel directly linked to the resonant cavity mode. This means that the decay channels γ_0 and γ_{cav} exist simultaneously. The additional decay channel due to the Purcell effect manifests itself in a reduced lifetime of the excited state:

$$\tau_C = \frac{1}{\gamma_0 + \gamma_{\text{cav}}} = \frac{1}{\gamma_0 + C_0\gamma_0} = \frac{1}{C_0 + 1}\tau_0. \tag{2.33}$$

A Purcell factor of $C = 1$ therefore corresponds to a reduction of the excited state lifetime by a factor of two. This lifetime reduction is a clear signature of the Purcell effect and often used to experimentally determine the Purcell factor. Another key feature of this effect is that all the photons emitted due to the Purcell effect with rate γ_{cav} are emitted

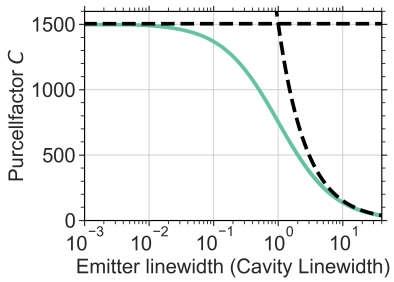

(a) Influence of non-vanishing emitter linewidths on the Purcell effect.

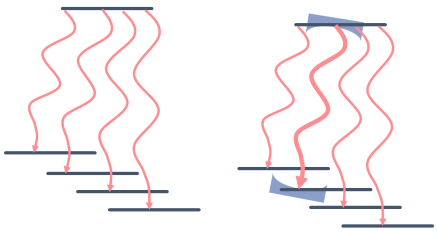

(b) Purcell effect for multiple decay pathways.

Figure 2.11.: (a) Calculated Purcell factor as a function of the emitter linewidth in terms of cavity linewidth. The dashed lines indicate the limits of the bad cavity and bad emitter regime. (b) Schematic illustration of the Purcell effect when multiple decay channels are present. Only the resonant transition is enhanced, leading to a reduction in the observed lifetime change and an increase in the effective branching ratio of the enhanced transition.

into the resonant cavity mode, that is their spatial extent, temporal extent, polarization etc. are determined by the cavity mode. This allows to efficiently collect the photons, since the fundamental cavity mode for a FP-cavity is a Gaussian mode, which is easy to collimate or fiber-couple, and focus onto a detector. Because the free space NA of an optical cavity is generally poor, in an experiment one typically only observes photons emitted due to the Purcell effect. The fraction of photons emitted into the cavity mode is given by

$$\beta = \frac{\gamma_{\mathrm{cav}}}{\gamma_0 + \gamma_{\mathrm{cav}}} = \frac{C_0}{C_0 + 1} \tag{2.34}$$

2.3.2. Modifications in realistic systems

When one enters values typical for the FFPCs employed in this work ($Q = 10^5$, $V = 8\,\lambda^3$) into Equation 2.27, one obtains large Purcell factors $C \approx 1000$, which would correspond to an extreme lifetime shortening by three orders of magnitude. However, the experimentally achieved Purcell factors are usually significantly lower. This discrepancy is largely explained by the fact that in the derivation, we have assumed an ideal two-level system, while in reality, we are largely dealing with defects or dopants embedded in the solid state. In such systems one needs to account for several effects that distinguish them from an ideal two-level system. In the following, I will discuss where the differences lie and how they impact the Purcell enhancement.

Finite emitter linewidth

In the derivation, we have assumed an infinitely narrow spectral linewidth of the emitter $\Delta\omega_0$ by setting $\Lambda(\omega) = \delta(\omega - \omega_0)$. This is of course physically impossible, but constitutes a good approximation when $\Delta\omega_0 << \Delta\omega_c$. However, solid state emitters usually experience additional broadening, making their linewidth comparable with that of a high Q resonator. The correct treatment is obtained by describing the emitter density of states as a Lorentzian with width $\Delta\omega_0$ [67]:

$$\rho(\omega) = \frac{2}{\pi\Delta\omega_0} \frac{\Delta\omega_0^2}{4(\omega - \omega_0)^2 + \Delta\omega_0^2}. \tag{2.35}$$

One then needs to solve the integral over two Lorentzians. The solution is found to be:

$$\begin{aligned} C_{\text{eff}} = \frac{\gamma_{\text{cav}}}{\gamma_0}\gamma_{\text{cav}} &= \frac{2\mu_{\text{eg}}^2}{\hbar\epsilon V_0} \frac{\omega_0\Delta\omega_{\text{cav}} + \omega_{\text{cav}}\Delta\omega_0}{4(\omega_0 - \omega_{\text{cav}})^2 + (\Delta\omega_{\text{cav}} + \Delta\omega_0)^2} \\ &\overset{\omega_0=\omega_c}{=} \frac{3}{4\pi^2}\left(\frac{\lambda}{n}\right)^3 \frac{Q_{\text{eff}}}{V}, \end{aligned} \tag{2.36}$$

where we recover the usual expression for the Purcell factor by replacing the quality factor of the cavity Q by the effective quality factor Q_{eff}, which accounts for the emitter linewidth:

$$Q_{\text{eff}} = \left(\frac{1}{Q_{\text{cav}}} + \frac{1}{Q_{\text{em}}}\right)^{-1} = \left(\frac{\Delta\omega_{\text{cav}}}{\omega_{\text{cav}}} + \frac{\Delta\omega_{\text{em}}}{\omega_{\text{em}}}\right)^{-1}. \tag{2.37}$$

It is evident that the broader linewidth dominates this expression and that Equation 2.27 is obtained in the limit $\omega_{\text{em}} << \omega_{cav}$, which is sometimes referred to as the *bad cavity regime*. Equivalently, the other limit $\omega_{\text{cav}} << \omega_{em}$ is called the *bad emitter regime*. The two limits and the effective Purcell factor according to Equation 2.36 are depicted in Figure 2.11, showcasing their range of validity. It is notable that there is a significant deviation up to $\Delta\omega_{\text{cav}}/\Delta\omega_{\text{em}} \approx 10$ from the idealized formula. Therefore, for an accurate prediction of the Purcell factor the complete formula 2.36 should be used.

Branching ratio

As opposed to an ideal two-level system, most real atoms and solid state emitters posses multiple energy levels and allowed transitions connecting them. However, only one transition (not accounting for degeneracy) is resonant with a cavity mode at a time. Consequently, only the rate of this transition is enhanced according to the Purcell effect (Equation 2.27), while the other decay rates remain unchanged. This is schematically depicted in Figure 2.11. Because the excited state lifetime is the inverse of all decay rates,

the lifetime change due to the Purcell effect is reduced by the branching ratio $\zeta_i = \frac{\gamma_i}{\sum_j \gamma_j}$ of the investigated transition i.

$$\tau_c = \frac{1}{(C\gamma_i + \sum_{j\neq i} \gamma_j)} = \frac{1}{\zeta C + 1}\tau_0 = \frac{1}{C_{\text{eff}} + 1}\tau_0. \tag{2.38}$$

We define the effective Purcell factor C_{eff} as the Purcell factor that is extracted from the apparent lifetime reduction as $C_{\text{eff}} = \frac{\tau_0}{\tau_c} - 1$. In the common case where one is interested in one specific transition, one nevertheless enhances the rate of "useful" photons by the ideal Purcell factor C, even though the lifetime is only reduced by C_{eff}. The fraction of useful photons is changed by the Purcell effect to:

$$\zeta_c = \frac{\zeta C}{1 + \zeta C} = \frac{C_{\text{eff}}}{1 + C_{\text{eff}}}. \tag{2.39}$$

Spatial and vectorial overlap

In the derivation of the Purcell effect, we have assumed an ideal dipolar overlap with the electric field ($\vec{\mu}||\vec{E}$). The relevant electric field is the vacuum field fluctuation of the cavity mode, that is the direction is determined fully by the resonant cavity mode field evaluated at the position of the emitter $\vec{r_0}$. A non perfect overlap results in a correction of the Purcell factor by $\xi = \cos^2(\theta)$, where theta is the angle between $\vec{E}(\vec{r}_0)$ and $\vec{\mu}$.
Likewise, we have explicitly assumed that the emitter is positioned at an intensity maximum by inserting the mode volume of the cavity $V \propto \frac{1}{\max(\varepsilon(\vec{r})|\vec{E}(\vec{r})|^2))}$. For an emitter positioned arbitrarily in the cavity, the intensity has to be evaluated at the position of the emitter $\vec{r_0}$, leading to a correction factor of $\frac{\varepsilon(\vec{r_0})|\vec{E}(\vec{r_0})|^2}{\max(\varepsilon(\vec{r})|\vec{E}(\vec{r})|^2)}$.

Considering all of these effects, it becomes clear that in an experiment, the Purcell factor can easily be significantly reduced. Many of these factors can be alleviated by accounting for them in the experimental design. For example , a spacer layer of optimized optical path length can be added to a mirror, to position an emitter in an intensity anti-node. The dipolar overlap can be optimized for solid state emitters by utilizing a single crystal cut along the right crystal axis to position the dipole in plane with respect to the cavity mode. Finally, the Purcell effect increases for narrow and stable cavities and emitter linewidths.
I want to conclude the discussion of the Purcell effect with the comment that even though I have heavily relied on a quantum mechanical picture in this treatment, the Purcell effect can be understood in a completely classical manner as an interference effect (see for example [68, 69]). Such a treatment leads to the same formula. Classical scattering processes, such as Rayleigh scattering, can therefore also be Purcell enhanced [69].

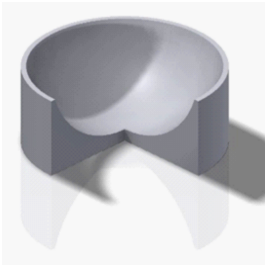

(a) CAD drawing of the target geometry.

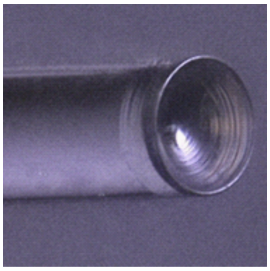

(b) Image of the 3D-direct laser written profile on the uncoated endfacet of the fiber.

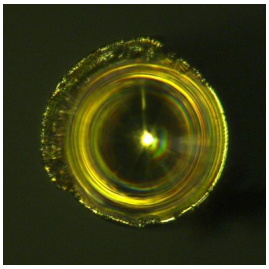

(c) Front view image of the gold coated mirror profile.

Figure 2.12.: Pictures of the 3D-laser written hemispheric mirror profiles on the fiber end facets. Reproduced from [70].

2.4. A fiber-based Fabry-Pérot-resonator with highly symmetric 3D-printed mirror profiles

In the following, I will present the characterization of a FFPC which possesses a large radius of curvature while maintaining a high degree of rotational symmetry and a close to spherical shape over its entire diameter. This was achieved by utilizing the additive fabrication process of 3D-direct laser writing (DLW) to fabricate the mirror profile on the fiber endfacet. This enables operation close to the theoretical stability limit, where the beam waist significantly reduces, opening up a new interesting regime of FFPCs. The results presented in this section are published in [70]. The mirror profiles were produced by Ksenia Weber in the group of Professor Dr. Harald Giessen at University of Stuttgart. The measurements where in large parts conducted by Johannes Höfer, a bachelor student in the group under my supervision. I also analyzed previous measurements on a very similar fiber by Julia Benedikter, a former doctoral student in the group. Further details can be found in their respective theses [42, 71].

2.4.1. 3D-direct laser writing

3D-direct laser writing (DLW) is an additive micro-structuring technique, that relies on focusing a laser beam into a photoresist. When light is absorbed, it creates a free radical which triggers the polymerization of a small volume element referred to as a voxel. By using a resist where the polymerization is triggered by two-photon absorption, the polymerization volume is kept small (on the order a few $(100\,\mathrm{nm})^3$), because the intensity in the focus is just enough to trigger the polymerization, which in a simple model can be described as being triggered when a certain polymerization threshold is exceeded [72, 73]. This process necessitates high laser intensities, which is typically why

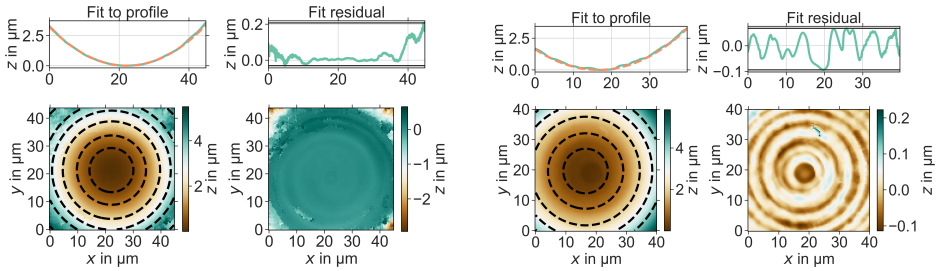

(a) Reconstruction of Fiber A.

(b) Reconstruction of Fiber B.

Figure 2.13.: White light interferometric reconstruction of the two printed mirror profiles analyzed. The spherical fit yields a radius of curvature of (a) $R_c = 78\,\mu m$ and (b) $R_c = 84\,\mu m$. The residual reveals a wavy structure, which corresponds to the writing path during the fabrication. Adapted from [70].

pulsed, high power Ti:Sa lasers are used. By moving the focus through the resist, using for example galvanometer-based mirror positioning systems, one can realize almost arbitrary 3D shapes, with very little limitations on aspect ratio.
This technique lends itself to the fabrication of micro-optical elements, including but not limited to: lens arrays, reflectors, waveguides, beam splitters and grating couplers. A good overview can be found in reference [74]. Furthermore, the technique has been used to produce resonant optical structures, such as whispering gallery mode resonators [75, 76, 77], and photonic crystal cavities [78, 79]. The group of Professor Dr. Harald Giessen, which produced the mirror profiles in this work, has also pioneered printing of multi-lense systems on the endfacets of optical fibers, that serve as objectives [80]. Furthermore, there have been first examples of monolithic FPs cavities printed on the end facets of optical fibers, mainly for sensing applications [81, 82].

2.4.2. Spherical mirror profiles produced by 3D-direct laser writing

In this work, this technique was used by our collaborators in the Giessen Group to produce spherical mirror profiles with radii of curvature around 70 µm to 80 µm. The utilized fiber is HI 1060 Flex (Corning) and the used photoresin is IPS-S (Nanoscribe GmbH). They were coated with a 50 nm layer of gold to achieve a reflectivity of $R \approx 98\,\%$.

Images of the fiber mirrors produced via this method are depicted in Figure 2.12. To characterize the achieved geometry and surface properties, two fiber profiles (hence termed fiber A and fiber B) were analyzed in the white-light interferometric setup described in Section 2.2.1. Reconstructions and fit residuals of both fibers are depicted in Figure 2.13. The spherical fits yields radii of curvature of 78 µm and 85 µm for Fiber A and B, respectively. This agrees well with the targeted geometry. During the fabrication and

development process, shrinking can occur, which varies depending on the used writing parameters and photoresist. Therefore, variations are expected. It is worth pointing out that the profile is well fit by a sphere over the whole lateral extent. This is different to mirror profiles produced via CO_2 laser ablation, where significant deviations appear at the edge of the profile (compare Section 2.2.1). The uniform profile shape should enable stable cavity operation close to the theoretical stability limit $d_{\mathrm{max}} = R_{\mathrm{c}}$.
It is evident from the fit residual that the mirror surface exhibits significant elevations that follow a spiral shape. These features stem from the direct laser writing process and follow the path the laser focus takes through the photoresist.
In the following, the operation of the fiber mirrors close to the cavity stability limit is investigated.

2.4.3. Cavity characterization

A cavity was assembled with a macroscopic, planar DBR mirror ($T = 400\,\mathrm{ppm} \,@\, \lambda = 940\,\mathrm{nm}$), mounted on top of a stack of a 3D positioning unit based on piezo slip-stick actuation (Attocube), and the fiber mirror mounted inside a v-groove, which can be longitudinally moved by a few µm via a piezo actuator. The cavity was probed with a narrow linewidth laser at 940 nm coupled into the fiber and the cavity transmission was monitored with a sensitive photo diode[1]. In order to characterize the cavity performance, the finesse was measured as a function of the cavity length. The result for both fibers are displayed in Figure 2.14.
The finesse varies between 100 and 200 for the two fibers. This corresponds to additional losses of between 4 % and 0.8 %. If these losses are fully ascribed to scattering loss at the printed fiber mirror, this would correspond to a rms surface roughness of 15 nm respectively 6 nm in the Rayleigh limit. The surface roughness extracted from the fits displayed in Figure 2.13 is on the order of 40 nm, and therefore even larger losses are expected. However, because the large variations vary on length scales comparable to the wavelength, the Rayleigh limit does not fully hold. Interestingly, the spiral printing pattern matches the circular symmetry of the Laguerre-Gaussian mode, which could reduce the resulting scattering losses.

The finesse drops when approaching the stability limit $d = R_c$. Additionally, there are sharp drops at distinct mirror separations. These are commonly attributed to resonant mode mixing [43]. An intuitive explanation is that the fundamental mode is resonant at the same time as a higher order mode of a mode family with lower fundamental mode number q. This facilitates an energy exchange between the two modes. Because the higher order mode experiences significantly more loss, it serves as an additional loss channel and degrades the finesse of the fundamental mode.
Notably, we are able to measure cavity resonances for mirror separation $d > R_c/2$,

[1] Thorlabs APD130A

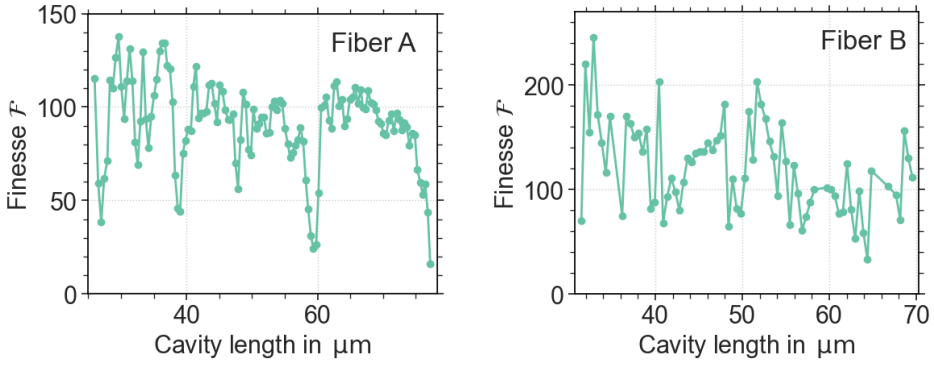

(a) Fiber A

(b) Fiber B

Figure 2.14.: Finesse as a function of the cavity length for both fibers. Dips at distinct cavity lengths corresponding to resonant mode mixing [43] are observed. The finesse is generally declining when approaching the stability limit $d = R_c$. The data was acquired by Julia Benediker (a) and Johannes Höfer (b), respectively. Adapted from [70].

which is typically the limit for CO_2-laser machined mirror profiles due to diffraction losses at the curved mirror profile. Instead, we observe stable cavity modes close to the theoretical stability limit of $d = R_c$. This is evident also in Figure 2.15, where we show the mode spectrum as a function of the cavity length. This is achieved by recording the cavity transmission as a function of cavity detuning at a certain cavity mirror distance at zero detuning. The zero detuning cavity length is then gradually offset in steps of $\lambda/2$. The first FSR of the recorded spectra are then plotted on top of each other, while centering the spectra on the first peak. One observes that the cavity dispersion of the higher order modes agrees very well with the theoretical behavior predicted by Equation 2.10. This confirms the validity of the radius of curvature of $R_c = 78\,\mu m$, extracted from the profile reconstruction in Figure 2.13. It also shows that due to the profile being well fit by a spherical over a large transverse extent of 40 µm, the cavity modes experience very little diffraction and clipping losses, even when the mode waist on the curved mirror becomes large. Furthermore, we do not observe a polarization splitting of the cavity modes. This indicates a high degree of rotational symmetry and the presence of Laguerre-Gaussian modes over Hermite-Gaussian modes.

2.4.4. Applications of resonators operated close to the stability limit

So far, I have shown that the 3D-printed mirror profiles enable operation close to the stability limit. The surface roughness, while not outstanding, is compatible with metallic mirror coatings, enabling operation of a cavity with a finesse $\mathcal{F} \approx 100$ to 200. Now, I

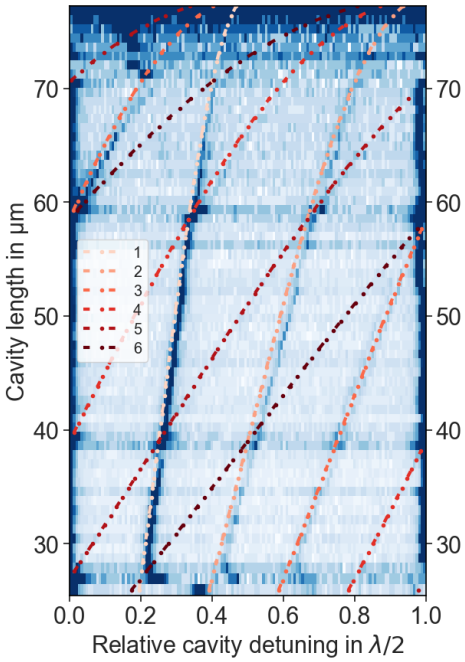

Figure 2.15.: Mode spectrum of the cavity formed by Fiber A. The dashed-dotted lines are the i-th higher order modes predicted by Equation 2.10, using the radius of curvature $R_c = 78\,\mu\text{m}$ extracted by the fit to the profile reconstruction. The good agreement between theoretical prediction and measurement is evident. Data was acquired by Julia Benedikter. Adapted from [70].

want to give a practical outlook how this can be used in applications or experiments. The main advantage of operating a cavity close to the stability limit is a small mode waist w_0, similar to very short cavity lengths (Recall Equation 2.18 and Figure 2.3). One consequence is an increase in the Purcell factor, which is proportional to $C_0 \propto \frac{\mathcal{F}}{w_0^2}$ (see eq. 2.27). It is potentially easier to operate the cavity very close to the stability limit rather than minimizing the cavity length, since the minimal achievable mirror separation is often limited by geometrical constraints such as the mirror profile depth. It also allows for a larger volume to integrate the sample. One exemplary use-case are experiments on trapped ions, where the ion has to be kept far away from any surface charges [83, 84]. Additionally, operating at long cavity lengths facilitates coupling in laser beams orthogonal to the cavity axis [83] or crossed fiber cavities [85]. One downside of this approach is the increased demand on cavity stability, since the longitudinal stability is often increased by pressing the mirrors into each other [86]. To illustrate the potential for Purcell enhancement, the expected ideal Purcell factor according to Equation 2.27 is calculated for the measured finesse values $\mathcal{F}$ displayed in Figure 2.14 (a) and the

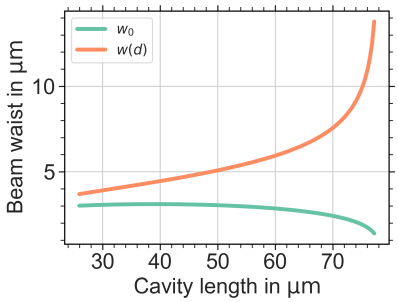

(a) Calculated mode waist at the planar mirror w_0 and at the fiber mirror $w(d)$ for Fiber A as a function of cavity length.

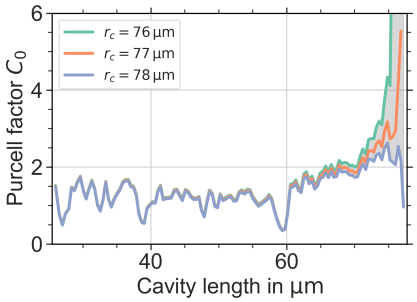

(b) Predicted ideal Purcell factor as a function of cavity length calculated from the measured finesse for Fiber A (see Figure 2.14) for slightly different radii of curvature. The uncertainty of the measurement and fit for the radius of curvature is about $\pm 1\,\mu m$.

Figure 2.16.: Estimated Purcell effect when operating the 3D-printed cavity mirrors close to the stability limit. Adapted from [70].

corresponding calculated beam waist w_0 according to Equation 2.18, The calculated beam waist and the Purcell effect are shown in Figure 2.16. Evidently, the achievable Purcell effect is highly dependent on very closely approaching the stability limit, as it changes significantly for slightly different radii of curvature and therefore different stability limits. Nevertheless, this illustrates the potential benefits of operating the cavity in this regime.

In summary, I have shown that 3D-DLW can be utilized to fabricate concave mirror profiles on the endfacets of optical fibers with a high degree of control over the achieved geometry. This results in a spherical profile over the whole lateral extent of the mirror and high degree of rotational symmetry. The surface roughness is sufficient for operating a cavity with a gold coating, leading to observed finesse values on the order of $\mathcal{F} = 100$ to 200. We study the finesse and mode structure as a function of the mirror separation and observe a stable cavity up to the theoretical stability limit $d = R_c$. I have outlined the benefits of operating the cavity in such a regime, such as the increase in Purcell factor. Unfortunately, this could not be demonstrated directly, since the cavity was operated at room temperature and no suitable emitter system was available.
In the following, I want to give a short outlook on what I believe could be further achieved in this system. First of all, an obvious path towards improving the device would be to further reduce the scattering losses by improving the surface roughness by more sophisticated fabrication methods. First promising steps towards this have been achieved by my colleague Jonas Grammel in cooperation with the group of Professor Martin Wegener. Some of these results can be found in the bachelor thesis of Marc Schuhmann [87]. By reducing the surface roughness, employing a longer probing

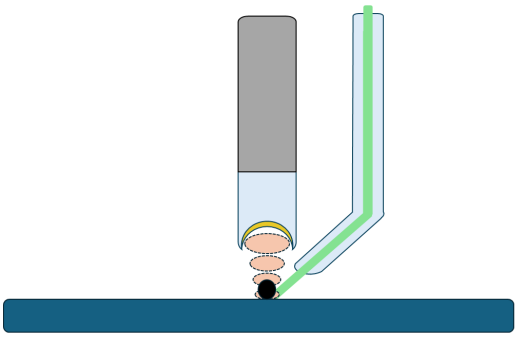

Figure 2.17.: Illustration of a 3D-printed fiber mirror forming a plano-concave cavity with side excitation of a nanoparticle via a bent photonic waveguide.

wavelength $\lambda = 1550\,\text{nm}$, and applying a DBR coating, finesse values of $\mathcal{F} > 600$ could be observed. While this is a significant improvement, it is still 2-3 orders of magnitude smaller than state of the art micro-cavities (see Section 2.2.1) produced by chemical etching or CO_2 laser milling. There also is no clear path forward, since high finesse coating $\mathcal{F} \approx 10^5$ require atomically flat surfaces, which requires reflow processes. These have been demonstrated for polymeric photonic structures, but usually go hand in hand with an uncontrolled change in the geometry, sacrificing the main advantage of the bottom-up approach of 3D-DLW. Nevertheless, it would be interesting to investigate smoothening of the surface, for example by careful thermal treatment using a CO_2 laser, as was recently demonstrated for FIB milled mirror profiles [55].

Nevertheless, it seems useful to limit the applications to experiments where the requirements on the finesse are relaxed, but that can greatly benefit from creative utilization of the freedom in the design space of the structure. For example, engineering of the asymmetry of the mirror profile can be used to define the higher order transverse mode splittings and polarization splitting, which could be useful for polarization dependent measurement or imaging methods utilizing higher order modes [88]. One could also imagine adding additional photonic structures to the end facet. For example, one could add a photonic waveguide at the side of the fiber and mirror profile with an angled end facet and possibly focusing optics on top. This would allow illuminating the cavity volume or a sample on the opposing mirror from the side and using the cavity only for readout of, for example, resonant light coupled to the cavity mode via the Purcell effect. Such a scheme would enable efficient excitation of the sample without any limitations imposed by the cavity mirror coatings, and reduce background fluorescence and scattered light due to its off-axis nature. A sketch of such a configuration is depicted in Figure 2.17.

3. Ytterbium doped nanoparticles for cavity based quantum networks

After introducing the optical resonator platform used in this work in the previous section, I now turn to the quantum system that will form a quantum node. In this chapter, I will introduce a new candidate for a near-infrared emitting node in a cavity based quantum network, namely ytterbium dopants in yttria (Y_2O_3) nanocrystals. I will start with a quick overview of the properties of rare earth ions in the solid state, which make them prime candidates to realize a spin-photon interface. I then give an overview of the various successful implementations of these ions in quantum network applications, especially when coupling them to optical cavities.
I will briefly discuss the advantages of incorporating ytterbium ions into Y_2O_3 nanocrystals instead of using bulk samples. Then, I will present a thorough characterization of the optical properties of these nanocrystals at room temperature. I show that these nanoparticles can be integrated into a open, fiber-based Fabry-Pérot (FP) cavity and observe fluorescence signals from the nanoparticles inside the cavity at room temperature. Finally, I investigate the optical properties of an ensemble of Yb^{3+}:Y_2O_3 nanocrystals at cryogenic temperatures, concluding with an experimental determination of the optical coherence time T_2, an important benchmark for a system in quantum information processing.

3.1. Rare earth ions for quantum information processing

The rare earth metals are composed of the elements from $_{57}$La to $_{71}$Lu, which are also called lanthanides. Additionally, $_{21}$Sc and $_{39}$Y are usually also referred to as rare earth metals, but not as lanthanides. Despite their name implying otherwise, rare earths are not particular scarce [89]. These elements posses a partially filled 4f shell, which determines many of their characteristic properties.
When forming complexes in the solid state, rare earth metals predominantly form trivalent positive ions, with an electronic configuration of $[Xe]4f^N$, where N refers to the N-th position in the lanthanide series. I will restrict myself to this important case and will from now on implicitly refer to the trivalent positive rare earth ions simply as rare earth ions (REIs). For almost all rare earth species, these ions posses highly coherent optical transitions, ranging from the ultraviolet (Gd^{3+}, $\lambda \approx 310\,\mathrm{nm}$) to the near infrared ($Er^{3+}$, $\lambda \approx 1550\,\mathrm{nm}$) [90, 91]. It is the spectroscopy of the optical transitions of these ions

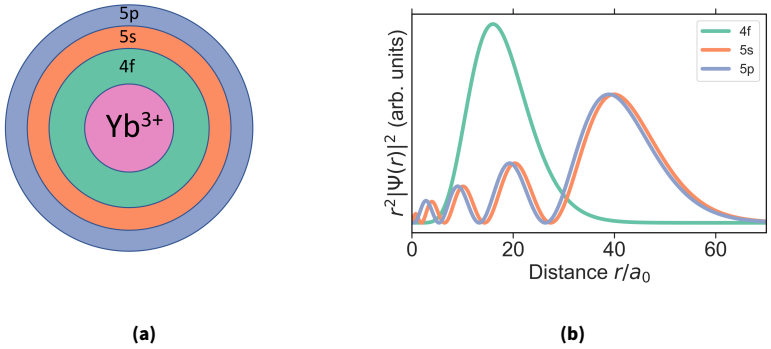

Figure 3.1.: The partially filled 4f-shell characteristic of rare earth ions is shielded by the fully occupied 5s and 5p orbitals, making them insensitive to external electric fields.

that this work concerns itself with.
While rare earth metals can form stoichiometric crystals, their optical properties are more commonly studied as dopants, that is they replace some native element in the crystal structure. The fraction of rare earth ions compared to the native elements is called the doping concentration and is chosen dependent on the application. The optical properties of rare earths are used widely. The most famous example might be the use of Nd:YAG as a gain material for a solid state laser emitting at $\lambda = 1064\,\text{nm}$. By frequency doubling the infrared light can be converted to the characteristic green laser light at $\lambda = 532\,\text{nm}$. Nd:YAG lasers find applications in material processing, in laboratories for spectroscopy and as pump lasers, in medical applications and different sensing techniques [92, 40]. Other REI-based laser systems include fiber lasers, that are used for telecommunication and high power applications such as material processing [93]. The optical properties of rare earth ions are also used as fluorophores [94] and for optical upconversion [91]. It is thanks to all of these developments, dating back to the sixties [95], that the optical properties of REIs in solids are very well studied. This wealth of knowledge serves as an excellent starting point for making use of these ions for quantum information applications. But in order to understand these applications, lets first discuss the physics of the optical transitions in rare earth ions.

3.1.1. Rare earth ions in solids

Trivalent REIs posses filled 5s and 5p orbitals, while the 4f shell is only partially filled. The optical transitions of interest in this work are all transitions within the 4f shell. These transitions are remarkably insensitive with respect to their surroundings. Somewhat uniquely to solid state emitter systems, this allows one to treat the ion like a free ion in vacuum, and account for the influence of the surrounding host material in a perturbative

manner. This perturbative treatment is done via crystal-field theory, which I will touch on later. The robustness against the environment is reflected in the fact that the optical properties are very similar for very different host materials. For example, the transition wavelength typically shifts by only a few nanometers at most between different host materials [91]. An intuitive explanation for this imperviousness can be obtained when comparing the center of mass of the radial probability density of the electron $r^2|\Psi(r)|^2$, or in a simpler picture, the average distance of the electron to the nucleus, between the different orbitals. The 4f electrons are located much closer to the nucleus. Because the 5s and 5p orbitals are filled, they screen the 4f electrons from the surrounding electric fields, making them insensitive to the environment. This is schematically illustrated in Figure 3.1.

Energy level scheme

Since REIs are many electron systems, analytical solutions of the Schrödinger equation do not exist. Typically, the energy levels are described by a Hamiltonian [91]:

$$\mathcal{H} = \mathcal{H}_0 + \mathcal{H}_\mathrm{C} + \mathcal{H}_\mathrm{SO}. \tag{3.1}$$

Here, $\mathcal{H}_0$ describes an electron in the potential of the nucleus, analogous to the hydrogen atom, $\mathcal{H}_\mathrm{C}$ are the sum over all the electron-electron Coulomb interactions, and $\mathcal{H}_\mathrm{SO}$ describes the spin-orbit coupling of an electron. All of these terms sum up the contributions of all N electrons.
To facilitate solutions,the central field approximation is used, where one adds to the centrosymmetric Coulomb potential of the nucleus an effective centrosymmetric potential that describes the average potential caused by the other electrons:

$$\mathcal{H}_0' = \sum_{i=1}^{N} \frac{-\hbar^2}{2m_\mathrm{e}} \nabla_i^2 + \sum_{i=1}^{N} \frac{1}{4\pi\epsilon_0} \frac{Ze^2}{r_i} - \left\langle \sum_{i<j}^{N} \frac{1}{4\pi\epsilon_0} \frac{e^2}{r_{ij}} \right\rangle. \tag{3.2}$$

To compensate, the electron-electron term then only describes deviations from this mean, therefore representing a small correction. The central field Hamiltonian can be solved with the Hartree-Fock method, essentially constructing superpositions of hydrogen-like solutions while ensuring anti-symmetry of the wavefunctions. The energy levels are in general split by the Coulomb interaction into different terms, described by the quantum numbers L and S, which represent the angular momentum and spin. These levels are further split by the spin-orbit interaction, with a remaining degeneracy of $2J+1$. J is the total angular momentum as known from atomic physics. Consequentially, these states are usually labeled in the well-known Russel-Saunders notation ${}^{2S+1}L_J$ [96, 91].[1]

[1] This implies that S and L are good quantum numbers and J can be calculated in the LS coupling. However, the contributions from spin-orbit coupling and coulomb interaction are of similar order of magnitude for many rare earth ions, which technically places them in an intermediate coupling regime. Nevertheless, these quantum numbers at least describe the predominant wavefunction constituents [96].

So far, we have treated the ion as completely free. In reality, the ions are doped inside a crystal and are influenced by their environment. This influence is modeled by an electric field perturbing the free ion, the so called crystal field. This further splits the J levels into crystal field levels. The degree to which the degeneracy is lifted is determined by the site symmetry the ion is doped into: generally the lower the symmetry, the more levels are observed. These levels are typically labeled by an additional quantum number (τ), which increases within a manifold with increasing energy of the levels.
The crystal field is the reason that optical transitions within the 4f-shell, which are forbidden by dipole selection rules, are even observable at all: they act as a perturbation that admixes eigenstates with different parity, therefore weakly allowing electric dipole transitions [91]. As a consequence, the strength of the optical transition heavily depends on the site symmetry within the crystal, and therefore the host material, with lower symmetries typically resulting in stronger optical transitions. Nevertheless, the optical transitions are very weakly allowed compared to other optically active defects in solids such as the nitrogen-vacancy center in diamond or the silicon vacancy in silicon carbide. This is evident by the excited state lifetime, which for rare earth ions is on the order of 1 ms, while typical values for the aforementioned defects are below 10 ns [97, 98, 99].
One further differentiates between ions that posses an even and uneven number of electrons, which are referred to as non-Kramers and Kramers ions respectively. Kramers ions posses an unpaired electron spin. Therefore, the crystal field levels are at least doubly degenerate. The degeneracy is lifted when a DC magnetic field is applied, leading to a Zeeman splitting.
Finally, for REI isotopes that posses a nuclear spin, the energy levels are further split by the hyperfine interaction. The magnitude of this splitting is typically 10 MHz to 100 MHz for non-Krammers and several GHz for Kramers ions.

Energy level scheme of Yb^{3+}

The trivalent positive Ytterbium ion possesses a relatively simple energy level structure, due to its electronic configuration $[Xe]4f^{13}$. Because 13 out of 14 electrons in the 4f-shell are filled, it can be treated as a one hole system. Therefore, there is no splitting due to the Coulomb-interaction between electrons and only spin-orbit coupling splits the levels into two levels $^2F_{7/2}$ and $^2F_{5/2}$. The crystal field then further splits these levels into up to $(2J + 1)/2$ Kramers doublets [100]. Finally, two isotopes of Ytterbium posses a nuclear spin: ^{171}Yb ($I = 1/2$, natural abundance: 14.1 %) and ^{173}Yb ($I = 5/2$, natural abundance: 16.1 %), and therefore show a hyperfine splitting [101]. A schematic of the resulting energy level scheme is depicted in Figure 3.2.
For quantum information applications, which require long coherence times, the main transition of interest is the one between the lowest levels in each crystal field manifold. The reason is that higher lying levels can easily decay into lower levels, for example via phonon-assisted mechanisms, fundamentally limiting the achievable coherence times. For Yb^{3+}, this is the $^2F_{7/2}(0) \rightarrow {}^2F_{5/2}(0)$ transition, which is, depending on the host material, located between 970 nm to 985 nm. A distinct advantage of Ytterbium compared

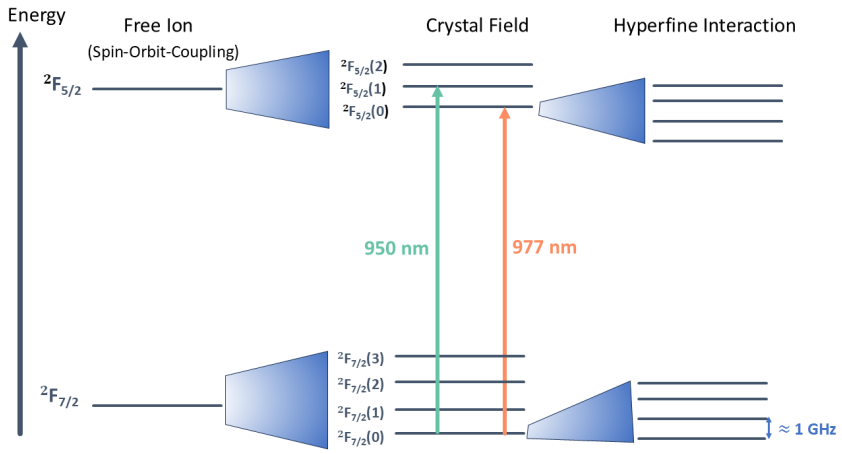

Figure 3.2.: Level scheme of Yb^{3+}:Y_2O_3. Note that the hyperfine splitting in yttria has not been reported and is assumed to be similar to other host materials.

to other rare earth ions is that this transition possesses a large branching ratio ζ, that is there is a high chance that the excited state decays via this coherent transition [102, 103]. This naturally increases the amount of useful photons. The exact value depends on the host material and is hard to measure in our experiment. Typical values are in the range of $\zeta \approx 20\,\%$ to $30\,\%$ (in comparison, the coherent transition in Eu^{3+} typically has a branching ratio of $\zeta \approx 1\,\%$ [104]).

ZEFOZ point at zero field

The ^{171}Yb isotope, which possesses a nuclear spin $I = 1/2$, is of particular importance for quantum information technologies. Related works have shown that in sufficiently low symmetry sites, the eigenstates are inseparable superposition states of the nuclear and electronic spin 1/2 states [105]. This makes the transition frequencies insensitive to first order to magnetic field fluctuations. Such fluctuations are usually one of the main contributions to decoherence, which makes working at such a point highly desirable. Note that this phenomena is in principal not unique to ^{171}Yb: For many rare-earth ions, such zero first order zeeman (ZEFOZ) points exist for a particular applied magnetic field. However, finding such a point is experimentally hard and typically requires complicated crystal field theory calculations to determine the starting point for the search, as well as very precise instrumentation to stabilize the working point. For ^{171}Yb however, this point exists at zero magnetic field, eliminating much of the experimental overhead.

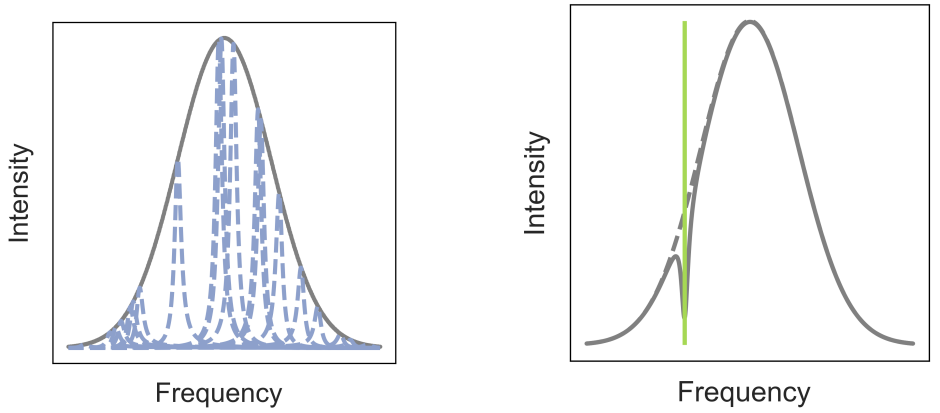

(a) The transition frequencies of individual rare earth ions (blue) are distributed over a large frequency range. For large ensembles, the transitions appear inhomogeneously broadened (gray).

(b) Concept of spectral holeburning. A strong laser depopulates states at a at a fixed frequency, leading to a dip in absorption at this frequency.

Figure 3.3.: Schematic illustration of how an ensemble of ions forms the inhomogeneous line and how the absorption profile can be manipulated via spectral hole burning, allowing measurements of the homogeneous linewidth even in inhomogeneously broadened ensembles.

Inhomogeneous broadening

As discussed before, individual REIs posses exceptionally narrow linewidths when doped into solids, down to the Fourier transform limit imposed by the lifetime $\Gamma_0 = \frac{1}{2\pi T_1}$, which is on the order of 1 kHz [106, 107]. However, the spectral position of the single ion resonances is distributed over a broad spectral range, up to several GHz, due to the inhomogeneous crystalline environment [108, 96]. When probing a large ensemble of ions, for example by spectroscopy of a macroscopic crystal, this inhomogeneous broadening leads to an observed linewidth that is much larger than the individual ion linewidth. This is schematically depicted in Figure 3.3 (a). To distinguish the two, the individual ion line is called the *homogeneous linewidth* and the observed, apparent larger linewidth is called the *inhomogeneous linewidth* due to its source being the inhomogeneous environment [1]. In principle, this phenomenon is not unique to rare earth ions. However, the ratio of the two can be uniquely large, on the order of $\frac{\Gamma_{\text{inhom.}}}{\Gamma_{\text{hom}}} \approx 10^6$.
This property can be both a blessing and a curse. On the one hand, direct measurements of the homogeneous linewidth are not possible by measuring ensembles, and require more sophisticated spectroscopic techniques. On the other hand, the large ratio offers

[1] While the broadening mechanism is different, this has many parallels in the spectroscopy of Doppler-broadened gases and many techniques can be adapted from this field.

great potential for *spectral multiplexing*. The idea is that for a small number of ions, the individual ion lines can be resolved spectrally using a narrow linewidth laser due to their inhomogeneously shifted transition frequency, even when multiple or many ions spatially overlap with the laser beam. Continuing this thought, one can easily address multiple ions by applying multiple frequency tones. This constitutes a naturally available multi-ion quantum register within a spatially limited spot. Proposals exist how such a register can be used, to build for example a small quantum processing node [109]. The lineshape of the inhomogeneous line depends on the physical origin and homogeneity of the dominant broadening mechanism [110].

Spectral hole burning

As discussed previously, the inhomogeneous broadening complicates the measurement of the homogeneous linewidth. However, the homogeneous linewidth is of great interest, since it is directly related to the optical coherence time $T_2 = \frac{1}{\pi\Gamma_{\text{hom}}}$, the metric that ultimately determines the suitability for many quantum information processing applications. Spectral hole burning, which relies on optical pumping, is a commonly used technique to measure the homogeneous linewidth in REIs [96].
Spectral hole burning relies on depopulating at least one ground state via optical pumping. The population is then shelved in another energy level. The missing population manifests itself in a narrow dip in the absorption profile, a so called spectral hole. The minimal width of this feature is twice the homogeneous linewidth $\Gamma_{\text{hole}} = 2\Gamma_{\text{hom}}$, but the feature can appear broadened due the experimental conditions, such as power broadening or laser drifts. The change in the absorption profile is sketched in Figure 3.3 (b).
The shelving state can be the optically excited state with the typical optical lifetime of $\approx 1\,\text{ms}$, as I will make use of later in this thesis (Section 3.3). I will refer to this case as *transient spectral holeburning*, as the hole relaxes with the optical lifetime $T_1 \approx 1\,\text{ms}$. Alternatively, population can be transferred in adjacent hyperfine levels of the optical ground state, if the isotopes exhibiting a nuclear spin and the spin lifetime $T_{1,\text{spin}}$ is sufficiently long. These hyperfine-levels can exhibit extremely long lifetimes at cryogenic temperatures for some REIs, up to several days or even months [111]. I will refer to this case as *persistent spectral hole burning*[1]. This long lifetime allows for shaping the absorption profile of the inhomogeneous line, which enables many applications, both for quantum technologies and more conventional techniques. For example, long-lived spectral holes are used as narrow frequency filters, both optical [108] and for radio-frequencies [112], and for laser frequency stabilization [113, 114]. In terms of quantum communication applications, the atomic frequency comb (AFC)-protocol is a quantum memory protocol that relies heavily on spectral holeburning [115, 116].

[1] Persistent is to be understood as long compared to the optical lifetime. The hole relaxes with the spin lifetime $T_{1,\text{spin}}$. Truly irreversible holeburning can occur for example in biological samples.

3.1.2. Applications of rare earth ions in quantum information processing

Single ions integrated in optical cavities

The development of quantum network nodes has historically been pushed and pioneered in other material systems than REIs, such as defect centers in diamond, quantum dots, trapped ions and neutral atoms. Rare earth ions, despite their excellent coherence properties and being well studied previously, have only come under investigation in the last 10-15 years. One reason for this is the big initial hurdle of detecting the fluorescence of a single ion: While for all the aforementioned systems, this can be done in a confocal microscope quite comfortably, REIs require either extremely sensitive measurement techniques or an enhancement of the optical transition using an optical cavity. The first measurements of individual REIs dopants were done using either the dipole-allowed, and therefore much brighter, 4f-5d optical transition [117, 118], or via electronic readout of ionization caused by resonant optical excitation [119]. The first optical detection of a single ion using a 4f-4f transition was achieved for Pr^{3+}:Y_2SiO_5 in a confocal microscope using a solid immersion lens [98]. Still, the extremely low countrate below 100 counts/s is limiting for most applications or next steps.
A breakthrough in the field was the successful detection of single ions in optical cavities. The group of Andrei Faraon used a photonic crystal cavity directly milled into YVO_4 to detect individual Ytterbium dopants, demonstrating an effective Purcell factor of $C_{\text{eff}} \approx 120$ [120]. Similarly and simultaneously, the group of Jeff Thompson detected single erbium ions in Y_2SiO_5, using evanescent coupling to a silicon photonic crystal cavity placed on top of the sample. They achieved an effective Purcell factor of $C_{\text{eff}} \approx 660$ [121]. Both groups have since improved their setups and pushed the system to the forefront of solid-state qubits. Highlights include the demonstration of single-shot readout [120, 122], coherent coupling to an adjacent nuclear spin [123] respectively spin clusters [29], demonstration of photon indistinguishability [124] and recently also remote entanglement of two and three ions [28]. These impressive results showcase the great potential of REIs, but also illustrate how important a well working cavity system is in order to achieve this.
In parallel, there has also been some effort to couple REIs to open FP-cavities. Our group has pioneered the approach of integrating nanocrystals in a microscopic FFPC cavity, although single ion detection has remained elusive for the investigated Eu^{3+} ions, whose particular weak optical transitions are even more unfavorable than other REIs [125, 104]. Following the same approach, collaborators have detected single erbium ions in nanocrystals [126, 127]. Another team employed open FP-cavities to detect single erbium dopants in YSO membranes, demonstrating high Purcell factors of $C_{\text{eff}} \approx 110$ [120] and a large spectral multiplexing capability [128, 129, 130].

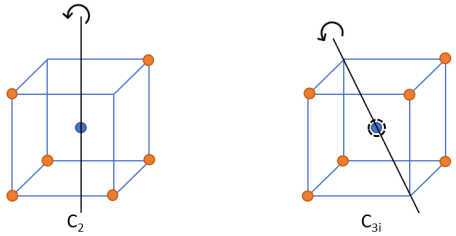

Figure 3.4.: Illustration of the two symmetry sites of yttrium ions in yttria. Blue dots are yttrium atoms, orange dots are oxygen atoms. The rotational symmetry axes and the inversion point are indicated. After [133].

3.1.3. Ytterbium doped yttria nanocrystals for cavity integration

As discussed above, rare earth ion doped nanocrystals are one promising approach for integrating rare earth ions into optical resonator, in particular into open cavities such as FP cavities. The requirements on the nanoparticles are as follows:

- Suitably **small** in order to introduce minimal scattering loss, enabling cavity operation with a high finesse in order to achieve the neccesary Purcell enhancement.
- **Coherence properties** should be well preserved and as close to bulk values as possible.

These two requirements seem to oppose each other, since a small particle diameter means close proximity of a large fraction of ions to the surface, where charges accumulate and typically lead to spectral diffusion [131]. Also, crystal defects are more likely to occur in nanocrystals due to their finite extent. Additional reasons for decoherence are "surface states and modified spin bath dynamics" [132]. It speaks to the robustness of the rare earth ions in respect to their environment that, even in nanocrystals, good optical and spin properties have been observed. Yttria (Y_2O_3) in particular has proven to be a good host material, combining suitability for nanoparticle synthesis with good coherence properties.

Yttria as a host material

Yttria (Y_2O_3) is a transparent crystal with a cubic crystal structure, often used as a host material for optically active rare-earth dopants. The dopants non-deterministically replace yttrium atoms in the lattice. There are two nonequivalent yttrium lattice sites in yttria, which exhibit a C_2 and C_{3i} symmetry. There are a total of 32 yttrium ions per unit cell, with 24 belonging to the C_2 and eight belonging to the C_{3i} site [134, 107]. The two different symmetry sites are depicted in 3.4.

Table 3.1.: Summary of homogeneous linewidths Γ_{hom} of rare earth ion dopants measured in Y_2O_3 nanocrystals. The homogeneous linewidths are measured by photon echo spectroscopy on a compressed powder of nanocrystals.

Dopant	Γ_{hom}	Temperature	Magnetic field	Particle diameter	Source
Eu^{3+}	85 kHz	1.4 K	-	60 nm	[138]
Pr^{3+}	315 kHz	1.4 K	-	150 nm	[132]
Er^{3+}	380 kHz	3 K	100 G	150 nm	[139]
Nd^{3+}	62 kHz	1.6 K	-	380 nm	[139]

Nanoparticles used in this work

The nanoparticles used in this work were provided by the group of Philippe Goldner at Chimie ParisTech. They have an ensemble averaged diameter of $\varnothing = 100$ nm and a doping concentration of 100 ppm. They were grown using the method of homogeneous precipitation. The synthesis is described in detail in [135, 136] and typically yields mono-crystalline or few crystalline domain nanocrystals. During the final step of the fabrication, they were annealed at a temperature of $T = 800\,^{\circ}\mathrm{C}$. Subsequent studies have shown that for other dopants, the coherence properties improve when the nanoparticles are subjected to an additional oxygen-treatment step and subsequently annealed at a temperature of $T = 1200\,^{\circ}\mathrm{C}$ [137].

Coherence in nanoparticles

The optical coherence for other REI dopants in yttria nanoparticles was determined in several studies. The measured homogeneous linewidths are summarized in Table 3.1. All of the conducted measurements used nanocrystals grown by the group of Philippe Goldner using the same technique as for the samples investigated in this work. Even though the synthesis and experimental techniques are extremely similar between these different nanocrystals, some care has to be taken when directly comparing them. For one, the size differs between them, and additionally some final treatment steps were done with different parameters. Nevertheless, it is remarkable that narrow optical homogeneous linewidths have been observed for all of these dopants, encompassing both Kramers and Non-Kramers ions in these nanoparticles. It should however be noted that the observed values are still typically roughly two to three orders of magnitude worse than in high quality bulk crystals, where the optical homogeneous linewidth can approach the transform limit given by the optical lifetime $\Gamma_0 = \frac{1}{2\pi T_1}$ [107].

There is not as much data available on the spin coherence of the dopant in nanocrystals. For the case of europium, spin coherence times of $T_{2,\mathrm{spin}} = 1.2$ ms, close to the value reported in bulk ($T_{2,\mathrm{spin}} = 12$ ms) [140] have been observed [141]. The fact that the spin coherence is less influenced by the finite size compared to the optical coherence is

attributed to the different dephasing mechanisms. The optical decoherence is supposedly limited by an electric interaction with the fluctuating charges at the surface, while the spin coherence is mainly limited by magnetic fluctuations.
Erbium nanoparticles have been successfully integrated into FFPCs at cryogenic temperatures, demonstrating switchable Purcell enhancement of ion ensembles [126] and the detection of individual Erbium dopants [127]. The progress on a very similar experiment using Eu^{3+}:Y_2O_3 nanoparticles is reported in the PhD thesis of my colleague Timon Eichhorn [104].

The initial goal of my thesis was to follow the same approach for ytterbium doped Y_2O_3 nanoparticles. I have touched on the motivation for using ytterbium instead of other rare earth ions previously in Section 3.1.1. To briefly summarize, the relatively strong branching ratio of the coherent ${}^2F_{7/2}(0) \rightarrow {}^2F_{5/2}(0)$ transition should lead to large effective Purcell factors, facilitating the detection of single ions compared to e.g. Eu^{3+}. At the same time, the coherence times can still be well preserved due to the existence of a ZEFOZ point at zero magnetic field. Additionally, cavity operation is slightly facilitated by reduced scattering losses and background fluorescence, due to the optical transition wavelength of $\lambda \approx 980\,\mathrm{nm}$. One significant drawback of Ytterbium ions is the lack of highly efficient detectors, due to the transition wavelength lying inconveniently between the bandgaps of Silicon and InGaAs, making both detector technologies inefficient at this wavelength. By very literally paying a price on the order of some ten thousand euros, this problem can be solved by using superconducting nanowire single photon detectors (SNSPDs), which can have high detection efficiency at these wavelengths as well as very little dark counts.

3.2. Room temperature studies and cavity integration of ytterbium in yttria nanocrystals

Before integrating these emitters into a cryogenic cavity, there are two avenues to explore. On the one hand, one can study the nanoparticles inside a cavity at room temperature. The expected Purcell factors are too low at room temperature to be useful for long-term applications. However, it serves as a nice proof of principle experiment, where one can already address many of the issues that will arise during the cryogenic experiments. At the same time, the cavity setup is much easier to operate and much easier to iterate on at room temperature. On the other hand, one would like to determine the optical properties of the ytterbium doped Y_2O_3 nanoparticles at cryogenic temperatures from an ensemble measurement without an optical cavity. Such measurements are easier and quicker[1]

[1] but not necessarily “easy” and “quick”.

to conduct than cryogenic cavity experiments, and are needed to determine whether a cryogenic cavity experiment holds enough promise. In the remainder of this chapter, I will address these two points, starting with the room temperature characterization of the ytterbium doped Y_2O_3 nanoparticles.

3.2.1. Room temperature spectroscopy using a confocal microscope

For a first spectroscopic investigation of Yb^{3+}:Y_2O_3 nanocrystals at room temperature, nanoparticles dispersed on a glass slide were investigated in a home-built confocal microscope. This setup allows for recording confocal microscope images, as well as taking photoluminescence spectra at distinct points by routing the light to a grating spectrometer, and finally allows measurements of the optical lifetime. The construction and use of the confocal microscope is described in detail in the master thesis of Tobias Krom [63]. A short summary of its properties can be found in the Appendix B. The presented setup is also used for room temperature characterization of the molecular complexes discussed in section 4. In the following, I show photoluminescence spectra and lifetime measurements that were conducted on small features, with their spatial extent limited by the resolution limit of the microscope. The resolution limit of the microscope is given by the pointspread function (PSF), which was experimentally determined to be 0.56 µm (see Appendix B). This spatial resolution limit is insufficient to distinguish single nanocrystals from small nanoparticle agglomerates by their spatial extent.

Photoluminescence spectrum

To measure the spectrum of the photoluminescence (PL), fluorescence light is coupled into a multi-mode fiber and is sent to a grating spectrometer, where the light is dispersed on a blazed grating and then imaged onto a cooled CCD camera. Three different gratings can be chosen. The spectral resolution of the spectrometer in the NIR regime is determined by measuring an attenuated laser beam at $\lambda = 940\,\text{nm}$ and fitting the result with a single Gaussian. This reveals a linewidth of $\Delta\lambda = 0.09\,\text{nm}$ for the 1200 l/mm grating, which provides the best spectral resolution.
The accuracy of the absolute wavelengths determined by the spectrometer relies on an accurate calibration. Calibration lamps that are commonly used in the visible range have only few peaks in the NIR. Therefore, I typically calibrated to the laser wavelength, where the absolute spectral position of the laser is measured with a wavemeter. This constitutes only a rough calibration and care should therefore be taken when evaluating absolute wavelength values. The measured photoluminescence spectra show no significant differences between different nanocrystals. An exemplary spectrum is depicted in Figure 3.5 and mainly shows the dominant $^2F_{7/2}(0) \rightarrow {}^2F_{5/2}(0)$ transition at 977.3 nm. The linewidth of the $^2F_{7/2}(0) \rightarrow {}^2F_{5/2}(0)$ transition is determined by a single

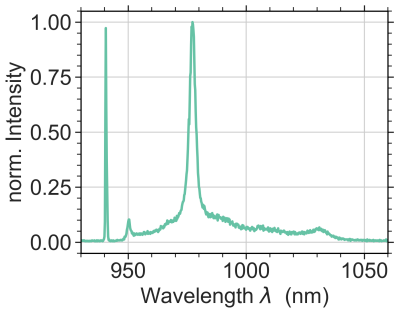

(a) Photoluminescence spectrum for a Yb^{3+}:Y_2O_3 nanocrystal at room temperature. The excitation laser at $\lambda = 940\,\mathrm{nm}$ and the onset of the long pass filter are visible.

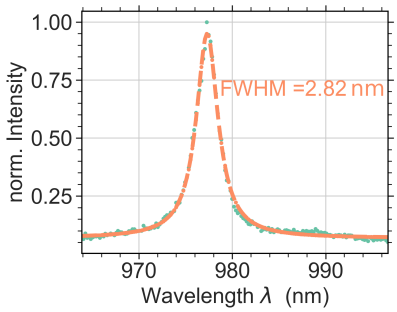

(b) Single Lorentzian fit to the ${}^2F_{7/2}(0) \rightarrow {}^2F_{5/2}(0)$ transition.

Figure 3.5.: Photoluminescence spectra of Yb^{3+}:Y_2O_3 nanocrystals taken at room temperature.

lorentzian with a width of $\Delta\lambda = 2.82\,\mathrm{nm}$. This gives a first indication for the homogeneity inside the nanocrystals[1]. The average linewidth of six investigated nanocrystals is $(2.83 \pm 0.03)\,\mathrm{nm}$.

Optical lifetime

In order to measure the excited state lifetime, the excitation light is pulsed and the detected photon events are time-correlated with the excitation pulse via correlation electronics [2]. The resulting histogram reveals the decay of the optical excited state. Unless stated otherwise, all lifetimes given in this thesis are determined from single exponential fits. On some occasions, bi- or multi-exponential decay with distinct time constants are observed. This indicates the presence of multiple contributions to the fluorescence, such as background fluorescence or multiple excited states.
The optical lifetime was measured on several emitters, showing an average lifetime of $\tau = (1.48 \pm 0.05)\,\mathrm{ms}$. Three exemplary measurements are depicted in Figure 3.6. It is worth to note that the excited state lifetime in nanoparticles is generally higher than in bulk crystals. This can be understood as the nanoparticle acting as a weak off-resonant resonator, slightly suppressing the local field [125]. Small variations in the lifetime can be explained by variations in nanoparticle size and homogeneity. In one case, a particularly

[1] At room temperature, the concept of homogeneous and inhomogeneous linewidths become somewhat blurred, because the homogeneous line broadens significantly and can become even broader than the inhomogeneous line.
[2] *TimeTagger*, Swabian Instruments

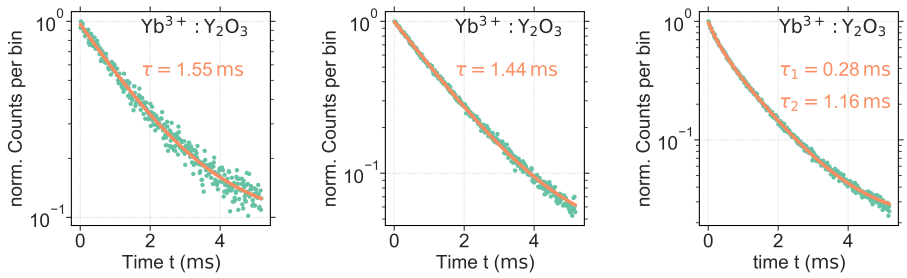

Figure 3.6.: Exemplary lifetime measurements of different Yb^{3+}:Y_2O_3 nanoparticles, showing slight variations. The measurement depicted in (c) shows a significantly faster, bi-exponential decay, only observed for one feature.

bright emitter showed both a significantly shorter lifetime and a bi-exponential decay characteristic, while still showcasing a characteristic photoluminescence spectrum and appearing as a point-spread limited feature.

3.2.2. Towards cavity integration of ytterbium doped yttria nanocrystals

In this section, I will summarize the efforts on integrating the Yb^{3+}:Y_2O_3 nanoparticles into a FFPC. Nanoparticles were distributed on DBR mirrors using spin-coating techniques. These mirrors were analyzed using cavity scanning microscopy. I found that the obtained nanoparticle density is suitable for cavity experiments. Finally, I observe room temperature fluorescence using a double resonance excitation scheme. I will conclude with a discussion on the expected Purcell factors and signal strengths, with an outlook on what a cryogenic experiment could achieve using the achieved parameters.

Mirror preparation

Two mirrors, hence labeled M1 and M2, were coated with Y_2O_3 nanoparticles. The mirrors are from the coating run described in section 2.2.1 and are chosen from the higher transmittance coating (230 ppm @ 985 nm) (see Section 2.2.2 for a summary of the utilized coating). Before depositing the nanoparticles, a checkerboard pattern was imprinted on the mirror using CO_2 laser machining. This allows to re-identify the same area in different setups. I prepared a solution of 250 µg Y_2O_3 and 50 µg of sodium dodecyl sulfate (SDS) in 250 µl of deionized water. SDS is used as a surfactant agent to prevent nanocrystals from forming agglomerates. For the same reason, a sonotrode was used to apply ultrasound to the solution for 30 minutes in order to break up already existing

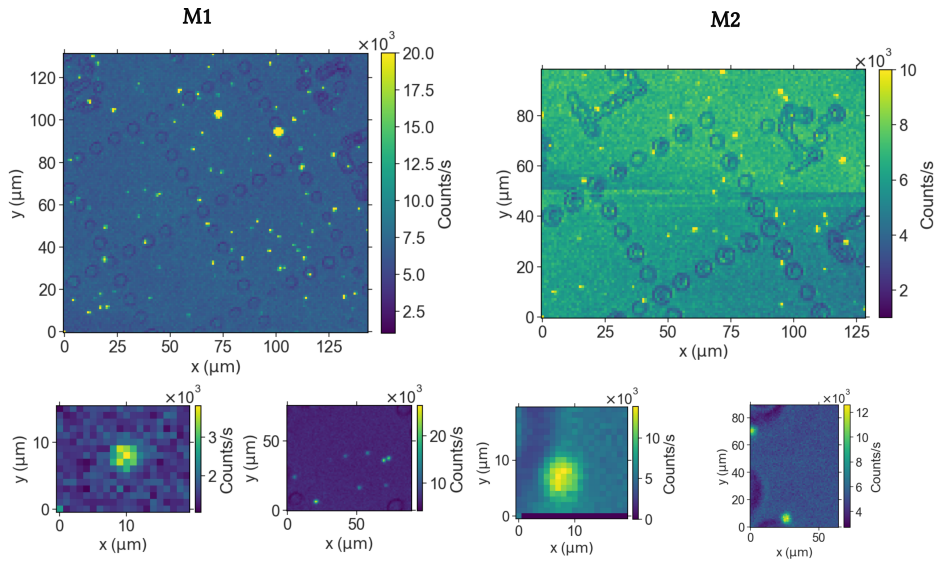

Figure 3.7.: Large scans and some small features in the confocal microsocope of M1 (left) and M2 (right). The large scans show part of the CO_2 machined grid on the mirror.

agglomerates. The recipe was adapted from Timon Eichhorn and Julia Benedikter. The mirrors were exposed to oxygen plasma to remove organic waste and activate oxygen bonds at the surface. A drop of 20 µl was dropped onto the mirror during an initial distribution spin-caoting step at 100 rpm for 30s. In a second step, the mirror was spun at a rotational frequency of 2000 rpm. For M2, the nanoparticle solution was centrifuged in a centrifuge for one minute at 1000 rpm, before pipetting 20 µl from the surface of the solution. This should preselect for smaller nanoparticle clusters. The mirrors where then analyzed using the confocal microscope described in Section 3.2. Some exemplary confocal scans are depicted in Figure 3.7. Both samples show a suitable density of point-like emitters, although many of these are likely nanoparticle agglomerates. The feature density is somewhat sparser for the segment in M2, in agreement with the additional centrifugation step. Note that while the average countrate of small features is higher for YM2, which could point to larger agglomerates, the setup was realigned between the two measurements and is therefore not directly comparable.
To differentiate single particles from agglomerates, I make use of the high sensitivity of a high finesse cavity to extinction losses. To that end, I assemble a FFPCs from M2 and a fiber mirror.

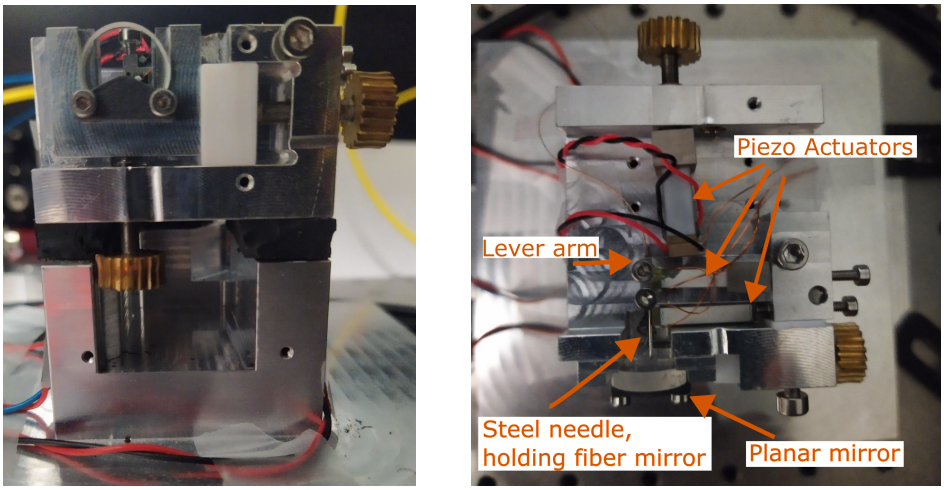

(a) Side view.

(b) Top view.

Figure 3.8.: Photographs of the fiber cavity assembly for room temperature.

Cavity assembly

The fiber and mirror were assembled in a home-built positioning unit, based on a design by Thomas Hümmer. The utilized fiber mirror is coated with the high reflectivity coating described in Section 2.2.2, with a nominal transmission of 25 ppm. The cavity is therefore expected to operate with a finesse $\mathcal{F} \approx 20000$ at $\lambda = 985\,\text{nm}$.
In the following, I will quickly sketch the principles of operations of the cavity setup. For a more detailed discussion and analysis of the design, the reader is referred to Thomas Hümmers' doctoral thesis [142], who originally designed and implemented these mechanics.
The cavity mechanics are depicted in Figure 3.8. An aluminum base block with high mass serves as the platform for the mechanics. The macroscopic mirror is clamped to the platform using a screwable mirror holder. The mirror holder can be moved transversely using two screws. The fiber mirror is glued into a syringe, with the fiber protruding only a few hundred micron to minimize bending motions. The syringe is clamped into a flexure arm, which can be bent and rotated by applying pressure, thereby enabling rapid movement of the fiber tip over the mirror. To enable these scanning mechanics, we use piezo-ceramic actuators, which exert forces at the designed contact points, producing bending motions. Because the bending amplitudes are small, this leads to an effectively decoupled and linearized movement in all three spatial directions, when actuating the respective piezo ceramics. The piezo mechanics are driven by analogue-digital converters

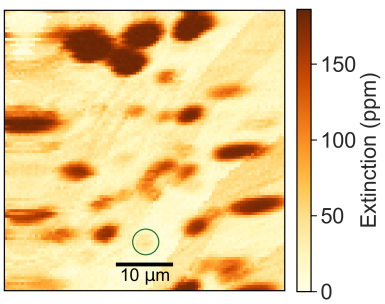

(a) Extinction map of mirror Yb-M2 with a bare cavity finesse of $\mathcal{F} = 20000$ at $\lambda = 985\,\mathrm{nm}$.

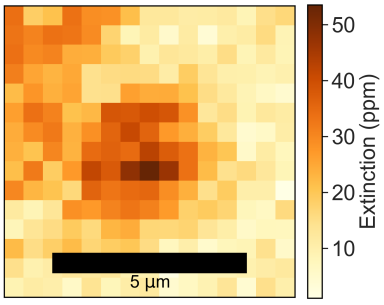

(b) Zoom on a pointspread limited feature marked in green in (a), with a peak extinction of $E \approx 50\,\mathrm{ppm}$.

Figure 3.9.: Characterization of the nanoparticle density and agglomeration via scanning cavity microscopy. Scalebars are estimated from the point-spread function.

[1], which are suitably amplified and low-pass filtered. In order to achieve a high stability and the desired piezo travel range, all axes need to be pre-loaded accordingly. This is achieved using a spring for the z-direction and screws pressing on the piezo actuators for the x-y direction.

Scanning cavity microscopy

The fast positioning capabilities of the cavity mechanics can be utilized to sensitively record extinction maps. Therefore, the peak cavity transmission T is recorded stepwise over the x-y scanning range of the platform. In order to do this quickly, a custom-built algorithm implemented on a FPGA board[2] is used to readout the peak transmission value of the cavity resonances. The observed extinction E can be calculated given the unperturbed peak transmission T_0 and the unperturbed finesse $\mathcal{F}$, as:

$$E = \frac{\pi}{\mathcal{F}} \left(\sqrt{\frac{T_0}{T}} - 1 \right). \tag{3.3}$$

Here, unperturbed refers to a "clean" mirror spot where there is no additional extinction. For the high finesse values used in this work ($\mathcal{F} = 20000$), an additional losses of 65 ppm results in a drop of the cavity transmission to half of the unperturbed peak transmission

[1] *NI-Card*,National Instruments
[2] StemLab 125-14, *Red Pitaya*, using custom code developed by Thomas Hümmer

T_0. Therefore, this constitutes an extremely sensitive extinction microscope, which has been successfully applied to study different samples. The spatial resolution is limited by the cavity waist (see section 2.1).
I make use of this sensitivity to study the distribution of nanoparticles. The scattering losses of a spherical particle of diameter d on a dielectric surface in the Rayleigh approximation scale as d^6:

$$E = \frac{8\pi^4}{27}\frac{d_{\mathrm{NP}}^6}{\lambda^2 w_0^4}\left(\frac{n_{\mathrm{med}}^2\left(n_{\mathrm{NP}}^2 - n_{\mathrm{med}}^2\right)}{n_{\mathrm{med}}^2 + \frac{5}{16}\left(n_{\mathrm{NP}}^2 - n_{\mathrm{med}}^2\right)}\right)^2, \tag{3.4}$$

with n_{NP} and n_{med} the refractive index of the nanoparticle and the surrounding medium, respectively [104]. The extinction measurement is therefore sensitive to the nanoparticle size and also agglomeration of nanoparticles, which due to small extent of the nanoparticles is not visible in the spatial extent of the nanoparticles. For the nominal nanoparticle diameter of 100 nm, and a wavelength of 985 nm, the expected scattering loss is $S = 15$ ppm, which corresponds to a drop in transmission to 83 % and a decrease in finesse to $\mathcal{F} = 19\,000$. Figure 3.9 shows an exemplary scanning cavity extinction map of the mirror Yb-M2. One observes many scattering features which can be attributed to the dispersed nanoparticles. Many feature show a pronounced extinction, which is indicative of large nanoparticle clusters. However, there are also spatially resolvable, fainter features with a peak extinction of 50 ppm, which could be explained by a single nanoparticle with a diameter of $d = 120$ nm, as depicted in Figure 3.9 (b). Due to the background variations observed in the scanning cavity measurement, it is unclear if the smaller extinction signals, that would be expected for smaller particles, could even be resolved without further optimization. I content myself with the fact that small scatterers, consistent with individual particles, can be resolved. Crucially, they show only small extinctions and should therefore not significantly perturb the cavity performance, thereby enabling the envisioned cavity experiments. A caveat is that it is not possible to assert which of the observed scatterers are indeed Yb^{3+}:Y_2O_3 nanoparticles - this requires spectroscopic measurements, that I will present in the following section.

Fluorescence studies at room temperature

Room temperature studies of fluorescence in a cavity can be quite challenging. First of all, the expected Purcell factor is low: The homogeneous linewidth is broad - often more so than the inhomogeneous linewidth, and therefore limits the Purcell factor (see Chapter 2.3.1). On the other hand, this means that all ions can be excited using a single frequency drive, which therefore all contribute to the fluorescence signal.

The second challenge is to separate the excitation light from the ion fluorescence. Multiple strategies can be employed: For one, the two can be separated temporally. An

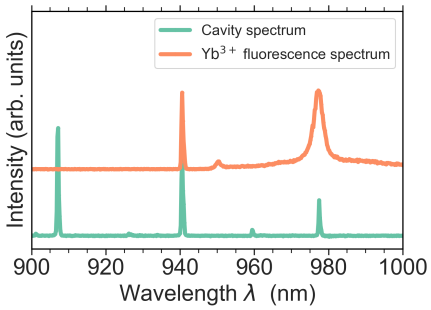

Figure 3.10.: Depiction of the double resonance scheme. The cavity length is adjusted such that a resonance at 940 nm allows in-coupling of the excitation light, and the next fundamental mode overlaps with the $^2F_{7/2}(0) \rightarrow {}^2F_{5/2}(0)$ transition of ytterbium at 978 nm, which one aims to enhance.

excitation pulse is sent on the sample, while the detection is blocked. The fluorescence decay after the excitation is recorded, ideally in a time-resolved manner. Due to the long lifetimes of ytterbium ions, this is achieved rather easily, for example by using AOMs to shape the optical excitation pulses. Typical rise times achieved in this manner are on the order of 60 ns, four orders of magnitude lower than the fluorescent lifetime. However, a high degree of suppression ($\approx$ 160 dB for 1 mW of excitation) of the excitation light is required, since sensitive single photon counters are employed for detection. This requires at least two cascaded double pass AOMs to fully suppress the excitation light.

A second approach is to employ spectral filtering. The ions are excited at a wavelength of 940 nm using the $^2F_{7/2}(0) \rightarrow {}^2F_{5/2}(1)$ transition. The excitation light is blocked using suitable longpass filter. This simple approach is complicated by the cavity: Since it blocks all non-resonant frequencies, the lower wavelength excitation needs to either be applied from the "side", that is with an angle to the cavity axis, or be coupled to a cavity mode that is simultaneously resonant with the $^2F_{7/2}(0) \rightarrow {}^2F_{5/2}(0)$ transition. The latter scheme is henceforth referred to as the double resonance scheme and is schematically depicted in Figure 3.10. Side excitation is extremely challenging using conventional optics, since the very low cavity lengths imposes significant geometrical constraints.

In this work, I combine a pulsed excitation with a double resonance scheme to minimize the background fluorescence. Therefore, the cavity length is adjusted such that there are cavity resonances at a wavelength of $\lambda = 940$ nm and at 978 nm, which amounts to a cavity length of $d = \frac{\lambda_1 \lambda_2}{2(\lambda_2 - \lambda_1)} = 12.1\,\mu$m. Both resonances can easily be monitored by recording the transmission of a broadband light source through the resonator on a spectrometer. The spectrum is depicted in Figure 3.10 in green.

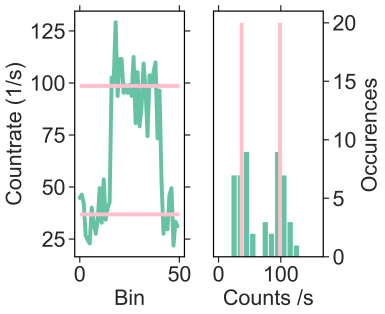

(a) Exemplary count rate trace and count histogram for mode order $q = 27$. Pink lines indicate the average countrate when the cavity is on- or off-resonant.

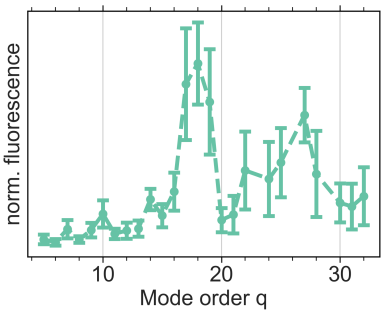

(b) Countrate normalized to the excitation intensity as a function of mode order q

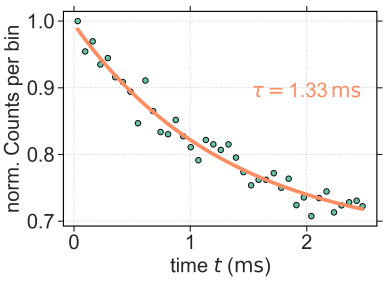

(c) Lifetime measurement revealing a decay time of about 1 ms, characteristic for rare earth ions.

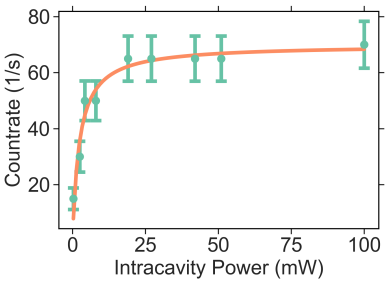

(d) Saturation measurement.

Figure 3.11.: Analysis of the fluorescence of Yb^{3+}:Y_2O_3 nanoparticles observed in the cavity

The cavity is then stabilized to the excitation laser at a wavelength of $\lambda = 940$ nm and the fluorescence is detected on a single photon counting module[1]. A 10 % fraction of the transmitted light is split off and monitored on a photo diode[2] to provide the feedback signal for active stabilization. The remaining 90 % of the transmitted light is guided into the fluorescence detection path, where the excitation is filtered using an optical long-pass filter[3]. When the cavity is on resonance, a slight increase in the countrate is detected at some longitudinal mode orders. An exemplary signal is depicted in Figure 3.11 (a). The sudden rise occurs once the cavity is stabilized on the excitation laser. The pink lines in the figure are the average of the 20 highest and 20 lowest values. The

[1] *COUNT NIR-50*, Laser Components
[2] *APD 130A*, Thorlabs
[3] *FELH950*, Thorlabs

fluorescence signal is determined as the difference between the two.
In order to verify whether this signal truly stems from ytterbium ions, I first vary the cavity length, that is the measurement is conducted as a function of the mode order. To account for the varying intra-cavity power due to the different transmitted intensities of different modes, the background corrected countrate is divided by the peak intensity of the transmitted laser intensity monitored on the reference photo diode. This is plotted as a normalized countrate as a function of the mode order q in Figure 3.11 (b). Two resonances around $q = 27$ and $q = 17$ are visible. The double resonance is expected at mode order $q = 26$, in reasonable agreement with the observed peak. The peak at lower mode order could be explained by a higher order transverse mode being resonant with the Yb^{3+} transition around 977 nm. For the employed fiber mirror radius of curvature $R_c = 30\,\mu m$, the second higher order mode family with $m + n = 2$ is expected at a wavelength of 977 nm for the fundamental mode order $q = 17$. We expect only even higher order modes to couple to the nanocrystal, since odd mode numbers exhibit a node in the center of their spatial profile (see Section 2.1.1). Therefore, this agrees well with the observation. Nevertheless, it is surprising that the signal is stronger than for the fundamental mode. Because of the higher mode volume and the difficulty to collect and focus the higher order modes onto a detector, one would expect a smaller observed countrate than for the fundamental mode order.
In order to further verify whether the observed signal stems from ytterbium ions, I investigate the optical lifetime in a pulsed experiment. Indeed, an exponential decay with a time constant of $\tau = 1.33\,ms$ is observed, similar to the optical lifetimes observed in the confocal microscope (see Figure 3.11 (c)). Such long lifetimes are characteristic for rare earth ions, and background signals usually decay on much smaller timescales. Due to the broad homogeneous linewidth, the expected Purcell effect is small, such that no significant change in the lifetime is expected. Finally, I investigate the saturation of the signal as a function of intracavity power, which is calculated from the transmitted intensity on the photodiode and the finesse $\mathcal{F}$. The result is depicted in Figure 3.11 (d). A clear saturation behavior is observed, which is characteristic for fluorescence stemming from discrete energy levels, such as rare earth ions.
All together, these measurements corroborate the hypothesis that some part of the observed signal stems from rare earth ions: the double resonance scheme works at the expected cavity lengths dictated by the Yb^{3+} transition energies, the long lifetime characteristic of rare earth ion fluorescence is observed, and the signal shows a clear saturation behavior. However, the observed countrates are extremely low, on the order of a 100 counts/s when subtracting the background. In order to understand this, let us look at the expected signal strength.

Purcell Estimate

In order to calculate the Purcell effect, one first needs to calculate the cavity mode volume. For the utilized radius of curvature $R = 30\,\mu m$ operating at a mode order of $q = 26$ at the resonant wavelength $\lambda = 977\,nm$, this corresponds to a beam waist $w_0 = 2.2\,\lambda$ and a

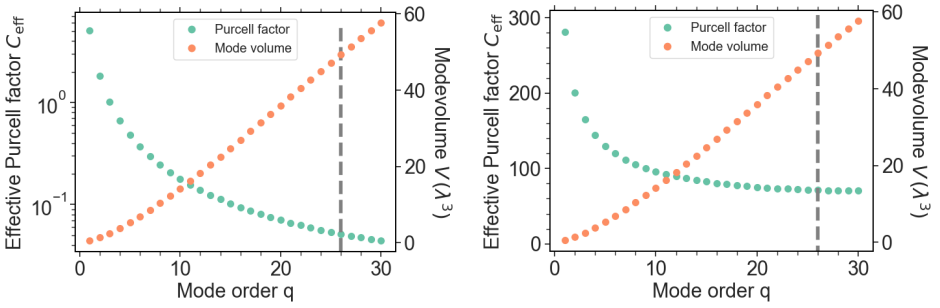

(a) Room temperature

(b) Cryogenic Temperature

Figure 3.12.: Calculated effective Purcell factor (green) for Yb^{3+}:Y_2O_3 and mode volume (orange) for the experimentally realized cavity at room temperature (a) and extrapolated to low temperatures ($T = 4.2\,\mathrm{K}$) (b). The gray dotted line indicates the working point imposed by the double resonance condition.

mode volume of $V = 49\,\lambda^3$. The quality factor is largely dominated by the homogeneous emitter linewidth determined from the PL measurements in Section 3.2 of $\Delta\nu = 920\,\mathrm{GHz}$. This results in an ideal Purcell factor of $C_0 = 0.18$, when accounting for a random transition dipole orientation within the nano-crystal with a factor of $1/3$. Assuming a branching ratio of $\zeta = 30\,\%$ into the coherent transition, the expected effective Purcell-factor is $C_{\mathrm{eff}} = 0.05$. Therefore, it is no surprise that no significant change of the optical lifetime is observed in the cavity. From the particle diameter and doping concentration, the number of ions inside a nanocrystal is estimated to be on the order of $n_{\mathrm{Ions}} \approx 1000$, which, for the calculated Purcell factor, should lead to a photon rate emitted into the cavity of 47000 photons. When accounting for the duty cycle (η_{DuC}), the collection ($\eta_{\mathrm{coll}} = 50\,\%$) and detection efficiency ($\eta_{\mathrm{det}} = 10\,\%$), as well as the outcoupling efficiency $\eta_{\mathrm{cav}} \approx 70\,\%$, we roughly expect an combined efficiency $\eta_{\mathrm{DuC}}\eta_{\mathrm{coll}}\eta_{\mathrm{det}}\eta_{\mathrm{cav}} = 1.7\,\%$, leading to an expected detected countrate of $\approx 1300\,\mathrm{cts/s}$. This is still one order of magnitude more than the experimentally observed signal, which might be explained by insufficient collection optics, decreasing η_{coll} . Overall, the observed count rate and lifetime change is reasonable within expectations, which further substantiates that the observed signal is indeed caused by fluorescence of Yb^{3+} ions.

The achievable Purcell factor in this specific configuration, which is an extreme realization of the bad emitter regime, scales very favorably with reducing the cavity length, and thereby the mode volume. This is plotted in Figure 3.12 for the cavity and emitter parameters realized in this setting. However, the double resonance technique employed here restricts the experiment to long cavity lengths, as indicated by the dashed dotted line. Some attempts were made to work at short cavity lengths, relying on resonant excitation together with time-resolved detection. However, it was not possible to sufficiently suppress the background using this technique here.

Predicted Purcell enhancement at cryogenic temperatures

The room temperature experiments here serve as a proof of feasibility for the envisioned cryogenic experiments: Nanoparticles were distributed on the sample mirror with a suitable density. A scanning fiber-cavity was setup and operated at the design finesse of $\mathcal{F} \approx 20000$ on clean mirror spots. Weak fluorescence signals were observed when nanoparticles were placed inside the cavity. I investigated the characteristics of the fluorescence and found that it shows signatures of Yb^{3+} ions.

Thinking back to the motivation of implementing an efficient node in a quantum network, it is clear that ultimately, cryogenic cavity experiments will be required. The reason is twofold: For one, the optical coherence time T_2 becomes significantly longer. This allows for much higher Purcell enhancement, which in turn will enable the detection of single ion signals via spectral multiplexing. Secondly, the spin lifetimes $T_{1,\mathrm{spin}}$ and coherence times $T_{2,\mathrm{spin}}$ significantly increase, which is of course a prerequisite to implement a spin-photon-interface. I estimate the Purcell effect of Y_2O_3 ions at cryogenic temperatures, using the room temperature cavity parameters, a finesse of $\mathcal{F} = 18\,000$ at the resonant wavelength $\lambda = 977\,\mathrm{nm}$ and the experimentally determined homogeneous linewidth of 6 MHz (see the following Section for the determination of the cryogenic homogeneous linewidth). The result is depicted in Figure 3.12 (b). Like in the case for room temperature experiments, the Purcell factor significantly increases at low cavity lengths. However, I find that even for long cavity lengths ($q = 26$) effective Purcell factors of $C_{\mathrm{eff}} = 71$ are feasible. This would enable the detection of single ions with a similar signal strength than what was achieved in the room temperature setup above for a signal stemming from 1000 ions. Indeed, for single ion coupling, the effect can be a factor of three larger, since I included a factor of 1/3 in the effective Purcell factor calculation to account for the random transition dipole orientation within the nanoparticle.
This parameter estimation, together with the successful room temperature characterization, truly motivates the investigation of the Yb^{3+}:Y_2O_3 nanoparticles inside the cavity system at low temperatures. I will return to the discussion of the feasibility of such an experiment at the end of this chapter. In this estimate, I have already used the cryogenic homogeneous linewidth. In the following section, I will present how this quantity was determined experimentally, together with a thorough investigation of the cryogenic properties.

3.3. Cryogenic spectroscopy of ytterbium doped yttria nanoparticles - Revealing the homogeneous linewidth

While the room temperature studies in the previous section are encouraging, cryogenic characterization is needed to determine the optical coherence time and ideally extract information about the spin properties. This will ultimately determine the suitability for

coherent experiments. In this section, I present the results of cryogenic spectroscopy of an ensemble of the ytterbium doped yttria nanoparticles. We study the photoluminescence spectra and photoluminescence excitation spectrum of the particles and can spectroscopically observe ytterbium ions in both crystal lattice sites. We confirm this by separately measuring the optical lifetimes of the two sites, and observe a significant difference, in accordance with the expectations. Finally, we measure the optical homogeneous linewidth of the ytterbium ions by performing transient spectral hole burning. The results presented in this section were obtained in close collaboration with Robin Wittmann, and additional information can be found in his thesis [143]. I will start by shortly describing the employed measurement setup, which will also be used in the following Chapter 4.

3.3.1. Experimental setup

Especially in the first years in the Group, we had only a limited number of cryostats, which were running complicated experiments, limiting the available space for cryogenic experiments. What we had however, was an ample supply of liquid helium due to the existing Helium infrastructure at the institute. My colleagues Evgenij Vasilenko and Kelvin Chung had already designed and tested a dipstick cryostat. This is mainly an evacuated metal tube which can be lowered into a Helium dewar [144, 145]. The liquid helium, which is direct contact with the tube outside, provides the cooling power. A small volume of gaseous helium is added to the evacuated volume inside of the tube, providing heat exchange between the sample and the tube walls. This technique is also known as exchange gas cooling. In later experiments, I used an even simpler variant of the dipstick concept, where the sample is directly immersed into liquid helium, as depicted in Figure 3.13. The dipstick cryostats relies on the very low thermal conductance of stainless steel at low temperature to thermally isolate the sample region from the outside of the dewar. One end of the tube is at room temperature, while the other end is thermalized at liquid helium temperature. It is remarkable that, nevertheless, liquid helium consumption rates were on the order of 0.1 l/h to 0.2 l/h, enabling continuous cooling of a single sample for up to three weeks.

Dipstick cryostat

The disadvantage of the dipstick approach is the limited direct optical access, possible only from the top by means of a window, which implies a reflection geometry for the measurement. Instead, we chose to forego any optical windows and couple light in using optical fibers. These are conveniently installed by drilling holes into blind flanges, feeding the fiber through the hole and then sealing the hole with epoxy glue. After the gluing process, bending protection can be added to the feed-through and the bare ends can be connectorized using standard fiber connector gear and techniques. In practice, it

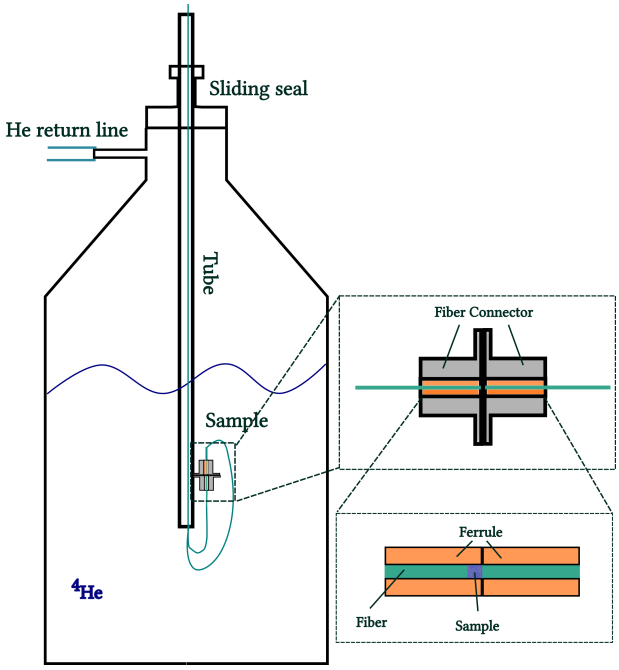

Figure 3.13.: Schematic sketch of dipstick cryostat and the fully fiber-coupled sample space used for the cryogenic measurements.

has proven helpful to add an overhead of fiber length on both sides of the feed-through, to reuse fibers for different samples without having to redo the feed-through.

Sample Geometry

The group of Philippe Goldner has pioneered an approach to measure coherent signals, such as photon echoes, from nano-crystalline or, more general, highly scattering powder, rare earth ion-based samples [146]. It is conceptually very simple: The powder is compressed between two glass slides, that are embedded in a copper sample holder for better thermalization. The thickness of the powder sample is chosen to achieve a sufficiently high optical depth, while also not being to thick in order to minimize scattering losses and achieve a measurable rest transmission. The optimal thickness depends of course on the properties of the sample, such as particle diameter and doping concentration, but is typically on the order of a few hundred microns [138].

In order to replicate this for fully fiber-based setup, we make use of standard fiber connectors and mating sleeves. Fibers are glued inside ceramic or stainless steel ferrules

with a borehole matching the fiber cladding radius. The fibers are cleaved and polished to be flush with the ferrule endfacets. Then, a mating sleeve matching the ferrule diameter aligns the two ferrule endfacets, and thereby the fiber cores, to each other. The ferrules are locked in place by a screwing mechanic. Due to precise machining, there is no discernible air-gap between the two endfacets. By purposely retracting one fiber before gluing, we can therefore create an enclosed space which we can use to immerse the sample. Light is then coupled in via one fiber and the transmission collected via the other. The transmission typically drops by several orders of magnitude once the scattering powder is introduced in the gap. To maximize the collected signal, we choose to use a multi-mode fiber with a large core diameter ($\varnothing = 200\,\mu m$) and a large numerical aperture ($NA = 0.5$) [1]. The sample space is sketched in Figure 3.13.

While this approach is conceptually simple, it took a long time to optimize all possible parameters, including ideal sample density, preparation methods, types of used fibers, thermalization, and many more. I started first tries on this approach and developed it together with the master students Xiaoyu Cheng and Christina Ioannou, whose theses I supervised. It has been continuously improved and further developed since then by other members in the group as well, spearheaded by my colleagues Evgenij Vasilenko and Vishnu Unni Chorakkunnath.

Measurement Setup

The rest of the experiment can be split in the preparation of the excitation light and the collection and analysis of the transmitted laser or the fluorescence. Sketches of the collection and detection path are depicted in Figure 3.14.
Optical excitation can be provided by two laser systems: a tunable external cavity diode laser [2], which emits in a wavelength range of $\lambda = 940\,nm$ to $985\,nm$, and a high power titanium sapphire laser [3]. Both are sent through an AOM in double-pass configuration to provide pulse shaping and frequency offsets. Depending on the requirements of the experiment, AOMs are driven by a fixed RF source or an arbitrary wave form generator (AWG)[4], in conjunction with a suitable amplifier [5]. The light is then coupled into an optical fiber and sent into the cryostat. The 1% port of a 99:1 fiber beam-splitter [6] can be used to measure the intensity in the fiber via a photodiode. This is useful to correct the transmitted signal for amplitude fluctuations, which can for example be caused by sweeping the driving frequency of the AOM.

[1] *FP200ERT*, Thorlabs
[2] *Velocity TLB-6719*, Spectra-Physics
[3] *SolsTiS*, M-Squared Lasers
[4] either *M3300A*, Keysight Technologies or *OPX*, Quantum Machines
[5] *ZHL-1-2W+*, Mini-Circuits
[6] *TW930R1F2*, Thorlabs

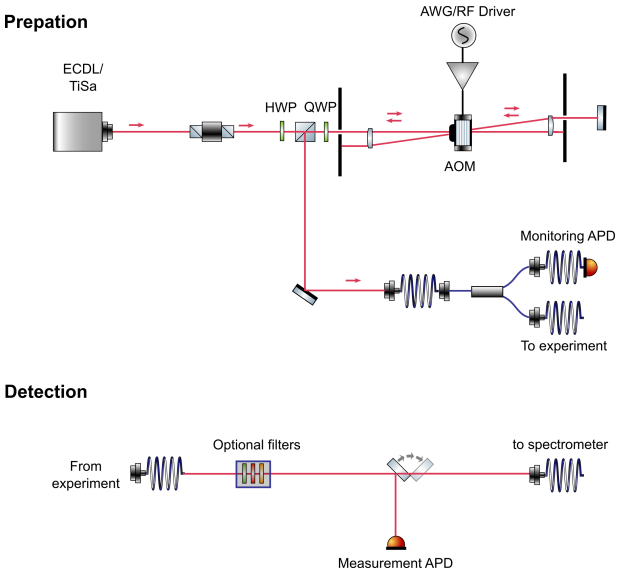

Figure 3.14.: Preparation and detection beam path for cryogenic ensemble spectroscopy

In the detection path, light is coupled out via the optical fiber coming from the sample. It is then collimated, sent through some filters which are exchanged depending on the measurement and then guided either onto a photodiode or coupled into another fiber which leads to the same spectrometer as used for the room temperature experiments. Two different photodiodes are employed depending on the sample and the experiment: A standard sensitive photodiode[1] (saturation power 1.5 µW, Bandwidth 0 MHz to 50 MHz), which enables heterodyning techniques, and a very sensitive (saturation power 15 nW) photodetector with a significantly reduced bandwidth 0 kHz to 100 kHz[2], to be able to resolve even very weak signals.

3.3.2. Spectroscopic observation of two crystal symmetry sites

The results discussed in this section were obtained in close cooperation with Robin Wittman and reported in detail in his master thesis [143]. I will shortly summarize the key findings. First, photoluminescence spectra were recorded at $T = 4.2$ K, as depicted in Figure 3.15. In contrast to room temperature experiments, the laser needs to be tuned to an exact resonance of the Yb^{3+} ions, because phonon-broadening mechanisms are heavily

[1] *APD 440A*, Thorlabs
[2] *APD 410A*, Thorlabs

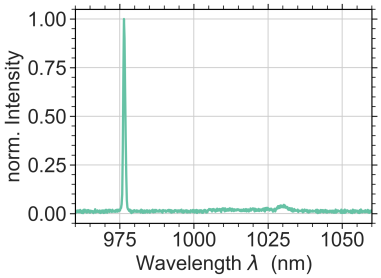

(a) Photoluminescence spectrum of a Yb^{3+}:Y_2O_3 nanocrystal ensemble at $T = 4.2\,\mathrm{K}$. Excitation laser is tuned to $\lambda = 951\,\mathrm{nm}$.

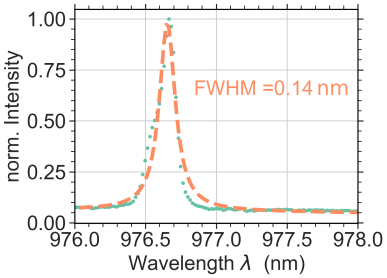

(b) Single lorentzian fit to the ${}^2F_{7/2}(0) \rightarrow {}^2F_{5/2}(0)$ transition which was recorded with a high resolution grating (grating constant $1200\,\mathrm{l/mm}$)

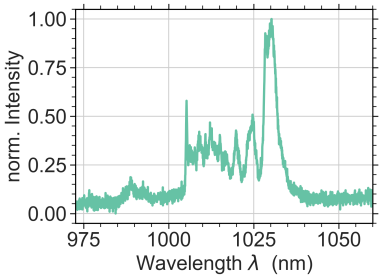

(c) High resolution spectrum above $1000\,\mathrm{nm}$, recorded when exciting the ${}^2F_{7/2}(0) \rightarrow {}^2F_{5/2}(0)$ transition. The steep edge stems from a longpass filter.

Figure 3.15.: Cryogenic photoluminescence spectra for Yb^{3+}:Y_2O_3. Data was taken by Robin Wittmann.

suppressed. The ions were first excited at $\lambda = 951\,\mathrm{nm}$ to record the fluorescence of the ${}^2F_{7/2}(0) \rightarrow {}^2F_{5/2}(0)$ transition. One can observe a significantly narrowing of the peak compared to room temperature. A Lorentzian fit to the peak yields a linewidth of $0.14\,\mathrm{nm}$, corresponding to an inhomogeneous linewidth in frequency space of $\Delta\nu = 43\,\mathrm{Ghz}$. It is evident that the Lorentzian does not perfectly match the lineshape. For a Lorentzian inhomogeneous line and a Gaussian resolution limit of the spectrometer, one would expect a convolution of the two, also called a Voigt-profile. However, these fits can also not appropriately describe the lineshape.
In addition, one observes a small bump around $\lambda = 1040\,\mathrm{nm}$, which is where one expects the ${}^2F_{7/2}(1) \rightarrow {}^2F_{5/2}(0)$ and ${}^2F_{7/2}(2) \rightarrow {}^2F_{5/2}(0)$ transitions. Note that the intensity of the peaks can not be compared directly, because the spectrometer is not intensity calibrated and the quantum efficiency of the silicon based camera drops significantly around $1000\,\mathrm{nm}$, which skews the perceived peak height. To increase the signal of the higher

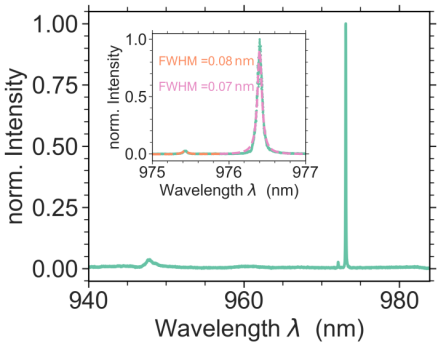

(a) Photoluminescence excitation spectrum of a Yb^{3+}:Y_2O_3 nanocrystal ensemble. The inset is a separate measurement at a slower scan speed. The excitation light is filtered out via a 1000 nm longpass filter.

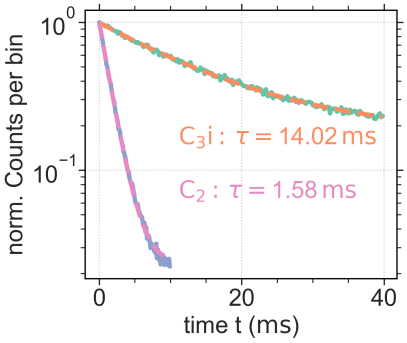

(b) Measurement of the optical lifetime for the excitation laser tuned in resonance with the resonance at $\lambda = 975.42$ nm (orange) and $\lambda = 976.40$ nm (pink). The larger difference supports the assignment to two crystal sites.

Figure 3.16.: (a) Photoluminescence excitation reveals two narrow lines around $\lambda = 976$ nm, with one being much more prominent than the other. When selectively exciting either of these resonances and measuring the optical lifetime in **(b)**, an order of magnitude longer lifetime is observed. This is consistent with the assignment of the transitions to the C_2 and C_{3i} crystallographic site, which posses significantly different transition strengths. Data was taken by Robin Wittmann [143].

wavelength multiplets, the laser is tuned on resonance with the ${}^2F_{7/2}(0) \rightarrow {}^2F_{5/2}(0)$ transition. The resulting spectrum centered around 1020 nm is depicted in Figure 3.15 (c), where the sharp increase at 1000 nm is due to the spectral edge of a long-pass filter. The peaks likely to the ${}^2F_{7/2}(1) \rightarrow {}^2F_{5/2}(0)$ and ${}^2F_{7/2}(2) \rightarrow {}^2F_{5/2}(0)$ transitions, although the noisy spectrum makes it hard to clearly separate them.

The inhomogeneous linewidths observed here are already approaching the resolution limit of the spectrometer. The optical depth of the sample was too low to observe absorption spectra, likely because the low ytterbium doping concentration of 100 ppm. Therefore, photoluminescence excitation (PLE) spectra were recorded by scanning the external cavity diode laser from 940 nm to 985 nm and detecting the fluorescence at wavelengths longer than $\lambda = 1000$ nm. The results are depicted in Figure 3.16 (a). Next to the the very prominent peak at $\lambda = 976.40$ nm, there is a much smaller, but similarly narrow peak at $\lambda = 975.42$ nm This peak is tentatively assigned to ions doped into the C_{3i} crystal site. Because the C_{3i} site possesses an inversion symmetry, the transition is purely magnetic, and therefore much more weakly allowed than the electric dipole transition of the C_2 site. Together with the lower density of sites per unit cell, this results in a significantly weaker signal [147, 148]. Lorentzian fits to both lines result in a

FWHM of $\Delta\nu_{C_{3i}} = 25.9\,\text{GHz}$ and $\Delta\nu_{C_2} = 22.3\,\text{GHz}$, which are, as expected, smaller than the values obtained for the photoluminescence spectra. The biggest uncertainty for the measurement is the calibration of the wavelength axis, which is done by recording the monitoring output of the ECDL laser. A wavemeter with sufficient measurement speed was not available for the measurement.

In order to verify the tentative assignment of the two peaks to the two in-equivalent crystal sites, the laser was tuned in resonance with one peak at a time and measurements of the fluorescent lifetimes were conducted. The resulting exponential decays are shown in Figure 3.16 (b). Indeed, an unexpectedly long lifetime of $\tau_{C_{3i}} = (14.02 \pm 0.15)\,\text{ms}$ is observed when exciting the weak resonance at $\lambda = 975.42\,\text{nm}$. In comparison, a value of $\tau_{C_2} = (1.57 \pm 0.01)\,\text{ms}$ is observed when exciting the dominant transition at $\lambda = 976.40\,\text{nm}$, which agrees well with the measurements at room temperature. This clearly implies that the less intense peak stems from a more strongly forbidden transition, consistent with the assignment to the C_{3i} crystal site.[1]

3.3.3. Determination of the optical coherence time

The property that we are most interested in is the homogeneous linewidth of the $^2F_{7/2}(0) \rightarrow {}^2F_{5/2}(0)$ transition, corresponding to the optical coherence time. This imposes an upper limit on the time the transitions can be coherently manipulated and also can limit the achievable Purcell enhancement when it is of similar magnitude as the cavity linewidth. For Europium dopants, photon echoes and spectral hole burning using the long lived hyperfine levels are routinely employed to measure these quantities using similar samples and experimental setups. For the sample employed here, both of these techniques were unsuccessful. The photon echo measurements are likely limited by the optical depth of the sample, as well as the optical coherence possibly being shorter than the possible pulse lengths, limited by the AOM rise times.
When attempting persistent spectral hole burning, we do not observe an initial drop in fluorescence when exciting ions at a fixed frequency, which would be a characteristic sign for spin pumping. Likely, this is because the hyperfine levels relax quickly, such that even a strong pump cannot polarize the spins sufficiently.
The spin lifetime in Yb^{3+}:Y_2O_3 has not been reported. However, it has been studied in Y_2SiO_5. There, it was found to scale as $T_{1,\text{spin}} \propto T^{-9}$ with temperature due to spin-lattice relaxations via a two-phonon Raman process above $T = 6\,\text{K}$ [106]. At lower temperatures, the spin lifetime is limited by resonant flip-flop processes between the Yb^{3+} ions, which depend on the doping concentration and the probed hyperfine levels [106, 149, 150]. Therefore, longer spin lifetimes are observed in crystals with low doping concentrations.

[1] The group of Philippe Goldner in Paris independently observed the existence of the second, less intense peak and initially suggested the assignment to the C_{3i} crystal site in a discussion.

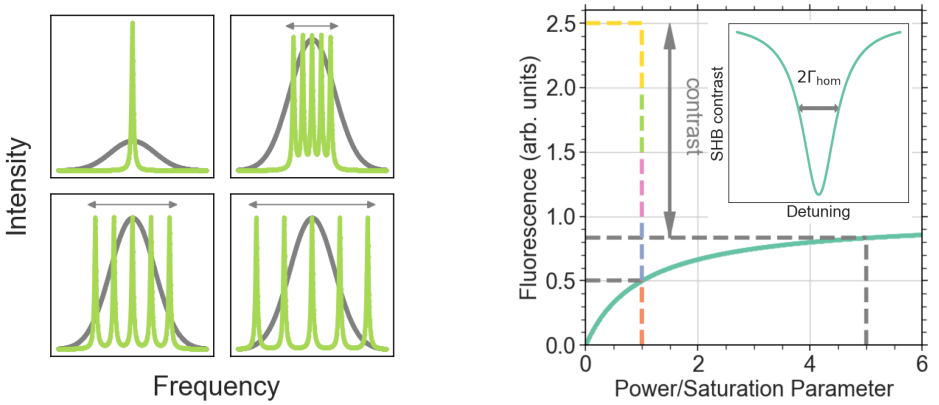

(a) When increasing the frequency spacing, the same optical intensity is distributed over multiple frequencies. The grey line represent the inhomogeneous linewidth of the emitter (not to scale).

(b) The difference in saturation at five times the saturation power versus one saturation power at five frequencies determines the contrast of a transient spectral hole measurement. Inset: Expected signal when measuring fluorescence as a function of detuning, revealing the homogeneous linewidth.

Figure 3.17.: An illustration of the measurement principle behind the transient spectral hole burning technique. The nonlinear fluorescence response of a saturated emitter is used to create a contrast when distributing the optical power over several frequencies. A detuning dependent measurement reveals an upper bound for the homogeneous linewidth

A spin lifetime on the order of ≈ 100 ms was observed in a 5 ppm doped Y_2SiO_5 sample at 3 K. Due to the comparatively high doping concentration of 100 ppm of our nanocrystal sample, we expect a significantly shorter spin lifetime.

Instead, we make use of transient spectral holeburning, which relies on transferring a significant population of the ground state to to the optically excited state. This limits the timescale of the experiment to significantly shorter than the optical lifetime of ≈ 1 ms. Therefore, the pump and the probe happen simultaneously. The mechanism is the same as for the well known optical saturation, and consequentially this technique can also be termed saturation spectroscopy. In the context of rare earth ions, this is also called transient spectral hole burning to differentiate it from the spin-pumping technique.
The principle is demonstrated in Figure 3.17. A frequency comb with n teeth, equal spacing in frequency and equal teeth intensity is created by modulation techniques. When the frequency spacing is much less than a homogeneous linewidth, this corresponds to exciting a single emitter with n times the power. However, when the spacing is much larger than the homogeneous linewidth, n emitters are excited by a single tooth intensity. When the optical power per tooth is comparable to the saturation power of a single homogeneous line, these two conditions lead to very different fluorescence strengths.

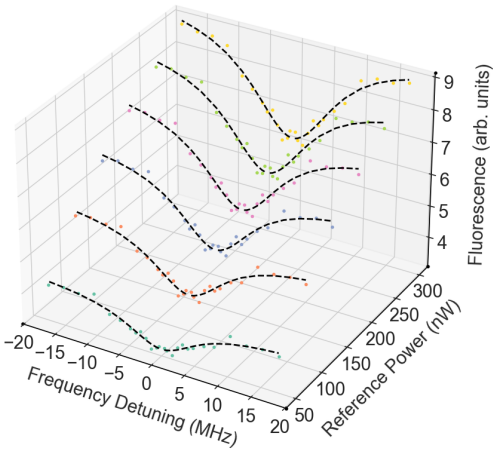

(a) Power dependent transient spectral hole measurements. The data is mirrored at zero detuning to emphasize the Lorentzian lineshape. In the experiment, the detuning of the two frequencies is absolute.

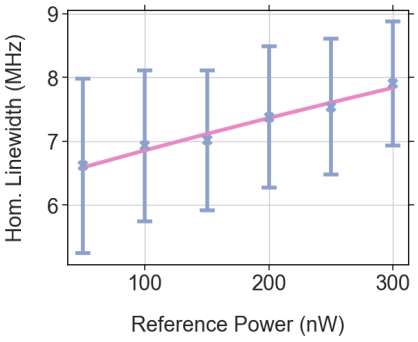

(b) Homogeneous linewidth obtained from the fits displayed in **(a)** as a function of optical power. Pink line indicates a fit to a square root power broadening law.

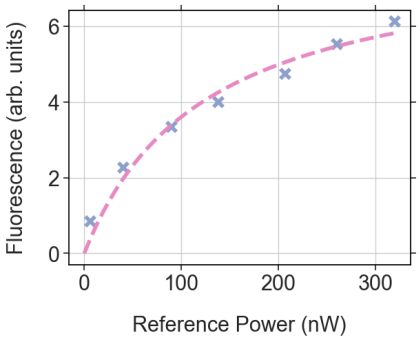

(c) Saturation behavior for a single excitation frequency, Fit by a saturation curve with a constant offset to account for the detector background.

Figure 3.18.: Power dependent measurements of the homogeneous linewidth of the ${}^2\mathrm{F}_{7/2}(0) \rightarrow {}^2\mathrm{F}_{5/2}(0)$ transition at the C_2 crystal site in Yb^{3+}:$\mathrm{Y}_2\mathrm{O}_3$ at $\lambda = 976.40\,\mathrm{nm}$. Extrapolating the power dependent linewidth measurement to zero excitation power yields a linewidth of $\Gamma_{\mathrm{hom}}^{\mathrm{C}_2} = (6.31 \pm 0.09)\,\mathrm{MHz}$. Data was acquired by Robin Wittmann.

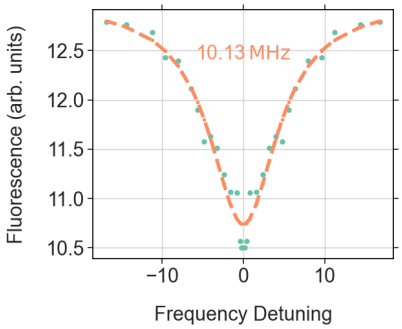

(a) Transient spectral hole burning measurement and lorentzian fit for the C_{3i} crystal site. The data is mirrored at zero detuning to emphasize the Lorentzian lineshape. In the experiment, the detuning of the two frequencies is absolute.

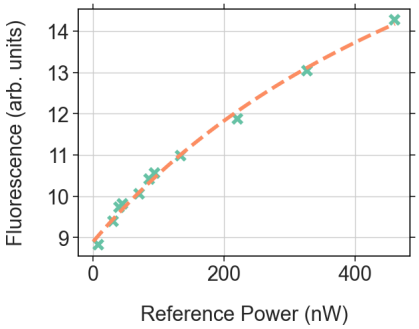

(b) Saturation behavior for the C_{3i} crystal site at a single excitation frequency. Fit by a saturation curve with a constant offset to account for the detector background.

Figure 3.19.: Measurements of the homogeneous linewidth of the ${}^2F_{7/2}(0) \rightarrow {}^2F_{5/2}(0)$ transition at the C_{3i} crystal site in Yb^{3+}:Y_2O_3 at $\lambda = 975.42\,\text{nm}$. Power dependent measurements were not possible due to the much weaker signal strength. The reference power used for the transient spectral hole measurement is 150 nW. The fit yields a homogeneous linewidth of $\Gamma_{\text{hom}}^{C_{3i}} = (5.06 \pm 0.56)\,\text{MHz}$, slightly smaller than observed for the C_2 site. Data was acquired by Robin Wittmann.

Recording the fluorescence[1] as a function of the teeth detuning reveals a lorentzian dip, whose width corresponds to twice the homogeneous linewidth. This is illustrated in Figure 3.17 (b). In our case, an AOM was used to create two teeth by suitable amplitude modulation. The detuning was monitored by recording the beat signal and the optical power was measured behind the sample. This reference power is roughly five to six orders of magnitude smaller than the power in front of the sample, due to the highly scattering sample. It is important to keep the power constant by compensating the AOM diffraction efficiency curve, since the expected contrast depends strongly on the used optical power. This measurement was done for both the C_2 and C_{3i} crystal sites. The results for the C_2 site are displayed in Figure 3.18. Here, the measurement was repeated for different excitation powers and the resulting linewidths were fit by square root power broadening law $\Gamma = \sqrt{1+S}\,\Gamma_0$. Extrapolation to zero power yields a homogeneous linewidth of $\Gamma_{\text{hom}}^{C_2} = (6.31 \pm 0.09)\,\text{MHz}$.
The measurement for the C_{3i} crystal site are displayed in Figure 3.19. Because the transition is much harder to saturate and the overall signals obtained are much weaker, a power dependent measurement was not possible. The homogeneous linewidth extracted from the spectral hole burning measurement at a reference power of 150 nW is $\Gamma_{\text{hom}}^{C_{3i}} = (5.06 \pm 0.56)\,\text{MHz}$.

[1]For a sufficient optical depth, this measurement can also be done in transmission

For both measurements, one observes a deviation in the center of the lorentzian: For the C_2 site, there appears to be a small peak, while for the C_{3i} site there is an additional, small dip. The cause of this is unknown, and could be caused by some flaw in the experimental setup. An additional, smaller dip could arise from an isotope possessing a significantly smaller linewidth, as has been observed in Yb^{3+}:$LiNbO_3$ [151, 152]. However, there is no such straightforward explanation for an additional peak as observed for the C_2 site.
It is worth noting that the homogeneous linewidth obtained by this measurement should be understood as an upper limit. While the results are unlikely to be limited by laser stability or power broadening, the high optical powers used here could potentially cause local heating of the sample. Additionally, photon echo measurements often yield longer coherence times due to many reasons: they can be detected with heterodyning techniques, making them quasi-background free, they rephase the coherence, compensating for some decoherence, and they probe the sample directly on the time scale of the coherence time, eliminating effects from spectral diffusion on longer timescales. Therefore, photon echo measurements might result in longer coherence times T_2, possibly making them comparable to the values obtained for other rare earth ions in Y_2O_3 nanocrystals (as summarized in Table 3.1).

In summary, the Yb^{3+}:Y_2O_3 nanoparticles were thoroughly characterized: At room temperature, small ensembles of a few nanocrystals were probed and the optical lifetime and photoluminescence spectra were measured. Then, a larger ensemble of nanocrystals was cooled down to $T = 4.2\,\mathrm{K}$ in home-built dipstick cryostat. Photoluminescence excitation spectroscopy revealed two distinct peaks that were assigned to the C_2 and C_{3i} crystal symmetry sites. Narrow inhomogeneous linewidths of $\Delta\nu_{C_2} = 22.3\,\mathrm{GHz}$ and $\Delta\nu_{C_{3i}} = 25.9\,\mathrm{GHz}$ were observed. The corresponding optical lifetimes were found to differ by a factor of 10, which supports the assignment to the two crystal sites. Finally, the homogeneous linewidth could be determined via transient spectral hole-burning to be as low as $\Gamma_{\mathrm{hom}}^{C_{3i}} = (5.06 \pm 0.56)\,\mathrm{MHz}$. This constitutes the first characterization of this material system. The coherence properties could potentially be improved by annealing at a higher temperature and an additional oxygen plasma treatment step, which for other rare earth ion species in the same nanocrystals have been shown to significantly improve the coherence properties. The coherence is also expected to improve for a lower Ytterbium doping concentration. although this would further reduce the signal strength. In addition, studies at temperatures lower than $T = 4.2\,\mathrm{K}$ would be of interest: both the optical coherence time and the spin lifetime are expected to improve. Increasing the coherence time by the aforementioned improvements would enable photon echo experiments, which have so far remained elusive for this material. Thereby, the coherence could be probed in a more elegant manner, which is less prone to systematic errors.
Nevertheless, the results presented here are already encouraging and compatible with the use for quantum information processing. However, the initially presented problem of the very low photon emission rate still stands, motivating the integration into a cavity platform. I have already discussed what photon rates might be attainable in a cryogenic

cavity experiment in Section 3.2.2. In the following, I want to discuss how attainable such an experiment is with the current status of the cryogenic cavity experiment.

3.4. Outlook

As discussed in Section 3.2.2, a cryogenic cavity experiment conducted on ytterbium doped nanocrystals should result in single ion count rates sufficient to spectrally resolve individual ytterbium ions. This would be a first important step towards the realization of a ytterbium-based quantum network node. However, one challenge arises: the narrow optical linewidth of 5 MHz was measured with a sample fully submerged in liquid Helium at ambient pressure, determining the temperature to be $T = 4.2\,\mathrm{K}$. However, cryostats that were available for the cavity experiment rely on cold fingers and plates, with which the cavity stage, the cavity mirror and finally the sample needs to be thermalized [1]. In the available cryogenic cavity setup, the lowest achievable temperature measured at the copper mirror holder, which contacts the sample mirror at the back, was $T = 18\,\mathrm{K}$. The temperature dependence of the optical coherence properties of Yb^{3+} ions in yttria is not reported in the literature. In this work, we could also not investigate this easily due to the simple nature of the used cryostat. However, the temperature dependence has been studied in great detail in other host materials, such as Y_2SiO_5 [106]. There, the homogeneous linewidth is found to scale with $\Gamma_{\mathrm{hom}} \propto T^9$, leading to an increase of the homogeneous linewidth of almost four orders of magnitude between $T = 4\,\mathrm{K}$ and $T = 20\,\mathrm{K}$. These values are of course hard to compare, since in the referred study the optical linewidths are also extremely narrow below 6 K ($\Gamma_{\mathrm{hom}} < 1\,\mathrm{kHz}$). Still, it is reasonable to expect a significant broadening of the homogeneous linewidth of the Yb^{3+}:Y_2O_3 nanoparticles at the elevated temperatures imposed by the current cryogenic cavity design. This might reduce the attainable Purcell factors and importantly makes the spectral resolution of individual rare earth ions extremely challenging, as they will start to spectrally overlap. Furthermore, the spin lifetime and coherence has been found to decrease drastically above temperatures of $T \approx 6\,\mathrm{K}$ [153]. For these reasons, I did not pursue cryogenic cavity experiments on ytterbium doped yttria nanoparticles.
Instead, cryogenic cavity experiments were conducted on color centers in silicon carbide, another promising candidate for quantum network node possessing optical transitions at wavelengths similar to ytterbium ions. Crucially, the homogeneous linewidths of these centers do not experience additional broadening at temperatures below 20 K, which makes them ideally suited for the current experimental realization of the cryogenic cavity setup. The results obtained in this material platform is detailed in Chapter 5. However, before further delving into this new material platform, I will discuss an interesting

[1] Accurately measuring the sample temperature is not straightforward and is best done by measuring some physical property of the sample with a known temperature behavior, such as the Boltzmann distributed occupation of ground states.

variant of ytterbium based quantum emitters, which I investigated using the methods introduced in Section 3.3: ytterbium ions in organic, molecular crystals.

4. Ytterbium ions in molecular systems for quantum information processing

In the previous chapter, I discussed and analyzed the optical and spin properties of Ytterbium ions that are doped with low concentration into a dielectric, transparent host crystal, in this case Y_2O_3 nanocrystals. While much of the research on rare earth ions has been conducted in such host materials, rare earth ions have also shown good optical coherence in more unusual hosts, such as amorphous glasses [154, 155, 156, 157, 158], and recently also molecular crystals [159, 160, 161]. Integrating REIs into organic molecules is of great interest, because it offers a way to deterministically and reproducibly engineer the ions environment, that is each molecule is identical and possesses the same symmetry, distance to neighboring ions and ancillaries.

The optical spectroscopy of rare earth ions in molecular complexes is inspired by their use as molecular magnets, which has been a very active and successful, albeit small field of research [162, 163, 164]. As an example, the nuclear spin degrees of freedom of a single Terbium ion in a single molecule can be driven by applying a radio-frequency tone. The spin state can be read out with a combination of magnetic fields sweeps and electronic measurements. These experiments are challenging because they require electronic contacting of a single molecule and low operation temperatures $T < 50\,\mathrm{mK}$. An implementation of the Grover algorithm has recently been demonstrated in such a system [164]. Adding the toolbox of optical spectroscopy to these systems opens up a plethora of improvements and new applications: By addressing the optical transitions of the REIs, once can significantly increase the speed with which the spin state is read out and initialized. Furthermore, if the optical transitions are coherent, the quantum information can be mapped onto photons, which can then be used as a resource for quantum communication, similar to the ideas presented in the previous chapter 3.

Our group has been involved in the work on spectroscopy of rare earth ion molecular systems from an early stage and I have contributed in various ways to these efforts. In the following, I will summarize what special considerations apply to molecular rare earth-ions compared to solid state hosts as discussed in Section 3.1.1. I will then present optical measurements on Yb-Trensal, a molecule for which coherent control of the electron spin has already been demonstrated successfully by other groups [165]. We find narrow inhomogeneous linewidths and a high optical depth, demonstrating the possibility for optical readout. At the same time, we find that optical spectroscopy is highly sensitive to variations in the environment of the molecules, and can serve as a probe for the homogeneity. In order to further study how the chemical structure

influences the optical properties, four additional molecular complexes were investigated. I will systematically compare their fluorescent properties and try to correlate them with their chemical structure. The systematic analysis corroborates the design principles employed in the synthesis and serve as a starting point for further studies.

4.1. Rare earth ions in molecular crystals

The molecules studied in this work belong to the field of metallo-organic chemistry and contain at least one rare earth ion. The ion(s) are surrounded (or, in chemistry terms *coordinated*) by organic ligands, which are mostly composed of carbon, hydrogen, oxygen and nitrogen. The large field of chemistry dealing with these types of molecules is therefore called coordination chemistry. The central ion also referred to as the *lanthanide center*. These molecules can crystallize in various crystal structures to form molecular crystals. Typically, crystallization is achieved from dissolved molecules. Therefore, the utilized solvent can co-crystallize and be a part of the crystal structure. In this chapter, I investigate the spectroscopic properties of Yb^{3+} ions in such molecules and how they are affected by their molecular and crystalline environment.
In order to understand why these molecular materials are of high interest for quantum information processing, one needs to compare them to REIs in conventional, solid state hosts. These usually Yttrium-based materials can be grown with extremely high quality, are commercially available and rare earth ions in these materials have already demonstrated outstanding optical and spin properties. However, it is not clear how much room for optimization is still left in these "conventional" hosts, as some fundamental limitations remain. The spatial distribution of ions in the host remain random. Therefore, if one chooses a low doping concentration, as is desirable for single ion experiments, the ions are sparse and ion-ion interactions are weak or close to nonexistent. While this can help to improve the coherence properties, such an interaction can be very beneficial. It can be used to realize two qubit gates, which are a necessary ingredient for quantum computing and can turn an ion coupled to a few surrounding ions into a small quantum processing node [29, 166, 167]. Also, coupled nearby spins can be used as an ancillary qubits where quantum information is stored, as was demonstrated for example for defect centers in diamond [168], and recently also a single Erbium ion [123].

Deterministic and reproduceable

For all of these applications, where one couples to a close-by quantum system one would like for this interaction strength to be known and always the same for each ion. This is especially important when one aims to scale up the number of quantum nodes in a network. This requires fixed and known ion-ancillary distances and dipole orientations, which is not the case for random dopants. In stark contrast, molecules are identical. One

can therefore synthesize molecules containing multiple rare earth ion centers, with well known interaction strength, which are the same for every molecule. This offers unique benefits for scaling up such systems. For example, one could design molecules that contain both ions that strongly interact with each other and can be used for computing, and weaker coupled spins that act as memory qubits. Following this approach, one could even use different rare earth ion species to combine the distinct advantages of the different species. Ideas like this have already been discussed for dopants in dielectric crystals [169, 109], but can easily be extended in a more controlled fashion to these molecular systems.

Engineering coherent properties

Similarly, the strength of this bottom-up approach also gives a lot of freedom to tune the desired optical properties. Following well known design principles, one can try to more strongly induce certain transitions by choosing suitably low symmetry sites for the rare earth ion to increase the branching ratio and reduce the radiative lifetime. In a similar fashion coherence properties can be improved by attaching suitable ligands to the molecule, for example separating all species with a high magnetic moment from the lanthanide center. Thereby, one decouples the REI from the spin bath, which is often the main source of dephasing. Another well known strategy is *deuteration*, where hydrogen atoms in the molecule are replaced by deuterium atoms. Due to the higher mass, they have a weaker magnetic moment. As we will see later on, this also reduces phonon eigenfrequencies and thereby suppresses non-radiative decay channels. Furthermore, the crystal can be diluted by an iso-structural molecule, where the lanthanide center is replaced with an optically inert center such as yttrium. When co-crystallizing both molecules, a lower concentration of optically active centers in the molecular crystal is achieved.

Efficient ion excitation - The antenna effect

Another effect that has been studied in the context of luminescent lanthanide centers as light sources is the so called antenna effect, or sensitized luminescence. Instead of resonantly exciting the weak optical transition of the lanthanide, one instead excites the organic ligand, which typically show strong absorption in the ultraviolet part of the electromagnetic spectrum. The ligand can then non-radiatively transfer the excitation on to the rare earth ion via an electron-exchange mechanism [170]. In this work, we usually chose to resonantly excite the REI center. However, the ligands are usually designed with the antenna effect in mind, which necessitates a somewhat close proximity of the ligand to the lanthanide center. This at times can be at odds with other design principles.

Challenges

While the discussion above paints a bright picture for the future of molecular crystals as host for rare earth ions, as always in science there are also drawbacks and challenges to overcome. First of all, the coherence properties that were observed so far are not yet comparable to the best results in dielectric crystals. The record optical coherence time for a molecular material containing Eu^{3+} ions are 10 µs for a stoichiometric molecular crystal, which improved in a diluted crystal up to 40 µs [159]. This material also showed long spin lifetimes, as indicated by long-lived spectral holes. Just recently, my colleagues Evgenij Vasilenko and Vishnu Unni Chorakkunnath were able to demonstrate coherent manipulation of the nuclear spin of the same molecular complex, with coherence times of up to 2 ms[1]. These results are very promising, and among the best reported for molecular complexes. Nevertheless, there is still a way to go to achieve the record values of coherence achieved by REIs in solid state hosts. It remains an exciting question how fast and how far this gap will be closed in the coming years.
Another well known issue for molecular materials are non-radiative decay channels, limiting the quantum efficiency and leading to a lower amount of extracted photons. The predominant limiting mechanism are multi-phonon relaxations due to the high oscillator frequency of the C-H bonds that are abundant in organic molecules. We will observe this effect in this chapter when studying different molecular Yb complexes. Therefore, I will quickly sketch the underlying mechanisms, following reference [171].

4.1.1. Quenching mechanism in organic molecules

The dominating non-radiative decay channel in REI-containing organic molecules is mediated by multi-phonon relaxation, where the REI relaxes by transferring its energy to overtones of molecular vibrations in its vicinity [171]. Because the optical transitions are within the 4f-shell, the electron density changes only slightly, and the distance between the ligand and the REI remains the same. Therefore, a large energy gap ΔE, corresponding to the the frequency of the optical transition, has to be bridged. In the most simple picture, the quenching rate Γ_{nr} due to the coupling to an harmonic oscillator with frequency ω_M are described by an energy-gap law:

$$\Gamma_{\mathrm{nr}} = A \exp(-B\frac{\Delta E}{\hbar\omega_M}), \tag{4.1}$$

where A, B are material dependent constants that are determined experimentally. Clearly, the rates become higher the lower the energy gap is. It is for this reason that infrared and near infrared emitting REI species suffer from strong non-radiative decays, while species emitting in the visible part of the electromagnetic spectrum such as Europium show quantum efficiencies close to unity.

[1]Not yet published, Details can be found in Evgenij Vasilenko's PhD thesis.

However, this model does not account for oscillator anharmonicity, how well the oscillator overtone matches the transition frequency, and is only valid for high overtones. Especially the anharmonicity of the oscillator can drastically increase the non-radiative transition rate. An intuitive explanation is that for a harmonic oscillator, dipole mediated transitions involving more than one phonon are forbidden by selection rules[1], and become more allowed as the oscillator becomes more anharmonic. With regards to organic molecules, stretching vibrations of O-H, C-H, and C=O bonds in descending order posses high frequencies and high anharmonicities, and should therefore be avoided or decoupled from the REI.
Multiple strategies exist to minimize the quenching due to multi-phonon relaxations. One approach is to replace hydrogen atoms by deuterium during the synthesis. This reduces the oscillator frequency due to the increase in the reduced mass, and simultaneously reduces the anharmonicity. This can demonstrably increase the quantum efficiency by more than a factor of six [172]. Another approach is to increase the distance between the emitter and the oscillator. The non-radiative decay rate due to a nearby oscillator drops of with $\frac{1}{r^6}$, as it can be described as a dipole-dipole type interaction. Other works suggest that careful removal of any remaining solvent from the molecular crystal can drastically improve the quantum efficiency [173]. Finally, the quantum efficiency can also be increased by increasing the radiative decay rate, e.g. inducing the optical transition more strongly. This has for example been achieved in Yb-cryptates [172]. Generally, the cross-section for vibrational relaxation does not depend on temperature, since phonons are created during the process, which therefore does not depend on the occupation number of the available phonon modes. However, in some cases, phonon-stimulated emission can occur, increasing the decay rate at high temperatures. In addition, molecules might undergo small geometric changes upon cooldown, slightly influencing the relevant distances and therefore modifying the non-radiative rates. This effect is expected to be small.

4.1.2. Purcell enhancement of a quenched transition

The quantum efficiency of an emitter is defined as the fraction of transitions that occur radiatively:

$$QE = \frac{\Gamma_{\mathrm{rad}}}{\Gamma_{\mathrm{rad}} + \Gamma_{\mathrm{non-rad}}}, \tag{4.2}$$

where $\Gamma_{\mathrm{rad}}, \Gamma_{\mathrm{non-rad}}$ are the radiative and non-radiative rates. Time-correlated photon excitation experiments used to determine the excited state lifetime are sensitive to all decay channels of the probed excited state. For a system with a low quantum efficiency, the excited state lifetime is dominated by the non-radiative decay.
The maximum countrate one can observe from such a measurement is given by Γ_{rad}.

[1] $\langle n| - ex|m\rangle \propto \langle n|(a + a^\dagger)|m\rangle = \delta_{nm+1} + \delta_{nm-1}$

However, this limit requires saturation of the emitter. The saturation power is however increased by a factor of $1/QE$ compared to the system with the same transition strength, if the non-radiative pathway did not exist. In the same fashion as for branching transitions as discussed in section 2.3.1, the effective Purcell effect is reduced compared to the ideal Purcell factor by a factor of the quantum efficiency:

$$C_{\text{eff}} = QE \cdot C_0. \tag{4.3}$$

Nevertheless, the detected photon rate scales with C_0. Consequentially, the rate of coherent photons can be drastically increased by Purcell enhancing the transition, even though the observed lifetime change may be small due to the low quantum efficiency. The molecular crystals may be integrated into the cavity in the form of thin crystals, similar to the dielectric membrane approach which I will discuss later in chapter 5. However, this requires careful optimization of the crystallization process. Alternatively, the molecules can be dissolved in an optical inert polymer, which can then form a flat, thin layer of the mirror, using techniques such as spin-coating. This requires further spectroscopic studies to investigate how such a polymeric matrix changes the molecular properties. First steps in this direction have been investigated in our group. In the remainder of this chapter, I will focus on the spectroscopic investigation of ensembles of molecular crystals, utilizing the techniques developed for nanocrystals described in 3.3.

4.2. Yb-Trensal - An exemplary molecular quantum system

Trensal is a trivial name for the ligand 2,2′,2′′-tris(salicylideneimino)triethylamine (H3trensal)[174, 175]. Its chemical structure is depicted in Figure 4.1 (a). Yb-Trensal is part of a iso-structural series of Lanthanide complexes, meaning that the Yb can be replaced by other Lanthanide ions, while retaining their shape and symmetry, with only slight changes to the bond lengths. Yb-Trensal crystallizes in a $P\bar{3}c1$ space group which posses a trigonal symmetry [174]. It has been studied in detail as a single molecular magnet. Achieved results so far include coherent control of all hyperfine levels with coherence times up to 24 µs, which could be further extended using dynamical decoupling [165], Rabi oscillations up to 40 MHz and magnetic coupling signatures to nearby hydrogen atoms [176]. Recently, high cooperativity coupling of the electronic and nuclear spin transitions to superconducting resonators at low temperatures $T < 600$ mK has been demonstrated [177]. This makes them a well studied system, with the spin degree of freedom carefully characterized already. While there has been some investigations on the transition wavelengths of the optical transition, no detailed studies have been done so far. Adding the toolkit of optics would allow for coherent manipulation using lasers, fast and efficient readout and potentially relax the requirements on the experimental setups in order to probe the spin degrees of freedom.

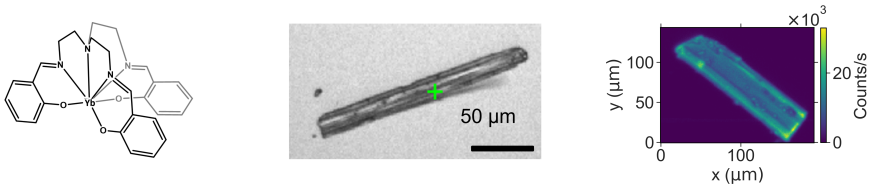

(a) Chemical structure formula of Yb-Trensal [179].

(b) Microscope image of a typical Yb-Trensal crystal.

(c) Confocal microscope image of a Yb-Trensal crystal.

Figure 4.1.: Chemical structure, optical and confocal images of a Yb-Trensal crystal.

In a related project lead by my coworker Evgenij Vasilenko, to which I also contributed, we investigated the optical properties of Eu-Trensal, the isostructual equivalent using Europium. The results are published in [178] and more details can be found in his PhD thesis. In summary, we found an optical lifetime of $T_{1,\mathrm{opt}} \approx 350\,\mu\mathrm{s}$, an inhomogeneous linewidth of 90 GHz, a homogeneous linewidth determined by spectral hole burning of $\Gamma_{\mathrm{hom}} = 2.8\,\mathrm{MHz}$ and a very long spin lifetime with two time constant, where the slower one is up to $T_{1,\mathrm{spin}} = 460\,\mathrm{s}$ [178]. These encouraging results on the optical properties of the Eu-equivalent, together with the well known coherent spin properties, motivate our investigation of the optical properties of Yb-Trensal, which I will discuss in the following.
This work was done in close collaboration with the Group of Mario Ruben at the IQMT of KIT. A team from his group, led by Senthil Kumar Kuppusamy, suggested and synthesized the molecules and regularly provided feedback.

4.2.1. Optical spectroscopy of Yb-Trensal

Yb-Trensal crystallizes in a long needle shape. The crystals are of various sizes and up to several millimeters in length. This shape is also visible in confocal microscopy. Exemplary crystals are depicted in Figure 4.1. Using a room temperature confocal microscope as described in 3.2, I investigate the photoluminescence and optical lifetime of the molecular crystals. In subsequent measurements, an ensemble of crystallites was investigated at low temperatures, using the same setup as described in chapter 3.3. Here, I conducted measurements on the photoluminescence spectra and absorption measurements of the inhomogeneous line.

Optical lifetime

The optical lifetime was measured both at room temperature and when immersed in liquid helium. A mono-exponential fit yields a lifetime of $\tau = 3.4\,\mu\mathrm{s}$ at room temperature

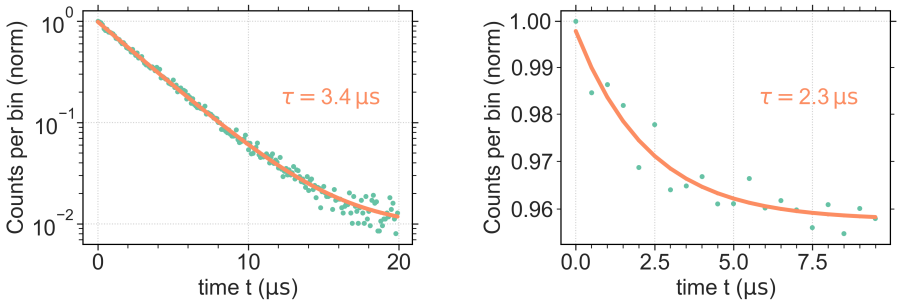

(a) Room temperature **(b)** 4.2 Kelvin

Figure 4.2.: Optical lifetime measurements of Yb-Trensal at room temperature and at cryogenic temperatures.

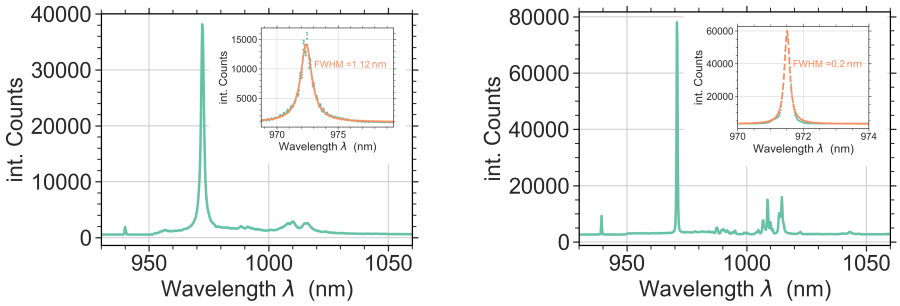

(a) Room temperature **(b)** 4.2 Kelvin

Figure 4.3.: Photoluminescence spectrum of Yb-Trensal at room temperature and cryogenic temperature. The $^2F_{7/2}(0) \rightarrow {}^2F_{5/2}(0)$ transition around 972 nm is fit by a single Lorentzian.

and $\tau = 2.3\,\mu s$ at cryogenic temperatures (see Figure 4.2). This is almost three orders of magnitude smaller than the $\approx 1\,ms$ typically observed for Ytterbium ions in solid state hosts, as the previous measurements show. As discussed previously, this is likely due to non-radiative relaxations promoted by the anharmonic vibrational modes of the ligands [172]. For a rough estimate of the quantum efficiency, I assume a radiative lifetime of $\tau_{rad} = 1\,ms$ and all other pathways to be non-radiative. This yields a quantum efficiency of $QE \approx \frac{\tau_{obs}}{\tau_{rad}} = 0.34\,\%$, indicating that the decay is dominated by the non-radiative relaxation pathways.

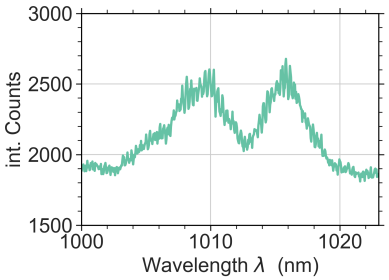

(a) Room temperature

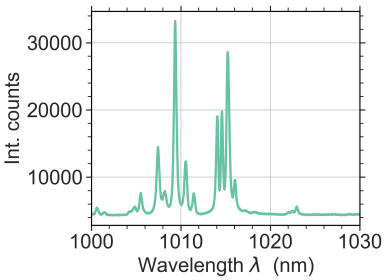

(b) 4.2 Kelvin

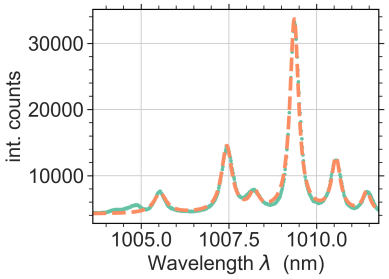

(c) Peaks around 1010 nm fit by six Lorentzians. Data taken at $T = 4.2\,\mathrm{K}$

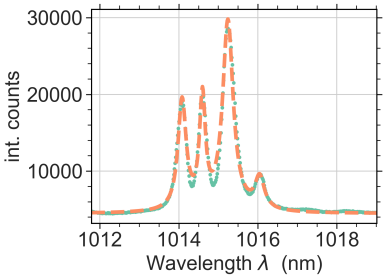

(d) Peaks around 1016 nm fit by four Lorentzians. Data taken at $T = 4.2\,\mathrm{K}$

Figure 4.4.: Photoluminescence spectrum of the higher wavelength transitions of Yb-Trensal. Two clusters of peaks can be identified.

Photoluminescence studies

Photoluminescence spectra of Yb-Trensal at room temperature and at $T = 4.2\,\mathrm{K}$ are depicted in Figure 4.3. One clearly observes the strong and narrow $^2F_{7/2}(0) \rightarrow {}^2F_{5/2}(0)$ transition around 972 nm. The observed inhomogeneous linewidth is $\Delta\nu = (355 \pm 5)$ GHz at room temperature and $\Delta\nu = (62.5 \pm 0.5)$ GHz at low temperatures. The linewidth of the $^2F_{7/2}(0) \rightarrow {}^2F_{5/2}(0)$ transition at room temperature is narrower than for the Yb^{3+}:Y_2O_3 nanocrystal sample (900 GHz, see section 3.2), and only slightly broader at low temperatures (43 GHz). This indicates a comparable high degree of homogeneity.
Additionally, two distinct peaks centered around 1010 nm and 1016 nm are visible. At cryogenic temperatures, six (four) individual lines can be resolved for the 1010 nm (1016 nm) transition. They are hypothesized to belong to the $^2F_{7/2}(1) \rightarrow {}^2F_{5/2}(0)$ and $^2F_{7/2}(2) \rightarrow {}^2F_{5/2}(0)$ transition. A zoom on theses transitions is depicted in Figure 4.4. The inhomogeneous linewidth extracted from lorentzian fits of these transitions are all of similar magnitude, the average is (98 ± 16) GHz for the transition around 1010 nm and (75 ± 15) GHz for the transition around 1016 nm. Notably, the inhomogeneous

linewidths are only slightly larger than for the coherent $^2F_{7/2}(0) \rightarrow {}^2F_{5/2}(0)$ transition.

Observation of different ion classes

The observation of multiple lines is somewhat unexpected. Due to the simple level structure of Yb^{3+}, one expects a singular peak for each transition, that can be split further by hyperfine interactions and a Zeeman shift when applying an external magnetic field. Both effects are too small to resolve them in the photoluminescence spectrum. Therefore, the likely explanations are either the existence of multiple distinct molecular structures, so called polymorphs, different crystal symmetry sites similar to the observation of the two sites in Y_2O_3 in Section 3.3, or multiple crystal structures when an ensemble of molecular crystals is probed. Due to the unknown exact mechanism, I refer to these distinct features as ion *classes*. We will observe similar effects for all molecules investigated in this work. Formation of multiple molecular classes or crystal sites should be visible in the X-ray-diffraction spectra used to determine the molecular and crystalline structure. There are however two caveats: For one, X-ray diffraction is usually carried out on a single crystal, which are grown in solution. In powder X-ray diffraction, when looking at a randomly oriented ensemble of small crystals, which is closer to the setting used in our experiment, one often observes additional peaks that are not predicted by the single crystal structure [180]. This could be an indication for different crystal structures or molecular conformations in a multi-crystal powder sample. Secondly, the molecular crystals studied in this work are grown from solution, and in some cases the solvent is known to co-crystallize. When performing X-ray diffraction, a crystal is taken out from the solution and analyzed. However, we obtain the samples as dried crystals and crystal powders, giving the volatile solvent enough time to partly vaporize. This can lead to changes and damage in the crystal structure.

Absorption spectroscopy

To finely resolve the inhomogeneous lines, I record the transmission through the sample as the laser frequency is swept. Only the $^2F_{7/2}(0) \rightarrow {}^2F_{5/2}(0)$ transition around 971 nm is visible in the absorption spectrum, although the $^2F_{7/2}(0) \rightarrow {}^2F_{5/2}(1)$ transition is expected around 950 nm. This transition is weaker and harder to resolve, which can explain its absence in the absorption scan. The peak in the optical density around 971 nm is fit by a lorentzian, yielding a linewidth of $\Delta\lambda = 0.18\,\text{nm}$ or $\Delta\nu = 57.3\,\text{GHz}$. This is slightly narrower than the inhomogeneous linewidth extracted from the PL measurements, indicating that for the PL measurement, there is small broadening from the instrument response function of the spectrometer.

Overall, the strong singular transition and reasonably narrow inhomogeneous linewidth, together with the well-known good spin properties, are encouraging. Highly of interest

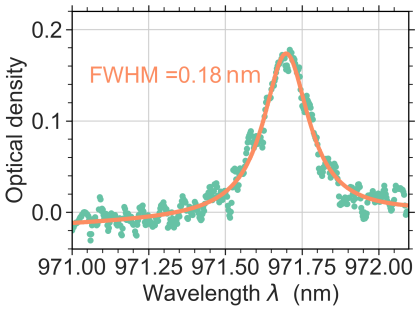

Figure 4.5.: Absorption scan of the ${}^2F_{7/2}(0) \rightarrow {}^2F_{5/2}(0)$ transition in Yb-Trensal. Fit by a single Lorentzian.

would be a measurement of the optical homogeneous linewidth. However, even after repeated attempts, neither spectral hole burning due to spin pumping, nor photon echoes could be observed. Using a transient spectral hole burning technique as discussed in section 3.3 was not possible, since we were unable to observe fluorescence saturation of the sample. As discussed in 4.1.1, the low quantum efficiency, together with the inefficient delivery to a scattering ensemble in the used setup, makes it difficult to achieve significant optical saturation.
In an attempt to overcome this, we chose to investigate diluted samples, which has been proven to improve the spin properties by reducing the Yb-Yb interactions. I will report on this in the following.

4.2.2. Optical spectroscopy of diluted Yb-Trensal

Our collaborators synthesized a batch of Yb-Trensal which was diluted with the isostructural yttrium analogue Y-Trensal, with a Ytterbium ratio of roughly 5%, estimated from the weight ratio of the precursors used for the synthesis. The resulting crystals appear visually identical. We repeat the spectroscopic measurements conducted for the diluted sample.

Photoluminescence Studies

Photoluminescence studies of an ensemble of crystals in the aforementioned fiber–ferrule based setup were conducted. The spectra at room temperature and at 4.2 K are depicted in Figure 4.6, together with a fit to the inhomogeneous line belonging to the ${}^2F_{7/2}(0) \rightarrow {}^2F_{5/2}(0)$ transition around 972 nm. Interestingly, the observed inhomogeneous linewidths are significantly broader than for the undiluted sample, both at room

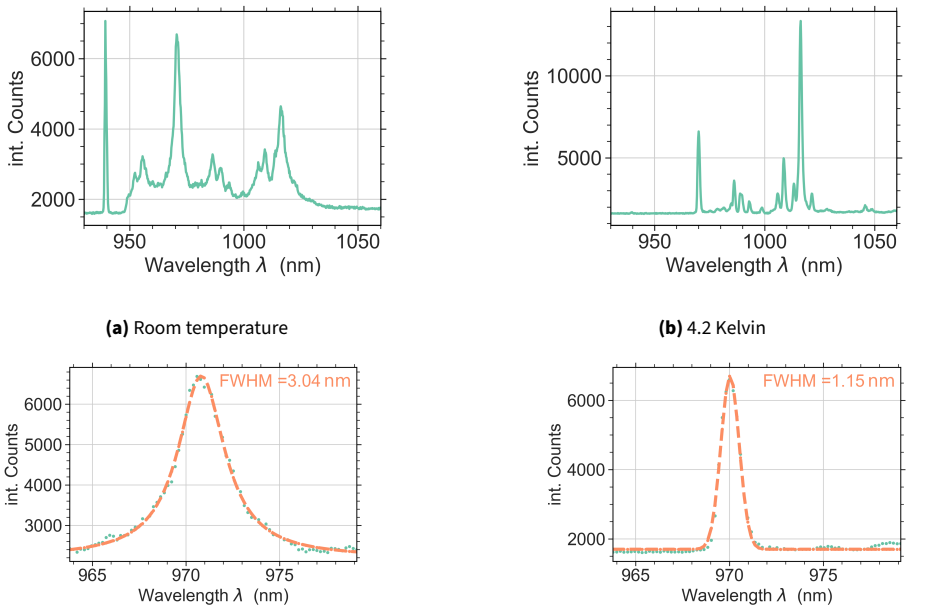

(a) Room temperature

(b) 4.2 Kelvin

(c) Lorentzian fit of the $^2\mathrm{F}_{7/2}(0) \rightarrow {}^2\mathrm{F}_{5/2}(0)$ transition at room temperature

(d) Gaussian fit of the $^2\mathrm{F}_{7/2}(0) \rightarrow {}^2\mathrm{F}_{5/2}(0)$ transition at $T = 4.2\,\mathrm{K}$

Figure 4.6.: Photoluminescence spectrum of the diluted Yb-Trensal molecule at room temperature and cryogenic temperature. The $^2\mathrm{F}_{7/2}(0) \rightarrow {}^2\mathrm{F}_{5/2}(0)$ transition around 972 nm is better fit by a gaussian at cryogenic temperatures.

temperature (undiluted: $\Delta\lambda = 1.12\,\mathrm{nm}$, diluted: $\Delta\lambda = 3.04\,\mathrm{nm}$) and cryogenic temperatures (undiluted: $\Delta\lambda = 0.20\,\mathrm{nm}$, diluted $\Delta\lambda = 1.15\,\mathrm{nm}$). In addition, the inhomogeneous line of the diluted sample is fit better by Gaussian lineshape at cryogenic temperatures, indicating a different dominating broadening mechanism than for the undiluted sample. This is in line with studies analyzing broadening as a function of REI doping concentration in dielectric hosts [181, 182, 183].The argument is that the inhomogeneous line is a measure for the homogeneity of the sample. The highest degree of homogeneity is obtained either for very low concentrations, where the chance of another dopant nearby is very low, or for very high concentrations, where all substitutional sites are occupied by a dopant. However, the increased inhomogeneity does not necessarily worsen the single ion properties: The homogeneous linewidth can nevertheless remain narrow [183]. When investigating the sample at cryogenic temperatures, again multiple lines at higher wavelengths are observed in the photoluminescence. Clusters around $\lambda = 990\,\mathrm{nm}$ and 1016 nm are depicted together with Lorentzian fits in Figure 4.7. However, the spectral structure significantly differs from the transitions observed in the undiluted Yb-Trensal sample. The spectra are directly compared in Figure 4.8. Note that the ions are excited

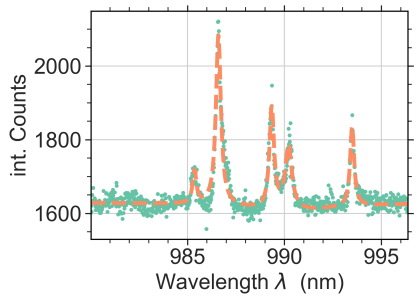

(a) Peaks around 990 nm fit by 5 Lorentzians.

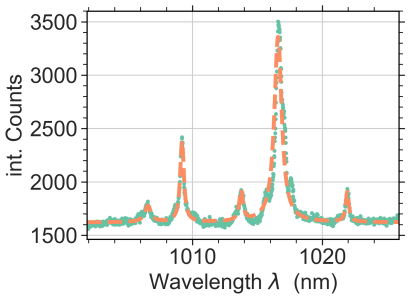

(b) Peaks around 1016 nm fit by 5 Lorentzians.

Figure 4.7.: Photoluminescence spectra of the higher wavelength transitions of the diluted Yb-Trensal molecular crystal. Two clusters of peaks can be identified.

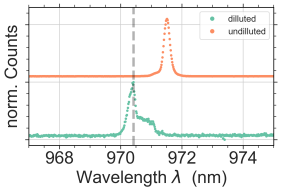

(a) Peaks around 971 nm.

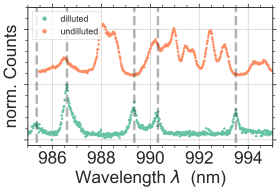

(b) Peaks around 990 nm.

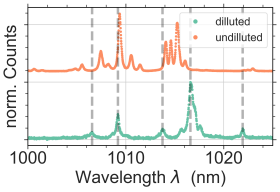

(c) Peaks around 1010 nm.

Figure 4.8.: Comparison between the photoluminescence spectra of the diluted and undiluted Trensal sample at $T = 4.2\,\mathrm{K}$. Grey-dashed lines are an guide to the eye, indicating the peak positions of the diluted sample.

at a wavelength of $\lambda = 940\,\mathrm{nm}$, where no sharp feature is observed in the absorption spectrum. We therefore assume that the excitation excites different classes in an equal manner.

For the stoichiometric sample, at least ten individual lines can be resolved in the spectral region between 1000 nm to 1025 nm. Meanwhile, in the diluted sample, only five peaks are clearly resolved in the same region. The only peak that can be identified in both spectra, based on the spectral position and height, is the peak located at 1009 nm. However, it is unclear whether this is due to an identical class in both samples, or simply a coincidence.
The peaks around 990 nm are analyzed in a similar fashion. Interestingly, they are much more clearly resolved for the diluted sample, because they appear smaller. To quantify this, an automated fit was performed on all visible lines. The average linewidth of the five peaks observed for the diluted sample is (0.28 ± 0.03) nm, respectively (0.63 ± 0.28) nm

for the 13 peaks observed for the undiluted sample, where the indicated error is the standard deviation of the mean of the linewidths as extracted from the fit.
The overall higher number of peaks observed for the undiluted sample is surprising. As discussed for the undiluted sample, the observation of multiple lines can be due to different classes of ions. Naively, one would expect this phenomenon to be stronger for the diluted sample, because the dilution introduces additional sources of disorder. The observation of less lines in the diluted sample is also inconsistent with the observation of a broader inhomogeneous linewidth of the $^2F_{7/2}(0) \rightarrow {}^2F_{5/2}(0)$ transition in the diluted sample, which is indicative of an increased disorder.

Absorption spectroscopy

In a next step, the optical transitions are probed by recording the transmission of the laser through the sample. The transmission spectrum and resulting optical density $OD = -\log(T)$ is displayed in Figure 4.9. Multiple strong and narrow absorption features are observed. Two clusters can identified: Cluster 1 in the range of 948 mn to 958 mn, and Cluster 2 around 969 nm to 972 nm. An additional peak is observed at 975.7 nm, which likely belongs to Cluster 2. Due to their spectral position, I assign the transitions belonging to Cluster 1 to the transition $^2F_{7/2}(0) \rightarrow {}^2F_{5/2}(1)$ and the transitions belonging to Cluster 2 to the coherent $^2F_{7/2}(0) \rightarrow {}^2F_{5/2}(0)$ transition, based on the values reported for Yb^{3+} ions in other hosts. Clearly, more lines per cluster are observed than can be explained by a single class of molecules. As I discussed when analyzing the photoluminescence spectra, one expects only a single line for each crystal field transition.
Again, the peaks belonging to each cluster are fit with Lorentzian lines (see Figure 4.9 (b-d)). The by far most prominent peak at $\lambda = 971$ nm can not be fully resolved via the absorption measurement, because the transmission in the center of the peak becomes smaller than the detection threshold of the detector. To more accurately determine the linewidth of the transition, I manually exclude the flattened top from the data and only perform the fit on the well resolved slopes. This is of course only an estimate, and information on any otherwise resolvable substructure is lost in the progress. The fit results are summarized in Table 4.1 and 4.2. The inhomogeneous line widths of the weaker satellite lines belonging to Cluster 2 are surprisingly narrow, down to 6 GHz. This approaches an interesting limit, since the hyperfine splitting is known to be on the order of 2 GHz to 3 GHz [177]. When the inhomogeneous linewidth becomes smaller than the hyperfine splitting, individual hyperfine transitions can be addressed optically, which is useful for spin manipulation and can even boost coherence times [150].
It is worth to note that the observation of many spectral features is somewhat counterintuitive, especially in comparison to the undiluted sample. In the undiluted sample, the analysis of the photoluminescence suggested more ion classes than for the diluted sample. However, the absorption spectrum only showcased a single spectral feature. For the diluted sample, the photoluminescence analysis of the $^2F_{7/2}(1) \rightarrow {}^2F_{5/2}(0)$ and $^2F_{7/2}(2) \rightarrow {}^2F_{5/2}(0)$ transitions points towards a lower inhomogeneity, while the inhomogeneous linewidth of the $^2F_{7/2}(0) \rightarrow {}^2F_{5/2}(0)$ transition indicated a higher degree

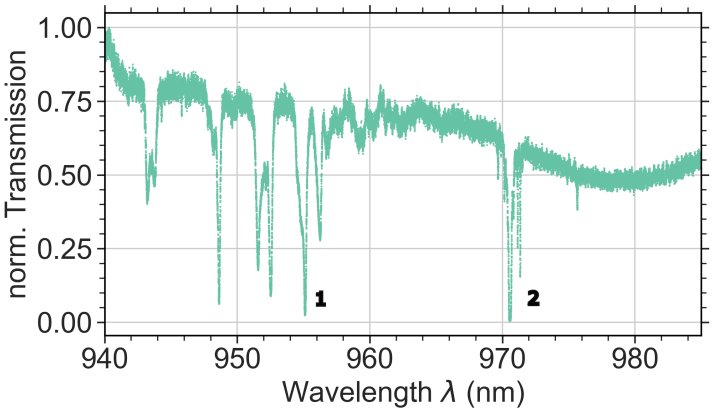

(a) Absorption spectrum of the diluted Yb-Trensal in the wavelength range 940 nm to 985 nm.

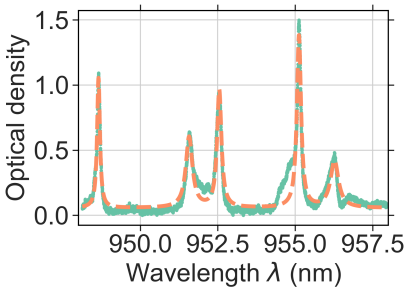

(b) Cluster **1** around 950 nm.

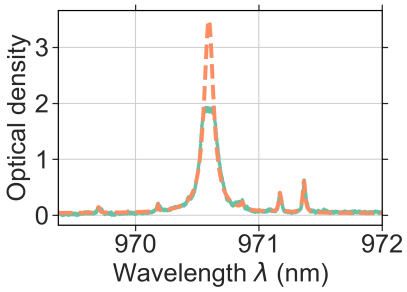

(c) Cluster **2** around 970 nm.

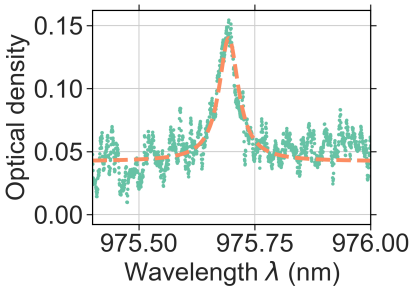

(d) Isolated peak at 975 nm, likely related to Cluster **2**.

Figure 4.9.: Absorption spectrum of the diluted Yb-Trensal sample at $T = 4.2\,\mathrm{K}$.

Table 4.1.: Fit results for the transitions around 950 nm in the diluted Yb-Trensal sample, as shown left to right in Figure 4.9 (b). σ_{FWHM} is the fit uncertainty.

Peak Number	Center Wavelength (nm)	FWHM (GHz)	σ_{FWHM} (GHz)	Optical density
1	948.65	36.7	0.7	1.00
2	951.58	85.2	1.9	0.54
3	952.55	56.0	0.9	0.90
4	955.12	53.0	0.6	1.32
5	956.27	101.1	3.1	0.36

Table 4.2.: Fit results for the transition around 972 nm in the diluted Yb-Trensal sample, as shown left to right in Figure 4.9 (c) and (d). σ_{FWHM} is the fit uncertainty.

Peak Number	Center Wavelength (nm)	FWHM (GHz)	σ_{FWHM} (GHz)	Optical density
1	969.7	6.5	3.1	0.10
2	970.18	3.4	1.9	0.12
3	970.59	31.9	0.4	3.45
4	970.86	8.0	3.2	0.11
5	971.17	7.2	1.0	0.34
6	971.37	8.0	0.6	0.56
7	975.69	16.1	0.4	0.10

of inhomogeneity compared to the undiluted sample. The absorption spectrum of the diluted sample clearly shows the existence of many observable clusters as individually well resolved lines assigned to the $^2\mathrm{F}_{7/2}(0) \rightarrow {}^2\mathrm{F}_{5/2}(1)$ and $^2\mathrm{F}_{7/2}(0) \rightarrow {}^2\mathrm{F}_{5/2}(0)$ transition, respectively.
One possible explanation could be the fact that the experiments on the diluted sample showcase a significant higher optical depth, because anticipating the lower Yb^{3+} concentration, significantly more sample material was used in the experiment. It is possible that similar faint absorption features as observed for the diluted sample also exist in the diluted sample, but could not be resolved due to the overall lower optical density.

Conclusion

In summary, we found that multiple narrow lines appear around the coherent $^2\mathrm{F}_{7/2}(0) \rightarrow {}^2\mathrm{F}_{5/2}(0)$ transition in the diluted sample. Some of these lines are very narrow, down to a few GHz. To the best of my knowledge, these are the most narrow inhomogeneous linewidths observed in an Ytterbium based molecular complex. At the same time, we achieve a large optical depth, even in a diluted sample. This is encouraging for future works.
Initially, the dilution was motivated by the reduction of the homogeneous linewidth. Unfortunately, I could not observe coherent signals from the sample. The extremely

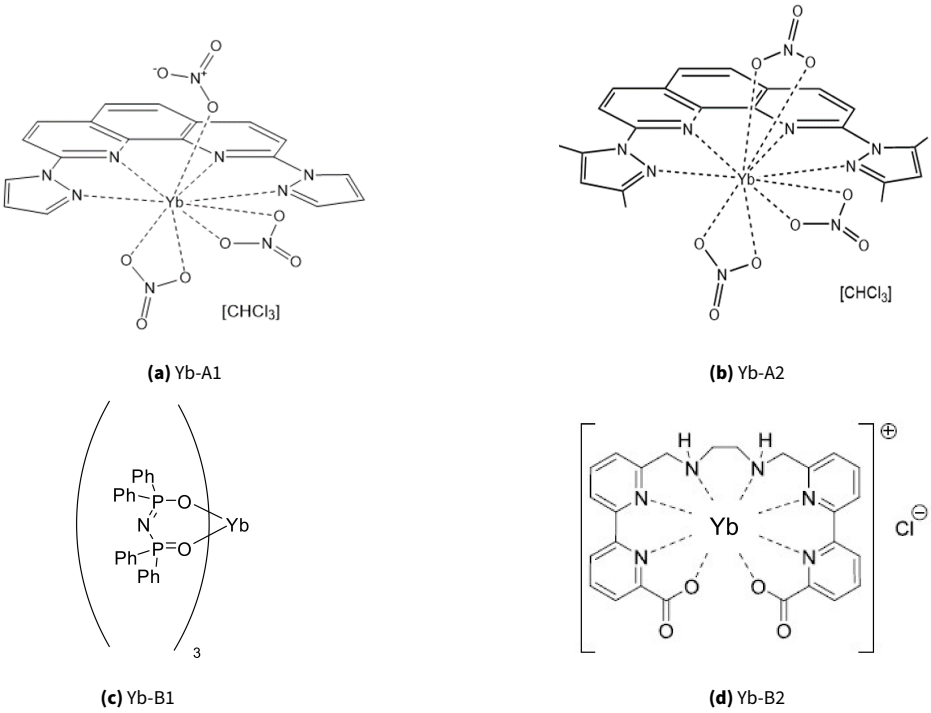

(a) Yb-A1 **(b)** Yb-A2

(c) Yb-B1 **(d)** Yb-B2

Figure 4.10.: Structural formulas of all Yb-based molecular materials investigated in addition to Yb-Trensal in this thesis.

low quantum efficiency makes the detection of these usually weak signals extremely challenging. Transient spectral hole burning, which was successfully applied to Yttria nanocrystals, relies on optical saturation. Achieving optical saturation was not possible for this sample, likely due to the low quantum efficiency, as discussed in section 4.1.1. Further possible directions to extract a homogeneous linewidth could be deuteration of the molecule, which is expected to improve the quantum efficiency and might enable transient spectral hole burning. In addition, studies on diluted samples at lower temperatures would be of interest, as the spin lifetime is expected to increase, which could enable persistent spectral hole burning experiments due to spin pumping.

4.3. Comparing different molecular design strategies - An overview

During the course of this thesis, several different Yb-based molecular complexes were investigated in varying detail. Yb-Trensal, as discussed above, stands out because its

usefulness for quantum information processing has already been demonstrated. However, it is clear that its low quantum efficiency limits the usefulness for many quantum communication protocols. As discussed above in Chapter 4.1.1, multiple strategies are known to increase the quantum efficiency. In the literature, one molecule has been reported to showcase the characteristic Yb^{3+} excited state lifetime $\tau \approx 1\,\mathrm{ms}$, indicating a high quantum efficiency [173]. Nevertheless, even if these design ideas are pursued in the synthesis of molecules, experimental investigation of the molecules is needed to determine the properties of interest, such as the excited state lifetime and the coherence properties of the molecular complexes.
Unfortunately, probing the homogeneous linewidths is difficult, as persistent spectral hole burning via spin pumping is usually not possible due to the short spin lifetimes. Photon echo spectroscopy is the most promising technique, but already requires a minimum optical coherence on the order of $\approx 1\,\mu\mathrm{s}$. Transient spectral hole burning requires saturation of the optical transition, which requires much higher powers than for conventional solid state hosts, due to the low quantum efficiency. In contrast, the inhomogeneous linewidth is easily measured, using PL-, PLE- and absorption spectroscopy, and can serve as a first indicator of the homogeneity of the sample. In the following, I will give an overview over the investigated molecules and try to link trends in the observation to the design principles which guided the synthesis. The investigation of these complexes were done in close cooperation with Robin Wittmann during his master thesis, which I supervised [143].

4.3.1. Overview of the investigated molecules

In addition to the already detailed discussion of Yb-Trensal, two other molecular complexes were prepared by the group of Mario Ruben. The complexes were synthesized by Sören Schittenhardt, and a lot of detailed information can be found in his thesis [180]. In the following, I will refer to these complexes as Yb-A1 and Yb-A2. Yb-A1 and Yb-A2 are based on the well-established (phen)-ligand (phen = 1-10,phenanthroline). The ligand used for Yb-A1 added two pyrazole ($(CH)_3N_2H$) units to the 2 and 9 position. The ligand for Yb-A2 is further modified by adding two methyl groups to each pyrazole unit. The resulting molecular structures of Yb-A1 and Yb-A2 are depicted in Figure 4.10.

Two additional molecular complexes were provided by Timo Neumann, a PhD student in the Group of Michael Seitz at Eberhard Karls University of Tübingen. The first, labeled Yb-B1 here, is based on a tpip-ligand (Tetraphenylimidodiphosphinate (tpip)) [184]. The second molecular complex Yb-B2 utilizes a Bipyridine ligand.[1] The molecular structures of the complexes are depicted in Figure 4.10.
All of these ligands strongly absorb in the UV spectral region and can be used to excite

[1] See Appendix A for matching the names employed in this thesis to the names used in the research group.

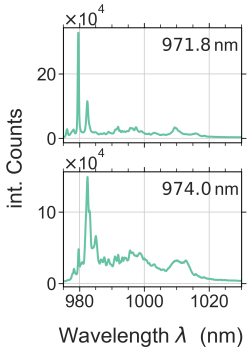

(a) Pl spectra of Yb-A1 upon selective excitation. Excitation wavelength is indicated as text in the plot.

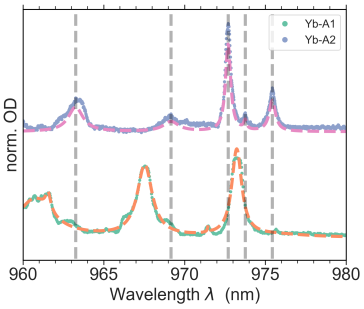

(b) Comparison of absorption spectrum of Yb-A1 and Yb-A2

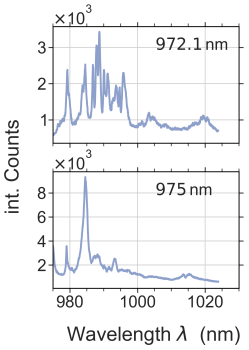

(c) Pl spectra of Yb-A2 upon selective excitation. Excitation wavelength is indicated as text in the plot.

Figure 4.11.: Comparison of the spectral properties of the phen-ligand based molecules Yb-A1 and Yb-A2. Data was acquired by Robin Wittmann.

Table 4.3.: Fit results for Yb-A1 and Yb-A2 of the transitions depicted in the absorption spectrum in Figure 4.11 (b). σ_{FWHM} is the fit uncertainty of the linewidth.

Yb - A1				
Peak Number	Center Wavelength (nm)	FWHM (GHz)	σ_{FWHM} (GHz)	Height (OD)
1	960.72	890	39	0.5
2	961.55	130	20	0.23
3	967.54	361	8	0.92
4	971.47	40	20	0.08
5	973.23	236	4	1.12
Yb-A2				
Peak Number	Center Wavelength (nm)	FWHM (GHz)	σ_{FWHM} (GHz)	Height (OD)
1	963.26	356	8	0.40
2	969.16	370	21	0.16
3	972.7	123	1	1.42
4	973.75	70	9	0.15
5	975.43	150	4	0.50

the REI via the antenna effect. They all follow a strategy to isolate the REI ion from close-by C-H ,N-H, O-H oscillators or solvent molecules in order to minimize non-radiative decay pathways.

4.3.2. Spectroscopic study of molecular homogeneity

In studying Yb-Trensal, we have found that the photoluminescence and absorption spectra can serve as a sensitive probe for the homogeneity of the sample. For one, we observe much more lines as are expected for the Yb^{3+} crystal field levels, pointing to different classes of molecules. This could be, among other reasons, due to the formation of dimers, the existence of different molecular conformations, or in-equivalent crystal lattice sites. This can be evidenced further by comparing the signatures of the individual resonances such as optical lifetime of PL spectrum upon selective excitation.
Additionally, the inhomogeneous linewidth of the individual features indicates the homogeneity of the ions belonging to this class. From this, information about for example the crystal quality can be extracted. In the following, I will give a short summary about these properties of the studied molecules. For the sake of clarity, similar molecular complexes are compared to each other first.

Yb-A1 and Yb-A2

The absorption spectra in the range of 960 nm to 980 nm for both Yb-A1 and Yb-A2 are depicted in Figure 4.11. Both show more lines than expected in this spectral region, indicating the formation of multiple classes of ions or molecules. Upon selective excitation the emission features change: the photoluminescence spectra become significantly different, as depicted in 4.11 (a) and (c). The observed excited state lifetime also depends on which resonance is excited, as indicated in Table 4.5. This confirms that these individual resonances really belong to different classes of ions or molecules. The observed inhomogeneous linewidths in absorption are again reasonably narrow: The dominant peak around 971 nm to 973 nm is $\Delta\nu = 123$ GHz wide for Yb-A2, and $\Delta\nu = 236$ GHz wide for Yb-A1. Some of the weaker features reach inhomogeneous linewidths on the order 30 GHz to 70 GHz. The fit result are summarized in Table 4.3. For Yb-A1 and Yb-A2, powder X-ray diffraction and magnetic susceptibility measurements performed by Sören Schlittenhardt also indicate the existence of at least one additional polymorph of the molecule [180], in accordance with the observation of multiple peaks here.

Yb-B1 and Yb-B2

Yb-B1 and Yb-B2 are chemically not directly related as the two complexes discussed above. Still, their photoluminescence spectra are similar in a sense that they show significantly less structure, hinting towards a higher degree of homogeneity. This is already evident from the absorption measurement of both molecular species depicted in 4.12. Both species show two transitions in the spectral region between 960 nm to 980 nm. For Yb-B1, one transition around 970 nm is both significantly stronger and more narrow. In the case of Yb-B2, the two transitions are of similar strength and width, but significantly more broad than the narrow transition in YB-B1. The fitted linewidths

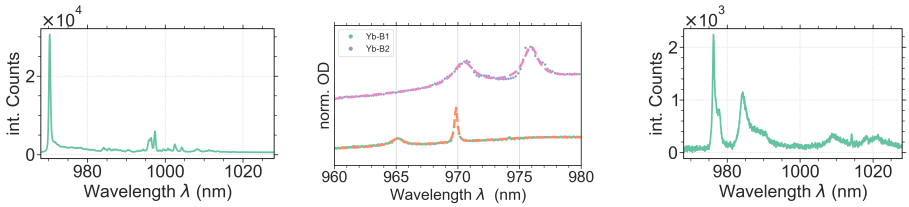

(a) PL spectra of Yb-B1

(b) Comparison of absorption spectrum of Yb-B1 and Yb-B2

(c) PL spectra of Yb-B2

Figure 4.12.: Comparison of the spectral properties of the molecules Yb-B1 and Yb-B2. Data was acquired by Robin Wittmann.

Table 4.4.: Fit results for Yb-B1 and Yb-B2 of the transitions depicted in the absorption spectrum in Figure 4.12

Yb - B1				
Peak Number	Center Wavelength (nm)	FWHM (GHz)	σ_{FWHM} (GHz)	Height (OD)
1	969.85	92	2	0.56
2	965.09	429	21	0.11
Yb-B2				
Peak Number	Center Wavelength (nm)	FWHM (GHz)	σ_{FWHM} (GHz)	Height (OD)
1	970.46	668	41	0.16
2	975.92	450	27	0.22

and peak positions are summarized in Table 4.4. The lowest inhomogeneous linewidth is observed for the transition at 969.85 nm for Yb-B1, with a FWHM of (92 ± 2) GHz, which is comparable to the values observed in other molecular complexes. No significant difference in the photoluminescence is observed when selectively exciting the resonances of both complexes. Still, only one transition is expected in this spectral window due to a single class of ions. The spectra are somewhat reminiscent of the two distinct peaks observed in Yb^{3+}:Y_2O_3 for two inequivalent lattice sites (compare section 3.3). Possibly, the crystals studied here also posses two distinct lattice sites.

Discussion

As discussed above, the complexes Yb-A1, Yb-A2 as well as Yb-Trensal show clear signs of several classes of molecules or ions in the sample, which are in one case also corroborated by x-ray diffraction measurements. Meanwhile Yb-B1 and Yb-B2 show these effects to a lesser extent, although their spectra can not be fully explained by a single class of ions. When comparing the chemical structure, it becomes clear that the multi-class samples

Table 4.5.: Overview of the measured excited state lifetime and their coordination spheres for the investigated Yb-based molecular complexes. Total number of hydrogen atoms bound to carbon atoms, if present, are given in brackets.

Molecule	Yb-Trensal	Yb-A1	Yb-A2	Yb-B1	Yb-B2
1st Coordination sphere	N_4O_3	N_4O_5	N_4O_6	O_6	N_6O_2
2nd coordination sphere	$C_9(6H)$	$N_5(1+)C_6(2H)$	N_5C_6	P_6	H_2C_{14}(8H)
Lifetime τ (μs) RT	3	28	27	43	4.1
Lifetime τ (μs) 4.2 K	2.4	29 (974 nm) 38 (971.8 nm)	31 (975 nm) 26 (973 nm)	46.5 (964.9 nm) 53 (969.75 nm)	1.6

tend to have lower symmetry. This makes the existence of frustrated conformations more likely, leading to multiple possible binding conformations. Another reason could be the non-uniform loss of lattice solvent during the crystallization, leading to damage in the crystals. This is especially relevant for both Yb-A1 and Yb-A2, as they co-crystallize with chloroform.

4.3.3. The optical lifetime - Probing the molecular environment

Optical lifetimes were recorded using pulsed excitation at $\lambda = 940\,\text{nm}$, unless specified otherwise. For some complexes, we observe different lifetimes when resonantly exciting different transitions. This is a further indication of the formation of different molecular classes. The results are summarized in Table 4.5 and visualized in Figure 4.13. One can broadly differentiate between molecules with low lifetimes on the order of a few µs, (Yb-Trensal, Yb-B2) and lifetimes which are approximately an order of magnitude higher 25 µs to 50 µs (Yb-A1, Yb-A2, Yb-B1).

Yb-A1 and Yb-A2 are easy to directly compare, since they only differ by the four additional methyl groups in the ligands of Yb-A2. Yb-A2 therefore possesses 12 additional C-H bonds, which are however pretty far removed from the lanthanide center. The observed excited state lifetime is slightly smaller for Yb-A2, indicating an increased non-radiative decay rate due to the additional C-H oscillators in agreement with the expectation.

Yb-B1 features the longest optical lifetime, of all the studied complexes with $\tau = 53\,\mu\text{s}$. This is in accordance with the first C-H bond only appearing between the fourth and fifth coordination sphere. Even then, there are only two C-H bonds at this position per Phenyl group, making it eight C-H bonds in total at a relatively large distance from the Ytterbium ion.

Yb-Trensal differs from the long-lived molecules mainly in that it posses 14 sp^3-hybridized C-H bonds between the second and third coordination sphere. Consequentially, there are more nearby high-frequency oscillators available to promote non-radiative decays. Finally, the measured excited state lifetime for Yb-B2 is 1.6 µs, the lowest optical lifetime observed for any of the studied molecules. The result for Yb-B2 is surprising, since a significantly longer lifetime of 14 µs have been reported for this complex in [185], albeit

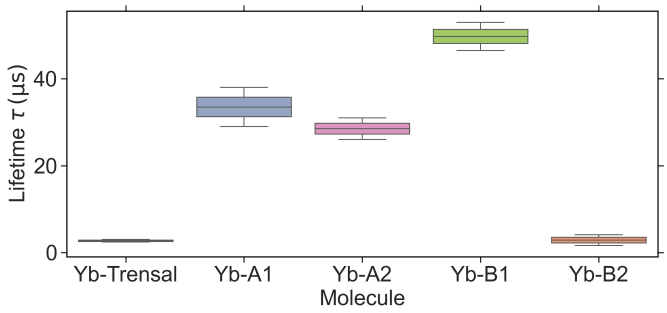

(a) Overview of the measured lifetimes for all molecular species under different conditions.

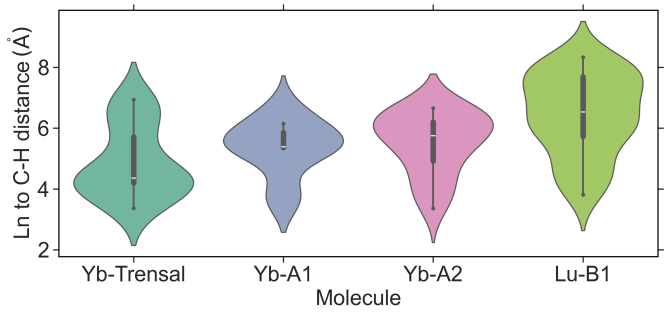

(b) Violin plot illustrating the spread of distances from H atoms in the molecule to the lanthanide center. Black dots show quartiles and whiskers of a boxplot, patch shows a symmetric kernel density estimate.

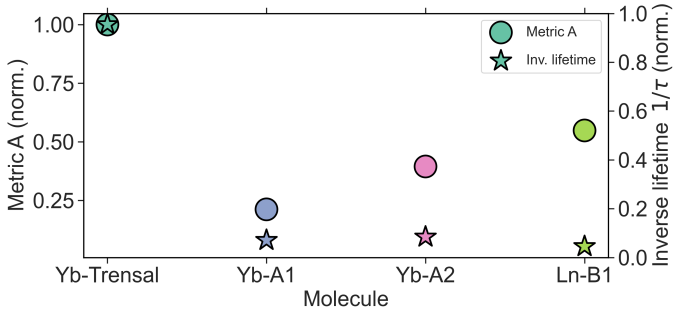

(c) Comparison of the metric calculated according to equation 4.4 and the inverse lifetime.

Figure 4.13.: Comparison between the optical lifetime and distribution of C-H bonds in the molecule. Metric A is normalized to the inverse lifetime of Yb-Trensal.

in solution (D_2O). Possibly, the molecule sample deteriorated between the synthesis and the measurement. However, the short lifetime is in accordance with Yb-B2 possessing two N-H bonds between the first and second coordination sphere, as well as additional C-H bonds between the second and third coordination sphere.
In an attempt to correlate this result with the mechanisms discussed in 4.1.1, the distance of the Ytterbium ion to the surrounding C-H oscillators was determined. Published structural files of the complexes Yb-Trensal, Yb-A1, Yb-A2 and Yb-B1 [186, 187, 179][1] were analyzed using the software OLEX2 [188]. Since there is no structural file published for Yb-B1, the Lutethium analogue was used instead. The program allows measuring the distance between the REI center and the hydrogen atoms, which are connected to carbon atoms. For Yb-Trensal and Lu-B1, which posses a trigonal symmetry, the distances were only determined for one of the ligand groups and assumed to be identical for the ligand groups. A violin plot in Figure 4.13 (b) depicts the statistical distribution of the so determined distances. The observed trend seems to roughly agree with the expectations: Notably, Yb-Trensal possesses many C-H oscillators with a distance below 4 Å, and also showcases the by far shortest lifetime. Yb-A1 and Yb-A2 are, as expected, very similar in terms of their optical lifetime and the distribution of hydrogen atoms around the lanthanide center. The slight changes in lifetime between the two are not evident from this simple analysis. Finally, Yb-B1, as expected, possesses many hydrogen atoms which are placed more than 6 Å away from the REI center, which can help explain the relative long lifetime.
As discussed in section 4.1.1, the non-radiative decay rate per C-H bond is expected to scale with $\frac{1}{r^6}$ for a dipole-dipole interaction. To get a feeling for the expected rates, a metric A defined as:

$$A = \sum_{\mathrm{H}} \frac{1}{r^6_{\mathrm{Yb-H}}}, \tag{4.4}$$

was calculated, where the sum is calculated over all hydrogen atoms in the molecule[2]. The resulting metric is expected to be proportional to the non-radiative decay rate. The resulting values are visualized in Figure 4.13 (c). In accordance with the hypothesis, this metric is the largest for Yb-Trensal. However, when looking at the other complexes, one observes the inverse correlation, that is the metric would predict the longest optical lifetime for Yb-A1. Also quantitatively, the metric differs by a factor of 2-4 between the studied molecules, while the optical lifetime varies by a factor of 10-20. Clearly, in order to achieve a qualitative understanding of these effects, a much more intricate modeling beyond the scope of this work would be required. Overall, this analysis is of course very crude and does not account for many relevant factors, such as the orientation of the lattice vibration, or how resonant the multi-phonon process is with the energy gap that needs to be bridged. Nevertheless, it illustrates that the hypothesized chemical design principals have been adhered to and show the right trend. While some attempts

[1] and private communication with Sören Schlittenhardt
[2] All of the hydrogen atoms are bound to carbon atoms in the investigated molecules.

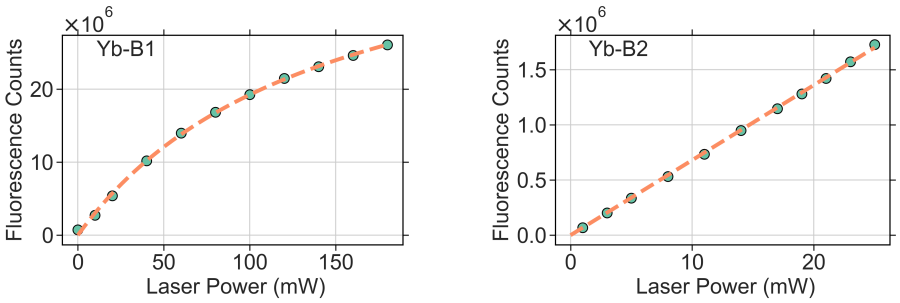

(a) Yb-B1 **(b)** Yb-B2

Figure 4.14.: Fluorescence saturation curves of Yb-B1 and Yb-B2. Powers are measured before coupling into the fiber to the sample. Data was acquired by Robin Wittmann.

were made, such as taking into account the expected $\frac{1}{r^6}$ scaling, no satisfying more quantitative correlation could be found. Nevertheless, this analysis may serve as a starting point for the design of future lanthanide-ligand complexes.

4.3.4. Suitability for coherent experiments

On most of these molecules, attempts were made to achieve spin-pumping or photon echoes, which were however unsuccessful. As discussed before, the most suitable way to measure the optical coherence times without these techniques is transient spectral hole-burning. As discussed a prerequisite is to achieve strong optical saturation in order to achieve a sufficient contrast. The fluorescence saturation of both Yb-B1 and Yb-B2 were recorded by integrating photoluminescence spectrum taken for different excitation powers and are depicted in Figure 4.14. We observe the onset of saturation for Yb-B1. By fitting a simple saturation curve of the form $I(P) = I_{\max}(\frac{1}{1+(S/P)})$, where I is the intensity of the measured signal and S is the saturation parameter, we obtain a saturation power of (145 ± 8) mW. Therefore, transient spectral hole burning seems attainable with this molecule. However, as mentioned before, a lot of laser power overhead is required experimentally. First, the laser power needs to be distributed onto two frequency tones. When increasing the distance between these tones, the laser power further decreases. Finally, the involved powers become so high that care needs to be taken in order not to damage any of the fiber-optical components involved. For these reasons, we were so far unable to perform transient spectral hole burning on this complex. However, I believe that by further optimization of the delivery of the laser to the sample, this should be attainable, hopefully revealing information about the coherent properties of the tpip-ligand based molecular complex Yb-B1.

In contrast to Yb-B1, Yb-B2 shows no signs of saturation in the investigated regime. However, the maximal probe power is significantly lower than for Yb-B1, as due to laser downtime, an ECDL laser with a maximal output power of 30 mW had to be used. Therefore, the curves can not be compared directly. Formally, one would expect a higher optical saturation power due to the faster relaxation of the excited state observed in section 4.3.3.

4.4. Outlook

In this section, five Yb-based molecular materials were studied using cryogenic laser spectroscopy. By recording absorption and photoluminescence spectra, information about the homogeneity of the samples could be extracted. We found that all of the investigated complexes tend to form different classes of molecules, as seen by one transition being visible at different frequencies slightly shifted to each other, and showing different signatures upon selective excitation. I analyzed the excited state lifetime and found significant differences of more than a factor of 20, showcasing the extreme sensitivity of the Yb^{3+} ion to the surrounding ligands. While even the longest-lived molecule complex is more than one order of magnitude below the expected radiative lifetime, this showcases the potential of careful chemical design of the molecular complexes. The molecule in question, Yb-B1, also showed a reasonably narrow inhomogeneous transition linewidth (90 GHz) and fluorescence saturation upon strong laser illumination, making it the most suitable candidate to investigate its coherent properties. While achieving transient spectral hole burning with the current molecular complex might be feasible by upgrading the experimental apparatus, it is also of interest to investigate a more refined version of this molecule. By deuteration of the complex, non-radiative relaxation rates could potentially be reduced even further, which also should lead to a reduced optical saturation power. In addition, it might also help the coherent properties, since deuterium's magnetic moment is also reduced compared to hydrogen. In addition, investigation of the molecules at lower temperatures $T < 1\,\mathrm{K}$ would be highly interesting, as the spin properties are expected to significantly improve, which might allow to detect spin signatures optically, for example via spectral hole burning.
By studying the optical properties of Yb-Trensal, I found evidence for the formation of additional molecular classes when diluted with an Yttrium equivalent. The diluted Yb-Trensal sample possessed the narrowest inhomogeneous lines at low temperatures of all molecular complexes studied in this thesis, on the order of a few GHz. This value is [1] smaller than the values reported for any other Yb-based molecular complex, comparing to [189]. Considering that Yb-Trensal has long been established as a excellent spin-qudit, this warrants further studies to gain information about the homogeneous linewidth of the complexes. As discussed above, both deuteration and working at lower temperatures

[1] to the best of my knowledge.

are expected to improve the coherent properties.

Clearly, the investigation of Yb-based organic complexes for quantum information technologies is still in the early stages, and progresses slower than for example the Eu-based analogues. Eu-based complexes have the additional advantage of the naturally high quantum efficiency and much higher spin lifetimes, enabling spin-pumping based spectral hole burning experiments [159, 178]. However, the impressive work conducted on Yb-Trensal and the newly reported (thiolfan)YbCl(THF) [189] show the promise that Yb-based molecular complexes hold. By employing its electronic spin, one can easily couple to magnetic fields, enabling sensing applications and strong microwave driving. This holds potential for many applications. For example, transduction of microwave photons, as they are used for quantum computing platforms, to optical photons could be realized. This has been demonstrated using Yb^{3+}:YVO [190, 191]. Crucially, efficient conversion requires both a high dopant density and a narrow inhomogeneous lines, which makes the use of stoichiometric molecular crystals appealing. By using custom-tailored molecular complexes, one could imagine matching the microwave and optical frequencies to existing platforms, while also controlling the transition strengths and coherences.

5. Color centers in a silicon carbide membrane coupled to a fiber-based Fabry-Pérot cavity

Up until this point, I have reported on the spectroscopic investigation of Yb^{3+} ions in different host materials and their suitability for integration into open access cavities, including a proof of concept experiment at room temperature. In order to achieve a significant enhancement of the emission rate, cavity-based experiments need to be performed at cryogenic temperatures. However, the available cryostats hosting the cavity experiment can only achieve temperatures down to $T = 15\,\mathrm{K}$ at the sample, due to the bulky nature of the cavity setup. This is expected to significantly worsen the coherence properties of Yb^{3+} ions. Therefore, cryogenic cavity experiments were instead conducted with another candidate for a spin-photon interface, namely the V2 color center in silicon carbide (SiC). This was motivated by the observation that the optical coherence of these color centers is well preserved up to temperatures of $T = 20\,\mathrm{K}$, making them ideally suited for the cryogenic cavity setup utilized here. Because these defects emit coherent light around $\lambda = 917\,\mathrm{nm}$, I can still make use of the cavity mirrors originally designed for the Yb^{3+} experiment.

In this chapter, I will present how we use a thin membrane of SiC to couple both multiple and individual color centers to an open fiber-based Fabry-Pérot cavity at cryogenic temperatures. I will start by introducing the silicon vacancy center in SiC. I will then present how we fabricate a thin membrane of SiC and incorporate it into a fiber-based microcavity. I study and model the coupled membrane-resonator system and observe a high membrane quality, as evidenced by a high cavity finesse. This allows me to extract information about the birefringence of the material and the thickness of the membrane. Finally, I will present cavity-enhanced measurements of silicon vacancy centers at cryogenic temperatures. I show that the cavity can be used to spectrally resolve several color centers in a single spatial mode. I confirm the single emitter character of such features by second-order auto-correlation measurements. By measuring the optical lifetime as a function of the cavity-emitter detuning, I demonstrate Purcell enhancement of the coherent transition of the V2 center. This results in a high rate of extracted photons, paving the way towards an efficient spin-photon interface.

The project presented in this chapter was done in collaboration with Jonathan Körber, a PhD student in the group of Jörg Wachtrup working on silicon carbide.[1] The results presented in this chapter are published in [192].

5.1. Silicon vacancy centers in silicon carbide

Many wide-bandgap semiconductor materials can host optically active lattice defects, where a lattice atom is either missing or replaced by an impurity atom. The resulting dangling electron bonds form an energy level scheme that resembles a free atom and can exhibit optical transitions. Color centers in the solid state have been studied for many years. While in the beginning, the investigation was driven by fundamental research, it was quickly realized that they can posses narrow optical transitions and often also an unpaired electron spin, which allows experiments at the intersection of spin physics and quantum optics [193]. In particular, the discovery of the nitrogen vacancy center (NV center) in diamond was a milestone, which spurred the rapid development of the field. Still today, the various color centers in diamond are the leading material platform for the realization of a solid state spin-photon interface [194, 99, 168]. However, there has been a growing interest in color centers in other materials. Among these, silicon and silicon carbide stand out [24, 195, 25] . Both host materials are extremely mature semiconductor materials: They can be grown with high purity and high control of the doping, they can be easily processed using established cleanroom technologies, and the processing can be scaled up to the wafer scale. Silicon suffers from its small bandgap (E_g = 1.12 eV), which makes it absorptive in the visible wavelength regime. This limits the useful color centers to those that emit in the near-infrared part of the spectrum. In any case, due to the small bandgap the defects are easily ionized upon optical excitation, which leads to blinking and spectral diffusion. The bandgap of 4H-SiC is 3.26 eV, placing it between Si and diamond (E_g = 5.47 eV) [196, 197].

Silicon Carbide

Silicon Carbide is a wide bandgap semiconductor material, where each Si atom is coordinated by four carbon atoms and vice versa, forming a tetrahedron. In a closed-packed hexagonal stacking, there are three possible types of Si-C bylayers arbitrarily labeled {A,B,C}. By stacking them in different periodic orders, different polytypes of SiC can be created [198]. Different polytypes are labeled according to the number of layers of

[1] Jonathan Körber initialized the experiment, fabricated the samples, initiated the implantation and irradiation runs and characterized the implanted emitters in a room temperature and cryogenic confocal microscope. He also did first cavity characterizations of the membrane-cavity system at room temperature in a scanning cavity microscope setup which I built. I continued the measurements in a cryogenic scanning cavity setup which was built by Maximillian Pallmann, a former PhD student in our group.

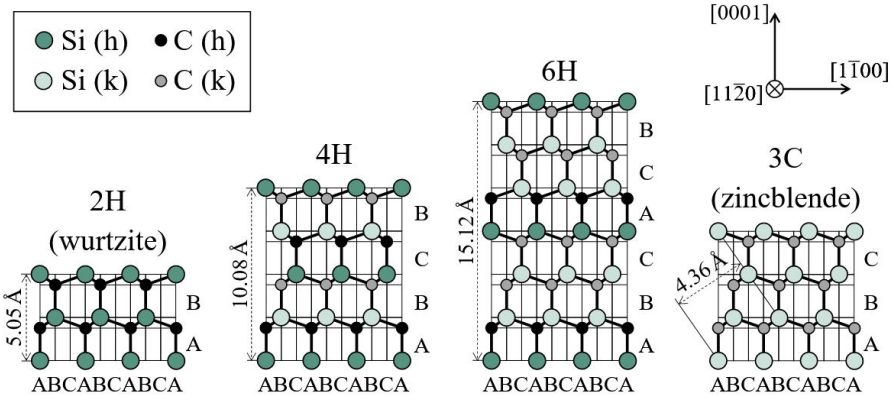

Figure 5.1.: Illustration of the crystal structures of the most common SiC polytypes. Reprinted with permission from [198].

Si-C bylayers ∈ {A,B,C} inside a unit cell, and the overall crystal symmetry. Over 150 different polytypes are known, which can vary significantly in their physical properties. A schematic illustration of the most common polytypes is depicted in Figure 5.1. In the following, I will limit the discussion to the 4H polytype, which is among the most studied and the polytype of all samples investigated in this work. There are two inequivalent silicon lattice sites in 4H-SiC, the hexagonal (h) and cubic (k) site. Silicon carbide is commonly used for high power electronic applications. This is due to a combination of a large bandgap, high critical electric field strength and ease of doping and fabrication [199]. It has also been studied for integrated photonic applications, where the combination of a high refractive index, a large bandgap and a high Kerr non-linearity makes them especially suitable for nonlinear photonics [200]. Silicon carbide can host many optically active defects with distinct properties. Conceptually simplest are the Si^-- vacancies, where a silicon atom is missing from the lattice, and binds an additional electron from the lattice. Moreover, there are for example chromium and vanadium centers where the dopants replace the silicon atom, as well as divacancies formed by a missing silicon and a missing neighboring carbon atom [201, 202, 203, 204, 205]. A detailed discussion and comparison of these defects exceeds the scope of this work and the interested reader is referred to the multiple review articles published on this matter [201, 25, 206]. In the following, I will focus on the Si^--vacancy in 4H-SiC.

5.1.1. The Si^--vacancy in 4H-SiC

The Si^- vacancy is formed when a silicon atom is removed from the lattice and binds an additional electron. The resulting dangling bonds are strongly localized and point towards the silicon vacancy. Therefore the C_{3v} symmetry of the defect is preserved [207,

208]. The four electrons from the dangling bonds together with an additional electron lead to a spin $S = 3/2$ system. Both, the ground and the optical excited state, consist of two doubly degenerate Kramer doublets with $m_s = \pm 3/2$ and $m_s = \pm 1/2$. The optical transitions are spin conserving, resulting in two optical transitions. The properties of the center depend on whether the missing silicon atom is at the hexagonal (h) or cubic (k) lattice site. The two centers are for convenience often referred to as the V1 (h) and V2 (k) center.
For both defects, the optically excited state can relax directly or via a phonon-assisted process [209]. The phononic relaxation is incoherent and spectrally broad. The coherent, direct emission results in a narrow line at low temperatures, and is commonly referred to as the zero phonon line (ZPL). The broad, incoherent emission is called the phonon side band (PSB). An exemplary, cryogenic PL spectrum of the V2 center depicting these two features is depicted in Figure 5.2 (b).
In order to give an overview over the achieved results of this platform, I will briefly introduce both centers, although the experimental investigation in this work focuses on the V2 center.

The V1 center

The zero phonon line of the V1 center is at $\lambda = 861\,\text{nm}$. The excited state lifetime is $\tau_{\text{V1}} = 6\,\text{ns}$. The experimentally reported branching ratio into the zero-phonon-line [1] is around $\zeta \approx 8\,\%$, roughly a factor of three higher than for the NV center in diamond [209].[2] The two spin doublets in the ground state can be driven efficiently with a resonant microwave drive, enabling coherent manipulation of the electron spin. Dephasing times of $T_2^* \approx 20\,\mu\text{s}$ and coherence times measured via single-spin echo sequences of $T_2^{\text{echo}} \approx 0.8\,\text{ms}$ of the electron spin have been reported at cryogenic temperatures [212]. For single V1 centers, narrow optical linewidths, down to a factor of two away from the transform limit and high single photon purity have been observed, even under strong off-resonant excitation [213]. This led to a demonstration of spin-controlled two-photon interference via Hong-Ou-Mandel interference [213], and recently the experimental realization of spin-photon entanglement [26]. Measurements and DFT calculations show that the homogeneous linewidth remains narrow up until temperatures of $T = 5\,\text{K}$ [209]. This allows for integration into standard liquid ^{4}He cryostats, given that the sample is well thermalized.

[1] In the context of vibrational assisted decay mechanism listed here, this is commonly referred to as the Debye-Waller factor.
[2] In earlier works, the value was erroneously reported to be much higher [210, 211].

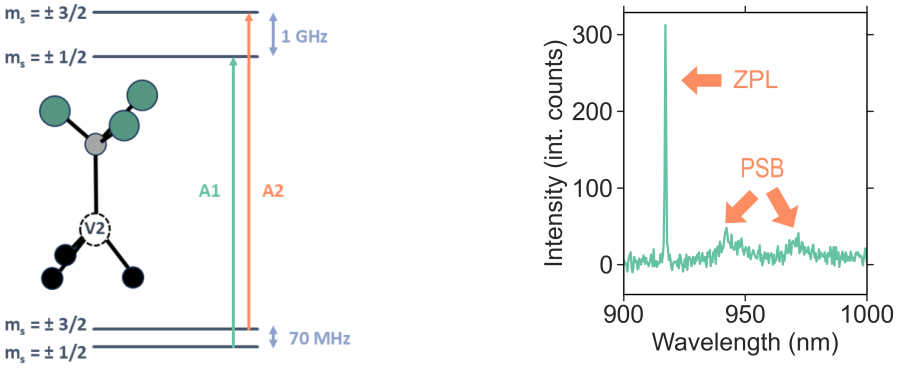

(a) V2 center level scheme.

(b) PL spectrum of a V2 center.

Figure 5.2.: (a) Simple level scheme and graphical representation of the V2 center in SiC. The ground and excited state respectively consist of two Kramer doublets split by a zero field splitting. The ground and excited state are connected by two optical transitions A_1 and A_2 separated by 1 GHz. (b) Photoluminescence spectrum of a V2 center at cryogenic temperature, showcasing the narrow zero-phonon-line and the weak phonon side band. The resolution of the spectrometer is insufficient to resolve the two spin-conversing transitions that make up the ZPL. Data was provided by Jonathan Körber.

The V2 center

Despite their conceptual similarity, the different lattice site of the V2 center leads to slightly different properties. The zero-phonon line of the optical transition is situated at $\lambda = 917\,\text{nm}$. The excited state zero-field splitting is $\Delta_{\text{ES}} \approx 1\,\text{GHz}$ [214], and the ground state zero-field splitting is $\Delta_{\text{GS}} \approx 70\,\text{MHz}$ [215]. A simple level scheme of the V2 center is depicted in Figure 5.2. In contrast to the V1 center, the two excited states show very different lifetimes ($\tau_{1/2} = 6.1\,\text{ns}$, $\tau_{3/2} = 11.3\,\text{ns}$) when selectively probed [216]. This is attributed to different coupling to non-radiatively relaxing, metastable states. The overall dynamics are quite complex, but have been studied in detail in [216]. An effective model considers three additional metastable states and an excitation power dependent coupling from one of the metastable states to a higher lying excited state.
In contrast to the V1 center, the optical linewidth of the V2 center only begins to broaden at temperatures above $T = 20\,\text{K}$, relaxing the requirements on the utilized cryostat [209]. This is especially important when thinking about technological applications in the future, where one will need to build many quantum processing nodes or repeater units. There, looser temperature requirements make the uspcaling more cost-efficient and less error-prone.
Recently, the V2 center has been used to demonstrate single-shot readout of an ancillary nuclear spin [217, 218], and was successfully integrated into a whispering gallery mode

resonator while retaining optical linewidths close to the lifetime limit [219]. In this work, I focus on the V2 center because of its relaxed requirements on temperature and its ZPL wavelength of $\lambda = 917\,\text{nm}$, making it compatible with the mirror coating designed for Yb^{3+} ions.

Remarkably, the good optical coherence properties of both V1 and V2 centers are preserved in nano-structures, even though they do not posses inversion symmetry like the Group-IV color centers in diamond. This makes them suitable for nanophotonic integration, one of the key requirement for scalable and efficient spin-photon interfaces. This is usually attributed to similar electron densities of the ground and excited state [216, 210, 209]. These arguments have not been confirmed experimentally and are based on density functional theory calculations. Some people in the community have expressed doubts about these arguments and ascribe the good coherence properties in nanostructure to a natural surface passivation of the nanostructures due to the formation of an oxide layer.[1] I tend to agree with this argument, as a strong linear stark tuning of V1 and V2 centers has been demonstrated in reference [220].

5.2. A thin SiC membrane inside a Fabry-Pérot resonator

Again, one needs to consider how to best integrate the host material of the defect into the cavity, while minimally impacting both the cavity performance and the emitter properties. An especially promising approach to introduce solid state quantum emitters into a FFPC is in the form of a thin membrane, which is bonded to a cavity mirror. This configuration is schematically depicted in Figure 5.3. This approach has been used and studied in various solid state quantum emitter systems, such as color centers in diamond [221, 222, 223, 224], rare earth ions in Y_2SiO_5 [128, 129, 130], and molecular thin films [225]. A special case are epitaxial grown quantum dots, where the defect can be grown directly in the DBR stack which later forms the cavity [226, 227].
The membrane thickness needs to be chosen such that an emitter located in the center of the membrane is well isolated from the electric noise at the surface and therefore retains good coherence properties. On the other hand, the membrane should be as thin as possible in order to introduce minimal absorption losses and to enable operation at short cavity lengths to maximize the Purcell enhancement. Furthermore, the surface roughness of the membrane should be small to minimize scattering losses. Recent work has shown that V2 centers can retain excellent coherence properties even in thin membranes. Optical linewidths below 100 MHz have been reported in membranes as thin as 0.6 µm [228]. This is encouraging for the integration of such a membrane into a FP cavity.

[1] Not published, mentioned in a talk by Christopher Anderson during 816. WE-Heraeus-Seminar: "Silicon Carbide: Classical and Quantum Technologies".

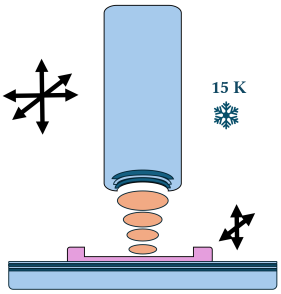

(a) Schematic of the cavity-membrane setup.

(b) Photograph of an assembled fiber cavity containing a SiC membrane.

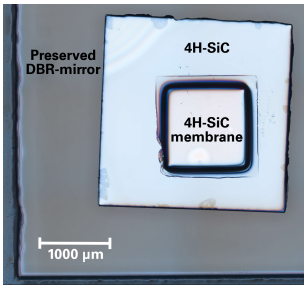

(c) Photograph of a SiC membrane. Picture was taken by Jonathan Körber.

Figure 5.3.: Illustration of the fiber-cavity membrane configuration. Reproduced from [192].

In the following I will first introduce how the cavity behavior changes when a dielectric membrane is introduced into the cavity. Then, I will shortly describe the fabrication procedure. I then present a careful characterization of the cavity performance upon integration of the membrane into the cavity. Finally, I will briefly discuss the creation of color centers and a characterization of their properties inside a thin membrane.

5.2.1. Dielectric membranes in cavities

In this section, I will give an overview of the effects that emerge upon introduction of a dielectric membrane directly bonded onto a dielectric mirror into a Fabry-Pérot cavity. This has been studied in detail in previous works, most commonly related to diamond membranes [229, 230, 231]. For a more in depth analysis I refer to the the doctoral thesis of my colleague Maximilian Pallmann [232].
When introducing a membrane into a FP resonator by bonding it onto a dielectric mirror, one essentially adds an additional interface to the cavity. Every roundtrip, a fraction of the light field propagating in the cavity is reflected at the air-dielectric interface and the dielectric-air interface according to $\frac{n_2-n_1}{n_2+n_1}$. The reflected fields then interfere with all other field components propagating in the cavity. This interference is determined by the optical length of the air-gap and the optical length of the dielectric membrane. Therefore, it is useful to study the emerging effects as a function of the membrane thickness and the probing wavelength.
An instructive way to understand this system is to think of it as two coupled resonators filled with air and the dielectric respectively. The coupling strength is determined by the refractive index difference between the membrane and the air. As we will see in the following, due to this coupling a characteristic anti-crossing behavior is observed in the cavity dispersion.

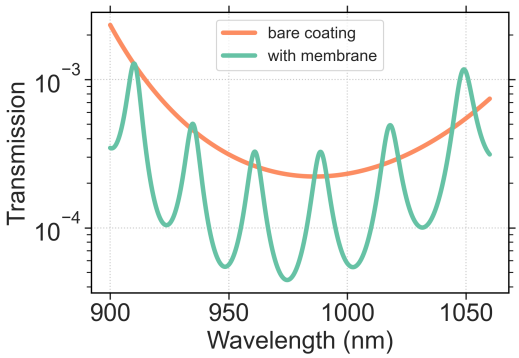

Figure 5.4.: Modification of the mirror transmission when a $d = 6.2\,\mu\text{m}$ thick silicon carbide membrane is bonded to the DBR stack of the planar cavity mirror. The periodic modulation is caused by constructive and destructive interference of the partial fields reflected at the membrane-air interface. Data is obtained via a transfer-matrix model simulation.

Bragg reflectors modified by dielectric membranes

It is instructive to first understand how the membrane changes the transmission of the DBR stack that forms the mirror. The membrane can be understood as an additional high refractive index layer. It is straightforward to extend the previously mentioned transfer matrix model for the DBR stacks to account for the membrane, by simply adding another refractive index slab to the coating. The resulting transmission is depicted in Figure 5.4 and is compared to the bare transmission of the mirror. We observe that the transmission of the modified coating shows a periodic modulation with the wavelength. The period of this modulation is given by $\frac{\lambda}{4nd}$, which is the free spectral range of the weak Fabry-Pérot etalon formed by the dielectric membrane. Note that for the coating used here, the transmission can be significantly reduced due to the membrane. This can be explained by the fact that the mirror coating is terminated with a low refractive index material. The membrane therefore adds as an additional high index layer, and can increase the reflectivity.

Cavity dispersion

The mixed mode character of an air-like and dielectric-like mode additionally manifests itself in the cavity dispersion, that is how the resonance wavelength shifts when the cavity air-gap is changed. For an empty cavity, the cavity resonance wavelength is $\lambda_\text{q} = \frac{2d_\text{air}}{q}$, and exhibits a linear slope $2/q$. If one considers the membrane simply as a dielectric slab of length d_mem, it acts as a Fabry-Pérot etalon with resonance wavelengths

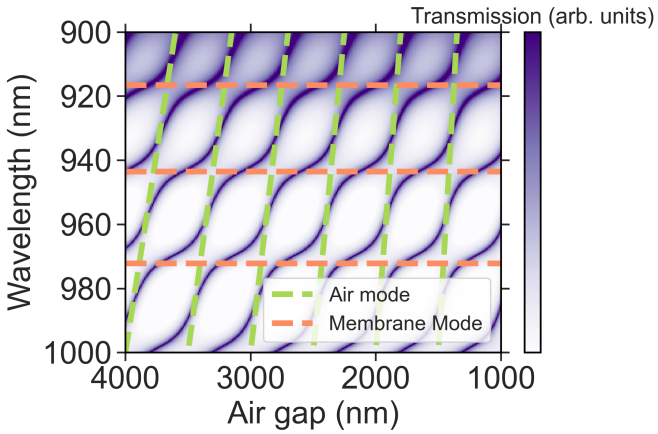

Figure 5.5.: The cavity dispersion of a membrane-cavity system can be understood as a coupling of air-like and dielectric like modes. The dispersion (purple) is obtained from a transfer matrix model. One observes an anti-crossing behavior between the air-like and dielectric-like modes.

$\lambda_u = \frac{2d_{mem}n_{mem}}{u}$, where u is the mode order of the etalon mode. The resonant wavelength is independent of the cavity air-gap. Figure 5.5 shows these two different resonance conditions, together with a simulated cavity dispersion of a full cavity-membrane system. The simulated cavity dispersion can be understood as a coupling between the pure air (green) and dielectric resonator modes (orange). Therefore, resonances that exhibit a steep dispersion are termed air-like, while resonances that exhibit a shallow dispersion are termed dielectric-like. These correspond to the low transmission and high-transmission cases in Figure 5.4, respectively.[1]

Field distribution in the cavity

We can further make use of the transfer-matrix model to study the field distribution inside the cavity for the case of an air-like and dielectric-like cavity mode. Figure 5.6 depicts the normalized absolute square of the electric field distribution along the cavity axis for the respective cases.
In the air-like case, the field inside the air-gap is enhanced compared to the field inside the membrane. Meanwhile in the dielectric-like case, the field is equally high inside the membrane and the air-gap.
Additionally, due to the boundary conditions, an air-like cavity mode possesses a field

[1]This is not necessarily the case, but depends on the details of the DBR mirror.

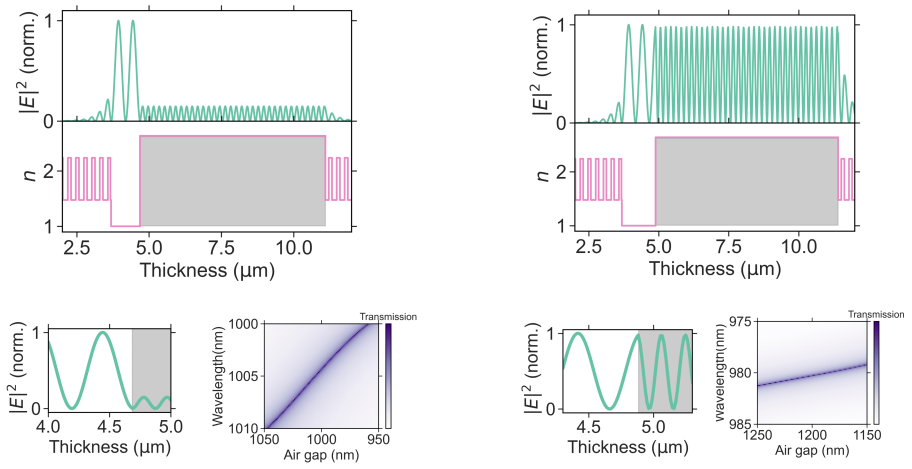

(a) Membrane air-like case

(b) Membrane dielectric-like case

Figure 5.6.: Top: Simulated intensity distribution for the two edge cases of an air-like (a) and a dielectric-like (b) cavity mode. The membrane is colored in gray. Bottom: Zoom of the field at the membrane surface, where the cavity field posses an node (antinode), respectively. Additionally, the local cavity dispersion is shown on the bottom right, which is steep for the airlike and shallow for the dielectric-like case.

node at the air-dielectric interface, while it showcases an anti-node for the dielectric-like case. This is shown in the insets of Figure 5.6.

Membrane Losses

As we have seen, the cavity field has a node (antinode) at the membrane surface for an air-like (dielectric-like) case. This directly affects the scattering loss the cavity experiences due to the membrane surface roughness. The loss is enhanced for the dielectric-like and suppressed for the air-like case. Taking the refractive index of air as $n_A = 1$, this can be described analytically as [229]:

$$S_{\text{mem}} = \sin^2\left(\frac{2\pi n_{\text{mem}} d_{\text{mem}} + \varphi}{\lambda}\right) \frac{(1+n_{\text{mem}})}{n_{\text{mem}}} (1-n_{\text{mem}})^2 \left(\frac{4\pi\sigma_{\text{rms}}}{\lambda}\right)^2, \tag{5.1}$$

where φ captures the relative phase due to the exit phase of the bare mirror coatings ($\varphi = 0$ if both mirrors are terminated by a high refractive index stack) and S_{mem} are the scattering losses at the membrane-air interface. Additionally, absorption losses inside the membrane occur according to Beer's law. They are described by:

$$A_{\text{mem}} = 1 - \mathrm{e}^{-2\alpha d_{\text{mem}}} \approx 2\alpha d_{\text{mem}}. \tag{5.2}$$

The intensity within the dielectric membrane compared to the air-gap can be derived by enforcing continuity conditions at the air-dielectric interface, yielding:

$$\frac{n_{\mathrm{mem}}E^2_{\mathrm{max,mem}}}{E^2_{\mathrm{max,a}}} = \left(\frac{1}{n_{\mathrm{mem}}}\sin^2\left(\frac{2\pi n_{\mathrm{mem}}d_{\mathrm{mem}}}{\lambda}+\varphi\right)+n_{\mathrm{mem}}\cos^2\left(\frac{2\pi n_{\mathrm{mem}}d_{\mathrm{mem}}}{\lambda}+\varphi\right)\right)^{-1}. \tag{5.3}$$

The absorption losses, and any other losses that occur within the membrane need to be rescaled by this factor. In the same manner one can rescale the bare planar mirror transmission by this factor to obtain the modulated transmission of the membrane-mirror stack.

Therefore, the total losses, which can be used to calculate the finesse as $\mathcal{F} = \frac{2\pi}{\mathcal{L}_{\mathrm{tot}}}$, read:

$$\mathcal{L}_{\mathrm{tot}} = T_{\mathrm{fiber}} + \frac{n_{\mathrm{mem}}E^2_{\mathrm{max,mem}}}{E^2_{\mathrm{max,a}}}\left(T_{\mathrm{mirror}} + A_{\mathrm{mem}} + S_{\mathrm{mem}}\right). \tag{5.4}$$

5.2.2. Calculation of the Purcell effect in a membrane

The figure of merit to maximize in our experiment is the Purcell factor. in this section, I will discuss how the mode hybridization influences the expected Purcell factor. It is convenient to use the formulation of the Purcell factor in terms of the mode volume V and the quality factor Q:

$$C_0 = \frac{3}{4\pi^2}\frac{\lambda^3}{n^3}\frac{Q}{V} \tag{5.5}$$

The effective quality factor can be extracted from a measurement of the cavity linewidth and the emitter linewidth, and their absolute wavelengths. This can be realized experimentally for the cavity linewidth by recording the cavity transmission while scanning a resonant laser over the cavity and monitoring the wavelength using a wavemeter. The mode volume is heavily dependent on the mode character of the cavity mode, since it is normalized to the intensity at the position of the emitter. As I discussed above, the relative intensity inside the membrane is significantly higher for a dielectric-like mode character. Again, I make use of the transfer matrix simulation to calculate the field distribution inside the resonator. Because the model is one-dimensional, it does not allow for a direct calculation of the mode volume. However, one can calculate an effective energy distribution cavity length, which captures the relative intensities, as:

$$L_{\mathrm{eff}} = \frac{\int n(z)^2|E(z)|^2dz}{\max(n(z)^2|E(z)|^2)}, \tag{5.6}$$

where care is taken that the denominator is evaluated inside the SiC membrane, corresponding to the maximal intensity for an emitter positioned in a field antinode. From this effective length, the mode volume V can be calculated as:

$$V = \frac{\pi w_0^2}{4} L_{\text{eff}}, \tag{5.7}$$

recovering the well-known formula for a FP cavity (Equation 2.17), which in this situation depends on the effective energy distribution cavity length L_{eff}. Additionally, the mode waist w_0 is also affected by refraction of the mode at the dielectric interface. It can be calculated by matching two Gaussian beams inside the membrane and inside the air-gap at the interface [229]. This yields:

$$w_{0,d} = \sqrt{\frac{\lambda_0}{\pi}} \left(\left(d_a + \frac{d_{\text{mem}}}{n_{\text{mem}}} \right) \left(R_{\text{c}} - \left(d_a + \frac{d_{\text{mem}}}{n_{\text{mem}}} \right) \right) \right)^{\frac{1}{4}} = \sqrt{\frac{\lambda_0}{\pi}} \left(L' \left(R_{\text{c}} - L' \right) \right)^{\frac{1}{4}}. \tag{5.8}$$

L' is a geometric length which allows to rewrite the beam waist formula in the same form as for a homogeneously filled cavity (see Equation 2.18) and is defined as:

$$L' = d_a + \frac{d_{\text{mem}}}{n_{\text{mem}}}, \tag{5.9}$$

not to be confused with the effective energy length defined above. One can see that the influence of the dielectric like membrane on the waist is reduced compared to that of the air gap by a factor of $\frac{1}{n_{\text{mem}}}$.

5.2.3. Membrane fabrication

I investigate two different SiC membranes in this thesis, henceforth labeled Membrane A and B (see Appendix A). Both samples were fabricated by Jonathan Körber at University of Stuttgart. I will briefly summarize the fabrication procedure. For a more detailed description, the reader is referred to [192] or Jonathan Körbers doctoral thesis[1].

- The starting material for the membrane is a high quality, roughly 10 µm thin, epitaxially grown monolayer (epilayer) of SiC, which is grown on commercial wafer cut along the crystallographic a-plane [2].
- The sample is thinned down to a thickness of $d \approx 40\,\mu\text{m}$ to 60 µm using a chemical-mechanical polishing technique.

[1] Not yet published
[2] The epilayer was grown by Misagh Ghezellou in the group of Prof. Jawad Ul-Hassan at Linköping University.

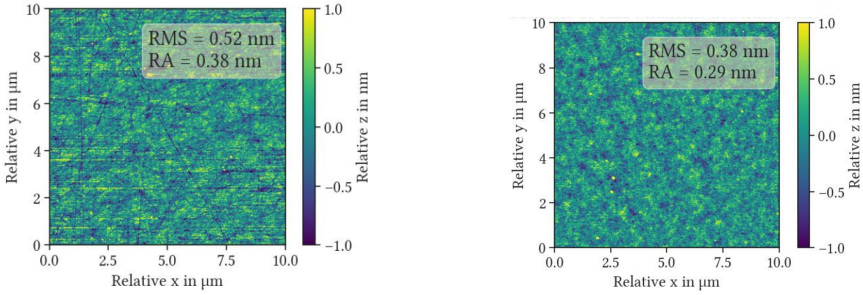

(a) Before etching.

(b) After etching.

Figure 5.7.: Measured height map of representative spots on the membrane recorded using an AFM. The root mean square (RMS) and arithmetic average (RA) surface roughness calculated over the entire map is shown in the inset and typically below 0.4 nm. Maps were recorded and provided by Jonathan Körber.

- The epilayer side of the sample is van der Waals bonded to a planar DBR mirror with a design transmission of $T = 230\,\text{ppm}$ at $\lambda = 985\,\text{nm}$ (The coating is described in section 2.2.2).
- The sample is thinned down to the final membrane thickness of 4 µm to 8 µm using a reactive ion etching technique. Thereby, only the high-quality epilayer part of the sample remains and forms the membrane. For membrane B, a mask is used during the etching to prevent damage to the membrane, such as etching pits and so-called micromasking.

A microscope image of Membrane B is depicted in Figure 5.3. After the fabrication, the surface quality is characterized using an atomic force microscope (AFM). Representative AFM images are depicted in Figure 5.7. The observed root mean square surface roughness is typically on the order of $\sigma_{\text{rms}} = 0.4\,\text{nm}$, corresponding to maximal scattering losses of 30 ppm, assuming a field anti-node at the interface.

5.2.4. Characterization of the cavity-membrane system

I assemble the cavity in a setup similar to the one described in 3.2.2. The cavity stage is located inside a closed-cycle cryostat[1]. The cavity mechanics and electronics were built up by my colleague Maximillian Pallmann. Details on the design and characterization can be found in his PhD thesis and in [86]. I exchanged the fiber mirror, sample mirror

[1]Cryostation, *Montana Instruments*

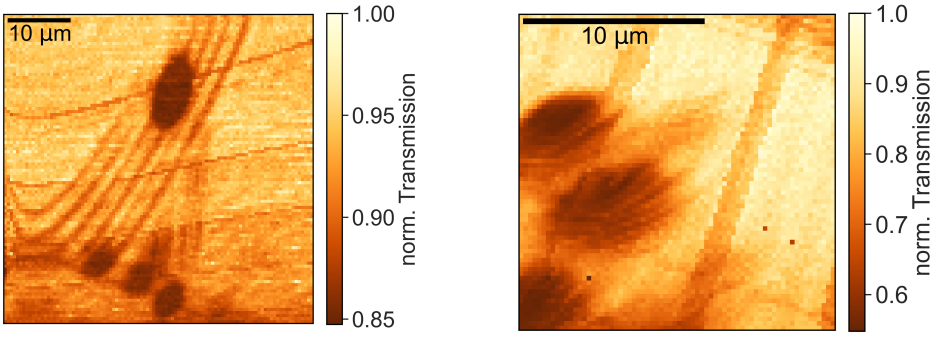

(a) Membrane A **(b)** Membrane B

Figure 5.8.: Exemplary cavity transmission scans on Membrane A and B. Stripes are scan artifacts that appear due to tilt when moving the fiber. Scalebar is estimated from the feature size of the observed defects.

and rebuilt the collection optics in order to be compatible with NIR wavelengths. Additional information about the optical and mechanical setup can be found in Appendix C. The assembled cavity is formed by the planar mirror with a DBR coating with a design transmission of $T = 230\,\text{ppm}$ at $\lambda = 985\,\text{nm}$, to which the SiC membrane is bonded, and a fiber mirror with a design transmission of $T = 25\,\text{ppm}$ at $\lambda = 985\,\text{nm}$. Due to the effects discussed in Section 5.2.1, the cavity losses heavily depend on the mode character, as we will see in the following.
The cavity was characterized, using a probing laser[1] with a wavelength between 940 nm to 985 nm. As a first characterization step, I perform scanning cavity transmission microscopy (see Section 3.2.2 for an explanation of the measurement technique). Exemplary transmission scans are depicted in Figure 5.8. I typically observe homogeneously bright areas with localized defects stemming from the fabrication. Notably, I do not notice a strong modulation of the transmission in the scan region, which would be expected if the mode composition changes significantly due to a varying membrane thickness [230]. This indicates that the membrane thickness typically varies significantly less than $\Delta d = \frac{\lambda}{4n} \approx 90\,\text{nm}$ over an area of roughly $40\,\mu\text{m} \times 40\,\mu\text{m}$.

Birefringence

The birefringence of silicon carbide [233] manifests itself in two different mode families with orthogonal polarization corresponding to the ordinary and extraordinary refractive index. For a given wavelength and position, the measured finesse and transmitted

[1] *Velocity TLB-6719*, Spectra-Physics

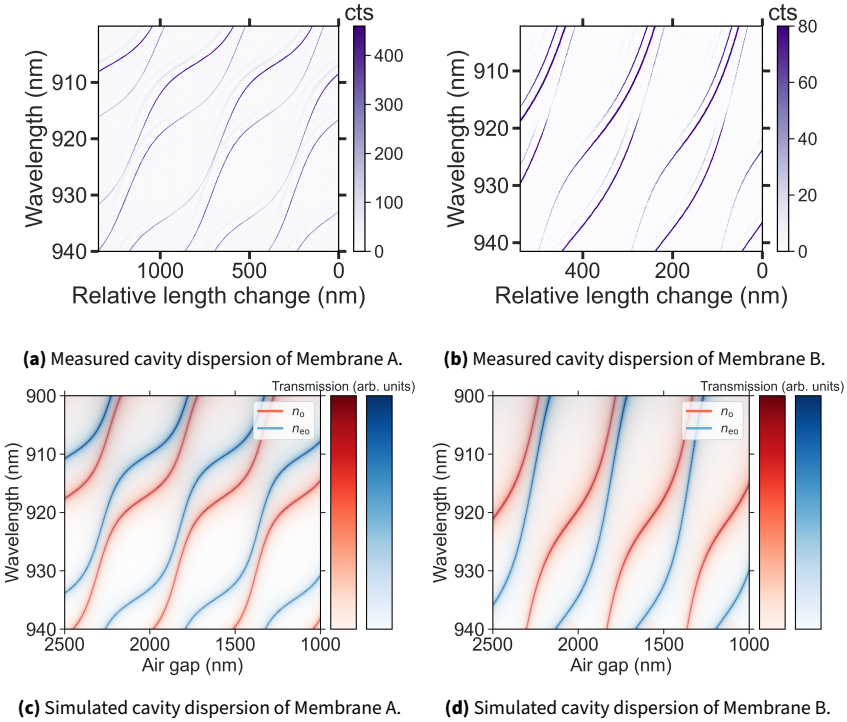

(a) Measured cavity dispersion of Membrane A.

(b) Measured cavity dispersion of Membrane B.

(c) Simulated cavity dispersion of Membrane A.

(d) Simulated cavity dispersion of Membrane B.

Figure 5.9.: Simulated and measured cavity dispersion for two SiC membranes A and B. The extracted membrane thicknesses are $d_A = 6.2\,\mu m$ and $d_B = 2.85\,\mu m$. Reproduced from [192].

intensity is significantly different between the two mode families. This is because their mode composition is different due to the different optical path length in the membrane. Since the birefringence is a much stronger effect than any other polarization dependent effect, it fully determines the polarization mode splitting. For some measurements, the additional resonances are confusing and may prevent automated data evaluation. One mode family can be suppressed by either adjusting the polarization of the probing beam or filtering the transmitted light using a polarization filter. This unambiguously confirms the origin of the two mode families.

Cavity Dispersion

In order to study the cavity-membrane system and extract the membrane thickness, I measure the cavity dispersion. Therefore, I couple a broadband light source[1] to the cavity and record the transmission spectrum using a spectrometer for varying cavity lengths. An exemplary dispersion measurement for two membranes with two different thicknesses are depicted in Figure 5.9. We observe the anti-crossing behavior characteristic for the hybridization between air-like and dielectric-like cavity modes. The two mode families corresponding to the two refractive indices can be identified. The same mode families possess the same local slope for a given wavelength. For both measurements, higher order modes are visible as faint, slightly offset traces. The periodicity between the dielectric- and air-like mode character in wavelength is larger for Membrane B than Membrane A. This indicates that Membrane B is thinner than Membrane A[2].
In order to model this more precisely and extract the membrane thickness, I again make use of the transfer matrix model code used to simulate the DBR mirror coatings. This allows to simulate the cavity dispersion for different membrane thicknesses. The simulated cavity membranes are depicted in Figure 5.9 (c) and (d). Clearly, we observe a good agreement of the simulated dispersion with the measured cavity dispersion, confirming the suitability of our model. The best agreement with the measured cavity dispersion is obtained for thicknesses of $d_\mathrm{A} = 6.2\,\mu\mathrm{m}$ and $d_\mathrm{B} = 2.85\,\mu\mathrm{m}$ for Membrane A and B respectively. These values are within the expected range for thickness measurements conducted after the fabrication, using a profilometer and a white-light interferometer.

Finesse

I measure the finesse at different wavelengths, and observe finesse values as large as $\mathcal{F} = 40\,000$. Notably, this value is twice as high as the highest finesse values observed for the same coating combination without the membrane. This is explained by the increased mirror reflectivity for an air-like cavity mode character, as discussed in Section 5.2.1.
In order to study this effect in more detail, I measure the finesse as a function of the probing wavelength at a clean mirror position for both polarization modes. The resulting wavelength dependent finesse is depicted in 5.10. One clearly observes the strong modulation caused by the varying mode composition. To extract the losses introduced by the membrane, I fit a full model based on the expected mode dependent losses given by Equation 5.4 to the data.
The result is depicted in Figure 5.10 (b). The refractive index was calculated using Sellmeyer equations with the coefficients reported in [233]. These values are fixed for the fitting procedure, which leaves the rms surface roughness σ_rms, the membrane thickness and the additional losses scaled with the relative mode character as free parameters. The fits yield a surface roughness of $\sigma_\mathrm{rms} = (720 \pm 30)\,\mathrm{pm}$ ($\sigma_\mathrm{rms} = (580 \pm 60)\,\mathrm{pm}$)

[1] Amplified spontaneous emission (ASE) background of a diode laser.
[2] Just like a longer FP-resonator has a smaller free spectral range.

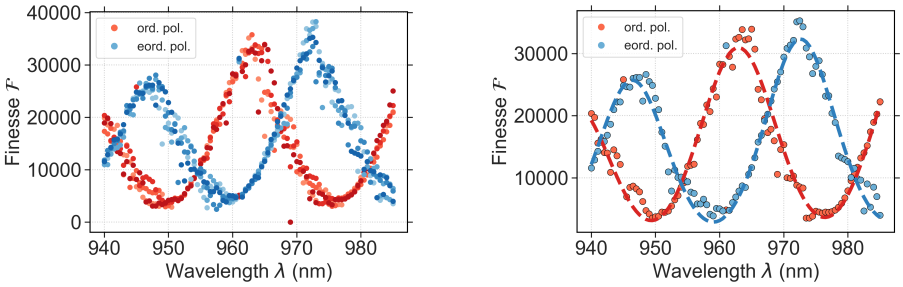

(a) Wavelength dependent finesse for both polarization modes.

(b) Fit of a full loss model to the wavelength dependent finesse.

Figure 5.10.: Wavelength dependent finesse for both polarization modes. (a) Shows the finesse of four consecutive longitudinal mode orders (light to dark points) per polarization mode and wavelength step . (b) A full loss model is fit to an exemplary set of data per polarization branch and shows good agreement with the data. (a) Reproduced from [192].

and additional losses weighted by the relative field intensities of $E = (215 \pm 7)$ ppm ($E = (211 \pm 15)$ ppm) for the two polarization modes, showing good agreement between the two datasets. The extracted surface roughness is slightly higher than the values measured with an AFM ($\sigma_{\mathrm{rms}} = 400$ pm to 500 pm), which might be due to a locally slightly increased surface roughness. Another possible explanation are additional scattering losses at the mirror-dielectric interface.
The additional losses of 200 ppm that scale with the mode character can be ascribed to a mix of absorption and effects due to the wavefront curvature of the cavity mode at the membrane interface [232]. Another possible reason could be additional scattering centers within the membrane, possibly created by the electron irradiation.
The membrane thicknesses extracted from the fit are $d = 7.03\,\mu$m and $d = 7.10\,\mu$m. This indicates that the literature values for the refractive index used in the simulation (taken from [233]) do not perfectly describe the system. This is not surprising, as we expect additional strain in the membrane due to the bond to the mirror, which can affect the refractive indices. Both obtained values are slightly thicker than the value $d = 6.2\,\mu$m extracted from the dispersion measurement depicted in Figure 5.9 (a), which was performed on the same membrane. I ascribe this to the fact that the measurements were performed at different positions on the membrane. A variation of the membrane thickness of 1 µm over the lateral extent of the membrane is plausible.
In these measurements, the system was probed around the center of the mirror coating stop-band, due to the availability of a far tuneable laser system. The V2 center ZPL lies around 917 nm. The finesse measured at this wavelength was up to $\mathcal{F} = 10\,000$, depending on the mode character, which varies between different spots on the membrane due to variations in the membrane thickness.

In summary, I extensively studied the cavity-membrane system. I find a high homogeneity of the sample and high finesse values exceeding $\mathcal{F} = 40\,000$, twice as high as for the system without a membrane. This shows that the SiC material platform is excellently suited for the integration as a membrane into an open resonator platform. The birefringence of SiC leads to two families of modes with distinct polarizations. I model the cavity membrane system using a transfer-matrix model and find excellent agreement with the measurements. Having established that the cavity-membrane system performs exceptionally well, I now turn to investigate the properties of the color centers in the membrane.

5.2.5. Color center characterization

Implantation

There are multiple strategies to create the desired color centers, which offer different degrees of control over defect density, lateral and depth position, and damage introduced to the crystal. Initially, we utilized an ion beam of ^{4}He to create defects [1]. This allowed to create single defects at predetermined lateral positions at a desired depth. However, we observed the creation of many fluorescing defects during the etching fabrication step. Therefore, the comparably low defect density utilized here was too low for cavity experiments.
Therefore, we subsequently made use of electron beam radiation. The sample is exposed to an electron beam with an average electron kinetic energy of 5 MeV and a fluence of $\approx 1.4 \times 10^{13}\,\mathrm{cm}^{-22}$. This leads to a higher color center density, which makes it harder to address single defects within an optical cavity, but makes the initial search easier. As we will see in the following, the observed emitter density is, depending on the membrane thickness, well suited for single color center experiments. Usually, samples are annealed after implantation or irradiation, in order to heal some damage introduced in the crystal and thereby reduce spectral diffusion of the defects. This was done for sample B, which was irradiated before bonding it to the mirror. Sample A was already bonded to the mirror before the electron irradiation, and therefore not annealed [3]. It should be noted that electron irradiation due to the low interaction cross-section creates defects with an equal likelihood at every depth of the membrane. Therefore, we expect a large variation in the emitter-cavity coupling, dependent on whether the emitters are located at a cavity field node or antinode.

[1] The ion beam implantation was done by Georgy Astakhov at Helmholtz-Zentrum Dresden-Rossendorf.
[2] The electron irradiation was carried out by Wolfgang Knolle at the Leibniz-Institute of Surface Engineering.
[3] Technically, we also tried to anneal a sample that was already bonded to the mirror. The result was not pretty. It turns out that DBR coatings start to delaminate around $T = 200\,^\circ\mathrm{C}$, causing the membrane to burst in many fragments.

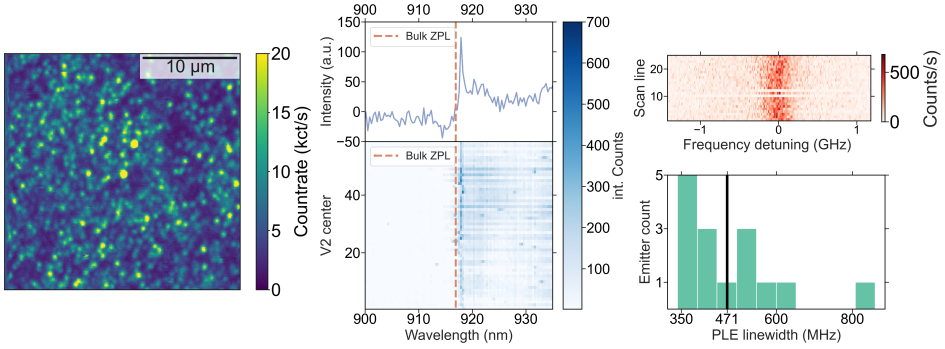

(a) Confocal image of Membrane A. **(b)** PL spectrum of multiple V2 centers **(c)** PLE measurement of V2 centers

Figure 5.11.: Characterization of Membrane B in a confocal microscope. (a) Exemplary confocal scan of Membrane B, showcasing a high emitter density. (b) Exemplary (top) and stacked (bottom) PL spectra at cryogenic temperatures, showcasing an offset of 1 nm of the ZPL wavelength. (c) Exemplary cryogenic PLE scans of a single emitter (top) and statistical distribution of extracted ZPL linewidths for 14 investigated color centers (bottom). The mean linewidth observed is (471 ± 132) MHz. Measurements were conducted by Jonathan Körber. I assisted for the cryogenic measurements. Adapted from [192].

Confocal Microscopy

In order to get a feeling for the emitter density created by the electron irradiation, room temperature confocal microscopy was carried out at the University of Stuttgart by Jonathan Körber. A typical confocal image is depicted in Figure 5.11 (a). As can be seen from the images, the emitter density is quite high. Notably, we observed during one fabrication run, where confocal microscopy was carried out before and after the etching of the membrane, that many of these defects seemed to appear during the etching process. Therefore it is unlikely that all of the observed point-like defects are V2 centers. In order to get a feeling the V2 center density, we followed a two-step characterization process:

1. The polarization of the emitted light is checked by comparing the countrates on two detectors after a polarizing beam splitter. The polarization is adjusted beforehand on a "verified" V2 center, such that the countrate is equal on both detectors. Since the V2 centers emission dipole is always oriented along the crystallographic c-axis, this is a signature of V2 centers.
2. The potential candidates identified in the first step were checked for a characteristic optically detected magnetic resonance (ODMR) signal at the characteristic electronic ground state splitting of 70 MHz.

Using this method, we found that of 14 preselected pointspread limited fluorescent spots, eight showed a characteristic ODMR signal. If we consider that the lateral extent of the optical cavity mode is a factor of $\left(\frac{w_{\text{cav}}}{w_{\text{conf}}}\right)^2 \approx \left(\frac{1.42\,\mu\text{m}}{0.46\,\mu\text{m}}\right)^2 \approx 10$ larger than that of the confocal microscope, we expect there to be at least one V2 center inside the cavity mode on average for such a dense sample. This is not a bad density to start with, since it makes it easier to spatially locate and screen emitters, as we will see later on. Note that the confocal measurements were conducted on the thicker Membrane A ($d = 6.2\,\mu\text{m}$). We therefore expect half the V2 center density for Sample B ($d = 2.8\,\mu\text{m}$).

Cryogenic characterization and determination of optical linewidths

In order to characterize the optical properties of the V2 centers inside the membrane, cryogenic PL and PLE measurements were conducted on Membrane A. The measurements were carried out at the University of Stuttgart together with Jonathan Körber. Photoluminescence spectra of pre-selected centers were taken at a temperature of $T = 8\,\text{K}$. The obtained PL spectra are depicted in Figure 5.11 (b). All investigated centers showed the characteristic ZPL around 917 nm. However, for this sample we observed that the mean center frequency was slightly shifted to longer wavelengths ($\lambda_{\text{ZPL}} = 917.5\,\text{nm}$) compared to the typically observed center frequency in bulk centers $\lambda = 916.5\,\text{nm}$. This may indicate a global strain in the membrane, possible due to the bonding to the DBR mirror.
In order to determine the homogeneous linewidth, PLE measurements were performed. Care has to be taken to avoid optical pumping into the unprobed spin level during the excitation. In order to avoid this, a second frequency tone of the resonant excitation laser was created using AOMs. The second tone is offset by 1 GHz and therefore resonant with the second spin-allowed optical transition, ensuring that both optical transitions are driven simultaneously and therefore avoiding optical pumping. However, this might slightly broaden the observed optical linewidths compared to a single frequency scan. The homogeneous linewidth was determined this way for 15 different emitters. The result is depicted in Figure 5.11 (c). The mean observed linewidth is $(471 \pm 132)\,\text{MHz}$. Significant contributions from power broadening and temperature broadening were excluded by conducting temperature and power dependent measurements. The observed linewidths are a factor of ≈ 20 times larger than the Fourier transform limited linewidth of $\Gamma_{T_1} = 22\,\text{MHz}$. Certainly, the membrane thickness of $d = 6.2\,\mu\text{m}$ can have an influence on the linewidth due to the proximity of the emitters to the surface. However, previous studies have shown optical linewidths below 150 MHz in similar membranes with thicknesses below $d = 1\,\mu\text{m}$ [228, 234]. Possible reasons could be the missing annealing step after electron irradiation, variations in the sample purity, or be related to strain, as possibly indicated by the shift of the ZPL center frequency. The additional broadening certainly poses a limit for experiments that require a high degree of photon indistinguishability such as quantum communication protocols. However, the linewidth is smaller or comparable to the expected cavity linewidth of the resonator. Therefore,

at least the demonstration of cavity enhancement is not expected to be limited by the additional broadening of the emitters. At the same time, the encouraging results on small linewidths in thin membranes show that while the linewidths in this sample might limit applications, this problem is not intrinsic to the defect or platform and can be solved by optimizing the fabrication process. Finally, it is worth to note that due to time constraints, we only investigated membrane A in this setup, while many of the measurements presented in the following were conducted on the thinner membrane B, which also was fabricated from a different batch of starting material. The fabrication process was also slightly altered, for example the sample was subjected to an additional annealing step after the electron irradiation, which is expected to improve the optical transition linewidth.
In summary, we have seen that the produced membranes are exceptionally well suited to integrate them into optical cavities. We have also studied the properties of the created emitters and found a suitable V2 center density and reasonably narrow optical transition, which should not limit the expected Purcell enhancements significantly for the expected cavity parameters. Equipped with this knowledge, we now turn to study the emitter properties within the optical cavity.

5.3. A single color center coupled to an optical cavity

Cavity fluorescence experiments rely on Purcell enhancing the zero phonon line. In order to achieve a sufficiently large Purcell enhancement, the ZPL needs to be smaller than the cavity linewidth (compare Chapter 2.3.1). Therefore, cavity-enhanced spectroscopy of V2 color centers requires cryogenic temperatures. The cavity setup is mounted in a closed-cycle cryostat with a nominal base temperature of $T = 2.5\,\mathrm{K}$. Due to the large thermal mass of the cavity setup, the minimal base temperature achieved is $T = 8\,\mathrm{K}$. We measure the temperature at the copper mirror holder, which is the closest to the sample, to be $T_{\mathrm{sample}} = 16.5\,\mathrm{K}$ at the lowest. This is principally sufficient for experiments with V2 centers. However, the sample mirror is clamped from the backside, which is why the sample is still isolated from the mirror holder by the few millimeter thick mirror. For the experiments presented in the following, we therefore added a copper strip thermally connecting the SiC membrane with the sample holder. However, we are not able to measure the temperature directly at the sample. Consequently, the color centers might experience additional broadening due to temperature. I will return to this question when discussing the measurement results.
When cooling down the cavity setup, the fiber mirror position in relation to the membrane changes as the many materials involved contract. To avoid crashing of the fiber mirror into the sample, the cavity resonances are monitored and the cavity length is adjusted using DC motors. Lateral drifts also occur during the cooldown, but are generally not problematic, since the membrane shows an excellent homogeneity. It just precludes a precise pre-characterization at room temperature, since one ends up at a different location on the membrane at cryogenic temperatures.

At cryogenic temperatures, we observe clean spots on the mirror where we also measure finesse values comparable to the high values observed at room temperature for an air-like cavity. Spatially locating emitters solely by their fluorescence is experimentally challenging, although possible [222]. Due to the high emitter density in our sample, I choose to position the cavity on the clean spots where the cavity performs well and check for emitter fluorescence. For strongly coupling emitters that warranted further investigation, the spatial overlap was manually optimized by observing the countrate at different spatial positions.

5.3.1. Cavity assisted spectral resolution of emitters

In order to investigate the color center fluorescence, I off-resonantly excite the emitters by coupling a laser at a wavelength of 785 nm into the fiber mirror. The mirror coating is almost transparent at this wavelength, which means that excitation light is present in the cavity for all cavity lengths. Due to the residual reflectivity, a small modulation of the transmission is nevertheless observed when scanning the cavity length. I account for this by referencing power dependent measurements on the transmitted excitation intensity. I use two different lasers depending on the experiment: A continuous-wave diode laser emitting at 785 nm[1], and a pulsed super-continuum source[2] which is spectrally filtered using an acousto-optic tuneable filter (AOTF)[3]. The excitation light is subsequently spectrally filtered using optical long-pass filters, and guided onto either a spectrometer or two single photon counting modules arranged in a Hanbury-Brown-Twiss (HBT) configuration. More information of the measurement setup can be found in Appendix C. When the cavity is non-resonant with any sharp ZPL, I observe a weak, broadband background fluorescence. This allows probing of the cavity transmission spectrum using a spectrometer, just as I have done when characterizing the cavity-membrane dispersion in Section 5.2.4. An exemplary measurement is depicted in Figure 5.12 (a). When varying the cavity length, I again observe the characteristic dispersion features, revealed by a spectrally broad background fluorescence.

In addition, one observes bright and spectrally narrow features for specific cavity lengths and therefore specific resonance wavelengths. This is due to the cavity Purcell enhancing the ZPL emission, which is fully scattered into the optical cavity mode and can therefore be collected efficiently. Many of them are clustered in the spectral region of 916 nm to 920 nm, where the V2 center ZPL is expected. Notably, the measurements show that only one mode family couples to the V2 color centers. This is explained by the fact that the optical dipole transition of the V2 center is oriented along the crystallographic c-axis, as is the extraordinary refractive index principal axis. Conversely, this means

[1] DBR785s, *Thorlabs*.
[2] SuperK Fianium, *NKT Photonics*.
[3] SuperK Select, *NKT Photonics*.

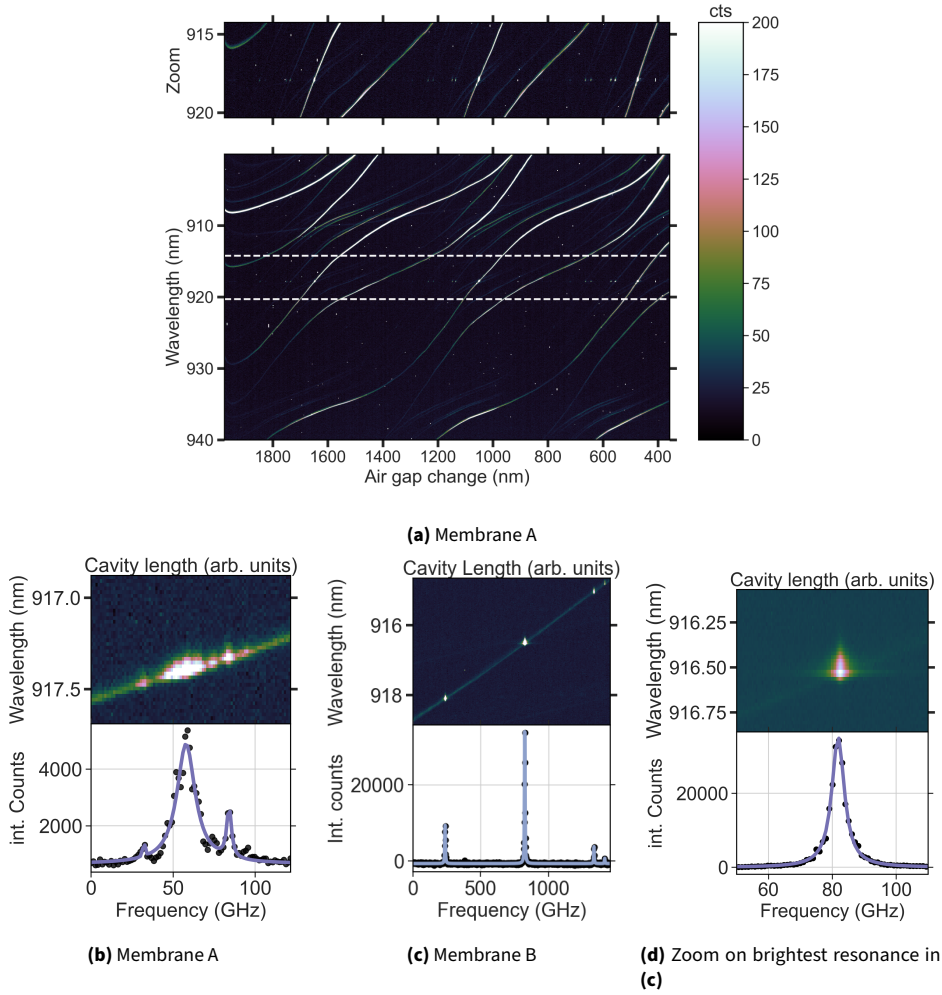

Figure 5.12.: (a) Under off-resonant excitation, a broadband background from the sample reveals the cavity dispersion. When individual emitters with sharp optical features are resonant with the cavity, they appear as bright spots in the dispersion, due to the Purcell effect. Noticeably, only the extraordinary refractive index mode couples to the ZPLs around 917 nm. (b) and (c): By integrating the spectrum along the wavelength axis and interpolating the local cavity dispersion, the spectral structure of the defects is extracted. (d) Zoom on the brightest peak in (c), showing the excellent fit by a single Lorentzian. Adapted from [192].

Table 5.1.: Fit results of the resonances depicted in Figure 5.12 (b) measured in Membrane A. Peaks are labeled left to right. σ_{FWHM} is the uncertainty of the fit.

Peak Number	FWHM (GHz)	σ_{FWHM} (GHz)	Intensity (int. Counts)
1	13.6	0.7	4200
2	3.3	0.8	1800

Table 5.2.: Fit results of the resonances depicted in Figure 5.12 (c) measured in Membrane B. Peaks are labeled left to right. σ_{FWHM} is the uncertainty of the fit. Spectral resolution is limited by the cavity linewidth of $\Delta_{\nu,\mathrm{cav}} = 3.44\,\mathrm{GHz}$.

Peak Number	FWHM (GHz)	σ_{FWHM} (GHz)	Intensity (int. Counts)
1	4.88	0.11	10400
2	4.84	0.03	35200
3	3.94	0.23	5000
4	3.79	0.68	1400

that there is an ideal dipole overlap with the color centers transition dipole, which otherwise would reduce the Purcell effect. Therefore, the strong birefringence, which fully determines the polarization axis of the cavity, inherently ensures an optimal dipolar overlap with the emitter. This a clear advantage over comparable platforms, such as color centers in diamond. There, the polarization splitting of a fiber cavity is determined by the mirror asymmetry and possibly strain inside the membrane. In-situ adjustment of these influences is experimentally challenging, usually leading to a non-ideal overlap of the cavity polarization axis with the emitter dipole, reducing the Purcell effect.

Determination of emitter linewidth

In order to further characterize the spectral properties of the emitter, I performed highly resolved dispersion scans on promising features. Exemplary measurements are depicted in 5.12 (b) and (c). Because the cavity dispersion is revealed by the broad background fluorescence, we can use the local dispersion to calibrate the applied piezo voltage in terms of resonance frequency shifts by fitting the local dispersion with a linear slope. Applying this calibration and integrating all spectrometer counts for each voltage position leads to a spectrum of the observed emitters. Crucially, the spectral resolution of the so-obtained spectrum is not limited by the spectral resolution of the spectrometer, but instead only by the cavity linewidth. Multiple narrow spectral features are seen in both dispersion measurements. However, we observe a stark contrast between Membrane A and B. The emitters in Membrane A are spectrally close to each other, within a range of $\Delta\nu \approx 100\,\mathrm{GHz}$. The individual emission lines of the V2 centers are overlapping, and the

most pronounced central peak is broad and shows some substructure, indicating that it is made up of multiple zero-phonon lines. On the other hand, for Membrane B, we observe spectrally narrow peaks that are distributed over a large frequency range of roughly $\Delta\nu = 1300\,\mathrm{GHz}$. This can be explained by the substantially thinner membrane ($d_\mathrm{A} = 6.2\,\mu\mathrm{m}$, $d_\mathrm{B} = 2.85\,\mu\mathrm{m}$). For one this reduces the probed volume and we consequentially on average expect half the amount of color centers within the cavity mode. Previous studies have shown that the spectral spread increases for thinner membranes, presumably due to the proximity to surfaces and additional stress in the membrane [228]. For the experimental investigation of single color centers, a more sparse distribution as observed in Membrane B is advantageous, since it allows to unambiguously select individual features using the spectral resolution capability of the cavity.
The measured spectra are fit with a series of Lorentzian peaks. The resulting FWHM widths are summarized in Tables 5.1 and 5.2. The values for Sample B are more reliable because there the individual peaks are well resolved and do not overlap. For this sample, the mean linewidth observed is 4.35 GHz. The difference between the highest and lowest measured value is more than 1 GHz. This can be an indication that some broadening contribution stems from the emitter linewidth and not solely the cavity linewidth. However, systematic errors such as cavity drifts might also explain this difference.

Influence of the cavity linewidth

Because the cavity linewidth is limiting the spectral resolution power, I measure the cavity linewidth for Membrane B by scanning a resonant laser over the cavity linewidth and recording the transmission while monitoring the laser wavelength using a wavemeter [1]. Exemplary scans are depicted in Figure 5.13. The mean linewidth calculated from 12 scans at a speed of 6.4 GHz/s is $(3.44 \pm 0.05)\,\mathrm{GHz}$. With this scan speed the cavity linewidth is probed on a few second time scale, and the measurement is therefore sensitive to cavity length fluctuations and drifts that occur on smaller timescales. This is comparable to the timescale on which the color center resonances are sampled in the spectrometer dispersion measurements in Figure 5.12. The extracted linewidths are therefore similarly broadened due to cavity length fluctuations and drifts. This indicates that the linewidths observed in the spectral measurements are not entirely limited by the cavity, but experience some additional broadening from the emitter. Because the convolution of a Lorentzian with FWHMs $\Delta\nu_1$ and $\Delta\nu_2$ is again a Lorentzian with FWHM $\Delta\nu_1 + \Delta\nu_2$, this would correspond to emitter linewidths between 0.4 GHz and 1.5 GHz. This is not entirely unreasonable, when we consider that the local temperature at the sample might be elevated. It is also worth to note that the confocal linewidth measurements were conducted on Sample A, which is more than twice as thick, and might therefore host defects with narrower optical linewidths. Finally, the fiber is brought into contact with the membrane during the measurement in order to reduce cavity length fluctuations. We

[1] 671 Series, *Bristol Instruments*

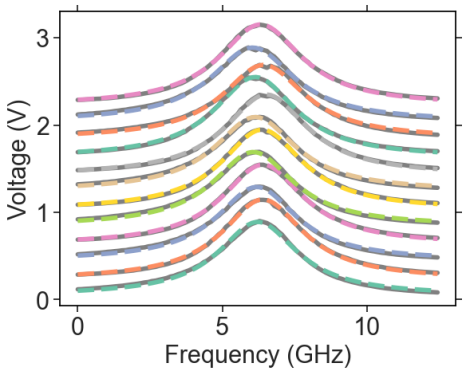

Figure 5.13.: Cavity linewidth measurement by scanning a resonant laser over the cavity linewidth (Scanspeed = 0.1 Hz). Scans are manually offset to each other. Colored lines are single Lorentzian fits to the measurement. The average cavity linewidth is (3.44 ± 0.05) GHz. Reproduced from [192].

suspect that this can introduce additional charge fluctuations on the membrane surface due to residual charges on the fiber.

In summary, I have investigated the spectral properties of the color centers in two SiC membranes of different thicknesses. We have found that the spectral distribution of ZPLs is narrow for the thicker Membrane A, while Membrane B shows a more sparse distribution which is spread over a larger spectral range. We also observe that the ZPLs of the V2 center only couple to the extraordinary refractive index axis, in accordance with the expectations. The spectral width of the color centers ZPL is in the range of 0.5 GHz to 1.5 GHz, indicating some additional broadening compared to the cryogenic PLE measurements discussed in Section 5.2.5.
In the next section, we now investigate the properties of individual narrow spectral features. From now on, I will focus on Membrane B, since the signals are stronger and the individual lines are well resolved.

5.3.2. Verification of single photon emission

Membrane B shows well-isolated emission lines, that are well fit by a single Lorentzian. This indicates that these features correspond to the ZPL of a single color center. In order to verify this, one needs to make use of photon statistics, which can be recorded using the HBT setup in the detection path. I will very briefly explain the concept, following Fishman et al. [235].

Second order intensity function

The second-order intensity correlation function, or auto-correlation function, is defined as:

$$g^{(2)}(\tau) = \frac{\langle I(t)I(t+\tau)\rangle}{\langle I(t)\rangle^2} = \frac{\left\langle a^\dagger(t)a^\dagger(t+\tau)a(t+\tau)a(t)\right\rangle}{\left\langle a^\dagger(t)a(t)\right\rangle\left\langle a^\dagger(t+\tau)a((t+\tau)\right\rangle} \tag{5.10}$$

$$= \frac{\left\langle N_{1,2}(t,\tau)\right\rangle}{\langle N_1(t)\rangle\langle N_2(t)\rangle}. \tag{5.11}$$

Here, brackets $\langle\rangle$ indicated a time average, and I is the light intensity. By assuming a single mode incident on the detector $g^{(2)}(\tau)$ can be written as a product of annihilation operators a and creation operator $a^\dagger$. Finally, it can be expressed in terms of the number of detected photons N_i at either detector and the number of coincidences $N_{1,2}(\tau)$ at delay time τ.
$g^{(2)}(\tau)$ measures the probability to detect a photon at a time delay τ, given that a photon was detected at a time $\tau = 0$. From this, information about the photonic quantum state and its corresponding photon statistics can be extracted. A coherent state, which describes for example laser emission, exhibits a Poissonian photon statistics in the Fock state basis $|n\rangle$, and is characterized by a "flat" autocorrelation function $g^{(2)}(\tau) = 1$. In contrast, a single photon Fock state $|1\rangle$, which is characteristic for a single emitter, is characterized by a dip at zero time delay $g^{(2)}(0) = 0$. The temporal shape of the dip depends on the detailed rate dynamics of the photon source, and careful analysis of this can reveal a lot of information about these dynamics, especially when there are more than two levels involved [236]. In many quantum optics experiments, it is simply used as a verification that the emission stems from a single emitter, when the auto-correlation dips below $g^{(2)}(0) < 0.5$ at zero time delay [1].

The second order auto-correlation is usually measured in a HBT type setup, were the incoming light is split in equal parts on a beam splitter and guided onto a single photon counter each. The electronic pulses signals from both detectors are analyzed using time-correlation electronics[2], which can record the timestamps of the incoming pulses with high accuracy, and also calculate the second order auto correlation in real time. It is not strictly necessary to use two detectors in every case, and rather a way to circumvent a technical limitation: The single photon detectors have a certain dead-time (typically 40 ns to 50 ns for our detectors), where no event can be detected after a previous detection event. For many quantum optical systems, the characteristic timescales are on the order of a few nanoseconds, such that a single detector can not fully resolve the

[1] This not a strictly sufficient criterion. There are some cases, for example for two emitters of different brightness, that can also lead to a autocorrelation value $g^{(2)}(0) < 0.5$ [235]. This is however mostly relevant in fringe cases, e.g. when $g^{(2)}(0)$ is close to 0.5.
[2] TimeTagger, *Swabian Instruments*

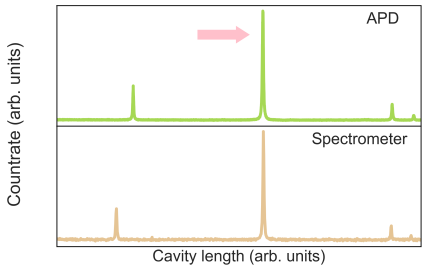

Figure 5.14.: Comparison of emitter spectrum recorded by sweeping the cavity extracted from a spectrometer measurement (same Data as in 5.12 (c)) and using single photon counting avalanche photodiodes (APD). Both measurements agree well with each other. The arrow marks the line we will investigate more carefully in the following.

short timescale dynamics. For rare earth ions, with characteristic optical lifetimes on the orders of milliseconds, one detector is fully sufficient.

Experimental Determination of $g^{(2)}(\tau)$

I analyze the emission from the the brightest peak observed in Membrane B using the single photon counters. To verify the alignment, I first measure the fluorescence emission when scanning the cavity under off-resonant excitation. This is essentially the same measurement as the spectrometer dispersion measurement reported in Figure 5.12, without the spectral resolution provided by the spectrometer grating. To avoid unwanted contributions from emitters that lie outside the spectral region of interest, I add a narrow bandpass filter, which only transmits light in the spectral region 915 nm to 922 nm[1]. This also helps greatly to suppress any background illumination impinging on the sensitive single photon detectors. Performing this measurement, I observe the same individual lines as in the integrated spectrometer measurement, confirming the alignment. The measurements using both techniques are compared to each other in Figure 5.14. The maximal countrate observed for the brightest peak is 35 000 cts/s for an excitation power of 640 µW, measured after the cavity. We focus on this bright feature to reduce the acquisition time of a highly resolved $g^{(2)}(\tau)$ function with a high signal-to-noise ratio [2]. Therefore, the cavity length is adjusted at the peak of the resonance. The observed countrate is monitored and an automatic repositioning to maximize the countrate is

[1] FBH920-10, *Thorlabs*
[2] The acquisition time for a given signal to noise ratio scales quadratically with the emitter count rate for a second order auto-correlation measurement, because every data points corresponds to two events.

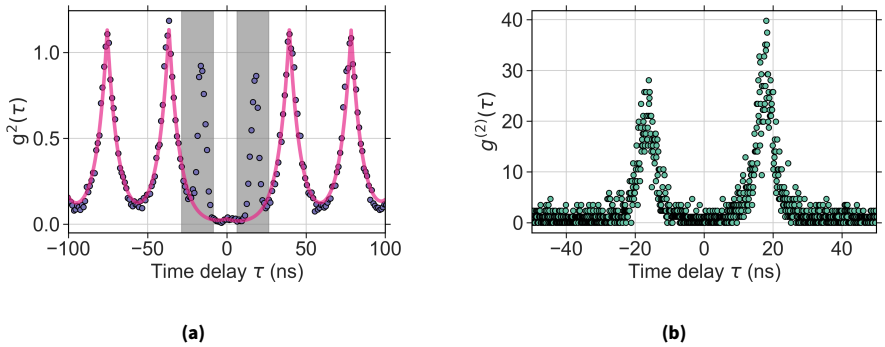

Figure 5.15.: (a) Pulsed second order autocorrelation measurement measured with the cavity resonant with a strong emission line. The grey shaded area is excluded from the fit due to artifacts, as discussed in the main text. (b) Artifacts in the $g^{(2)}(\tau)$ measurement caused by recombination emission of the silicon detectors, seen by the other detector. Reproduced from [192].

performed when the countrate drops below a certain threshold due to slow drifts of the cavity position.

The resulting auto-correlation is depicted in Figure 5.15. Note that this measurement was done using a pulsed laser source, because the available cw-laser caused large thermal drifts of the cavity length due to power fluctuations. This results in peaks corresponding to the fluorescence resulting from the excitation pulses, spaced in time by the pulse repetition rate. The temporal shape of the pulses is governed by the dynamics of the emitter. The peak amplitude is modulated by second-order autocorrelation envelope. We observe that the peak at zero time delay drops very close to zero. I fit the experimentally observed data, excluding the central peak, by a series of exponential decays with a fixed spacing corresponding to the repetition rate. All peaks share the same amplitude and FWHM. The amplitude is multiplied by an envelope function that includes a bunching term $A = a_\mathrm{b} \mathrm{e}^{-|\tau|/t_\mathrm{b}}$. The bunching is caused by the metastable states of the V2 center.

Then, I separately fit the central peak with a exponential decay that has the same temporal width as the outer lying peaks. I compare the peak area extracted from the fit of the central peak to the area of the outer lying peaks where the bunching has rolled off to extract the value for $g^{(2)}(0) = (0.024 \pm 0.024)$. The error is as large as the value, since the peak is barely resolvable. This demonstrates the strong single photon character of the emission of the investigated optical feature, clearly proving that the emission stems from an individual color center.

It is worth to emphasize that the single photon character is observed despite there being many emitters spatially located in the cavity mode. The combination of the spectrally detuned emitters and the spectral resolution power of the cavity allows to selectively couple to a single emitter, even though the excitation is non-discriminatory. This could

in the future enable spectral multiplexing by quickly switching the cavity length on demand to be resonant with different color center ZPLs.

Artifacts in the $g^{(2)}(\tau)$ measurement

In the $g^{(2)}(\tau)$ measurement depicted in Figure 5.15 two peaks at time delays $\tau = \pm 19\,\mathrm{ns}$ were excluded from the fit, indicated by a gray background. These are artifacts of the setup, which I was unfortunately unable to fully suppress. The peaks stem from recombination photon emission within the silicon detector chip, that are observed by the other detector, leading to a strong correlation. This is a known phenomenon which was investigated in detail already more than twenty years ago [237]. The temporal shape of the peak matches the expected temporal profile of the recombination emission, and the temporal offset between the peaks of $\tau = \pm 19\,\mathrm{ns}$ corresponds to an optical path length of 5.7 m. This matches well with the path length traveled for either photo detector to the cavity and back. Indeed, I observe that this artificial signal is always present, except, when the detectors are illuminated and the optical path to the cavity is blocked. I therefore assume that the artifact is generated from a recombination flash at either detector, is then collimated by the focusing lens, reflected from the backside of the cavity, which is highly reflective for any non-resonant light, guided back and finally hitting the other detector. It is astonishing that despite this highly inefficient path, the effect is so clearly visible. In the end, this is a demonstration of the high sensitivity of the correlation measurements, which can reveal strong correlations even for small overall amount of events. Often, spectral filtering is used to get rid of similar artifacts. In our case, this is not possible since the emission spectrally overlaps with the investigated emitter fluorescence. Other experiments used polarization filtering to prevent crosstalk between the detectors [238]. This is principally built into our setup as well, as we use a polarizing beam-splitter which polarizes the light on the way to the cavity and guides it back onto the detector that caused the flash on return. Even after adding additional polarization filtering, the artifacts were still visible. Therefore, I chose to simply exclude them from the fit. Ideally, an optical isolator based on the Faraday effect could be used to only transmit light from the cavity to the detectors and block any back reflection.
After having established that the emission stems from a single color center, I now turn to investigate and quantify the Purcell enhancement.

5.3.3. Investigation of the Purcell enhancement of a single color center

In the following, we investigate the same bright feature we have analyzed in the previous section, which was found to stem from a single color center. In order to determine the Purcell enhancement, I now conduct measurements of the optical lifetime as a function of the cavity emitter detuning. The repetition rate of the pulsed supercontinuum source is reduced to 7.8 MHz to fully resolve the optical decay dynamics. Figure 5.16 shows the different decay for a varying emitter-cavity detuning, measured as the mean count

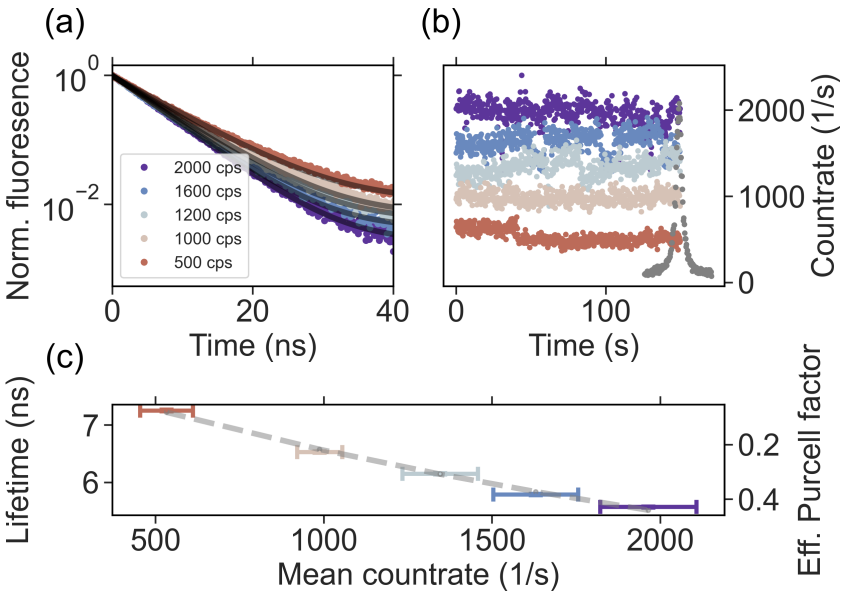

Figure 5.16.: Investigation of the Purcell effect of a silicon carbide color center coupled to an optical resonator. (a) Fluorescence decays at different cavity-emitter detunings. Gray lines are monoexponetial fits to the data with an offset to account for the background. The different detuning levels are displayed in (b), together with a sweep of the cavity over the emitter in gray. The extracted lifetimes as a function of the mean countrate and the corresponding effective Purcell factor during the measurement are plotted in Figure (c). The minimal lifetime observed is $\tau_{\mathrm{cav}} = 5.6\,\mathrm{ns}$. The gray line is a fit to the data used to extract the free space lifetime (see main text). Reproduced from [192].

rate observed during the measurement. Figure 5.16 (b) shows the corresponding single photon count traces, compared to a scan of the cavity line over the emitter line. The cavity is positioned at the respective detuning and manually kept on the same level for the duration of the measurement. I observe a faster decay as the cavity is more resonant with the emitter. The resulting lifetimes extracted from a mono-exponential fit are plotted as a function of the mean countrate during the measurement in Figure 5.16 (c). As expected, we observe a decreasing lifetime as the cavity is shifted into resonance with the emitter ZPL. This is a clear sign of Purcell enhancement of the emitter ZPL. The shortest optical lifetime observed when the cavity is fully in resonance with the emitter is $\tau_{\mathrm{cav}} = 5.6\,\mathrm{ns}$. For a conservative estimate, we assume the longest optical lifetime measured on the fringe of the resonance, $\tau_0 = 7.3\,\mathrm{ns}$ to be the free space lifetime of the emitter, in good agreement with the values reported in the literature ($\tau = 7.08\,\mathrm{ns}$) [97]. Taking this as a reference value allows us to calculate the effective Purcell factor as $C_{\mathrm{eff}} = \frac{\tau_0}{\tau_{\mathrm{cav}}} - 1$, which is also depicted in Figure 5.16 (c). The maximal effective Purcell

factor I observe is $C_{\text{eff}} = 0.3$. While this value appears low, it is important to consider that only the radiative emission into the ZPL is enhanced, which is only a small fraction of all decay channels. We can calculate the Purcell effect using the values reported in the literature for the branching ratio into the zero-phonon-line $\zeta = 0.08$ [209] and the quantum efficiency $QE = 0.3$ [216], yielding $C_0 = \frac{C_{\text{eff}}}{\zeta \cdot QE} \approx 13$. Therefore, the coherent photon emission rate is enhanced by a factor of 13 as the cavity becomes resonant with the emitter. Note that this calculation relies on the literature values, and it is unclear how strongly these are affected by the proximity to the surfaces and strain in the membrane. An alternative way to determine the free space lifetime, and therefore the effective Purcell enhancement, is to perform a fit to the lifetime as a function of the countrate of the form $\frac{A}{\Gamma_0+\Gamma_C}$ and extrapolate the lifetime at no cavity enhancement. The fit is indicated as a gray dashed line in Figure 5.16 (e). The extracted free space lifetime is $\tau_0 = (8.0 \pm 0.5)$ ms. This corresponds to an effective Purcell factor of $C_{\text{eff}} = (0.40 \pm 0.10)$ and an ideal Purcell factor of $C_0 = (18.1 \pm 4.0)$. The caveat is that the extracted free space lifetime is higher than typically reported for bulk V2 centers. I therefore will use the more conservative value of $C_0 = 13$ in the following.

I compare the measured Purcell factor to the predicted values. The predicted Purcell factor is calculated as discussed in Section 5.2.2. I use the linewidth extracted from the dispersion measurement depicted in Figure 5.12 to calculate the quality factor $Q = \frac{\nu}{\Delta\nu} = \frac{c}{4.8\,\text{GHz}\cdot 916.5\,\text{nm}} = 6.8 \times 10^4$. As discussed previously, this measurement contains both the emitter and the cavity linewidth, which are therefore both accounted for in the calculation. Making use of the transfer matrix model, the effective energy density cavity length is calculated to be:

$$L_{\text{eff}} = \frac{\int |n(z)E(z)|^2 dz}{\max(|n(z)E(z)|^2)} = 4.28\,\mu\text{m}. \tag{5.12}$$

Together with the mode waist in the membrane $w_d = 1.66\,\mu$m, the mode volume is calculated to be:

$$V = \frac{\pi w_0^2 L_{\text{eff}}}{4} = 12.0\,\lambda_{\text{ZPL}}^3 \tag{5.13}$$

This results in a predicted Purcell effect of $C_0 = 25.7$, twice as much as is observed experimentally. The discrepancies can be explained by a non-perfect spatial overlap of the emitter with the cavity mode, both transversally and along the optical axis. The observed lifetime change is therefore consistent with our expectations. We expect that through meticulous search and optimization, twice as high Purcell factors should be obtainable with the current experimental parameters. Nevertheless, the experimentally observed Purcell factor $C_0 \approx 13$ already results in a high rate of detected, coherent photons from a single emitter, and therefore constitutes an important first step towards an efficient quantum network node. I will shortly discuss this in the following.

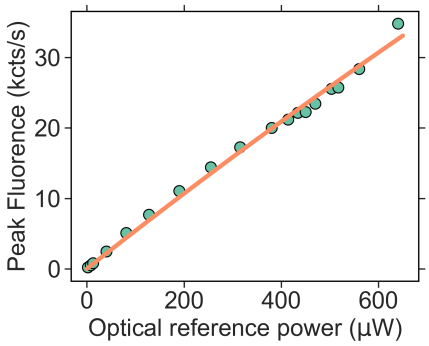

Figure 5.17.: Saturation measurement of a bright, cavity-coupled V2 center. Reference power is the time average of a pulsed laser measured after the cavity. The orange line is a saturation law fit to the data, which however shows an extremely high uncertainty, indicating that no significant saturation is observed. Reproduced from [192].

5.3.4. High rate emission of coherent, single photons

In order to quantify the achievable photon detection rates, I record the peak count rate observed when scanning the cavity over the ZPL as a function of the excitation power. Again, I make use of the pulsed super-continuum light source (repetition rate = 78.2 MHz). The referenced powers are mean continuous wave values recorded after the cavity. The resulting data is depicted in Figure 5.17. The maximum peak countrate observed is 35 kct/s. There is no clear sign of saturation observed. A saturation law fit of the form: $P(I_{\mathrm{exc}}) = \frac{P_{\mathrm{max}}}{1+I_{\mathrm{sat}}/I_{\mathrm{exc}}}$ to the data showcases only a linear behavior in the accessible power range. Conversely, this means that the countrate could be increased by a factor of five to ten, by simply utilizing a laser strong enough to drive the emitter into saturation. Additionally, it is worth to note that the silicon-based single photon detectors used to detect the emission have a poor detection efficiency in the NIR spectral region of $\eta_{\mathrm{det}} \approx 30\,\%$. By using state of the art superconducting nano-wire single photon detectors, this could be enhanced by another factor of three. Therefore, I estimate that the observable single photon countrate could be realistically increased by an order of magnitude, without any changes to the cavity-membrane system. I emphasize that all detected photons are scattered in the ZPL and can therefore be used for quantum communication protocols.

In order to gauge this, it is useful to compare this to the typical detected photon rates from a single emitter in the literature. Many works concerned mainly with the spin properties of the V2 center solely use the fluorescence to read out the spin-state. This can be done incoherently by collecting the PSB photons. In a state of the art confocal microscope, typical countrates of saturated single V2 centers are on the order of 10 kcts/s.

By using solid immersion lenses or nanopillars, the detected photon rate can be increased to about 50 kcts/s [239, 238]. Recently, antenna structures were employed to detect up to 150 kcts/s from a single color center [234] [1]. Selecting coherent photons from such a source requires additional spectral filtering and reduces the observed rate to 8 % of the observed value, even when the implemented filtering is lossless.
Reports on resonant enhancement of the ZPL are rarer. Single V2 center photon countrates, Purcell enhanced by a whispering gallery mode resonator of 400 kcts/s were reported by Lukiin et. al [219]. When considering that they drive their emitter into saturation and use SNSPD detectors, these rates are comparable to the ones observed in our work. Earlier works on V1 centers and di-vacancies in photonic crystal cavities observe significantly higher Purcell factors of $C_0 \approx 80$ [240] and $C_0 \approx 50$ [241]. Open access FP-cavities, such as the one used in this work, have the benefit of a high theoretical mode matching efficiency and a high directionality when properly designed. Consequentially, the observable photon count rate can be higher than for other cavity designs featuring comparable Purcell factors.

5.4. Outlook

In summary, I have demonstrated the Purcell enhancement of a single V2 center in silicon carbide when coupled to a high finesse FFPC. The sample is integrated into the cavity by bonding a thin membrane to a planar mirror. I find that SiC lends itself very well to this approach, that has previously been pioneered with diamond membranes: I observe a high finesse up to $\mathcal{F} = 40\,000$, which is almost twice as high as for the bare cavity system without the membrane. This is caused by a favorable interference effect for the appropriate membrane thickness, increasing the mirror reflectivity. While this is not unique to this material system, the membrane introduces only minimal additional losses to the system, which is a big challenge for the diamond platform. Additionally, the strong birefringence of SiC naturally ensures an optimal dipole overlap of the cavity mode with the emitter dipole transition moment, which is important to maximize the Purcell factor. I study the mode hybridization of the cavity membrane system and find that it can be described excellently by a mathematical model. When cooling down the system to cryogenic temperatures, narrow spectral features can be resolved using the cavity enhancement and an off-resonant excitation. Some of these features are well-separated and are well fit by a single Lorentzian. By analyzing the photon-statistics, I find a clear single photon character, proving that the emission stems from a single color center. The optical lifetime is analyzed as a function of the cavity-emitter detuning to determine

[1] The observed countrate is not a good figure of merit, because it depends on the detector efficiencies and how well the collection optics are aligned. An enhancement factor compared to an unstructured environment in the same setup is therefore commonly given. In our system, the enhancement is given by the Purcell factor, which however can not be directly compared to the empirically determined enhancement factor commonly quoted for the photonic structures discussed above.

the Purcell enhancement. I find an effective Purcell factor of 0.3, corresponding to an enhancement of the zero-phonon line by a factor of 13, which enables the detection of ZPL photon rates of up to 35 kcts/s. Thereby, I have realized an efficient source of coherent photons.
In the following, I want to give an outlook on further directions and improvements that this experiment could take. I will focus on realistic improvements, i.e. one that could be realized with equipment already present or soon available in the lab. The first thing that becomes apparent is that we observe high finesse values of up to $\mathcal{F} = 40000$ in the center of the stop-band, e.g. at $\lambda = 980$ nm, but we investigate transitions at 917 nm at the edge of the stop-band, where the maximal finesse values observed are rather on the order $\mathcal{F} = 4000$. The reason for this is that the mirror coating was originally designed in order to enhance the coherent transition of Yb^{3+} ions, as discussed at length in chapters 2 and 3. By utilizing an optimized mirror coating, we could therefore achieve a finesse of $\mathcal{F} = 40\,000$ at the emitter wavelength of $\lambda = 917$ nm. In this regime, the cavity linewidth is quite narrow (on the order of 400 MHz). This is more narrow than what we estimate from the observed linewidths in cavity experiments and on the same order as observed during the characterization in the confocal microscope. Therefore, the thermalization would likely need to be improved as well. The most straightforward approach would be to utilize an exchange-gas cryostat instead of the cold finger architecture employed here, as has been successfully demonstrated by my coworkers [242]. If realized, this could lead to a significant higher Purcell enhancement.
Another interesting direction to pursue is to focus on the spin properties of the V2 center. So far, our experiments can not probe these characteristics. There are multiple ways one could work towards this. An implementation of a direct and efficient microwave drive of the V2 center ground state would be one important ingredient. Recently, driving of a NV center electronic spin in a similar cavity-membrane architecture was achieved using striplines fabricated between the membrane and the mirror [243, 224]. Winding an antenna around the fiber mirror has been investigated in our group and was used to demonstrate driving of the electron spin of an ensemble of NV centers. One can also envision striplines fabricated on top of the membrane, although the design needs to provide sufficiently large gaps to not perturb the optical cavity mode, while still providing sufficiently strong driving. This would have the added benefit that it might also improve the local thermalization. Having realized a microwave drive, a first step would be the demonstration of ODMR. Here, the enhanced photon rate due to the cavity would speed up the measurement time due to the higher available count rates, even though the measurement scheme is equally sensitive to zero-phonon line photons and phonon-side band photons. This assumes that the cavity linewidth is of a similar magnitude as in this work ($\Delta\nu_{\mathrm{cav}} = 3.4$ Ghz), larger than the splitting of the two optical, spin-conserving transitions of the V2 center ($\Delta\nu = 1$ Ghz), and therefore enhances both transitions in an equal fashion.
The situation changes when the cavity linewidth becomes smaller than the splitting: Then the cavity can selectively enhance one or the other transition, just as it was used to spectrally select individual emitters. By enhancing only one spin-allowed transition, the rates of the system are heavily modified. Such a scheme could be used to, for

example, increase the contrast of an ODMR measurement or to initialize the emitter into a certain spin state. This setting is comparable to an experiment where one uses resonant lasers to selectively address the optical transitions, with the cavity replacing the laser as the spectrally selective element. However, it is very difficult for resonant experiments to extract ZPL photons from the sample, because one needs to separate the fluorescence from the excitation light. In the cavity setting sketched above, one can still use an off-resonant excitation, because the cavity takes care of the spectral selectivity. Therefore, it is straightforward to spectrally filter out the excitation light at 785 nm in the detection path and extract ZPL photons from the system. One can even envision a dynamic adjustment of the rates of the optical transitions by detuning the cavity to the transition, which might enable new protocols. Switching speeds as low as 100 µs have been demonstrated in FFPCs [126]. Such a scheme would make use of the quick tunability of open-access cavities, which is a distinct advantage compared to integrated nanophotonic resonators.

I want to point out that the presented cavity architecture can be easily extended to study other defects in silicon carbide such as the di-vacancies, or the vanadium center, by using a different mirror coating. This is another advantage over integrated photonic resonators, where a different emission wavelengths might require a fundamentally different design due to their lack of tunability. However, whether these novel defects offer a real advantage over the V2 center is at this point an open question.

6. Conclusion and outlook

In this thesis, I have investigated ytterbium ions and defect centers in silicon carbide for their suitability as cavity-based quantum nodes in a quantum network. Here, I want to summarize and contextualize the results and give an outlook how this work may be continued.

Ytterbium ions were studied as dopants hosted in yttria nanoparticles. I have demonstrated that the nanoparticles can be integrated into a high finesse FFPC without significantly hindering the cavity performance and observed first fluorescence signals that show characteristic signs of Yb^{3+} fluorescence at room temperature. Cryogenic ensemble measurements allowed for the detection of the homogeneous optical linewidth in this material, revealing an upper limit of the single ion linewidth of 5 MHz. Cryogenic cavity measurements on this material platform were precluded due to the cryogenic cavity design not achieving suitable low temperatures at the sample, limited by the design of the cavity mechanics and the employed cryostat.
Instead, I investigated color centers in a thin silicon carbide membrane in a cryogenic cavity setup. I studied the cavity-membrane system experimentally and found a good agreement with a simulation-based model, and only small losses introduced by the membrane. At cryogenic temperatures, the cavity was used to spectrally resolve individual color centers. I studied the emission properties of a well-coupled color center, and demonstrated a Purcell enhancement of the zero-phonon-line by a factor of 13, resulting in a high detected rate of photons scattered into the coherent zero-phonon-line. Thereby, I achieved one of the main goals initially laid out for this work: by coupling the optical transition of an individual quantum system to a Fabry-Pérot resonator, I could significantly enhance the coherent emission. Thereby, I have demonstrated that the cavity-membrane system presented here can be used to realize an efficient spin-photon interface, which might serve as a node in a quantum network.

Ytterbium ions or V2 centers

Having characterized two different quantum emitters in this work, the question which is more suited as a quantum network node naturally arises. In some way, it is not surprising that the V2 center cavity experiments were successful in demonstrating single emitter fluorescence: Due to the significantly shorter optical lifetime of $\tau \approx 7$ ns, even a moderate Purcell enhancement is sufficient to obtain a photon rate that is comfortably detected

using a single photon counting module. This is true despite the fact that the V2 centers optical properties are actually not that well-suited for coherent photon emission: due to the low branching ratio into the ZPL ($\zeta \approx 8\%$) and the existence of non-radiative decay mechanisms ($QE \approx 30\%$), only $\approx 2.4\%$ of excited state decays result in the emission of a coherent photon. In other words, a saturated V2 center emits a coherent photon every 300 ns without any photonic enhancement (every 22 ns for the Purcell enhancement $C_0 = 13$ demonstrated in this work).
When considering the long optical lifetime of ytterbium ions ($\tau = 1.5$ ms for the nanocrystals investigated in this work), it becomes clear that an extremely large Purcell enhancement of $C_0 \approx 17\,000$ is required to match even the non-enhanced coherent photon rates of the V2 center. That is despite the fact that a significantly larger fraction of the emitted light is scattered into the coherent ${}^2F_{7/2}(0) \rightarrow {}^2F_{5/2}(0)$ transition. The required enhancement is an order of magnitude higher than the highest Purcell factors achieved in state of the art experiments on such systems. Therefore, the achievable communication rates of REI-based quantum nodes will likely remain significantly lower than for the V2 center.
Even though they were not the focus of this work, the spin properties of the quantum emitter are equally as important when it comes to building a spin-photon interface. Spin echo coherence times of 10 ms have been reported in $Yb^{3+}:Y_2SiO_5$ [244]. Values reported for the V2 centers electron spin coherence are on the order of 10 µs to 100 µs, which could be extended to 20 ms by decoupling pulse sequences [217, 245]. Fundamentally, the coherence time of ytterbium ions could likewise be extended by a suitable decoupling sequence, as has been demonstrated in $Yb^{3+}:YVO_4$ [120]. In summary, the coherent spin properties of the two quantum systems are comparable, although decoupling sequences are needed in order for the V2 center to match the spin coherence of an ytterbium ion measured in a standard echo experiment.

When comparing the state of the art results obtained in SiC color centers and ytterbium ions in solids, it seems like the color center are naturally better suited for the use as quantum nodes in a network, because of their stronger optical transitions together with a comparable performance concerning their electron spin properties. One distinct advantage Ytterbium ions offer is their multiplexing capability: Due to their narrow homogeneous linewidths and large inhomogeneous broadening, many ions can be spectrally addressed in one spatial mode, making them inherently scalable.

Adapting the cavity-membrane system to ytterbium

The cryogenic experiments on the silicon carbide platform showcased the potential for integrating emitters in thin membranes. The cavity performance was ultimately limited by the non-ideal mirror coating, which was originally designed for enhancement of ytterbium fluorescence around $\lambda = 980$ nm. I already discussed the potential for cryogenic cavity experiments on the investigated ytterbium-doped nanoparticles in the

respective section. However, what about instead integrating ytterbium ions in the form of a thin membrane?
This approach is not entirely new and has been used successfully for erbium ions in a Y_2SiO_5 membrane [128, 129]. First steps on a similar experiment designed for praseodymium ions were conducted in our group by my colleague Sören Bieling. It was found that a well-fabricated membrane introduces minimal losses to the cavity, similar to the observations in this work.
Applying the membrane approach to ytterbium has multiple, distinct advantages. Firstly, it enables working in Y_2SiO_5, the most mature host material for rare earth ions. Ytterbium ions doped into Y_2SiO_5 at very low concentrations have shown excellent spin properties, as discussed above. At the same time narrow homogeneous linewidths of $\Gamma_{\text{hom}} = 122\,\text{Hz}$ which are predominantly limited by the optical lifetime, and narrow inhomogeneous linewidths ($\Gamma_{\text{inh}} \approx 1\,\text{Ghz}$) have been observed [246, 247]. The second big advantage membranes offer is that they enable working at much lower doping concentrations. The probed volume in an eight micron thick membrane is approximately a factor of 5000 larger that that of a 100 nm diameter nanoparticle. Conversely, the doping concentration could be reduced by this factor to the sub ppm level, while still probing thousands of ions in the cavity mode volume. Crucially, the coherence properties of ytterbium would greatly benefit, as Yb-Yb interactions have been found to be a limiting factor even in strongly diluted samples.
If we assume the membrane performance to be similar to the studied SiC membrane ($\mathcal{F} = 40\,000$ at $\lambda = 980\,\text{nm}$) and similarly thick membranes ($d = 3\,\mu\text{m}$), ideal Purcell factors on the order of $C_0 = 300$ can realistically be obtained. Such values are large enough to enable the detection of single dopants when accounting for setup efficiencies, although the resulting signal will be dimmer than what I observed experimentally for individual V2 centers. Besides single ion experiments, one could also make use of the relatively small inhomogeneous broadening, which can be on the order of the cavity linewidth, to couple many ions to a single cavity mode. This might enable cavity mediated collective effects, which can boost light matter interaction further, and may lead to various interesting physics to study.

Promise of the rare earth ion based molecular platform

The rare earth ion based molecular quantum emitters, which I investigated, hold the most transformative potential for future use in quantum networks. As evident from the results presented in this work, they are still in an early and exploratory stage, and far away from the performance of the more established quantum emitters in conventional host materials. However, as presented in this work, a large variation in their properties by attaching different ligands to the lanthanide centers has been found. Therefore, the promise of precise tailoring of their optical and coherent properties to match a targeted application by engineering the molecular environment, while still far away, seems to be attainable. This could break the cycle of blindly studying the many native color centers in semiconductor hosts, hoping to find one that lends itself naturally to the desired

application. Perhaps one day, it will be possible to come up with a list of requirements, for example for a quantum network node, and then design and synthesize a suitable molecular material that ticks all of the boxes. Somewhat ironically, quantum computers might be an important tool to accurately predict the molecules properties and guide their syntheses.

Only time will tell what technologies will form the backbone of quantum technologies in the future. What is clear is that any useful technology will not only need a well-working quantum system, but also integration into devices that serve to control and, in some aspects, enhance it. Hopefully, this thesis contributes a small part to the quest for efficient quantum nodes.

List of Figures

List of Tables

A. Sample overview

In this thesis, I have simplified the nomenclature of the investigated samples in order to improve readability. Here, I summarize the names of the investigated samples and their original identifiers.

Table A.1.: Ytterbium based molecular complexes

Name in this thesis	Name used internally	Chemical identifier
Yb-A1	SOR-156	(phen)-ligand with two additional Pyrazole units
Yb-A2	SOR-145	Additional Methyl Groups
Yb-B1	Yb-9	t-pip (Tetraphenylimidodiphosphinate) ligand
Yb-B2	Yb-13	Bypiridyne ligand
Yb-Trensal	Yb-Trensal (SKR-129)	2,2',2"-tris(salicylideneimino) triethylamine ligand

Table A.2.: Investigated silicon carbide membranes

Name in thesis/publication	Name internally
Membrane A	Membrane B
Membrane B	Membrane D

B. Room temperature confocal microscope setup

Here, I briefly describe the room temperature confocal setup utilized in Section 3.2 and Section 4.2. An image of the setup is depicted in Figure B.2. A detailed description can be found in Tobias Kroms master thesis, wo initially built the setup for Europium nanoparticles and wavelengths [63].

Laser system

The workhorse of the experiment is a tunable external cavity diode laser [1], which emits in a wavelength range of $\lambda = 940\,\text{nm}$ to 985 nm. The wavelength can be tuned coarsely over the full range with a motor acting on a grating and finely via a piezo actuator acting on the grating. The laser outputs up to $P_{\text{max}} = 40\,\text{mW}$ of power and the short-scale laser linewidth is specified to be less than $\delta_\nu < 200\,\text{kHz}$. To prevent strong back-reflection into the cavity, an external optical isolator[2] with 80 dB of suppression was added to the system. We use an AOM[3] in the so-called double pass configuration to temporally shape the pulses and provide frequency shift of up to 100 MHz. The light is then fiber-coupled and sent to the experiment.

Confocal Microscopy Setup

Excitation light is coupled out of a fiber, collimated with a lens and guided onto a dichroic mirror. It is then focused onto the sample by a high NA objective, which is mounted to a 3D positioning unit. The sample itself is clamped in a custom sample holder, which is mounted to a stack of nano-positioners, which enable movement in all three spatial axes with a precision of $\approx$ 100 nm and a travel-range of several micrometer [4]. When a fluorescing sample is brought into focus, the fluorescence is collected via the same objective, but passes the dichroic mirror due to its longer wavelength. Additional filters are used to suppress any remaining excitation light and possible to select spectral bands

[1] *Velocity TLB-6719*, Spectra-Physics
[2] *FI-980-5TIC*, LINOS
[3] *AOM 3200-124*, Gooch and Housego
[4] ECS3030, *Attocube*

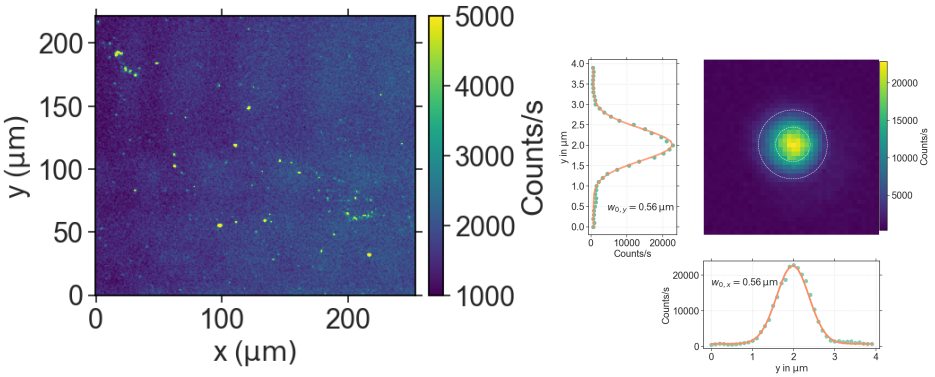

(a) Large scale confocal scan

(b) Point spread function

Figure B.1.: (a) Confocal images of Yb^{3+}:Y_2O_3 nanoparticles dispersed on a glass substrate. (b) Experimental determination of the PSF by imaging a Yb^{3+}:Y_2O_3 nanoparticle.

of interest in order to suppress background fluorescence. The fluorescence light is then routed to either a single photon counting module [1] via coupling to a single mode fiber, which simultaneously acts as a pinhole for the confocal microscope, or a fiber-coupled spectrometer [2].
This setup was routinely used to characterize Yb^{3+}-based emitters at room temperature. Besides creating confocal scans, it can be used to measure the optical lifetime by employing a pulsed excitation and correlation electronics to record the fluorescence decay, and to record PL spectra via the spectrometer.

Confocal scan

By raster scanning the sample through the focus using the nanopositioners and recording the fluorescence counts at every position, a fluorescence image or confocal microscope image is created. This shows the spatial distribution of fluorescing emitters with a spatial resolution given by the point-spread-function. For an exact derivation of the point-spread-function, see for example [248] . The point spread function can be determined experimentally by imaging a point-like feature (meaning much smaller than half a wavelength). A measurement of the point spread function using a Yb^{3+}:Y_2O_3 nanoparticle yields a PSF with waist $w_0 = 0.56\,\mu m$ and is depicted in Figure B.1, together with an example of a large scan spanning more than $200 \times 200\,\mu m^2$.

[1] *COUNT NIR*, Laser Components
[2] *Shamrock 500i* equipped with *iVAC316 LDC-DD camera*, Andor Technologies

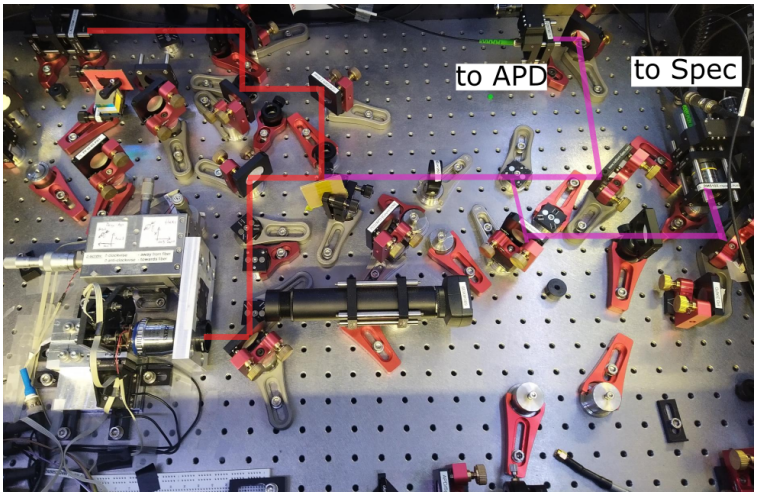

Figure B.2.: Photograph of the confocal microscope setup. Excitation beam path is indicated in red and detection beam path is indicated in pink.

C. Cryogenic cavity setup

Setup and beampath

As mentioned in the main text, the cryogenic cavity was built up by my colleague Maximillian Pallmann, and a detailed description, explanation of design choices and characterization can be found in his thesis [86]. Here, I briefly describe it.
Photographs of the cryogenic cavity setup are depicted in Figure C.1. The cavity is situated inside the sample chamber of a closed-cycle cryostat [1]. The main mechanics are balanced on springs to decouple it from high frequency mechanical noise. The top parts are thermalized to the cryostat cold plate using braided copper links. As described for the room temperature setup in 3.2.2, the fiber mirror can be scanned quickly using a combination of piezo ceramic actuators and a lever-arm mechanic. In addition, both the fiber mirror as well as the macroscopic mirror can be coarsely moved using DC motors and gears. The optical setup used for the SiC experiment is depicted in Figure C.2.

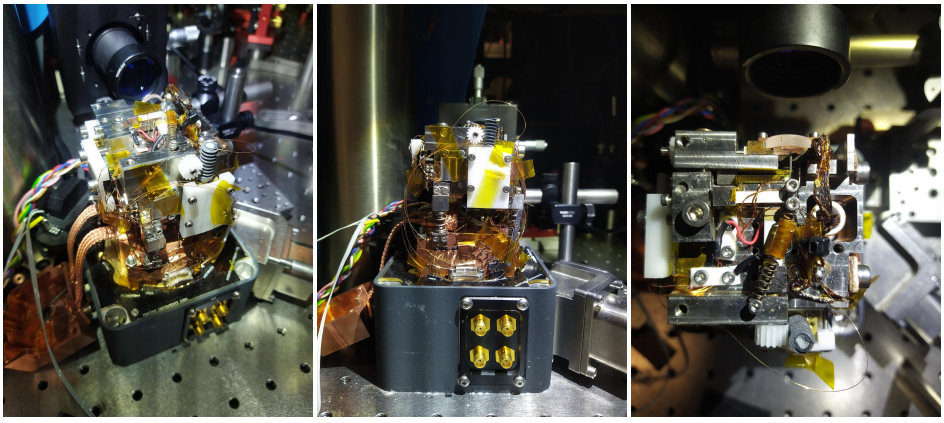

(a) (b) (c)

Figure C.1.: Photographs of the cryogenic cavity setup from different angles.

[1] Cryostation, *Montana Instruments*.

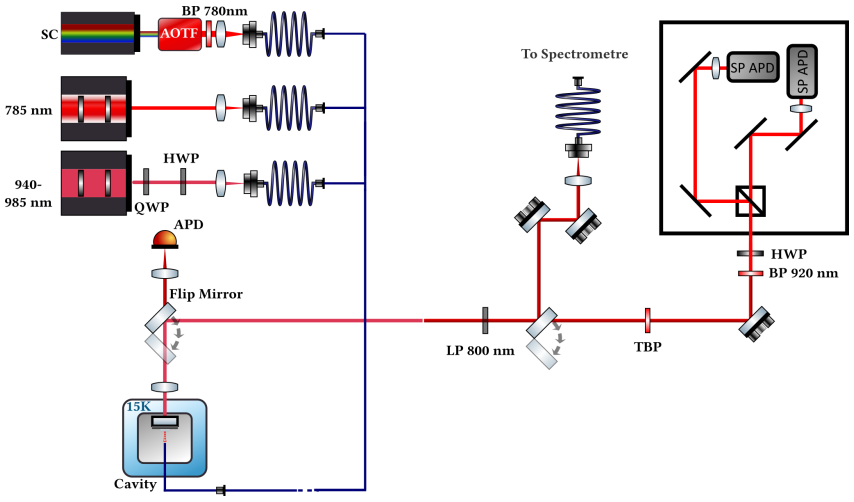

Figure C.2.: Optical beampath for the SiC experiment. Adapted from [232].

Cryogenic cavity stability

For most experiments in this work, one desires to keep a cavity resonant with a specific frequency, such as that of the probe laser or with the emission frequency of an emitter under investigation. Due to the high finesse cavities employed, this translates to high requirements on the cavity length fluctuations. A useful benchmark is the cavity linewidth in terms of cavity length detuning, that is how much the cavity length needs to be changed to cover one FWHMs of the cavity resonance. The cavity linewidth in detuning is given by

$$\Delta d = \frac{\lambda}{2F}. \tag{C.1}$$

For a finesse of $\mathcal{F} = 20000$ at a wavelength of $\lambda = 985\,\text{nm}$, the design parameters for the asymmetric coating used in this work, this translates to a cavity length variation of $\Delta d = 25\,\text{pm}$. In the experiment, it is desirable to keep the length fluctuations significantly below that value, for example in order to maximize the Purcell effect. The rigid design employed in our positioning unit results in low cavity length fluctuations, typically on the order of tens of pm, with record values significantly below 1 pm [86].

Operating a cavity in a noisy cryostat, such as the cold cycle cryostat employed in this work, is technological extremely challenging, and often a limiting factor for such experiments. Here, I want to emphasize the works of my colleagues Timon Eichhorn and Maximillian Pallmann, who carefully engineered and improved these cavity systems for years, to the point where cavity length fluctuations on the order of few picometer rms fluctuations are possible. For in-depth discussion and characterization on improving

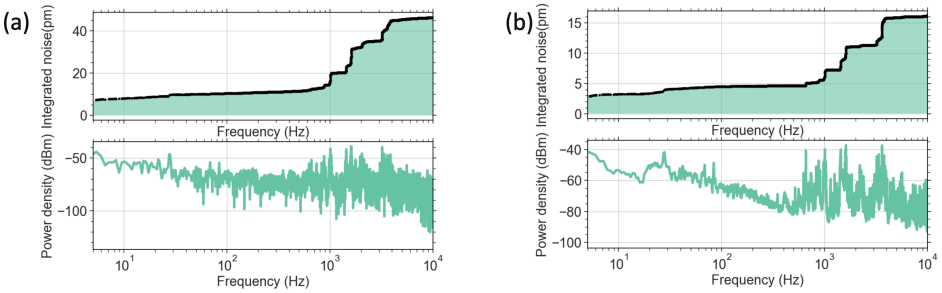

Figure C.3.: Noise spectrum and cumulative rms length fluctuations of a FFPC for two different configurations inside a closed-cycle cryostat. (a) Open cavity configuration (b) Fiber mirror is brought into contact with the membrane. Reproduced from [192].

the cavity length stability, I refer to their PhD theses and their joint paper [86, 232, 104]. I was very lucky to take over one such running system and therefore saving a lot of time which would otherwise need to be spent on optimizing the stability.

The longitudinal cavity stability was measured for the experiment with the SiC membrane described in section 5.3 during the experimental run where all the cryogenic data presented here was obtained. Therefore, the resonator was positioned on the flank of a Lorentzian shaped cavity resonance of known finesse $\mathcal{F} = 1400$ and height. The deviations from the set point can then be converted by the linearized slope into cavity length fluctuations. Additionally, spectral information about the noise can be extracted via its Fourier transform. The resulting noise spectrum is plotted together with the integrated cavity rms noise in Figure C.3 for two different configurations. In Figure (a), the cavity is operated in a standard open configuration, that is there is a significant air-gap between the mirror and the membrane. For the measurement depicted in Figure (b), the fiber mirror is pressed into the membrane, forming a quasi-monolithic cavity. Even in this configuration, the cavity length can still be tuned by several 100 nm, even though significantly higher voltages need to be applied to the piezoceramic actuators. However, the cavity length fluctuations are heavily reduced, in this case by a factor of three, from 45 pm to 15 pm. All fluorescence measurements presented in Section 5.3 were taken in this configuration.
However, the contact configuration also has some downsides. For one, it is unclear how it affects the local sample temperature. The fiber is not well thermalized and may introduce local heating at exactly the position that is investigated. Additionally, experiments on fiber-coupled optical waveguides have supposedly shown that fibers can introduce free charge carriers stemming from the fiber surface into a semiconductor material when

they are brought into contact [1]. In addition, strain may be introduced in the membrane. All of these effects can perturb the emitter properties. Strain is an exception insofar as some semiconductor color centers, such as the tin-vacancy center in diamond, actually profit from high strain environments and strain engineering is therefore of high interest for the community. However, strain tuning would ideally be independent from tuning of the resonator frequency.

[1] Private communication with University of Stuttgart

D. Additional autocorrelation measurements

In the main text, the discussion focuses on one bright ZPL in Membrane B. The cavity-resolved fluorescence spectrum in the thicker Membrane A showed a more narrow distribution of ZPLs frequencies, making it harder to resolve individual ZPLs. However, by investigating far detuned emitters, individual emitters could also be resolved in this system. Figure D.1 shows a pulsed $g^{(2)}(\tau)$ measurement for a far detuned ZPL (marked by a pink arrow). The extracted value for $g^{(2)}(0)$ is $g^{(2)}(0) = (0.15 \pm 0.09)$ without background correction, indicating a clear single photon character.

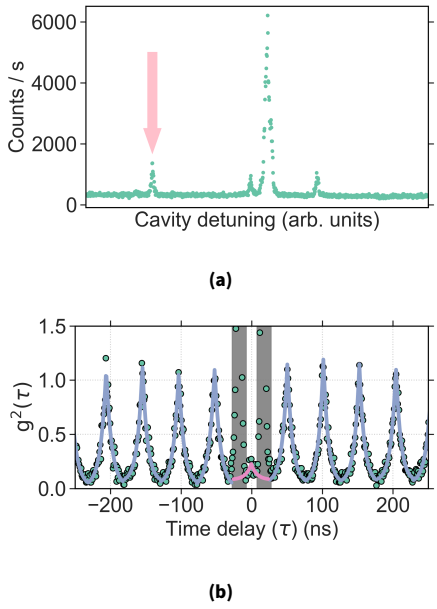

Figure D.1.: (a) Cavity resolved emitter spectrum. The arrow marks the detuned ZPL were the auto-correlation was investigated. (b) Fitted second-order auto-correlation measured on the marked line in (a).

E. List of publications

- **Jannis Hessenauer**[†], Jonathan Körber[†], Misagh Ghezellou, Jawad Ul-Hassan, Georgy V. Astakhov, Wolfgang Knolle, Jörg Wrachtrup, and David Hunger. Cavity enhancement of V2 centers in 4H-SiC with a fiber-based Fabry-Pérot microcavity. *Optica Quantum*, 3(2):175–181, April 2025. [192]

  [†] These authors contributed equally.

- **Jannis Hessenauer**, Ksenia Weber, Julia Benedikter, Timo Gissibl, Johannes Höfer, Harald Giessen, and David Hunger. Laser written mirror profiles for open-access fiber Fabry-Perot microcavities. *Optics Express*, 31(11):17380, May 2023. [70]

- Senthil Kumar Kuppusamy, Evgenij Vasilenko, Weizhe Li, **Jannis Hessenauer**, Christina Ioannou, Olaf Fuhr, David Hunger, and Mario Ruben. Observation of Narrow Optical Homogeneous Linewidth and Long Nuclear Spin Lifetimes in a Prototypical [Eu(trensal)] Complex. *The Journal of Physical Chemistry C*, 127(22):10670–10679, June 2023. [178]

F. List of talks and posters

Only contributions as first author/presenter are listed.

1. *Towards cavity-enhanced single ion spectroscopy of* Yb^{3+}*:*Y_2O_3. Poster
   KSOP Summer School, online, 2020
2. *Optically addressable rare-earth ion materials for quantum nodes*, Talk
   Optics and Photonics Seminar, Karlsruhe, 2020
3. *Towards cavity-enhanced single ion spectroscopy of* Yb^{3+}*:*Y_2O_3. Poster
   Karlsruhe Days of Optics and Photonics, online, 2021
4. *Fully fiber-coupled devices for efficient cryogenic spectroscopy of single and small ensembles of rare earth ions*, Poster (shared contribution with Evgenij Vasilenko)
   718. WE-Heraeus-Seminar: "Optically Addressable Spin Qubits for Quantum Networks and Quantum Computing", Bad Honeff, 2021
5. *Towards cavity-enhanced single ion spectroscopy of* Yb^{3+}*:*Y_2O_3. Poster
   DPG Frühjahrstagung der Sektion Atome, Moleküle, Quantenoptik und Photonik, Online, 2022
6. *Molecular rare earth ions as optically addressable spin qubits*, Talk
   Optics and Photonics Seminar, Karlsruhe, 2022
7. *Rare earth ion materials in micro-cavities as optically addressable qubits for quantum information* Poster, DPG Tagung der Sektion Kondensierte Materie, Regensburg, 2022
8. *Cavity-enhanced Spectroscopy of REI-doped Nanomaterials.* Talk (shared with Timon Eichhorn)
   Rare Earth Ion Meeting, Edinburgh, 2022
9. *Towards cavity-enhanced single ion spectroscopy of* Yb^{3+}*:*Y_2O_3. Poster
   KSOP Summer School, Bad Herrenalb, 2022
10. *Rare earth ions in molecular crystals for quantum information application.* Poster
    Quantum Matter, Madrid, 2023
11. *Novel* Yb^{3+}*-based materials for integration in open micro-cavities.* Poster
    Rare Earth Ion Meeting, Lund, 2023

12. *SiC color centers and rare earth ions in fiber-based Fabry-Pérot resonators.* invited Talk
    Group Seminar of the 3rd physics institute, Stuttgart, 2023
13. *Color centers in silicon carbide integrated into a fiber-based Fabry-Pérot microcavity.* Talk
    DPG Frühjahrstagung der Sektion Atome, Moleküle, Quantenoptik und Photonik, Freiburg, 2024
14. *Color centers in silicon carbide integrated into a fiber-based Fabry-Pérot microcavity.* Poster
    816. WE-Heraeus-Seminar: "Silicon Carbide: Classical and Quantum Technologies", Bad Honeff, 2024
15. *Purcell enhancement of single defects in silicon carbide coupled to a a fiber-based Fabry-Pérot microcavity.* Talk
    DPG Frühjahrstagung der Sektion Atome, Moleküle, Quantenoptik und Photonik, Bonn, 2025

G. Abbreviations and symbols

G.1. Abbreviations

cQED	cavity quantum electrodynamics
NV	nitrogen vacancy
SiC	silicon carbide
FFPC	fiber-based Fabry-Pérot cavity
FP	Fabry-Pérot
DBR	distributed Bragg reflector
FSR	free spectral range
LIGO	laser interferometer gravitational-wave observatory
WGM	whispering gallery mode
FIB	focused ion beam
DLW	direct laser writing
AOM	acousto-optic modulator
NIR	near infrared
NA	numerical aperture
ZEFOZ	zero first order zeeman
InGaAs	indium gallium arsenide
SNSPD	superconducting nanowire single photon detector
PSF	pointspread function
AWG	arbitrary wave form generator
FWHM	full width at half maximum
ECDL	external cavity diode laser
ASE	amplified spontaneous emission

REI	rare earth ion
AFC	atomic frequency comb
SDS	sodium dodecyl sulfate
PL	photoluminescence
PLE	photoluminescence excitation
OD	optical density
rms	root mean square
SiC	silicon carbide
AFM	atomic force microscope
ZPL	zero phonon line
PSB	phonon side band
HBT	Hanbury-Brown-Twiss
ODMR	optically detected magnetic resonance

G.2. Symbols

d	cavity length
λ	wavelength
q	longitudinal mode order
T_i	mirror transmission
A_i	mirror absorption
S	scattering losses
E	additional cavity extinction losses
I	intensity
$\mathcal{F}$	finesse
w_0	mode waist
z_0	Rayleigh range
ζ	Gouy phase
Δ_{FSR}	free spectral range
$\Delta\nu$	cavity linewidth
Q	quality factor
τ	cavity lifetime
V	mode volume
R_{c}	radius of curvature
ϵ	mode matching factor
P_{peak}	intracavity power at an antinode
η_i	outcoupling efficiency
σ_{rms}	root mean square surface roughness
C_0	(ideal) purcell factor
γ	transition rate
$\vec{\mu}$	dipole moment
$\rho(\omega)$	photon density of states
$\Lambda(\omega)$	emitter density of states
τ_0, T_1	excited state lifetime

τ_C	Purcell enhanced lifetime
β	collection efficiency
ζ	branching ratio
C_{eff}	effective purcell factor
Γ_{hom}	homogeneous linewidth
Γ_{inhom}	inhomogeneous linewidth
T_2	coherence time
QE	quantum efficiency
OD	optical density
$g^{(2)}(\tau)$	second order autocorrelation function

Bibliography

[1] UN General Assembly (78th sess. ;2023-2024). International Year of Quantum Science and Technology, 2025 : resolution / adopted by the General Assembly. June 2024. URL: https://digitallibrary.un.org/record/4052700 (visited on 03/04/2025).

[2] Jonathan P. Dowling and Gerard J. Milburn. Quantum technology: the second quantum revolution. *Philosophical Transactions of the Royal Society of London. Series A: Mathematical, Physical and Engineering Sciences*, 361(1809):1655–1674, June 2003. DOI: 10.1098/rsta.2003.1227.

[3] C. L. Degen, F. Reinhard, and P. Cappellaro. Quantum sensing. *Reviews of Modern Physics*, 89(3):035002, July 2017. DOI: 10.1103/RevModPhys.89.035002.

[4] Scott E. Crawford, Roman A. Shugayev, Hari P. Paudel, Ping Lu, et al. Quantum Sensing for Energy Applications: Review and Perspective. *Advanced Quantum Technologies*, 4(8):2100049, 2021. DOI: 10.1002/qute.202100049.

[5] Nabeel Aslam, Hengyun Zhou, Elana K. Urbach, Matthew J. Turner, et al. Quantum sensors for biomedical applications. *Nature Reviews Physics*, 5(3):157–169, March 2023. DOI: 10.1038/s42254-023-00558-3.

[6] T. D. Ladd, F. Jelezko, R. Laflamme, Y. Nakamura, et al. Quantum computers. *Nature*, 464(7285):45–53, March 2010. DOI: 10.1038/nature08812.

[7] Roman Rietsche, Christian Dremel, Samuel Bosch, Léa Steinacker, et al. Quantum computing. *Electronic Markets*, 32(4):2525–2536, December 2022. DOI: 10.1007/s12525-022-00570-y.

[8] Yudong Cao, Jonathan Romero, Jonathan P. Olson, Matthias Degroote, et al. Quantum Chemistry in the Age of Quantum Computing. *Chemical Reviews*, 119(19):10856–10915, October 2019. DOI: 10.1021/acs.chemrev.8b00803.

[9] P.W. Shor. Algorithms for quantum computation: discrete logarithms and factoring. In *Proceedings 35th Annual Symposium on Foundations of Computer Science*, pages 124–134, November 1994. DOI: 10.1109/SFCS.1994.365700.

[10] Jeroen Groenewegen-Lau and Antonia Hmaidi. China's long view on quantum tech has the US and EU playing catch-up | Merics. December 2024. URL: https://merics.org/en/report/chinas-long-view-quantum-tech-has-us-and-eu-playing-catch (visited on 03/07/2025).

[11] W. K. Wootters and W. H. Zurek. A single quantum cannot be cloned. *Nature*, 299(5886):802–803, October 1982. DOI: 10.1038/299802a0.

[12] William K. Wootters and Wojciech H. Zurek. The no-cloning theorem. *Physics Today*, 62(2):76–77, February 2009. DOI: 10.1063/1.3086114.

[13] Zheshen Zhang and Quntao Zhuang. Distributed quantum sensing. *Quantum Science and Technology*, 6(4):043001, July 2021. DOI: 10.1088/2058-9565/abd4c3.

[14] Marcello Caleffi, Michele Amoretti, Davide Ferrari, Jessica Illiano, et al. Distributed quantum computing: A survey. *Computer Networks*, 254:110672, December 2024. DOI: 10.1016/j.comnet.2024.110672.

[15] Rodney Van Meter and Simon J. Devitt. The Path to Scalable Distributed Quantum Computing. *Computer*, 49(9):31–42, September 2016. DOI: 10.1109/MC.2016.291.

[16] H. J. Kimble. The quantum internet. *Nature*, 453(7198):1023–1030, June 2008. DOI: 10.1038/nature07127.

[17] Stephanie Wehner, David Elkouss, and Ronald Hanson. Quantum internet: A vision for the road ahead. *Science*, 362(6412):eaam9288, October 2018. DOI: 10.1126/science.aam9288.

[18] Robert Bedington, Juan Miguel Arrazola, and Alexander Ling. Progress in satellite quantum key distribution. *npj Quantum Information*, 3(1):1–13, August 2017. DOI: 10.1038/s41534-017-0031-5.

[19] Koji Azuma, Sophia E. Economou, David Elkouss, Paul Hilaire, et al. Quantum repeaters: From quantum networks to the quantum internet. *Reviews of Modern Physics*, 95(4):045006, December 2023. DOI: 10.1103/RevModPhys.95.045006.

[20] Nicolas Gisin and Rob Thew. Quantum communication. *Nature Photonics*, 1(3):165–171, March 2007. DOI: 10.1038/nphoton.2007.22.

[21] M. Pompili, S. L. N. Hermans, S. Baier, H. K. C. Beukers, et al. Realization of a multinode quantum network of remote solid-state qubits. *Science*, 372(6539):259–264, April 2021. DOI: 10.1126/science.abg1919.

[22] C. M. Knaut, A. Suleymanzade, Y.-C. Wei, D. R. Assumpcao, et al. Entanglement of nanophotonic quantum memory nodes in a telecom network. *Nature*, 629(8012):573–578, May 2024. DOI: 10.1038/s41586-024-07252-z.

[23] P.-J. Stas, Y. Q. Huan, B. Machielse, E. N. Knall, et al. Robust multi-qubit quantum network node with integrated error detection. *Science*, 378(6619):557–560, November 2022. DOI: 10.1126/science.add9771.

[24] Daniel B. Higginbottom, Alexander T. K. Kurkjian, Camille Chartrand, Moein Kazemi, et al. Optical observation of single spins in silicon. *Nature*, 607(7918):266–270, July 2022. DOI: 10.1038/s41586-022-04821-y.

[25] Stefania Castelletto and Alberto Boretti. Silicon carbide color centers for quantum applications. *Journal of Physics: Photonics*, 2(2):022001, April 2020. DOI: 10.1088/2515-7647/ab77a2.

[26] Ren-Zhou Fang, Xiao-Yi Lai, Tao Li, Ren-Zhu Su, et al. Experimental Generation of Spin-Photon Entanglement in Silicon Carbide. *Physical Review Letters*, 132(16):160801, April 2024. DOI: 10.1103/PhysRevLett.132.160801.

[27] Andreas Reiserer and Gerhard Rempe. Cavity-based quantum networks with single atoms and optical photons. *Reviews of Modern Physics*, 87(4):1379–1418, December 2015. DOI: 10.1103/RevModPhys.87.1379.

[28] A. Ruskuc, C.-J. Wu, E. Green, S. L. N. Hermans, et al. Multiplexed entanglement of multi-emitter quantum network nodes. *Nature*, 639(8053):54–59, March 2025. DOI: 10.1038/s41586-024-08537-z.

[29] Andrei Ruskuc, Chun-Ju Wu, Jake Rochman, Joonhee Choi, and Andrei Faraon. Nuclear spin-wave quantum register for a solid-state qubit. *Nature*, 602(7897):408–413, February 2022. DOI: 10.1038/s41586-021-04293-6.

[30] C. E. Bradley, J. Randall, M. H. Abobeih, R. C. Berrevoets, et al. A Ten-Qubit Solid-State Spin Register with Quantum Memory up to One Minute. *Physical Review X*, 9(3):031045, September 2019. DOI: 10.1103/PhysRevX.9.031045.

[31] Igor Aharonovich, Dirk Englund, and Milos Toth. Solid-state single-photon emitters. *Nature Photonics*, 10(10):631–641, October 2016. DOI: 10.1038/nphoton.2016.186.

[32] Andreas Reiserer. *Colloquium* : Cavity-enhanced quantum network nodes. *Reviews of Modern Physics*, 94(4):041003, December 2022. DOI: 10.1103/RevModPhys.94.041003.

[33] Johannes Borregaard, Anders Søndberg Sørensen, and Peter Lodahl. Quantum Networks with Deterministic Spin–Photon Interfaces. *Advanced Quantum Technologies*, 2(5-6):1800091, 2019. DOI: 10.1002/qute.201800091.

[34] Ravitej Uppu, Leonardo Midolo, Xiaoyan Zhou, Jacques Carolan, and Peter Lodahl. Quantum-dot-based deterministic photon–emitter interfaces for scalable photonic quantum technology. *Nature Nanotechnology*, 16(12):1308–1317, December 2021. DOI: 10.1038/s41565-021-00965-6.

[35] Rikizo Ikuta, Toshiki Kobayashi, Tetsuo Kawakami, Shigehito Miki, et al. Polarization insensitive frequency conversion for an atom-photon entanglement distribution via a telecom network. *Nature Communications*, 9(1):1997, May 2018. DOI: 10.1038/s41467-018-04338-x.

[36] Yiru Zhou, Pooja Malik, Florian Fertig, Matthias Bock, et al. Long-Lived Quantum Memory Enabling Atom-Photon Entanglement over 101 km of Telecom Fiber. *PRX Quantum*, 5(2):020307, April 2024. DOI: 10.1103/PRXQuantum.5.020307.

[37] Kerry J. Vahala. Optical microcavities. *Nature*, 424(6950):839–846, August 2003. DOI: 10.1038/nature01939.

[38] Bahaa E. A. Saleh and Malvin C. Teich. *Fundamentals of photonics*. Wiley, Hoboken, N.J., 2. ed. Edition, 2007.

[39] Matthias Mader. *A scanning cavity microscope*. Dissertation, Ludwig-Maximilians-Universität München, July 2018.

[40] Anthony E. Siegman. *Lasers /*. University science books. Oxford University Press [u.a.], Oxford [u.a.] : 1986.

[41] Simin Feng and Herbert G. Winful. Physical origin of the Gouy phase shift. *Optics Letters*, 26(8):485–487, April 2001. DOI: 10.1364/OL.26.000485.

[42] Julia Benedikter. *Microcavity enhancement of silicon vacancy centres in diamond and europium ions in yttria*. PhD thesis, Ludwig-Maximilians-Universität München, July 2019.

[43] Julia Benedikter, Thomas Hümmer, Matthias Mader, Benedikt Schlederer, et al. Transverse-mode coupling and diffraction loss in tunable Fabry–Pérot microcavities. *New Journal of Physics*, 17(5):053051, May 2015. DOI: 10.1088/1367-2630/17/5/053051.

[44] Julia Benedikter, Thea Moosmayer, Matthias Mader, Thomas Hümmer, and David Hunger. Transverse-mode coupling effects in scanning cavity microscopy. *New Journal of Physics*, 21(10):103029, October 2019. DOI: 10.1088/1367-2630/ab49b4.

[45] Hyeongrak Choi, Mikkel Heuck, and Dirk Englund. Self-Similar Nanocavity Design with Ultrasmall Mode Volume for Single-Photon Nonlinearities. *Physical Review Letters*, 118(22):223605, May 2017. DOI: 10.1103/PhysRevLett.118.223605.

[46] M. S. Tame, K. R. McEnery, Ş K. Özdemir, J. Lee, et al. Quantum plasmonics. *Nature Physics*, 9(6):329–340, June 2013. DOI: 10.1038/nphys2615.

[47] D Hunger, T Steinmetz, Y Colombe, C Deutsch, et al. A fiber Fabry–Perot cavity with high finesse. *New Journal of Physics*, 12(6):065038, June 2010. DOI: 10.1088/1367-2630/12/6/065038.

[48] Johannes F. S. Brachmann, Hanno Kaupp, Theodor W. Hänsch, and David Hunger. Photothermal effects in ultra-precisely stabilized tunable microcavities. *Optics Express*, 24(18):21205, September 2016. DOI: 10.1364/OE.24.021205.

[49] Noha Gaber, Maurine Malak, Frédéric Marty, Dan E. Angelescu, et al. Optical trapping and binding of particles in an optofluidic stable Fabry–Pérot resonator with single-sided injection. *Lab on a Chip*, 14(13):2259–2265, 2014. DOI: 10.1039/C3LC51438B.

[50] J. Nelson and S. Iles. Creating sub angstrom surfaces on planar and spherical substrates. In *Optifab 2019*, volume 11175, pages 6–16. SPIE, November 2019. DOI: 10.1117/12.2536689.

[51] Georg Wachter, Stefan Kuhn, Stefan Minniberger, Cameron Salter, et al. Silicon microcavity arrays with open access and a finesse of half a million. *Light: Science & Applications*, 8(1):37, April 2019. DOI: 10.1038/s41377-019-0145-y.

[52] Naijun Jin, Charles A. McLemore, David Mason, James P. Hendrie, et al. Microfabricated mirrors with finesse exceeding one million. *Optica*, 9(9):965, September 2022. DOI: 10.1364/OPTICA.467440.

[53] D. Hunger, C. Deutsch, R. J. Barbour, R. J. Warburton, and J. Reichel. Laser micro-fabrication of concave, low-roughness features in silica. *AIP Advances*, 2(1):012119, January 2012. DOI: 10.1063/1.3679721.

[54] Daqing Wang, Hrishikesh Kelkar, Diego Martin-Cano, Dominik Rattenbacher, et al. Turning a molecule into a coherent two-level quantum system. *Nature Physics*, 15(5):483–489, May 2019. DOI: 10.1038/s41567-019-0436-5.

[55] Patrick Maier, Simon Rupp, Niklas Lettner, Johannes Hecker Denschlag, and Alexander Kubanek. Fabrication of Mode-Matched, Low-Loss Optical Resonators by Combination of FIB-Milling and CO$_2$ Laser Ablation. January 2025. DOI: 10.48550/arXiv.2501.09577. URL: http://arxiv.org/abs/2501.09577 (visited on 03/19/2025).

[56] Konstantin Ott, Sebastien Garcia, Ralf Kohlhaas, Klemens Schüppert, et al. Millimeter-long fiber Fabry-Perot cavities. *Optics Express*, 24(9):9839–9853, May 2016. DOI: 10.1364/OE.24.009839.

[57] Benedikt Schlederer. *Development of a CO_2 laser setup for fiber end facet machining and characterization*. Master's thesis, Ludwig-Maximilians-Universität München, November 2014.

[58] Sh. A. Furman. *Basics of optics of multilayer systems*. Ed. Frontieres, Gif-sur-Yvette Cedex : 1992.

[59] G. Rempe, R. J. Thompson, H. J. Kimble, and R. Lalezari. Measurement of ultralow losses in an optical interferometer. *Optics Letters*, 17(5):363–365, March 1992. DOI: 10.1364/OL.17.000363.

[60] C. Koks and M. P. Van Exter. Microcavity resonance condition, quality factor, and mode volume are determined by different penetration depths. *Optics Express*, 29(5):6879, March 2021. DOI: 10.1364/OE.412346.

[61] Manuel Uphoff, Manuel Brekenfeld, Gerhard Rempe, and Stephan Ritter. Frequency splitting of polarization eigenmodes in microscopic Fabry–Perot cavities. *New Journal of Physics*, 17(1):013053, January 2015. DOI: 10.1088/1367-2630/17/1/013053.

[62] Larissa Kohler, Matthias Mader, Christian Kern, Martin Wegener, and David Hunger. Tracking Brownian motion in three dimensions and characterization of individual nanoparticles using a fiber-based high-finesse microcavity. *Nature Communications*, 12(1):6385, November 2021. DOI: 10.1038/s41467-021-26719-5.

[63] Tobias Krom. *Development of a low temperature all-fiber resonator platform with integrated Eu^{3+}:Y_2O_3nanocrystals*. Master's thesis, Karlsruher Institut für Technologie (KIT), July 2021.

[64] Christopher Hins. *Installation and characterization of a fiber-based Fabry-Pérot cavity at low temperatures*. Bachelor's Thesis, Karlsruher Institut für Technologie (KIT), December 2020.

[65] E. M. Purcell, H. C. Torrey, and R. V. Pound. Resonance Absorption by Nuclear Magnetic Moments in a Solid. *Physical Review*, 69(1-2):37–38, January 1946. DOI: 10.1103/PhysRev.69.37.

[66] Mark Fox. *Quantum optics: An introduction*. Oxford master series in physics ; Oxford University Press, Oxford ; first edition edition, 2006.

[67] A. Meldrum, P. Bianucci, and F. Marsiglio. Modification of ensemble emission rates and luminescence spectra for inhomogeneously broadened distributions of quantum dots coupled to optical microcavities. *Optics Express*, 18(10):10230, May 2010. DOI: 10.1364/OE.18.010230.

[68] Jonathan P. Dowling. Spontaneous emission in cavities: How much more classical can you get? *Foundations of Physics*, 23(6):895–905, June 1993. DOI: 10.1007/BF01891512.

[69] Michael Motsch, Martin Zeppenfeld, Pepijn W H Pinkse, and Gerhard Rempe. Cavity-enhanced Rayleigh scattering. *New Journal of Physics*, 12(6):063022, June 2010. DOI: 10.1088/1367-2630/12/6/063022.

[70] Jannis Hessenauer, Ksenia Weber, Julia Benedikter, Timo Gissibl, et al. Laser written mirror profiles for open-access fiber Fabry-Perot microcavities. *Optics Express*, 31(11):17380, May 2023. DOI: 10.1364/OE.481685.

[71] Johannes Höfer. *Characterization of fiber based microresonators with scanning cavity microscopy*. Bachelor's Thesis, Karlsruher Institut für Technologie (KIT), September 2021.

[72] Antonio Balena, Marco Bianco, Ferruccio Pisanello, and Massimo De Vittorio. Recent Advances on High-Speed and Holographic Two-Photon Direct Laser Writing. *Advanced Functional Materials*, 33(39):2211773, 2023. DOI: 10.1002/adfm.202211773.

[73] Joachim Fischer and Martin Wegener. Three-dimensional optical laser lithography beyond the diffraction limit. *Laser & Photonics Reviews*, 7(1):22–44, March 2012. DOI: 10.1002/lpor.201100046.

[74] Diana Gonzalez-Hernandez, Simonas Varapnickas, Andrea Bertoncini, Carlo Liberale, and Mangirdas Malinauskas. Micro-Optics 3D Printed via Multi-Photon Laser Lithography. *Advanced Optical Materials*, 11(1):2201701, 2023. DOI: 10.1002/adom.202201701.

[75] Zhao-Pei Liu, Yan Li, Yun-Feng Xiao, Bei-Bei Li, et al. Direct laser writing of whispering gallery microcavities by two-photon polymerization. *Applied Physics Letters*, 97(21):211105, November 2010. DOI: 10.1063/1.3517493.

[76] Simon Woska, Alexander Münchinger, Dominik Beutel, Eva Blasco, et al. Tunable photonic devices by 3D laser printing of liquid crystal elastomers. *Optical Materials Express*, 10(11):2928, November 2020. DOI: 10.1364/OME.402855.

[77] Tobias Grossmann, Simone Schleede, Mario Hauser, Torsten Beck, et al. Direct laser writing for active and passive high-Q polymer microdisks on silicon. *Optics Express*, 19(12):11451–11456, June 2011. DOI: 10.1364/OE.19.011451.

[78] Markus Deubel, Georg von Freymann, Martin Wegener, Suresh Pereira, et al. Direct laser writing of three-dimensional photonic-crystal templates for telecommunications. *Nature Materials*, 3(7):444–447, July 2004. DOI: 10.1038/nmat1155.

[79] Georg von Freymann, Alexandra Ledermann, Michael Thiel, Isabelle Staude, et al. Three-Dimensional Nanostructures for Photonics. *Advanced Functional Materials*, 20(7):1038–1052, 2010. DOI: 10.1002/adfm.200901838.

[80] Timo Gissibl, Simon Thiele, Alois Herkommer, and Harald Giessen. Two-photon direct laser writing of ultracompact multi-lens objectives. *Nature Photonics*, 10(8):554–560, August 2016. DOI: 10.1038/nphoton.2016.121.

[81] Jeremiah C. Williams, Hengky Chandrahalim, Joseph S. Suelzer, and Nicholas G. Usechak. Two-Photon Nanomachining of a Micromechanically Enhanced Optical Cavity Sensor on an Optical Fiber Tip. *Advanced Photonics Research*, 3(7):2100359, 2022. DOI: 10.1002/adpr.202100359.

[82] F. Ortiz-Huerta, L. Chen, M. Taverne, J. P. Hadden, et al. Fabrication of hybrid Fabry-Perot microcavity using two-photon lithography for single-photon sources. *Optics Express*, 26(25):33245, December 2018. DOI: 10.1364/OE.26.033245.

[83] A. Stute, B. Casabone, P. Schindler, T. Monz, et al. Tunable ion–photon entanglement in an optical cavity. *Nature*, 485(7399):482–485, May 2012. DOI: 10.1038/nature11120.

[84] B. Brandstätter, A. McClung, K. Schüppert, B. Casabone, et al. Integrated fiber-mirror ion trap for strong ion-cavity coupling. *Review of Scientific Instruments*, 84(12):123104, December 2013. DOI: 10.1063/1.4838696.

[85] Manuel Brekenfeld, Dominik Niemietz, Joseph Dale Christesen, and Gerhard Rempe. A quantum network node with crossed optical fibre cavities. *Nature Physics*, 16(6):647–651, June 2020. DOI: 10.1038/s41567-020-0855-3.

[86] Maximilian Pallmann, Timon Eichhorn, Julia Benedikter, Bernardo Casabone, et al. A highly stable and fully tunable open microcavity platform at cryogenic temperatures. *APL Photonics*, 8(4):046107, April 2023. DOI: 10.1063/5.0139003.

[87] Marc Schuhmann. *Characterization of 3D printed concave mirror structures in optical microcavities*. Bachelor thesis, Karlsruher Institut für Technologie (KIT).

[88] Matthias Mader, Jakob Reichel, Theodor W. Hänsch, and David Hunger. A scanning cavity microscope. *Nature Communications*, 6(1):7249, November 2015. DOI: 10.1038/ncomms8249.

[89] Klaus Reinhardt. Seltene Erden. *Chemie in unserer Zeit*, 18(1):24–34, 1984. DOI: 10.1002/ciuz.19840180104.

[90] Roger M Macfarlane. High-resolution laser spectroscopy of rare-earth doped insulators: a personal perspective. *Journal of Luminescence*, 100(1):1–20, December 2002. DOI: 10.1016/S0022-2313(02)00450-7.

[91] Bernard Jacquier and Guokui Liu. *Spectroscopic properties of rare earths in optical materials*. Springer Tsinghua University Press, Berlin Tsinghua, 2005.

[92] Walter Koechner. *Solid-state laser engineering :* Springer, Berlin ; 5., rev. and updated ed. Edition, 1999.

[93] Elias Snitzer. Rare earth fiber lasers. *Journal of the Less Common Metals*, 148(1):45–58, April 1989. DOI: 10.1016/0022-5088(89)90009-X.

[94] Anthony Barros, Nicolas Ledos, Rodolphe Valleix, Jérémy Cathalan, et al. High-Performance Rare-Earth-Free Fluorophores: toward White LEDs. *ACS Applied Optical Materials*, 2(5):834–841, May 2024. DOI: 10.1021/acsaom.4c00102.

[95] J. E. Geusic, H. M. Marcos, and L. G. Van Uitert. Laser oscillations in Nd-doped yttrium aluminium, yttrium gallium and gadolinium garnets. *Applied Physics Letters*, 4(10):182–184, May 1964. DOI: 10.1063/1.1753928.

[96] Philippe Goldner, Alban Ferrier, and Olivier Guillot-Noël. Chapter 267 - Rare Earth-Doped Crystals for Quantum Information Processing. In Jean-Claude G. Bünzli and Vitalij K. Pecharsky, editors, *Handbook on the Physics and Chemistry of Rare Earths*. Volume 46, pages 1–78. Elsevier, January 2015. DOI: 10.1016/B978-0-444-63260-9.00267-4.

[97] Charles Babin, Rainer Stöhr, Naoya Morioka, Tobias Linkewitz, et al. Fabrication and nanophotonic waveguide integration of silicon carbide colour centres with preserved spin-optical coherence. *Nature Materials*, 21(1):67–73, January 2022. DOI: 10.1038/s41563-021-01148-3.

[98] T. Utikal, E. Eichhammer, L. Petersen, A. Renn, et al. Spectroscopic detection and state preparation of a single praseodymium ion in a crystal. *Nature Communications*, 5(1):3627, May 2014. DOI: 10.1038/ncomms4627.

[99] F. Jelezko and J. Wrachtrup. Single defect centres in diamond: A review. *physica status solidi (a)*, 203(13):3207–3225, 2006. DOI: 10.1002/pssa.200671403.

[100] N. C. Chang, John B. Gruber, Richard P. Leavitt, and Clyde A. Morrison. Optical spectra, energy levels, and crystal-field analysis of tripositive rare earth ions in Y2O3. I. Kramers ions in C2 sites. *The Journal of Chemical Physics*, 76(8):3877–3889, April 1982. DOI: 10.1063/1.443530.

[101] Juris Meija, Tyler B. Coplen, Michael Berglund, Willi A. Brand, et al. Isotopic compositions of the elements 2013 (IUPAC Technical Report). *Pure and Applied Chemistry*, 88(3):293–306, March 2016. DOI: 10.1515/pac-2015-0503.

[102] Sacha Welinski, Alban Ferrier, Mikael Afzelius, and Philippe Goldner. High-resolution optical spectroscopy and magnetic properties of Yb^{3+} in Y_2SiO_5. *Physical Review B*, 94(15):155116, October 2016. DOI: 10.1103/PhysRevB.94.155116.

[103] Jonathan M. Kindem, John G. Bartholomew, Philip J. T. Woodburn, Tian Zhong, et al. Characterization of$^{171}Yb^{3+}$:$YVO_4$for photonic quantum technologies. *Physical Review B*, 98(2):024404, July 2018. DOI: 10.1103/PhysRevB.98.024404.

[104] Timon Eichhorn. *Cavity-enhanced Spectroscopy of Individual Europium-doped Nanoparticles*. Dissertation, Karlsruher Institut für Technologie (KIT), Karlsruhe, August 2024.

[105] Antonio Ortu, Alexey Tiranov, Sacha Welinski, Florian Fröwis, et al. Simultaneous coherence enhancement of optical and microwave transitions in solid-state electronic spins. *Nature Materials*, 17(8):671–675, August 2018. DOI: 10.1038/s41563-018-0138-x.

[106] Federico Chiossi, Eloïse Lafitte-Houssat, Alban Ferrier, Sacha Welinski, et al. Optical coherence and spin population dynamics in $^{171}Yb^{3+}$:Y_2SiO_5 single crystals. *Physical Review B*, 109(9):094114, March 2024. DOI: 10.1103/PhysRevB.109.094114.

[107] R. M. Macfarlane and R. M. Shelby. Sub-kilohertz optical linewidths of the $^7F_0$ $^5D_0$ transition in Y_2O_3:Eu^{3+}. *Optics Communications*, 39(3):169–171, October 1981. DOI: 10.1016/0030-4018(81)90048-1.

[108] C. W. Thiel, Thomas Böttger, and R. L. Cone. Rare-earth-doped materials for applications in quantum information storage and signal processing. *Journal of Luminescence*. Selected papers from DPC'10, 131(3):353–361, March 2011. DOI: 10.1016/j.jlumin.2010.12.015.

[109] Adam Kinos, David Hunger, Roman Kolesov, Klaus Mølmer, et al. Roadmap for Rare-earth Quantum Computing. March 2021. DOI: 10.48550/arXiv.2103.15743. URL: http://arxiv.org/abs/2103.15743 (visited on 03/21/2025).

[110] A. M. Stoneham. Shapes of Inhomogeneously Broadened Resonance Lines in Solids. *Reviews of Modern Physics*, 41(1):82–108, January 1969. DOI: 10.1103/RevModPhys.41.82.

[111] Flurin Könz, Y. Sun, C. W. Thiel, R. L. Cone, et al. Temperature and concentration dependence of optical dephasing, spectral-hole lifetime, and anisotropic absorption in Eu^{3+}:Y_2SiO_5. *Physical Review B*, 68(8):085109, August 2003. DOI: 10.1103/PhysRevB.68.085109.

[112] Lothaire Ulrich, Sacha Welinski, Anne Louchet-Chauvet, Julien de Rosny, et al. High Rejection and Frequency Agile Optical Filtering of RF Signals Using a Rare Earth Ion-Doped Crystal. *Journal of Lightwave Technology*, 40(20):6901–6910, October 2022. DOI: 10.1109/JLT.2022.3170216.

[113] Thomas Böttger, G. J. Pryde, C. W. Thiel, and R. L. Cone. Laser frequency stabilization at 1.5 microns using ultranarrow inhomogeneous absorption profiles in Er^{3+}:$LiYF_4$. *Journal of Luminescence*. Proceedings of the Ninth International Meeting on Hole Burning, Single Molecule, and Related Spectroscopies: Science and Applications, 127(1):83–88, November 2007. DOI: 10.1016/j.jlumin.2007.02.012.

[114] G. J Pryde, T Böttger, R. L Cone, and R. C. C Ward. Semiconductor lasers stabilized to spectral holes in rare earth crystals to a part in 1013 and their application to devices and spectroscopy. *Journal of Luminescence*. Proceedings of the Seventh International Meeting on Hole Burning, Single Molecules and Related Spectroscopies: Science and Applications, 98(1):309–315, July 2002. DOI: 10.1016/S0022-2313(02)00285-5.

[115] Mikael Afzelius, Christoph Simon, Hugues De Riedmatten, and Nicolas Gisin. Multimode quantum memory based on atomic frequency combs. *Physical Review A*, 79(5):052329, May 2009. DOI: 10.1103/PhysRevA.79.052329.

[116] Hugues de Riedmatten, Mikael Afzelius, Matthias U. Staudt, Christoph Simon, and Nicolas Gisin. A solid-state light–matter interface at the single-photon level. *Nature*, 456(7223):773–777, December 2008. DOI: 10.1038/nature07607.

[117] Roman Kolesov, Kangwei Xia, Rolf Reuter, Mohammad Jamali, et al. Mapping Spin Coherence of a Single Rare-Earth Ion in a Crystal onto a Single Photon Polarization State. *Physical Review Letters*, 111(12):120502, September 2013. DOI: 10.1103/PhysRevLett.111.120502.

[118] R. Kolesov, K. Xia, R. Reuter, R. Stöhr, et al. Optical detection of a single rare-earth ion in a crystal. *Nature Communications*, 3(1):1029, August 2012. DOI: 10.1038/ncomms2034.

[119] Chunming Yin, Milos Rancic, Gabriele G. de Boo, Nikolas Stavrias, et al. Optical addressing of an individual erbium ion in silicon. *Nature*, 497(7447):91–94, May 2013. DOI: 10.1038/nature12081.

[120] Jonathan M. Kindem, Andrei Ruskuc, John G. Bartholomew, Jake Rochman, et al. Control and single-shot readout of an ion embedded in a nanophotonic cavity. *Nature*, 580(7802):201–204, April 2020. DOI: 10.1038/s41586-020-2160-9.

[121] A. M. Dibos, M. Raha, C. M. Phenicie, and J. D. Thompson. Atomic Source of Single Photons in the Telecom Band. *Physical Review Letters*, 120(24):243601, June 2018. DOI: 10.1103/PhysRevLett.120.243601.

[122] Mouktik Raha, Songtao Chen, Christopher M. Phenicie, Salim Ourari, et al. Optical quantum nondemolition measurement of a single rare earth ion qubit. *Nature Communications*, 11(1):1605, March 2020. DOI: 10.1038/s41467-020-15138-7.

[123] Mehmet T. Uysal, Mouktik Raha, Songtao Chen, Christopher M. Phenicie, et al. Coherent Control of a Nuclear Spin via Interactions with a Rare-Earth Ion in the Solid State. *PRX Quantum*, 4(1):010323, March 2023. DOI: 10.1103/PRXQuantum.4.010323.

[124] Salim Ourari, Łukasz Dusanowski, Sebastian P. Horvath, Mehmet T. Uysal, et al. Indistinguishable telecom band photons from a single Er ion in the solid state. *Nature*, 620(7976):977–981, August 2023. DOI: 10.1038/s41586-023-06281-4.

[125] Bernardo Casabone, Julia Benedikter, Thomas Hümmer, Franziska Oehl, et al. Cavity-enhanced spectroscopy of a few-ion ensemble in Eu^{3+}:Y_2O_3. *New Journal of Physics*, 20(9):095006, September 2018. DOI: 10.1088/1367-2630/aadf68.

[126] Bernardo Casabone, Chetan Deshmukh, Shuping Liu, Diana Serrano, et al. Dynamic control of Purcell enhanced emission of erbium ions in nanoparticles. *Nature Communications*, 12(1):3570, June 2021. DOI: 10.1038/s41467-021-23632-9.

[127] Chetan Deshmukh, Eduardo Beattie, Bernardo Casabone, Samuele Grandi, et al. Detection of single ions in a nanoparticle coupled to a fiber cavity. *Optica*, 10(10):1339, October 2023. DOI: 10.1364/OPTICA.491692.

[128] Alexander Ulanowski, Benjamin Merkel, and Andreas Reiserer. Spectral multiplexing of telecom emitters with stable transition frequency. *Science Advances*, 8(43):eabo4538, October 2022. DOI: 10.1126/sciadv.abo4538.

[129] Alexander Ulanowski, Johannes Früh, Fabian Salamon, Adrian Holzäpfel, and Andreas Reiserer. Spectral Multiplexing of Rare-Earth Emitters in a Co-Doped Crystalline Membrane. *Advanced Optical Materials*, 12(15):2302897, 2024. DOI: 10.1002/adom.202302897.

[130] Benjamin Merkel, Alexander Ulanowski, and Andreas Reiserer. Coherent and Purcell-Enhanced Emission from Erbium Dopants in a Cryogenic High- Q Resonator. *Physical Review X*, 10(4):041025, November 2020. DOI: 10.1103/PhysRevX.10.041025.

[131] John G. Bartholomew, Karmel de Oliveira Lima, Alban Ferrier, and Philippe Goldner. Optical Line Width Broadening Mechanisms at the 10 kHz Level in Eu^{3+}:Y_2O_3 Nanoparticles. *Nano Letters*, 17(2):778–787, February 2017. DOI: 10.1021/acs.nanolett.6b03949.

[132] D. Serrano, C. Deshmukh, S. Liu, A. Tallaire, et al. Coherent optical and spin spectroscopy of nanoscale Pr^{3+}:Y_2O_3. *Physical Review B*, 100(14):144304, October 2019. DOI: 10.1103/PhysRevB.100.144304.

[133] H Forest and G Ban. Evidence for Eu Emission from Two Symmetry Sites in Eu^{3+}:Y_2O_3. 116(4), 1969.

[134] G. Schäfer and S. Scheller. Paramagnetische Resonanz von Er^{3+} in Y_2O_3. *Physik der kondensierten Materie*, 5(1):48–57, May 1966. DOI: 10.1007/BF02422881.

[135] Shuping Liu, Alexandre Fossati, Diana Serrano, Alexandre Tallaire, et al. Defect Engineering for Quantum Grade Rare-Earth Nanocrystals. *ACS Nano*, 14(8):9953–9962, August 2020. DOI: 10.1021/acsnano.0c02971.

[136] Karmel de Oliveira Lima, Rogéria Rocha Gonçalves, Domitille Giaume, Alban Ferrier, and Philippe Goldner. Influence of defects on sub-å optical linewidths in Eu^{3+}:Y_2O_3. *Journal of Luminescence*, 168:276–282, December 2015. DOI: 10.1016/j.jlumin.2015.08.012.

[137] A. Fossati, D. Serrano, S. Liu, A. Tallaire, et al. Optical line broadening mechanisms in rare-earth doped oxide nanocrystals. *Journal of Luminescence*, 263:120050, November 2023. DOI: 10.1016/j.jlumin.2023.120050.

[138] A. Perrot, Ph. Goldner, D. Giaume, M. Lovrić, et al. Narrow Optical Homogeneous Linewidths in Rare Earth Doped Nanocrystals. *Physical Review Letters*, 111(20):203601, November 2013. DOI: 10.1103/PhysRevLett.111.203601.

[139] Mohammed K. Alqedra, Chetan Deshmukh, Shuping Liu, Diana Serrano, et al. Optical coherence properties of Kramers' rare-earth ions at the nanoscale for quantum applications. *Physical Review B*, 108(7):075107, August 2023. DOI: 10.1103/PhysRevB.108.075107.

[140] J Karlsson, N Kunkel, A Ikesue, A Ferrier, and P Goldner. Nuclear spin coherence properties of $^{151}Eu^{3+}$ and $^{153}Eu^{3+}$ in a Y_2O_3 transparent ceramic. *Journal of Physics: Condensed Matter*, 29(12):125501, March 2017. DOI: 10.1088/1361-648X/aa529a.

[141] D. Serrano, J. Karlsson, A. Fossati, A. Ferrier, and P. Goldner. All-optical control of long-lived nuclear spins in rare-earth doped nanoparticles. *Nature Communications*, 9(1):2127, December 2018. DOI: 10.1038/s41467-018-04509-w.

[142] Thomas Hümmer. *Cavity-enhanced Hyperspectral Raman and Absorption Microscopy*. PhD Thesis, Ludwig-Maximilians-Universität München, 2019.

[143] Robin Wittmann. *Optical spectroscopy of trivalent ytterbium ions in solid state host materials at cryogenic temperatures*. Master's thesis, Karlsruher Institut für Technologie (KIT), Karlsruhe.

[144] D. A Wigley. A simple, versatile, capsule technique for low temperature experiments of long duration. *Cryogenics*, 6(6):359–361, December 1966. DOI: 10.1016/0011-2275(66)90138-X.

[145] S. Chandrasekaran, Y. Hariharan, T. S. Radhakrishnan, and V. Subramanian. Simple dipstick cryostat with versatile temperature controller for high thermal stability. *Cryogenics*, 19(11):669–672, November 1979. DOI: 10.1016/0011-2275(79)90070-5.

[146] F. Beaudoux, A. Ferrier, O. Guillot-Noël, T. Chanelière, et al. Emission of photon echoes in a strongly scattering medium. *Optics Express*, 19(16):15236, August 2011. DOI: 10.1364/OE.19.015236.

[147] Churna Bhandari, Cüneyt Şahin, Durga Paudyal, and Michael E. Flatté. Distinguishing erbium dopants in Y_2O_3 by site symmetry: *Ab initio* theory of two spin-photon interfaces. *Physical Review Materials*, 7(12):126201, December 2023. DOI: 10.1103/PhysRevMaterials.7.126201.

[148] Shobhit Gupta, Yizhong Huang, Shihan Liu, Yuxiang Pei, et al. Dual epitaxial telecom spin-photon interfaces with correlated long-lived coherence. October 2023. DOI: 10.48550/arXiv.2310.07120. URL: http://arxiv.org/abs/2310.07120 (visited on 03/06/2025).

[149] M. Businger, A. Tiranov, K. T. Kaczmarek, S. Welinski, et al. Optical Spin-Wave Storage in a Solid-State Hybridized Electron-Nuclear Spin Ensemble. *Physical Review Letters*, 124(5):053606, February 2020. DOI: 10.1103/PhysRevLett.124.053606.

[150] Sacha Welinski, Alexey Tiranov, Moritz Businger, Alban Ferrier, et al. Coherence Time Extension by Large-Scale Optical Spin Polarization in a Rare-Earth Doped Crystal. *Physical Review X*, 10(3):031060, September 2020. DOI: 10.1103/PhysRevX.10.031060.

[151] Kangwei Xia, Fiammetta Sardi, Colin Sauerzapf, Thomas Kornher, et al. Tunable microcavities coupled to rare-earth quantum emitters. *Optica*, 9(4):445, April 2022. DOI: 10.1364/OPTICA.453527.

[152] Zsolt Kis, Gabor Mandula, Krisztian Lengyel, Ivett Hajdara, et al. Homogeneous linewidth measurements of Yb^{3+} ions in congruent and stoichiometric lithium niobate crystals. *Optical Materials*, 37:845–853, November 2014. DOI: 10.1016/j.optmat.2014.09.022.

[153] Hee-Jin Lim, Sacha Welinski, Alban Ferrier, Philippe Goldner, and J. J. L. Morton. Coherent spin dynamics of ytterbium ions in yttrium orthosilicate. *Physical Review B*, 97(6):064409, February 2018. DOI: 10.1103/PhysRevB.97.064409.

[154] Y. Sun, R. L. Cone, L. Bigot, and B. Jacquier. Exceptionally narrow homogeneous linewidth in erbium-doped glasses. *Optics Letters*, 31(23):3453–3455, December 2006. DOI: 10.1364/OL.31.003453.

[155] Matthias U. Staudt, Sara R. Hastings-Simon, Mikael Afzelius, Didier Jaccard, et al. Investigations of optical coherence properties in an erbium-doped silicate fiber for quantum state storage. *Optics Communications*, 266(2):720–726, October 2006. DOI: 10.1016/j.optcom.2006.05.007.

[156] R. M. Macfarlane, Y. Sun, P. B. Sellin, and R. L. Cone. Optical Decoherence in Er^{3+}-Doped Silicate Fiber: Evidence for Coupled Spin-Elastic Tunneling Systems. *Physical Review Letters*, 96(3):033602, January 2006. DOI: 10.1103/PhysRevLett.96.033602.

[157] J. Hegarty, M. M. Broer, B. Golding, J. R. Simpson, and J. B. MacChesney. Photon Echoes below 1 K in a Nd^{3+} Doped Glass Fiber. *Physical Review Letters*, 51(22):2033–2035, November 1983. DOI: 10.1103/PhysRevLett.51.2033.

[158] Dapeng Ding, David van Driel, Lino M. C. Pereira, Jared F. Bauters, et al. Probing interacting two-level systems with rare-earth ions. *Physical Review B*, 101(1):014209, January 2020. DOI: 10.1103/PhysRevB.101.014209.

[159] Diana Serrano, Senthil Kumar Kuppusamy, Benoît Heinrich, Olaf Fuhr, et al. Ultra-narrow optical linewidths in rare-earth molecular crystals. *Nature*, 603(7900):241–246, March 2022. DOI: 10.1038/s41586-021-04316-2.

[160] Kuppusamy Senthil Kumar, Diana Serrano, Aline M. Nonat, Benoît Heinrich, et al. Optical spin-state polarization in a binuclear europium complex towards molecule-based coherent light-spin interfaces. *Nature Communications*, 12(1):2152, December 2021. DOI: 10.1038/s41467-021-22383-x.

[161] Senthil Kumar Kuppusamy, David Hunger, Mario Ruben, Philippe Goldner, and Diana Serrano. Spin-bearing molecules as optically addressable platforms for quantum technologies. *Nanophotonics*, 13(24):4357–4379, November 2024. DOI: 10.1515/nanoph-2024-0420.

[162] Romain Vincent, Svetlana Klyatskaya, Mario Ruben, Wolfgang Wernsdorfer, and Franck Balestro. Electronic read-out of a single nuclear spin using a molecular spin transistor. *Nature*, 488(7411):357–360, August 2012. DOI: 10.1038/nature11341.

[163] Jiang Liu, Yan-Cong Chen, Jun-Liang Liu, Veacheslav Vieru, et al. A Stable Pentagonal Bipyramidal Dy(III) Single-Ion Magnet with a Record Magnetization Reversal Barrier over 1000 K. *Journal of the American Chemical Society*, 138(16):5441–5450, April 2016. DOI: 10.1021/jacs.6b02638.

[164] C. Godfrin, A. Ferhat, R. Ballou, S. Klyatskaya, et al. Operating Quantum States in Single Magnetic Molecules: Implementation of Grover's Quantum Algorithm. *Physical Review Letters*, 119(18):187702, November 2017. DOI: 10.1103/PhysRevLett.119.187702.

[165] Riaz Hussain, Giuseppe Allodi, Alessandro Chiesa, Elena Garlatti, et al. Coherent Manipulation of a Molecular Ln-Based Nuclear Qudit Coupled to an Electron Qubit. *Journal of the American Chemical Society*, 140(31):9814–9818, August 2018. DOI: 10.1021/jacs.8b05934.

[166] Nicklas Ohlsson, R Krishna Mohan, and Stefan Kröll. Quantum computer hardware based on rare-earth-ion-doped inorganic crystals. *Optics Communications*, 201(1):71–77, January 2002. DOI: 10.1016/S0030-4018(01)01666-2.

[167] Janus H. Wesenberg, Klaus Mølmer, Lars Rippe, and Stefan Kröll. Scalable designs for quantum computing with rare-earth-ion-doped crystals. *Physical Review A*, 75(1):012304, January 2007. DOI: 10.1103/PhysRevA.75.012304.

[168] Carlo Bradac, Weibo Gao, Jacopo Forneris, Matthew E. Trusheim, and Igor Aharonovich. Quantum nanophotonics with group IV defects in diamond. *Nature Communications*, 10(1):5625, December 2019. DOI: 10.1038/s41467-019-13332-w.

[169] F. Kimiaee Asadi, N. Lauk, S. Wein, N. Sinclair, et al. Quantum repeaters with individual rare-earth ions at telecommunication wavelengths. *Quantum*, 2:93, September 2018. DOI: 10.22331/q-2018-09-13-93.

[170] Koen Binnemans. Interpretation of europium(III) spectra. *Coordination Chemistry Reviews*, 295:1–45, July 2015. DOI: 10.1016/j.ccr.2015.02.015.

[171] Elisabeth Kreidt, Christian Kruck, and Michael Seitz. Nonradiative deactivation of lanthanoid luminescence by multiphonon relaxation in molecular complexes. In *Handbook on the physics and chemistry of rare earths*. Volume 53, pages 35–79. Elsevier, Amsterdam, 2018.

[172] Christine Doffek and Michael Seitz. The Radiative Lifetime in Near-IR-Luminescent Ytterbium Cryptates: The Key to Extremely High Quantum Yields. *Angewandte Chemie International Edition*, 54(33):9719–9721, 2015. DOI: https://doi.org/10.1002/anie.201502475.

[173] Ori Ezrah Mor, Tal Ohana, Adrien Borne, Yael Diskin-Posner, et al. Tapered Optical Fibers Coated with Rare-Earth Complexes for Quantum Applications. *ACS Photonics*, 9(8):2676–2682, August 2022. DOI: 10.1021/acsphotonics.2c00330.

[174] Kasper S. Pedersen, Jan Dreiser, Høgni Weihe, Romain Sibille, et al. Design of Single-Molecule Magnets: Insufficiency of the Anisotropy Barrier as the Sole Criterion. *Inorganic Chemistry*, 54(15):7600–7606, August 2015. DOI: 10.1021/acs.inorgchem.5b01209.

[175] Necla Gündüz, Turgut Gündüz, Michael Hursthouse, Harold G. Parkes, et al. X -Ray crystallographic, 1 H, and 13 C nuclear magnetic resonance investigation of the potentially heptadentate ligand trensal, 2,2,2-tris(salicylideneimino)triethylamine. *Journal of the Chemical Society, Perkin Transactions 2*, 0(7):899–902, 1985. DOI: 10.1039/P29850000899.

[176] Kasper S. Pedersen, Ana-Maria Ariciu, Simon McAdams, Høgni Weihe, et al. Toward Molecular 4f Single-Ion Magnet Qubits. *Journal of the American Chemical Society*, 138(18):5801–5804, May 2016. DOI: 10.1021/jacs.6b02702.

[177] Victor Rollano, Marina C. de Ory, Christian D. Buch, Marcos Rubín-Osanz, et al. High cooperativity coupling to nuclear spins on a circuit quantum electrodynamics architecture. *Communications Physics*, 5(1):1–9, October 2022. DOI: 10.1038/s42005-022-01017-8.

[178] Senthil Kumar Kuppusamy, Evgenij Vasilenko, Weizhe Li, Jannis Hessenauer, et al. Observation of Narrow Optical Homogeneous Linewidth and Long Nuclear Spin Lifetimes in a Prototypical [Eu(trensal)] Complex. *The Journal of Physical Chemistry C*, 127(22):10670–10679, June 2023. DOI: 10.1021/acs.jpcc.3c02903.

[179] Kasper S. Pedersen, Jan Dreiser, Høgni Weihe, Romain Sibille, et al. CCDC 1044477: Experimental Crystal Structure Determination. 2016. DOI: 10.5517/CCDC.CSD.CC141VTV. URL: http://www.ccdc.cam.ac.uk/services/structure_request?id=doi:10.5517/ccdc.csd.cc141vtv&sid=DataCite (visited on 12/24/2024).

[180] Sören Schlittenhardt. *Magnetic and photoluminescent properties of rare-earth complexes of pyrazole-substituted 1,10-phenanthroline*. Dissertation, Karlsruher Institut für Technologie (KIT), Karlsruhe, 2023.

[181] S. Welinski, C. W. Thiel, J. Dajczgewand, A. Ferrier, et al. Effects of disorder on optical and electron spin linewidths in Er^{3+},Sc^{3+}:Y2SiO5. *Optical Materials*. In honor of Professor Georges Boulon for his outstanding contributions to Optical Materials, 63:69–75, January 2017. DOI: 10.1016/j.optmat.2016.09.039.

[182] C. W. Thiel, W. R. Babbitt, and R. L. Cone. Optical decoherence studies of yttrium oxyorthosilicate Y_2SiO_5 codoped with Er^{3+} and Eu^{3+} for optical signal processing and quantum information applications at 1.5 microns. *Physical Review B*, 85(17):174302, May 2012. DOI: 10.1103/PhysRevB.85.174302.

[183] Thomas Böttger, C. W. Thiel, R. L. Cone, and Y. Sun. Controlled compositional disorder in Er^{3+}:Y_2SiO_5 provides a wide-bandwidth spectral hole burning material at 1.5 µm. *Physical Review B*, 77(15):155125, April 2008. DOI: 10.1103/PhysRevB.77.155125.

[184] Andrew P. Bassett, Rik Van Deun, Peter Nockemann, Peter B. Glover, et al. Long-Lived Near-Infrared Luminescent Lanthanide Complexes of Imidodiphosphinate "Shell" Ligands. *Inorganic Chemistry*, 44(18):6140–6142, September 2005. DOI: 10.1021/ic0482436.

[185] Christian Kruck. *Design und Tuning einer neuen Klasse oktadentater Chelatliganden für lumineszente Lanthanoidkomplexe*. Dissertation, Eberhard Karls Universität Tübingen, Tübingen, 2018.

[186] Cea-Olivares, Raymundo, Díaz-Vera, Susana, López-Cardoso, Marcela, Tlahuext, Hugo, et al. CCDC 2246677: Experimental Crystal Structure Determination. DOI: 10.5517/CCDC.CSD.CC2FDVG5. URL: http://www.ccdc.cam.ac.uk/services/structure_request?id=doi:10.5517/ccdc.csd.cc2fdvg5&sid=DataCite (visited on 01/29/2025).

[187] Raymundo Cea-Olivares, Susana Díaz-Vera, Marcela López-Cardoso, Hugo Tlahuext, et al. The synthesis, spectroscopic characterization, and crystallographic study of the tetra-phenylimido-diphosphinates of Sc, Y, La, and Lu. *Journal of Molecular Structure*, 1297:136917, February 2024. DOI: 10.1016/j.molstruc.2023.136917.

[188] Oleg V. Dolomanov, Luc J. Bourhis, Richard J. Gildea, Judith A. K. Howard, and Horst Puschmann. *OLEX2* : a complete structure solution, refinement and analysis program. *Journal of Applied Crystallography*, 42(2):339–341, April 2009. DOI: 10.1107/S0021889808042726.

[189] Ashley J. Shin, Changling Zhao, Yi Shen, Claire E. Dickerson, et al. Toward liquid cell quantum sensing: Ytterbium complexes with ultranarrow absorption. *Science*, 385(6709):651–656, August 2024. DOI: 10.1126/science.adf7577.

[190] John G. Bartholomew, Jake Rochman, Tian Xie, Jonathan M. Kindem, et al. On-chip coherent microwave-to-optical transduction mediated by ytterbium in YVO_4. *Nature Communications*, 11(1):3266, December 2020. DOI: 10.1038/s41467-020-16996-x.

[191] Tian Xie, Rikuto Fukumori, Jiahui Li, and Andrei Faraon. Scalable microwave-to-optical transducers at single photon level with spins. July 2024. DOI: 10.48550/arXiv.2407.08879. URL: http://arxiv.org/abs/2407.08879 (visited on 01/23/2025).

[192] Jannis Hessenauer, Jonathan Körber, Misagh Ghezellou, Jawad Ul-Hassan, et al. Cavity enhancement of V2 centers in 4H-SiC with a fiber-based Fabry–Perot microcavity. *Optica Quantum*, 3(2):175–181, April 2025. DOI: 10.1364/OPTICAQ.557206.

[193] A. Gruber, A. Dräbenstedt, C. Tietz, L. Fleury, et al. Scanning Confocal Optical Microscopy and Magnetic Resonance on Single Defect Centers. *Science*, 276(5321):2012–2014, June 1997. DOI: 10.1126/science.276.5321.2012.

[194] Marcus W. Doherty, Neil B. Manson, Paul Delaney, Fedor Jelezko, et al. The nitrogen-vacancy colour centre in diamond. *Physics Reports*. The nitrogen-vacancy colour centre in diamond, 528(1):1–45, July 2013. DOI: 10.1016/j.physrep.2013.02.001.

[195] Aaron M. Day, Madison Sutula, Jonathan R. Dietz, Alexander Raun, et al. Electrical manipulation of telecom color centers in silicon. *Nature Communications*, 15(1):4722, June 2024. DOI: 10.1038/s41467-024-48968-w.

[196] M.N. Yoder. Wide bandgap semiconductor materials and devices. *IEEE Transactions on Electron Devices*, 43(10):1633–1636, October 1996. DOI: 10.1109/16.536807.

[197] Tsunenobu Kimoto and James A. Cooper. *Fundamentals of Silicon Carbide Technology: Growth, Characterization, Devices, and Applications*. Wiley, 1st edition, September 2014. DOI: 10.1002/9781118313534.

[198] Gernot Gruber. *Performance and Reliability Limiting Point Defects in SiC Power Devices*. PhD thesis, Technische Universtät Graz, Graz, 2016.

[199] Gang Liu, Blair R. Tuttle, and Sarit Dhar. Silicon carbide: A unique platform for metal-oxide-semiconductor physics. *Applied Physics Reviews*, 2(2):021307, June 2015. DOI: 10.1063/1.4922748.

[200] Peng Xing, Danhao Ma, Kelvin J. A. Ooi, Ju Won Choi, et al. CMOS-Compatible PECVD Silicon Carbide Platform for Linear and Nonlinear Optics. *ACS Photonics*, 6(5):1162–1167, May 2019. DOI: 10.1021/acsphotonics.8b01468.

[201] Daniil M. Lukin, Melissa A. Guidry, and Jelena Vučković. Integrated Quantum Photonics with Silicon Carbide: Challenges and Prospects. *PRX Quantum*, 1(2):020102, December 2020. DOI: 10.1103/PRXQuantum.1.020102.

[202] William F. Koehl, Berk Diler, Samuel J. Whiteley, Alexandre Bourassa, et al. Resonant optical spectroscopy and coherent control of Cr^{4+} spin ensembles in SiC and GaN. *Physical Review B*, 95(3):035207, January 2017. DOI: 10.1103/PhysRevB.95.035207.

[203] Gary Wolfowicz, Christopher P. Anderson, Berk Diler, Oleg G. Poluektov, et al. Vanadium spin qubits as telecom quantum emitters in silicon carbide. *Science Advances*, 6(18):eaaz1192, May 2020. DOI: 10.1126/sciadv.aaz1192.

[204] Kevin C. Miao, Joseph P. Blanton, Christopher P. Anderson, Alexandre Bourassa, et al. Universal coherence protection in a solid-state spin qubit. *Science*, 369(6510):1493–1497, September 2020. DOI: 10.1126/science.abc5186.

[205] David J. Christle, Paul V. Klimov, Charles F. De Las Casas, Krisztián Szász, et al. Isolated Spin Qubits in SiC with a High-Fidelity Infrared Spin-to-Photon Interface. *Physical Review X*, 7(2):021046, June 2017. DOI: 10.1103/PhysRevX.7.021046.

[206] Stefania Castelletto, Alberto Peruzzo, Cristian Bonato, Brett C. Johnson, et al. Silicon Carbide Photonics Bridging Quantum Technology. *ACS Photonics*, 9(5):1434–1457, May 2022. DOI: 10.1021/acsphotonics.1c01775.

[207] Ö. O. Soykal, Pratibha Dev, and Sophia E. Economou. Silicon vacancy center in 4H-SiC: Electronic structure and spin-photon interfaces. *Physical Review B*, 93(8):081207, February 2016. DOI: 10.1103/PhysRevB.93.081207.

[208] Erik Janzén, Adam Gali, Patrick Carlsson, Andreas Gällström, et al. The silicon vacancy in SiC. *Physica B: Condensed Matter*, 404(22):4354–4358, December 2009. DOI: 10.1016/j.physb.2009.09.023.

[209] Péter Udvarhelyi, Gergő Thiering, Naoya Morioka, Charles Babin, et al. Vibronic States and Their Effect on the Temperature and Strain Dependence of Silicon-Vacancy Qubits in 4H-SiC. *Physical Review Applied*, 13(5):054017, May 2020. DOI: 10.1103/PhysRevApplied.13.054017.

[210] Péter Udvarhelyi, Roland Nagy, Florian Kaiser, Sang-Yun Lee, et al. Spectrally Stable Defect Qubits with no Inversion Symmetry for Robust Spin-To-Photon Interface. *Physical Review Applied*, 11(4):044022, April 2019. DOI: 10.1103/PhysRevApplied.11.044022.

[211] Roland Nagy, Matthias Widmann, Matthias Niethammer, Durga B. R. Dasari, et al. Quantum Properties of Dichroic Silicon Vacancies in Silicon Carbide. *Physical Review Applied*, 9(3):034022, March 2018. DOI: 10.1103/PhysRevApplied.9.034022.

[212] Roland Nagy, Matthias Niethammer, Matthias Widmann, Yu-Chen Chen, et al. High-fidelity spin and optical control of single silicon-vacancy centres in silicon carbide. *Nature Communications*, 10(1):1954, December 2019. DOI: 10.1038/s41467-019-09873-9.

[213] Naoya Morioka, Charles Babin, Roland Nagy, Izel Gediz, et al. Spin-controlled generation of indistinguishable and distinguishable photons from silicon vacancy centres in silicon carbide. *Nature Communications*, 11(1):2516, May 2020. DOI: 10.1038/s41467-020-16330-5.

[214] Hunter B. Banks, Öney O. Soykal, Rachael L. Myers-Ward, D. Kurt Gaskill, et al. Resonant Optical Spin Initialization and Readout of Single Silicon Vacancies in 4H-SiC. *Physical Review Applied*, 11(2):024013, February 2019. DOI: 10.1103/PhysRevApplied.11.024013.

[215] S. A. Tarasenko, A. V. Poshakinskiy, D. Simin, V. A. Soltamov, et al. Spin and Optical Properties of Silicon Vacancies in Silicon Carbide – A Review. *physica status solidi (b)*, 255(1):1700258, 2018. DOI: 10.1002/pssb.201700258.

[216] Di Liu, Florian Kaiser, Vladislav Bushmakin, Erik Hesselmeier, et al. The silicon vacancy centers in SiC: determination of intrinsic spin dynamics for integrated quantum photonics. *npj Quantum Information*, 10(1):1–9, July 2024. DOI: 10.1038/s41534-024-00861-6.

[217] Erik Hesselmeier, Pierre Kuna, Wolfgang Knolle, Florian Kaiser, et al. High-Fidelity Optical Readout of a Nuclear-Spin Qubit in Silicon Carbide. *Physical Review Letters*, 132(18):180804, May 2024. DOI: 10.1103/PhysRevLett.132.180804.

[218] Xiao-Yi Lai, Ren-Zhou Fang, Tao Li, Ren-Zhu Su, et al. Single-Shot Readout of a Nuclear Spin in Silicon Carbide. *Physical Review Letters*, 132(18):180803, May 2024. DOI: 10.1103/PhysRevLett.132.180803.

[219] Daniil M. Lukin, Melissa A. Guidry, Joshua Yang, Misagh Ghezellou, et al. Two-Emitter Multimode Cavity Quantum Electrodynamics in Thin-Film Silicon Carbide Photonics. *Physical Review X*, 13(1):011005, January 2023. DOI: 10.1103/PhysRevX.13.011005.

[220] Daniil M. Lukin, Alexander D. White, Rahul Trivedi, Melissa A. Guidry, et al. Spectrally reconfigurable quantum emitters enabled by optimized fast modulation. *npj Quantum Information*, 6(1):1–9, September 2020. DOI: 10.1038/s41534-020-00310-0.

[221] Viktoria Yurgens, Yannik Fontana, Andrea Corazza, Brendan J. Shields, et al. Cavity-assisted resonance fluorescence from a nitrogen-vacancy center in diamond. *npj Quantum Information*, 10(1):1–8, November 2024. DOI: 10.1038/s41534-024-00915-9.

[222] Rigel Zifkin, César Daniel Rodríguez Rosenblueth, Erika Janitz, Yannik Fontana, and Lilian Childress. Lifetime Reduction of Single Germanium-Vacancy Centers in Diamond via a Tunable Open Microcavity. *PRX Quantum*, 5(3):030308, July 2024. DOI: 10.1103/PRXQuantum.5.030308.

[223] Maximilian Ruf, Noel H. Wan, Hyeongrak Choi, Dirk Englund, and Ronald Hanson. Quantum networks based on color centers in diamond. *Journal of Applied Physics*, 130(7):070901, August 2021. DOI: 10.1063/5.0056534.

[224] Yanik Herrmann, Julius Fischer, Stijn Scheijen, Cornelis F. J. Wolfs, et al. A low-temperature tunable microcavity featuring high passive stability and microwave integration. *AVS Quantum Science*, 6(4):041401, December 2024. DOI: 10.1116/5.0233296.

[225] Weizhe Li. *Cavity-Enhanced Spectroscopy of Molecular Rare-earth-ion Complex*. Master's thesis, Karlsruher Institut für Technologie (KIT), Karlsruhe, November 2023.

[226] J. Maisch, J. Grammel, N. Tran, M. Jetter, et al. Investigation of Purcell enhancement of quantum dots emitting in the telecom O-band with an open fiber cavity. *Physical Review B*, 110(16):165301, October 2024. DOI: 10.1103/PhysRevB.110.165301.

[227] Daniel Najer, Immo Söllner, Pavel Sekatski, Vincent Dolique, et al. A gated quantum dot strongly coupled to an optical microcavity. *Nature*, 575(7784):622–627, November 2019. DOI: 10.1038/s41586-019-1709-y.

[228] Jonah Heiler, Jonathan Körber, Erik Hesselmeier, Pierre Kuna, et al. Spectral stability of V2 centres in sub-micron 4H-SiC membranes. *npj Quantum Materials*, 9(1):1–8, April 2024. DOI: 10.1038/s41535-024-00644-4.

[229] Suzanne B Van Dam, Maximilian Ruf, and Ronald Hanson. Optimal design of diamond-air microcavities for quantum networks using an analytical approach. *New Journal of Physics*, 20(11):115004, November 2018. DOI: 10.1088/1367-2630/aaec29.

[230] Jonathan Körber, Maximilian Pallmann, Julia Heupel, Rainer Stöhr, et al. Scanning Cavity Microscopy of a Single-Crystal Diamond Membrane. *Physical Review Applied*, 19(6):064057, June 2023. DOI: 10.1103/PhysRevApplied.19.064057.

[231] Erika Janitz, Maximilian Ruf, Mark Dimock, Alexandre Bourassa, et al. Fabry-Perot microcavity for diamond-based photonics. *Physical Review A*, 92(4):043844, October 2015. DOI: 10.1103/PhysRevA.92.043844.

[232] Maximilian Pallmann. *Purcell-enhanced emission and collective effects of nitrogen-vacancy centers in diamond coupled to a microcavity*. Dissertation, Karlsruher Institut für Technologie (KIT), Karlsruhe, May 2023.

[233] Shunchong Wang, Minjie Zhan, Gang Wang, Hongwen Xuan, et al. 4H-SiC: a new nonlinear material for midinfrared lasers. *Laser & Photonics Reviews*, 7(5):831–838, 2013. DOI: 10.1002/lpor.201300068.

[234] Jonathan Körber, Jonah Heiler, Philipp Fuchs, Philipp Flad, et al. Fluorescence Enhancement of Single V2 Centers in a 4H-SiC Cavity Antenna. *Nano Letters*, 24(30):9289–9295, July 2024. DOI: 10.1021/acs.nanolett.4c02162.

[235] Rebecca E. K. Fishman, Raj N. Patel, David A. Hopper, Tzu-Yung Huang, and Lee C. Bassett. Photon emission correlation spectroscopy as an analytical tool for quantum defects. *PRX Quantum*, 4(1):010202, March 2023. DOI: 10.1103/PRXQuantum.4.010202.

[236] Maximilian Pallmann, Kerim Köster, Yuan Zhang, Julia Heupel, et al. Cavity-Mediated Collective Emission from Few Emitters in a Diamond Membrane. *Physical Review X*, 14(4):041055, December 2024. DOI: 10.1103/PhysRevX.14.041055.

[237] Christian Kurtsiefer, Patrick Zarda, Sonja Mayer, and Harald Weinfurter. The breakdown flash of silicon avalanche photodiodes-back door for eavesdropper attacks? *Journal of Modern Optics*, 48(13):2039–2047, November 2001. DOI: 10.1080/09500340108240905.

[238] Marina Radulaski, Matthias Widmann, Matthias Niethammer, Jingyuan Linda Zhang, et al. Scalable Quantum Photonics with Single Color Centers in Silicon Carbide. *Nano Letters*, 17(3):1782–1786, March 2017. DOI: 10.1021/acs.nanolett.6b05102.

[239] F. Sardi, T. Kornher, M. Widmann, R. Kolesov, et al. Scalable production of solid-immersion lenses for quantum emitters in silicon carbide. *Applied Physics Letters*, 117(2):022105, July 2020. DOI: 10.1063/5.0011366.

[240] David O. Bracher, Xingyu Zhang, and Evelyn L. Hu. Selective Purcell enhancement of two closely linked zero-phonon transitions of a silicon carbide color center. *Proceedings of the National Academy of Sciences*, 114(16):4060–4065, April 2017. DOI: 10.1073/pnas.1704219114.

[241] Alexander L Crook, Christopher P Anderson, Kevin C Miao, Alexandre Bourassa, et al. Purcell enhancement of a single silicon carbide color center with coherent spin control. *Nano letters*, 20(5):3427–3434, 2020.

[242] Timon Eichhorn, Nicholas Jobbitt, Sören Bieling, Shuping Liu, et al. Multimodal Purcell enhancement and optical coherence of Eu^{3+} ions in a single nanoparticle coupled to a microcavity. *Nanophotonics*, February 2025. DOI: 10.1515/nanoph-2024-0721.

[243] Stefan Bogdanović, Madelaine S. Z. Liddy, Suzanne B. van Dam, Lisanne C. Coenen, et al. Robust nano-fabrication of an integrated platform for spin control in a tunable microcavity. *APL Photonics*, 2(12):126101, November 2017. DOI: 10.1063/1.5001144.

[244] L. Nicolas, M. Businger, T. Sanchez Mejia, A. Tiranov, et al. Coherent optical-microwave interface for manipulation of low-field electronic clock transitions in $^{171}Yb^{3+}$:Y_2SiO_5. *npj Quantum Information*, 9(1):1–7, March 2023. DOI: 10.1038/s41534-023-00687-8.

[245] D. Simin, H. Kraus, A. Sperlich, T. Ohshima, et al. Locking of electron spin coherence above 20 ms in natural silicon carbide. *Physical Review B*, 95(16):161201, April 2017. DOI: 10.1103/PhysRevB.95.161201.

[246] Eloise Lafitte-Houssat, Alban Ferrier, Mikael Afzelius, Perrine Berger, et al. Optical homogeneous and inhomogeneous linewidths in $^{171}Yb^{3+}$:Y_2SiO_5. *Optics and Spectroscopy*, 130(1):23, 2022. DOI: 10.21883/OS.2022.01.51885.29-21.

[247] Eloïse Lafitte-Houssat, Alban Ferrier, Sacha Welinski, Loïc Morvan, et al. Optical and spin inhomogeneous linewidths in $^{171}Yb^{3+}$:Y_2SiO_5. *Optical Materials: X*, 14:100153, May 2022. DOI: 10.1016/j.omx.2022.100153.

[248] Lukas Novotny and Bert Hecht. *Principles of nano-optics*. Cambridge University Press, Cambridge [u.a.] : 1. publ., repr. with corrections edition, 2007.

Acknowledgments

Finally, I arrive at the most pleasant part of this thesis: thanking all the excellent people that contributed to this work, without whom this work would not be as complete, and the time spent on it far less fun.

First and foremost, I want to sincerely thank my advisor David Hunger, for taking me onto this five year journey into experimental quantum optics. There are many things I am grateful for: Your remarkable quick thinking and endless streams of ideas, your pragmatic advice and sometimes also hands-on help in the lab, your optimism that things will work out and your enthusiasm when they finally do. I felt that during my time here, I have learned a lot, as an experimentalist and as a physicist, thanks to your guidance. Most importantly, I want to thank you for giving me a lot of freedom in letting me choose my projects, and always giving me the feeling to have my back. I could always rely on you and be open with you, which I really appreciate.

I want to thank Professor Dr. Heinz Kalt for agreeing to co-supervise this thesis. During my time as a master student in his group, I first came to enjoy working in an optics lab, which certainly played a big role in my decision to pursue a doctoral degree. His way of looking at physics, in understanding it from the basics without taking any shortcuts, and explaining things as complicated as they have to be, but not more, have certainly shaped my thinking as a physicist.

Next, I want to thank my colleagues in the research group:
Thanks to Timon, for making me feel welcome in the group when I started here. I have really enjoyed our many discussions, both physics and non-physics related, over the years. Thanks to Nick, for proofreading the bulk of this thesis, and generally taking over a a metric ton of unpleasant work, not just from me but the whole group. Your determination to help out others is remarkable, and I think will be rewarded in time. Thanks to my long-time office mates, Shalom and Jonas. Besides our three person discussions about the very basics of physics, which sometimes spiraled out of control: Jonas for expert IT- and programming help during day- and night-times, and Shalom for tea, being a source of calm in all the chaos, and sometimes, unexpectedly, and hilariously being the source of chaos when everything seems calm. Thanks to Evgenij, for suffering with me through the same ups and downs of the PhD journey, often in a synchronized manner. I enjoyed our 'impromptu solutions" (Pfusch) during the early times on the various dipstick experiments. Thanks to Max, for letting me take over his cavity baby and showing me how to tame it. Thanks to Kerim for your contagious good mood and all the discussion on the SiC project. It was nice to see the two experiments starting to work almost simultaneously. Thanks to Jeremias for the interesting discussions about physics,

where I learned a lot, and food, where we almost always agreed. It is always nice to see how much physics can be conveyed by wild arm movements and the occasional dance move. Thanks to Svenja, for being patient with me while I finished the SiC experiments. I enjoyed showing you the ropes of the cryo-cavity, and hopefully it will soon produce nice results on the third completely different emitter. Thanks to Andras and Vishnu, for bringing much needed fresh energy in the group. Thanks to Vishnu for the many discussions about the ensemble spectroscopy.
I want to thank 'my 'master students Xiaoyu Cheng, Christina Ioannou, and Robin Wittmann and bachelors students Johannes Höfer and Christopher Hinz. Their hard work ultimately lead to a lot of the results in this thesis. I know that this was not always easy, especially in the beginning where we did not have established setups and a lot of trial- and error was involved. I feel that I have learned a lot from all our discussions and your questions, and hope to have contributed a small part to your development as scientists as well.
All the other current and former members of the group, I want to thank for all the good times in and outside of the lab, and the always pleasant and helpful atmosphere.

Very importantly, I want to thank Jonathan Körber for the excellent cooperation on the SiC project. You initiated this project, but were always nothing but supportive, even when it became clear that I would take over the cavity experimental part. I think this project was special because we shared a sense of motivation, and a similar approach both in the lab and when discussing physics.

I also want to thank the many cooperation partners on the material site: Thanks to Philippe Goldner and Diana Serrano for the nanocrystals and hosting me in Paris. Thanks to the Ruben group at KIT and the Seitz group in Tübingen, especially my fellow PhD students Sören and Timo, for the nice collaborations and discussions.

Besides the scientific part, there are the people that keep the institute running and allow us to mess around in the lab. Thanks to Steffi Baatz and Claudia Alaya for handling all the paperwork, and solving all questions organizational. Thanks to Michael Meyer and his team from the workshop for machining all kinds of, sometimes unreasonable, parts and making technical drawings out of pencil sketches. Thanks to Jannis Reth, Patrik Rust, and Kevin Zych for the help in fixing all things electronics. Thanks to Michael Pfirrmann for taking care of the Helium infrastructre and always finding a way to procure a can of Helium when desperately needed. Thanks to Lars Behrens for IT infrastructure support and thanks to Kornelia Hugle for managing the chemistry lab. Thanks to everyone who proofread parts of this thesis and has made it better.

Finally, I want to thank my family and my friends for putting up with me and my thesis related antics, and for reminding me that there is much fun and Dolce Vita to be had outside of a lab.